DISSERTATION | DOCTORAL THESIS

Titel | Title

Stationary optomechanical entanglement detection

verfasst von | submitted by

Corentin Gut BSc MSc

angestrebter akademischer Grad | in partial fulfilment of the requirements for the degree of

Doktor der Naturwissenschaften (Dr.rer.nat.)

Wien | Vienna, 2024

Studienkennzahl lt. Studienblatt | Degree programme code as it appears on the student record sheet:	UA 796 605 411
Dissertationsgebiet lt. Studienblatt | Field of study as it appears on the student record sheet:	Physik
Betreut von | Supervisor:	Univ.-Prof. Dr. Markus Aspelmeyer

ABSTRACTS

Measurement apparatuses mark the boundary between the probabilistic quantum description of nature, and the intrinsic definiteness of observations; this is the Heisenberg–von Neumann cut between unitary and projective dynamics, in the related models of measurement devices. The closer the cut is to the observer, the larger their knowledge and control of the apparatus' quantum state – possibly enabling quantum enhancement of the measurement. We propose a protocol to demonstrate that the motion of an object is entangled with the light probing its position in optomechanical devices; thus shifting the cut towards the photodetection.

Our scheme applies in a broad range of parameters and for comparatively little experimental efforts (e.g., datasets generated for another purpose can be used). In particular, it applies to the stationary regime where optomechanical entanglement has not yet been experimentally verified. Theoretical analyses of five currently existing implementations (membranes, photonic crystal, and levitated nano-particles with and without cavity) indicate that they are limited by the presence of additional mechanical modes. We find that reducing the temperature of the mechanical bath(s) is the most efficient way to overcome the limitations. Additionally, high temperatures set stringent constraints on the stability of the mechanical frequency during the measurement.

We perform extensive, systematic, and creative analyses of experimental datasets from four of these devices. The gathered experience highlighted several pitfalls in certifying Gaussian entanglement from measurement records and we propose solutions to mitigate them. Unfortunately, we could not demonstrate entanglement convincingly

Our protocol entails, first, a general verification theorem to infer light–mechanics entanglement form entanglement between measurable modes of light only. Second, we propose an explicit procedure based on successive and non-overlapping temporal modes of light; it is designed for high-Q mechanical devices, in the high-temperature limit, and in the unresolved sideband regime or without an optical cavity. Third, the exact symbolic expression of the measured state can be computed, enabling fast parameter sweeps. Fourth, we provide an explicit approximate expression for the Einstein-Podolsky-Rosen (EPR) variance test of entanglement. It allows to understand and interpret physically how our protocol detects entanglement in terms of the devices' parameters.

ZUSAMMENFASSUNG (GERMAN SUMMARY)

Messapparate markieren die Grenze zwischen der probabilistischen Quantenbeschreibung der Natur und der intrinsischen Determiniertheit von Beobachtungen; dies ist der Heisenberg-von Neumann-Schnitt zwischen unitärer und projektiver Dynamik in den entsprechenden Modellen von Messgeräten. Je näher der Schnitt beim Beobachter liegt, desto größer ist Wissen und aie Kontrolle über den Quantenzustand des Apparats - was möglicherweise eine quantenverbesserte Messung ermöglichen könnte. Wir schlagen ein Protokoll vor, mit dem gezeigt werden kann, dass die Bewegung eines Objekts mit dem Licht verschränkt ist, welches seine Position in optomechanischen Systemen misst; dadurch verschiebt sich der Schnitt in Richtung der Photodetektion.

Unser Protokoll ist in einem weiten Regime von Parametern und mit vergleichsweise geringem experimentellem Aufwand anwendbar (z. B. auf Datensätze, welche für andere Zwecke erzeugt wurden, können hierfür verwendet werden). Insbesondere gilt es für den stationäre Systeme, in dem die optomechanische Verschränkung noch nicht experimentell verifiziert wurde. Theoretische Analysen von fünf derzeit existierenden Implementierungen (Membranen, photonische Kristalle und levitierte Nanoteilschen mit und ohne optischen Resonator) zeigen, dass die Beobachtung von Verschränkung von zusätzlicher mechanischer Moden verhindert wird. Wir stellen fest, dass die Absenkung der Temperatur des mechanischen Bades (der mechanischen Bäder) der effizienteste Weg ist, um diese Einschränkungen zu überwinden. Außerdem stellen hohe Temperaturen strenge Anforderungen an die Stabilität der mechanischen Frequenz während der Messung.

Wir führen umfangreiche, systematische und kreative Analysen von experimentellen Datensätzen von vier dieser Geräte durch. Die gesammelten Erfahrungen haben mehrere Fallstricke beim Nachweis der Gaußschen Verschränkung anhand von Messdaten aufgezeigt und wir schlagen Lösungen vor, um diese zu vermeiden. Leider konnten wir Verschränkung nicht überzeugend nachweisen

Unser Protokoll beinhaltet erstens ein allgemeines Verifikationstheorem, um von der Verschränkung zwischen messbaren Lichtmoden auf die Verschränkung zwischen Licht und Mechanik zu schließen. Zweitens schlagen wir ein explizites Verfahren vor, das auf sequenziell und nicht überlappenden zeitlichen Lichtmoden basiert; es ist für mechanische Geräte mit hohem Q, im Hochtemperaturbereich und im unaufgelösten Seitenbandregime oder ohne optischen Resonator konzipiert. Drittens kann der genaue analytische Ausdruck des gemessenen Zustands berechnet werden, was schnelle Parametersweeps ermöglicht. Viertens liefern wir einen expliziten Näher-

ungsausdruck für den Einstein-Podolsky-Rosen (EPR) Varianz Verschränkungstest. Er erlaubt use physikalisch zu verstehen, wie unser Protokoll Verschränkung in Bezug auf die Parameter der Geräte erkennt.

ACKNOWLEDGEMENTS

The Ph.D. experience is a privilege and I want to acknowledge that I benefited from systemic support for accessing and pursuing this valuable and enriching experience. I have asked many questions and received accordingly many answers; I am thankful to all my teachers who took the time to explain to me everything, more, the rest, several times.

I wish to express my sincere gratitude to Markus Aspelmeyer for offering this adventure and providing a secure, worry-free, and resourceful research environment. I am also profoundly thankful to Klemens Hammerer, who guided the most important parts of my research. I acknowledge generous and friendly scientific exchanges with Aisling Johnson, Albert Schliesser, Claus Gärtner, Jason Hölscher-Obermaier, Jens Eisert, Jinkun Guo, Joshua Slater, Kahan Dare, Klemens Winkler, Lorenzo Magrini, Manuel Reisenbauer, Marek Gluza, Nathan Walk, Ramon Mogadas Nia, Sebastian Hofer, Simon Gröblacher, Su Direkci, Uros Delic, Victor Camerena, Witlef Wieczorek, and Yanbei Chen who contributed directly to the material presented in this thesis.

I grew scientifically a lot thanks to the thoughtfully crafted OMT training programme (and its smooth and cadenced unfolding made possible by Antonnella). Thank you OMT-fellows for sharing with me your thoughts and insights on physics, for taking me to your labs, clean rooms, and favourite restaurants, but also to karaoke and a cricket game. I learnt so much about the diversity in-and-of optomechanics while hanging out with you! I am very grateful for the time I spent in the group of Florian Marquardt in Erlangen: for the numerous exchanges, the fresh ideas, and all the cake.

I cannot think of an important thought I had in the last years that I would not submit to the scrutiny of Klemens Winkler. Although I know it well by now, I continue to be amazed by your thoroughness and precision, Klemens. Thank you for being the reliable scientist and friend with whom I learnt and discovered the vast majority of the content in the coming pages.

Thank you Jason, Sebastian, Ramon, Josh, Claus, and Witlef for teaching me The Basics, as well as the way to the entrance of Chelsea (I wished you'd tell me how to get out too). Thank you Jonas for the lessons on POVM's, the bike, and the good tips around Hannover. Thank you Sahand for the meshgrid trick and the best selection of coffees and craft beers in town. Thank you Hannover-theorists for the hands-on hut-building experiences (free of injuries). Thank you Uros for being my consistent reference for everything optomechanical.

Thank you Tobias for explaining noise to me. Thank you Hans for the engaging statistics discussions, advice on night trains, and your insights on physics of slow mo. Thank you Lorenzo for showing me that cavities are over-rated. Thank you Jeremias for the fabulous culinary experiences. Thank you Mathias for all the details and secret tips on Austrian wine, soldering, and Vienna. Thank you 3rd-floor-office-levitation-people for your patience with my questions and sharing wonder at the construction works. Thank you Aisling, Philip, Gerard, and Nikolai for your kindness and advice along the way. Thank you Ayub, Victor, and Rémi for your supporting words and taking me on your adventures. Thanks all of you Aspels for being friendly and resourceful colleagues; I cultivated my awe for experimental realisations in your close company – it is a precious gift that I will nourish further! This last year, I really enjoyed the late afternoon trans-Atlantic meetings with Su and Yanbei and the impressive science that came out of it.

Thank you Alain for teaching me how to quiet my mind and direct my energy (overflow). Thank you Wolfgang for the German language and these first steps towards science in engaged, long, and late discussions. While researching entangled mirrors, I got entangled with quite a crowd of beautiful minds, in Switzerland, Germany, and Austria. Thank you my friends, for your friendship that I have the chance to enjoy across borders, for teaching me some essentials of how I think today, for taking care of me, and for the time and attention that your offer in all these experiences that make me up.

Lastly, it is my immense luck that there are Alysée, Michelle, Philippe, Florian, Melvin, and Kim. I could receive all the valuable teachings I've just made a big fuzz of because you enable it in the first place.

SOFTWARE AND DATA AVAILABILITY

All the non-free software listed below were used with a licence from the University of Vienna. This PDF document was generated on Overleaf; the LaTeX-template is `classicthesis` (v4.6) by A. Miede and I. Pletikosić. The text was improved (e.g. minimising language mistakes and improving the reading flow) with AI-based grammar and paraphrasing tools, namely: QuillBot, ChatGPT4, and Writefull; I reviewed every changes and a version of the thesis prior using AI tools is available on [Gut24, `Thesis_beforeAIinputs.zip`].

All images, figures and plots in this document were produced with the Python library Matplotlib [Hun07] (v3.8.2) and the Free, open source, vector graphics editor Inkscape (v1.0.2). The colours are Paul Tol's "medium-contrast" palette, which is colour-blind safe with

optimised contrast for printing in greyscale [Tol] – be considerate of resources and refrain from printing this document if possible.

Calculations and data were performed and generated with: Wolfram Mathematica (v13.3.1.0) for symbolic calculations; Python (v3.9.2) with various libraries, notably NumPy (v1.22.4) [Har+20]; Jupyter-notebook (v6.4.7); and Matlab (vR2021a and vR2012a), with the convex optimisation package CVX [GB14]. The Mathematica code for cavity devices was developed by Klemens Winkler and myself, with contributions from Sebastian Hofer [Gut24, compute exactCM 1MechMode .nb] [1]. The Mathematica code for cavityless devices is the work of Klemens Winker [Gut24, cavless anaSim .nb] [2]. The Python code simulating the cavityless levitated particle in back-scattering configuration [Gut24, cavless numSim .py] [3] is the work of Lorenzo Magrini. [4]

I participated in none of the experimental work to produce and gather the datasets studied in the following; detailed credit is provided in the text. I analysed the experimental data with Matlab (vR2012a) using an in-house software, whose creators and principal developers were Sebastian Hofer and Jason Hölscher-Obermaier with contributions from Witlef Wieczorek, and, starting 2017, myself.

All the necessary information to produce this document and (most of) its content are available in the companion Zenodo repository [Gut24] (e.g. raw codes, data, images, etc.). Excluded are the (large) experimental datasets and the data analysis software; they will be made available upon request. They are stored digitally at the Institute for Quantum Optics, Quantum Nanophysics and Quantum Information at the University of Vienna:

`//share.univie.ac.at/a511-quantum/Work/Mirror/Theory/Stationary_Optomechanical_Entanglement/` (restricted access).

FUNDING

The research presented here was funded, shortly, by the Leibniz University Hannover (öffentlicher Dienst Land Niedersachsen, Germany) and mostly by various projects at the University of Vienna (Austria): *QLev4G*, European Training Network *OMT* (Marie Curie Skłodowska fellowship), *IQLev*, *Thermodynamik mit levitierter Optomechanik*, and *Q-Xtreme: Macroscopic Quantum Superpositions*.

1. File path: `Thesis_CGut_StationaryOptomechanicalEntanglement/Software_code/Analyitic_computations/compute_exactCM_1MechMode.nb`
2. File path: `Thesis_CGut_StationaryOptomechanicalEntanglement/chapter_structure/10ch_CandidateExp/Processing_and_data/backScattLev/cavless_anaSim.nb`
3. Folder path: see footnote 2.
4. Explicit permission was obtained from the authors whose work I use and present in the following [Gut24].

CONTENTS

We chose to lighten the notation as much as possible, at the cost of having context-dependent expressions. Operators are prominent in the entire thesis and are *not* highlighted with hats unless otherwise stated. The Fourier transform of a function or operator $h(t)$ is denoted $h(\omega)$, i.e. it is recognisable only from the arguments; see also our conventions Eqs. (C.8) of the Fourier transform (especially how it behaves w.r.t. the adjunction). Unless explicitly stated we use angular frequencies with [rad Hz] units: $\omega = 2\pi\nu$ with ν in hertz. Arrays of elements (vectors) are written in **bold-type font**. Matrices are denoted with capital letters. Integral boundaries are written out explicitly only in the first occurrence, afterwards they are left tacit (unless they change). Integration over multiple variables are denoted by a single integral symbol, but the (infinitesimal) integration variables are always explicit. The reduced Planck constant $\hbar \coloneqq h/(2\pi)$ and the speed of light c are never set to 1, but work with rescaled dimensionless variables. Dimensionfull operators are denoted with capital letters (e.g. Q for position) and their corresponding dimensionless operators are denoted by lowercase letters (e.g. q). We use quantum optical conventions for the commutation relations where (dimensionless Hermitian) quadratures commute to i (the imaginary unit) and ladder operators commute to 1. The zero-point fluctuations (zpf) of harmonic oscillators quadratures follow the optomechanical convention. Quadrature of (massive) harmonic oscillators are q (position) and p (momentum), and those of a light field are x (amplitude) and y (phase). r or $\mathbf{r}$ is a place holder for quadratures, ladder operators or vector thereof. We use the dot notation for (total) time derivatives; and we do not use primes to indicate derivatives. A definition is indicated by the symbol $\coloneqq$, approximations are indicated by $\approx$, $\sim$ indicates the scaling or order of magnitude, and the big-O notation $\mathcal{O}(\square)$ is for the usual asymptotic scaling. The empty box symbol $\square$ is a dummy placeholder (not a differential operator). The expectation value brackets $\langle\square\rangle$ are either the quantum mechanical expectation value $\mathrm{Tr}[\square\rho]$ or the mathematical expected value $\mathbb{E}[\square]$. The terms "vacuum" and "shotnoise" are used interchangeably in this thesis. We use *italic-type fonts* is used to emphasisea term or to introduce an important (possibly technical/jargon-like) term that will come up regularly.

Symbols	Definitions and comments
$\square$	Dummy placeholder.
δ_{jk}, $\delta(\square)$, $\Theta(\square)$	Kronecker-delta symbol, Dirac-delta distributions, and Heaviside step function.
$\mathbb{1}, \mathbb{1}_n$	Identity operator or matrix; subscript n indicates the dimensions.
$\mathcal{N}(\mathbf{m}, \sigma)$	(Multivariate) normal/Gaussian distribution with (vector) of first moment(s) $\mathbf{m}$ and (matrix of co-)variance(s) σ.
$\mathrm{var}[\square]$, $\mathrm{std}[\square]$	Variance $\mathrm{var}[x] \coloneqq \mathbb{E}[x^2] - \mathbb{E}[x]^2 \equiv \langle x^2 \rangle - \langle x \rangle^2$; standard deviation $\mathrm{std}[x] \coloneqq \sqrt{\mathrm{var}[x]}$.
$q_{\mathrm{zpf}}, p_{\mathrm{zpf}}$	Position and momentum zero-point fluctuations of a massive harmonic oscillator mode in [m] and [kg m/s] Eqs. (2.14): $q_{\mathrm{zpf}} \coloneqq \sqrt{\hbar/(2m\omega_m)}$ and $p_{\mathrm{zpf}} \coloneqq \sqrt{\hbar m \omega_m/2}$.

Symbols	Definitions and comments
$\mathbf{r}^{\mathrm{q}}$, $\mathbf{r}^{\mathrm{l}}$, $\mathbf{r}$	Vector of dimensionless operators, superscript indicates representation: (q) quadrature, (l) ladder, () unspecified; $\mathbf{r}^{\mathrm{l}} = \mathrm{R}_n \mathbf{r}^{\mathrm{q}}$ with $\mathrm{R}_n = \bigoplus_1^n \left(\begin{smallmatrix} 1 & \mathrm{i} \\ 1 & -\mathrm{i} \end{smallmatrix}\right)/\sqrt{2}$ Eqs. (2.18) and (C.4).
Ω	2M-by-2M *symplectic form* Eq. (3.2) encoding bosonic commutation relations Eqs. (2.15): $\left[\mathbf{r}_j, \mathbf{r}_k\right] = \mathrm{i}\,\Omega_{jk}$, $\Omega \coloneqq \bigoplus_{l=1}^{M} \left(\begin{smallmatrix} 0 & 1 \\ -1 & 0 \end{smallmatrix}\right)$, with $\mathbf{r} = \mathbf{r}^{\mathrm{q}}, \mathbf{r}^{\mathrm{l}}$.
σ	Covariance matrix Eq. (3.8c): $\sigma \coloneqq \left\langle \mathbf{r}\mathbf{r}^{\mathsf{T}} \right\rangle_{\mathrm{sym}} - \langle \mathbf{r} \rangle^2$, with symmetrised expectation value; equivalent to the state of a Gaussian state (when 1st moments are zero).
Σ, σ	Covariance matrices estimated from measured data Eq. (H.4); lowercase for calibrated dimensionless case; cf. Appendix H.

Frequencies below are in [rad Hz] (unless stated otherwise); in multi-mode scenario, j indexes the mode.

ω_m, ω_j	Mechanical resonance frequency; in multi-mode scenario ω_1 is the targeted mode.
γ_m, γ_j	Mechanical damping rate (FWHM).
Q_j, Q_{jk}	Matrix of mechanical quality factors $Q_{jk} \coloneqq \omega_j/\gamma_k$, $\gg 1$ Eq. (5.16).
κ	Cavity linewidth (FWHM).
n_{th}, n_j	Thermal bath occupation number for temperature T_j in [K] Eqs. (A.26) and (A.27): $n_j = (e^{\hbar\omega_j/(k_B T_j)} - 1)^{-1} \approx \frac{k_B T_j}{\hbar \omega_j}$, in this document $n_j \gg 1$ (5.17).
$g_0, g_{0,j}$	Single-photon optomechanical coupling.
g, g_j	(Dressed) optomechanical coupling Eq. (5.8), in this document $g_j \gg g_{0,j}$ Eq. (8.3).
$\omega_d, \omega_{\mathrm{cav}}, \Delta$	Drive frequency, cavity resonance frequency, and detuning $\Delta \coloneqq \omega_d - \omega_{\mathrm{cav}}$, assumed zero in the protocol Eq. (8.5).
$\Gamma_j^{\mathrm{ro}}, \Gamma_j^{\mathrm{ba}}$	Readout rate by the light Eq. (5.24a): $\Gamma_j^{\mathrm{ro}} \coloneqq \frac{4g_j^2}{\kappa}$; see Sec. 4.3 for comments on Γ_j^{ba}.
Γ_j^{th}	Thermal decoherence rate Eq. (5.24b): $\Gamma_j^{\mathrm{th}} \coloneqq \gamma_j n_j$.
Γ_j^{tot}	"Total rate" of the dynamics Eq. (5.24d): $\Gamma_j^{\mathrm{tot}} \coloneqq \Gamma_j^{\mathrm{ro}} + \Gamma_j^{\mathrm{th}}$.
C, C_j	Optomechanical cooperativity Eq. (5.24c): $C_j \coloneqq \Gamma_j^{\mathrm{ro}}/\Gamma_j^{\mathrm{th}}$.
χ_j	Mechanical susceptibility Eq. (5.23d): $\chi_j(\omega) \coloneqq 2\omega_j/(\omega_j^2 - \omega^2 + \mathrm{i}\,\gamma_j\omega) = (\omega - \omega_j^-)^{-1} - (\omega - \omega_j^+)^{-1}$, with $\omega_j^{\pm} \approx \pm\omega_j - \mathrm{i}\,\gamma_j/2$ Eqs. (9.18).
χ_{opt}	Susceptibility of the cavity Eq. (5.23e): $\chi_{\mathrm{opt}}(\omega) \coloneqq \sqrt{\kappa}/(\kappa - 2\mathrm{i}\,\omega) \approx 1/\sqrt{\kappa}$ Eq. (9.20).
f_E, f_L	Early and late temporal mode functions Eqs. (8.7): $f_E(t) \coloneqq \sqrt{2\Gamma} e^{\Gamma T_{\mathrm{sep}}/2} e^{-\mathrm{i}\,\omega_E t}\, \Theta(-t - T_{\mathrm{sep}}/2)$ with $\omega_E \coloneqq \bar{\omega} + \mathrm{i}\,\Gamma$, and $f_L(t) \coloneqq f_E(-t)$.
F_α, F^{tm}	Matrices of mode profiles; F_α ($\alpha = E, L$) are diagonal in ladder operator representation Eq. (9.3): $F_\alpha(\omega) = \mathrm{diag}[f_\alpha(\omega), f_\alpha^*(-\omega)]$; $F^{\mathrm{tm}} = (F_E, F_L)^{\mathsf{T}}$ Eq. (9.5).
Γ	Temporal modes decay rate (Lorentzian bandwidth, HWHM) Eqs. (8.7).
$\bar{\omega}$	Temporal modes demodulation frequency Eqs. (8.7); ideally $\bar{\omega} = \omega_1$.
T_{sep}	Delay between early and late modes; $T_{\mathrm{sep}} \gtrsim \kappa^{-1} > 0$ in this document; cf. Sec. 7.2.
$\delta\omega, d$	Mismatch between temporal modes demodulation and targeted mode Eq. (8.8): $\delta\omega \coloneqq \bar{\omega} - \omega_1 = \omega_1\, d$, in this document $\lvert d \rvert \ll 1$.

Symbols	Definitions and comments
$\Delta\omega, D$	Frequency difference with target mode Eq. (5.11): $\Delta\omega \coloneqq \omega_2 - \omega_1 = \omega_1 D$.
ν	Shorthand notation: $\nu \coloneqq \frac{\Gamma}{\omega_1}$, in this document $1 \gg \nu^2 \gg Q_1^{-2}$ Eq. (9.30).
σ^{out}, σ^{tm}	State of cavity output light Eq. (9.9) and of the temporal mode of the light Eq. (9.11).
Δ_{EPR}	EPR-variance Eq. (3.13), $\Delta_{EPR} \coloneqq \mathrm{var}\left[x_1 + x_2^\theta\right] + \mathrm{var}\left[p_1 - p_2^\theta\right]$ (θ denotes rotation of the second party); $\Delta_{EPR} < 2 \Rightarrow$ ent.
W_{opt}, W_{opt}^{cross}, w^{cross}	Optimised witness, necessary and sufficient for entanglement of Gaussian states [HE06]; cf. Sec. 3.4.2. Cross-validated witness matrix W_{opt}^{cross} with witness value $w^{cross} = \mathrm{Tr}[W_{opt}^{cross}\sigma^{cross}]$ Eq. (11.1).

Acronyms & abbreviations

logneg	Logarithmic negativity
BS	Beam splitter
dar	Darknoise
ent.	Entanglement
FWHM	Full width at half maximum
HWHM	Half width at half maximum
lhs	Left-hand side
PPT	Positive partial transpose
PSD	Power spectral density
QLE	Quantum Langevin equations
rhs	Right-hand side
sho	Shotnoise
sig	Signal
std	Standard deviation
tm	Temporal modes
th	Thermal
TMS	Two-mode squeezing
vac	Vacuum
zpf	Zero-point fluctuations

1 INTRODUCTION

I recall well my mindset after the masters: eagerness to dive "deep" into quantum mechanics: I was ready to study anything, but please, make it quantum! I think it was less than two months after I had started the PhD – I was already in Hannover as a guest student in Klemens Hammerer's group – that I had to learn my first "profound" lesson about quantum optomechanics; in the approximate words of Klemens: "Corentin, you know, the thing about these optomechanical systems is that they are essentially classical". Sounds like a bad start for a student who wants to learn nature's quantum secrets, hum?... Since then, I have put a great deal of effort figuring out for myself what is classical and what is quantum in linear/Gaussian optomechanics. This is a regime where classical and quantum predictions overlap – where they merge and also depart from each other. Insights into the classical-versus-quantum topic are an important outcome for me, and they will appear repeatedly in this document (like a tune in the background).

This thesis looks at entanglement between light and the motion of a mass that interact with each other – this is optomechanics. This work assumes that quantum mechanics is the more fundamental or accurate model of nature. Importantly, it is possible to make non-quantum models of the optomechanical systems at hand that lead to the same predictions, but whose interpretation differs; we will carefully make this point clear in Part I.

Two cornerstones of this thesis are stationarity and demonstrability. Entanglement in optomechanical devices is well understood and numerous experiments have demonstrated it in diverse configurations: between separated mechanical oscillators mediated by light [Rie+18; OK+18], between different light tones mediated by a mechanical oscillator [Bar+19; Che+20], and between light and mechanics in a pulsed regime [Pal+13]. However, it remains an outstanding goal to demonstrate light–mechanical entanglement in the stationary regime. The goal of this thesis is to propose and explore a protocol that can be performed with currently existing optomechanical devices. The result of close collaborations between theorists and experimentalists is, in my opinion, an interesting mix of general and abstract thoughts with practicable consequences. Arguably, the main success of our work is that our protocol has been used to study real-life experimental data; and the main failure is that none of the attempts have succeeded yet...

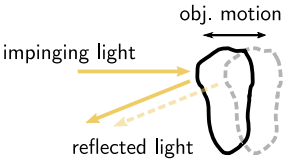

Fig. 1.1 Light carries momentum so that its reflection "kicks" the surface and alters the object's momentum. Simultaneously, the moving surface alters the frequency of the reflected light (Doppler effect), thereby, its momentum.

1.1 OPTOMECHANICS

The central physical platforms at the focus of this thesis are optomechanical devices. They are systems where electromagnetic radiation interacts with the motion of an object; one refers to the object and its motion as the *mechanical* part of the optomechanical device. In this work, we specifically treat mechanical systems that are solid-state objects and the electromagnetic radiation will always be light at optical frequencies (i.e. from mid-infrared ~ 1 THz to mid-ultraviolet ~ 1000 THz). The interaction is momentum exchange between the radiation and the object's motion: the light exerts *radiation pressure* on the object, while the momentum (**k**-vector) of the reflected (scattered) light depends on the object's motion; see Fig. 1.1.

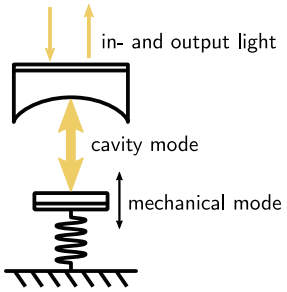

Fig. 1.2 Schematic of a *cavity optomechanical device*: the mechanical mode is a mirror on a spring, it interacts (via radiation pressure) with a cavity mode, which is the interface to the drive (in) and measurement (out) channels. Mirrors, springs, cavity, and lasers illustrate engineering and control.

We also restrict our attention to devices for which a quantum description is possible and actually relevant. Relevant in the sense that the predictions are different from non-quantum – or *classical*[1] – physical theories; and they are measurable. A typical feature of quantum optomechanical devices is low mechanical losses of the mechanical part (i.e. under-damped, high-Q regimes); that is good isolation. In addition, a high degree of control over the processes affecting the system is necessary. This implies, for instance, working in vacuum, at low temperatures, engineering of the mechanical degree of freedom via nano-/micro-fabrication, and engineering of the light using a cavity; see Fig. 1.2. Lastly, measurements must be accurate down to the "quantum regime" in order to resolve quantum effects: prominently in this work, the effects of *quantum noise* limit how well one can know the state of a (quantum) system.

1.2 QUANTUM–CLASSICAL PREDICTION BOUNDARY

As mentioned already, the working hypothesis in this thesis is that quantum mechanics is the underlying, more fundamental theory, and classical ones are accurate in limit cases – typically where the number of degrees of freedom and/or excitations involved are macroscopically large (alike Newtonian mechanics being the low velocity limit of special relativity). Experiments operating "deep in the quantum regime" (i.e. far away from the boundary where classical and quantum predictions still match) legitimate this hypothesis because they

1. We often resort to the fuzzy jargon terminology of *classical* to qualify physical models and theories and distinguish them from *non-classical* ones, like quantum mechanics. It is a handy concept, but a precise meaning is hard to state in a way that makes everyone happy. My definition – which is good enough for the scope of this thesis – is: classical theories are established physical theories that are not (or do not include) quantum mechanics. Examples relevant in this document are: Newtonian mechanics, thermodynamics, and statistical mechanics. By extension, one might speak of classical systems, states, descriptions, models, etc.

provide observations not predicted (or incompatible) with classical theories. Important examples are: single-photon anti-bunching (sub-unit second-order coherence $g^{(2)}$) demonstrating the particle nature of light [Cla74]; single-photon interference showing the wave nature of light (particles) [GRA86]; matter-waves with electrons [DG27] up to large molecules [Fei+19], and, of course, Bell non-locality [FC72; AGR81; AGR82; ADR82; Hen+15; Giu+15; Sha+15].

Albeit bearing a relevant and informative quantum description, the devices we treat are not deep in the quantum regime. They are at the boundary where classical and quantum predictions are the same – but interpretations differ. We will explain that limits on measurement precision derive from the principles of quantum mechanics. The interpretation is that uncertain knowledge of a state (and therefore achievable measurement) is a fundamental property of nature. On the other hand, a classical model must be supplemented with an ad hoc noise process to explain any limitation preventing more precise knowledge. Classically, there is no fundamental limit as to how well a state can be known and measured; hence the interpretation is that infinitely precise measurements are unfeasible in practice and realistic models must be completed (or fixed) with some unknown added noise.

As a matter of fact, the Gaussian optomechanical entanglement we study corresponds to a reduction of (quantum) noise below some threshold, and it is the quantum interpretation that implies that this is something special – entanglement indeed. In contrast, classical models do not see anything special about the reduction of ad hoc unknown noise (beyond the mere associated precision improvement). Therefore, a successful detection of optomechanical entanglement does not allow one to decide which of the quantum or classical interpretations is correct.

1.3 ENTANGLEMENT

Entanglement is a correlation that can exist between at least two quantum systems. This correlation is of quantum nature because it cannot be described using other established physical theories (which do not incorporate quantum mechanics). Just as there is no way to describe colours in a world that is black and white, there is no way for the grey-scale classical theories to describe colourful entanglement from quantum mechanics (metaphor inspired by F. Jackson's "knowledge augment" or "epiphenomenal qualia" [Jac82; Jac86]).

Correlations are (or encode) information, whether they are classical or quantum. Entanglement correlations can be used to perform certain tasks differently, and sometimes better than with classical correlations: prominently quantum computations use entangled *qubits* and are more

efficient (i.e. require fewer operations) than normal computers for these tasks [NC10]. Entanglement can be seen as a *resource* – like heat in thermodynamics. [2]

Two systems originally not entangled – or *separable* – are entangled after they interacted, in general. Put differently, obtaining a separable joint state after an interaction in the quantum formalism should be thought of as an atypical scenario. However, it is far more common to observe separable states than entangled ones in physics laboratories. From the quantum point of view, I like to understand this contrast as a "dilution" effect: because any interaction leads to entanglement, and because, realistically, the systems under consideration will interact with many other systems forming their environments (e.g. gas molecules, black body radiation from objects and walls around them, etc.), therefore entanglement dilutes across all the systems that interacted. Like heat, entanglement must be *concentrated* to be used or detected. Like heat, this is achieved, for example, by isolating the systems one wants to entangle.

Quantum mechanically, entanglement is ubiquitous and omnipresent at all times. An operator can use it (as a resource) if they know enough about how entanglement is shared or diluted across systems. In fact, knowledge and usage of entanglement are closely related to the degree of control and characterisation of the systems. Conversely, ignorance and lack of control are essentially what make entanglement difficult to observe or impossible to use. Roughly speaking, the dichotomy knowledge-versus-ignorance is closely related to entanglement and separability, and it characterises the difference between measurements and decoherence.

1.4 EXAMPLE OF A QUANTUM POSITION SENSOR

An optomechanical device is a prototypical sensor that measures the position of the mechanical degree of freedom. Because we (can) describe it in full quantum mechanical terms, it is a minimal implementation of a quantum measurement apparatus. Partly because the quantum description is equivalent to a classical one, the full quantum model is workable and has exact analytical solutions. Moreover, currently existing systems are appreciably affected by quantum effects [AKM14]. Therefore, (quantum) optomechanical devices offer an opportunity to study theoretically and experimentally the details of quantum measurements, which is relevant both from a fundamental and a technological point of view.

2. Entanglement is not heat. The analogy here is meant as a "warm-up thought" for unfamiliar readers. Importantly, this analogy quickly stops to hold when one examines its consequences: for instance, there is no second law for entanglement [LR23].

Quantum mechanics sets constraints [3] on how precisely a state can be determined. It is technologically useful to acknowledge and understand these constraints if one wants to build very precise measurement devices. An extreme example is the gravitational wave observatory Advanced LIGO that was limited by quantum noise (at large frequencies in the measurement band) when it made the first detection of a gravitational wave in 2015 [Abb+16]. Moreover, a thorough understanding of quantum noise allows one to overcome certain of its limitations, as is currently the case in LIGO and Virgo gravitational wave detectors that use squeezed light to mitigate their quantum noise [Aba+11; BHS19; Tse+19; Ace+19]. Furthermore, the study of quantum noise is a central topic in the field of "quantum metrology", where our understanding of quantum mechanics allows to improve sensors, for example by mitigating quantum noise or making them less intrusive [GLM06; GLM11].

Generally speaking, the principles (axioms) of quantum mechanics look like a set of modelling and calculating rules that make accurate and useful predictions about nature, but for which we miss an interpretation. For instance, according to the axioms of quantum mechanics, it is not clear why quantum measurement apparatuses – in which projective dynamics happen – are different from other devices – whose evolution is unitary. This criticism was already clearly formulated by von Neumann in his book [VN96, Ch. 6] published in 1932. The contrast between projective and unitary dynamics relates to the contrast between the definite measurement results – a fundamentally classical notion – and the indefinite nature of quantum states that can be superpositions. A candidate for this discrepancy is the large scale difference between typically microscopic quantum systems and the macroscopic world where measurement results are meaningful and modelled. Assuming that the quantum theory is more fundamental than classical theories, then why are its effects (like superpositions) not observed at macroscopic scales? Decoherence is a mechanism that explains the emergence of classical physics for an observer from incomplete information: the full quantum state of an imperfectly isolated system becomes inseparable from the state of its environment, which is inaccessible to the observer [Sch07; Zeh70; Zur82; Zur03]. Importantly, the decoherence mechanism relies on both unitary and projective dynamics and it does not explain why both are required [Sch19].

There are several alternatives to the projective dynamics and its apparent necessity for making accurate predictions. On the one hand, it has been argued that the universe is a pure state with "branches" and observers follow one branch every time they make a measurement; globally, all the possible configurations (all the branches of

3. Depending on the context or how they affect the system, they are also called quantum limits or quantum noise.

observers experiencing different measurement results) do happen in a quantum superposition; this is (roughly) H. Everett's "relative state" (or "many-world") formulation of quantum mechanics [Eve57]. Another approach is to assume that quantum mechanics is not the theory underlying macroscopic phenomena; it thus stops making accurate predictions as the size of the systems increases. Examples of proposals going in that direction are "collapse models" that typically assume a generalised Schrödinger equation with additional terms; see for example this recent review [BDU23] or the thesis of my colleague Philipp Köhler [Kö21]. Because measurement apparatuses map and amplify microscopic quantum states to macroscopic measurement results, they are the machines where the scale conversion happens, and it seems sensible to look for answers in their study.

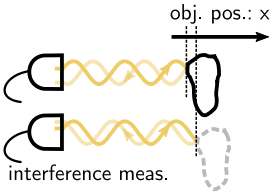

Fig. 1.3 Changes in position of the object change the point of reflection of the sent radiation. The reflected light thus has a different phase that can be measured by interfering sent and reflected light.

Let us make an example: consider a sensor measuring the position of an object based on the light reflected from it – this is an optomechanical device. Depending on where the reflection occurs along the travelling electromagnetic wave, the reflected wave will have a different phase than the one travelling towards the object; see Fig. 1.3 for a depiction. This means that the position of the object and the (physcial) phase of the reflected light are correlated. We deduce the phase difference from the interference of the light sent with its reflection. With an accurate model and characterisation of all these steps, the position of the reflecting surface is deduced from a measurement of the interference intensity.

This is a classical description of a position sensor. The quantum version requires first changing the wording and calling entanglement the correlation between the object's position and the phase (quadrature[4]) of the reflected light. Second, in the quantum formalism, a measurement is (effectively) described by a projection of the state being measured onto the basis of the observable being measured. Because this projected state is, in general, different from the one before the measurement, this implies that the measurement perturbed the state (from the perspective of the observer). In the present example, the object is projected onto the eigenstate of position associated with the measured position (eigen)value. This is arguably the simplest and most common (quantum) model for position sensing with such a device. The measurement outcome from the projection is then classically correlated with the phase of the light. After the projective dynamics, the quantum description is not necessary to make accurate predictions; in practice, one thus resorts to (non-quantum) classical Maxwell equations to model how phase information is recovered from the interference.

In this quantum measurement model, one can assume that it is the reflected light that experiences projection onto an eigenstate of the

4. Physical and quadrature phases are discussed in the next chapter.

phase quadrature, rather than the object directly; further down the line, one can model that it is the interfered light that is projected by the intensity measurement; even further, one can assume that the electrons in the photocurrent are projected into a definite current value; and so on. The axioms of quantum mechanics provide no guidance as to "where" the projective dynamics are correctly modelled, and the matter is left to the skills of the physicists making the model. This issue was discussed by von Neumann [VN96, Ch. 6] who proposed that the position of the cut marking the projective dynamics *must* be irrelevant – as long as it is consistent with the quantum theory. This cut is known as the *Heisenberg–von Neumann cut*. Figure 1.4 depicts the cut in the model above where the object's state is projected onto the position eigenbasis.

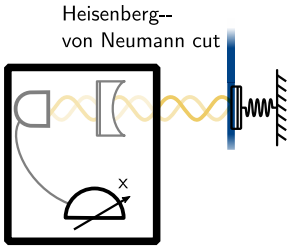

Fig. 1.4 Mechanical state is projected onto a position eigenstate correlated classically to different relative phases of in- and out- going light: this is the simplest correct model of this quantum position sensor.

Assuming that it is the reflected light that is projectively measured by its phase quadrature observable, then the projective dynamics happen at the interference detection; see Fig. 1.5. A quantum description of the optomechanical state (mechanics + reflected light) describes the correlation that encodes the object's position onto the light's state – this correlation is precisely the optomechanical entanglement we want to demonstrate. Its observation in an experiment implies that the projective dynamics have not yet happened, thus validating the model of Fig. 1.5 with a shifted Heisenberg–von Neumann cut compared to Fig. 1.4.

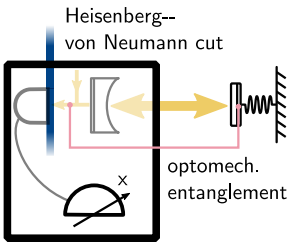

Fig. 1.5 Heisenberg–von Neumann cut is shifted at the interface of photodetection. There, the light is projected onto a phase quadrature eigenstate. Before the projection, the correlation encoding the mechanical position onto the light is optomechanical entanglement.

Importantly, both models with different positions of the cut lead to equivalent predictions for the measurement results – as conjectured by von Neumann. In particular, both lead to the (effective) projection of the object's position state. In the scenario with a shifted cut, this happens precisely because the reflected light and the object are entangled. What is more, in the quantum formalism, projecting the light's state *instantaneously* projects the object's state; this is an update of the information about the state available to the observer; see also App. B for a discussion of non-local realism, Bell inequalities, and the (Gaussian) entanglement detection discussed in this work.

1.5 SUMMARY OF RESULTS

We have introduced the broad framework in which the research presented in this thesis stands: it is a particular case study of quantum measurement. We believe that our approach, based on measurements and geared towards experimental realisation, is useful and interesting to study quantum measurement devices more broadly. Importantly, the concepts exposed above are well established and understood, and have already been verified by a number of experiments. Measurement, decoherence, and the "emergence of a classical world" remain, however, the subject of intense studies and debates. This is certainly due to the

rich fundamental physics and high technological potential associated with it.

The contribution of this work is a very particular application of entanglement being the mediator of information in a quantum measurement. A successful demonstration of stationary optomechanical entanglement would amount to a verification of the equivalence of the shifted von Neumann–Heisenberg cut. It is important to note that optomechanical entanglement has been demonstrated in a pulsed scheme [Pal+13; Hof+11a] that corresponds to single-shot measurements, while, in the stationary regime we consider, we are in the continuous monitoring regime – and an experimental verification remains an open challenge.

The results presented in this document are:

- We provide a detailed description of an experimentally viable protocol to demonstrate entanglement between a mechanical oscillator and the light that interacted with it – at all times, in the stationary regime [Gut+20]. More specifically, we provide a general entanglement verification theorem that allows to certify optomechanical entanglement from measurements with few assumptions compared to existing proposals. We propose an explicit experimental protocol compatible with already existing experimental setups. Moreover, the scheme requires relatively little experimental effort, in principle; we could even re-use datasets that were obtained for other purposes.
- We model the protocol and provide the exact analytical state of the detectable state in symbolic form; this allows for efficient/fast parameter sweep compared to simulations based on time evolution of the dynamics.
- We also compute an approximate formula for the EPR-variance (a sufficient test of entanglement); it enables physical interpretation and understanding of the role of the different parameters in this (sub-optimal) detection of entanglement; moreover, we determine from it the relevant/optimal parameter regimes for entanglement detection and we find that they are currently accessible.
- We analysed experimental datasets from four devices that are different implementations of optomechanics – highlighting the diversity of the field and the generality of the formalism – in different operation regimes. Crucially, none of these experiments succeeded in demonstrating stationary optomechanical entanglement; moreover, we are aware of at least one additional unsuccessful attempt to perform the protocol, with another device in another group, independently from our effort.
- This worrying score of five attempts and zero success leads to additional theoretical insights that provide plausible explanations for why the theoretical model predicts detectable entanglement but experimental verification remained evasive. Firstly, we realise that

the original model (involving a single mechanical mode) would always predict detection of entanglement making the result trivial as a result of a too simplistic model [5]; second, additional mechanical modes (and probably any spectral features) far from the mechanical frequency of interest, relative to the filters defining the modes tested for entanglement, do significantly alter the feasibility of the protocol. The subsequent, non-trivial, theoretical predictions indicate that lowering the temperature of the baths driving the mechanical modes is the most efficient way to enter regimes of detectable entanglement. Lastly, the mechanical frequency must be much more stable than anticipated.

- In the process of analysing the experimental data, we learn how to alleviate false-positive entanglement with conservative unit calibration and an entanglement test that mitigate bias. We find that the use of evaluations accounting for the possible multiple mechanical modes is always beneficial for detecting entanglement. And processes, even relatively far detuned in frequency, to influence the results.

5. Einstein's famous warning resonates loud here: "Make it as simple as possible, but not simpler".

Part I

THEORETICAL CONCEPTS

PREFACE TO PART I

The purpose of this part is to introduce the physical concepts and tools required to understand the protocol we propose in Part II as well as the physical systems we are concerned with. In this part, no original formal results are presented and suitable references are provided along the way. Notations and conventions are also made explicit.

We attempt to highlight the gist of what it means to observe Gaussian entanglement between an object and the apparatus measuring it. In so doing, we argue that the root of the entanglement and quantumness discussed in this thesis lies in the non-commuting properties of conjugated quadratures. This is in essence the message of Ch. 2.

The systems of interest have states in infinite-dimensional Hilbert spaces that are conveniently handled with the *continuous variables* formalism presented in Ch. 3. Moreover, the states that are most accessible and practicable in experimental studies form the subset of Gaussian states that bear a mathematically convenient and powerful description. In particular, several computationally efficient entanglement tests are available.

The wanted optomechanical entanglement is, in essence, the entanglement existing between an object and a probe measuring it before the effective projective dynamics of a quantum measurement. In fact, this is the same entanglement correlation that exists between the object and its environment leading to decoherence: the difference being the flow of information relative to the observer (or the model). Our analysis explicitly incorporates measurement and decoherence; the mathematical framework and formalism to do so are called *open-system* dynamics and it is introduced in Ch. 4.

Lastly, in Ch. 5, we provide a physical description and discussion of what optomechanical systems are – and how the mechanical and optical parts can be implemented. The interaction is restricted to radiation pressure, the optomechanical Hamiltonian is introduced, and the corresponding unitary dynamics are briefly discussed. Then the full quantum open-system model is stated and its solutions in frequency space are given. They are the basis for the proposed protocol of Part II.

2

ELEMENTS OF QUANTUM MECHANICS

This section introduces the necessary physical concepts used in this work. In so doing, formalism and notation are laid out. We attempt to convey our physical understanding and interpretation through a discussion of the formal mathematical tools. For precise, rigorous, and thorough derivations and discussions of the quantum theory, we recommend standard textbooks like [CTDL05; SN20]; for quantum optics we recommend [VW94; Lou00; GAC10; WM06].

2.1 CONTINUOUS POSITION AND MOMENTUM OBSERVABLES

Consider a quantum object characterised by its position Q. We assume that this object has no other internal or external degree of freedom. Position is an *observable* – i.e. it can be measured – therefore Q is a Hermitian operator[1] in the quantum formalism with the property $Q = Q^\dagger$. The eigenvalues of Hermitian operators are real, and they correspond to the measurable quantity of the observable: here, the possible positions of the object. We assume infinite space, therefore Q is an infinite-dimensional operator with infinitely many eigenvalues.[2] We use Dirac bra–ket notation [CTDL05]: for each position eigenvalue $q \in \mathbb{R}$ there is an associated position eigenvector $|q\rangle$, such that $Q|q\rangle = q|q\rangle$. The set $\{|q\rangle : q \in \mathbb{R}\}$ of all eigenvectors that diagonalise Q forms the orthonormal *position basis* of a Hilbert space $\mathcal{H}$

$$\langle q|q'\rangle = \delta(q - q') \tag{2.1a}$$

$$\int_{-\infty}^{\infty} dq\, |q\rangle\langle q| = 1. \tag{2.1b}$$

The *position representation* of arbitrary states $|\psi\rangle \in \mathcal{H}$ is thus

$$|\psi\rangle = \int_{-\infty}^{\infty} dq\, \langle q|\psi\rangle\, |q\rangle \tag{2.2a}$$

where

$$\psi(q) \coloneqq \langle q|\psi\rangle \tag{2.2b}$$

1. There is no hats on operators in this thesis (except in App. H where it is explicitly mentioned).

2. The infinite and unbounded nature of the position observable leads to some mathematical complications in order to speak precisely about its diagonalisation via the spectral theorem; see [CTDL05, Ch. 3] for a brief discussion of that point and [Hal13] for the full rigorous explanations.

is a complex valued function that we call the state's *wavefunction* (in position representation).

Changes in position (translations) of the object are described, by definition, by the *canonical momentum*[3] P. In quantum mechanics, P is an operator that is Hermitian because it is observable/measurable. P is defined formally, in position representation, from its operational action on a wavefunction: $\mathsf{P}\psi(q) \coloneqq -i\hbar\partial_q\psi(q)$, so that

$$\mathsf{P} \coloneqq -i\hbar\partial_q. \tag{2.3}$$

$\hbar$ is the reduced Planck constant and $i \coloneqq \sqrt{-1}$ is the imaginary unit. The real eigenvalues p – so that $\mathsf{P}|p\rangle = p|p\rangle$ – are associated with the eigen-momentum states $|p\rangle$. They also form an orthonormal and complete basis of the Hilbert space $\mathcal{H}$

$$\langle p|p'\rangle = \delta(p-p') \tag{2.4a}$$

$$\int_{-\infty}^{\infty} dp\,|p\rangle\langle p| = 1. \tag{2.4b}$$

With the expression of P in position representation Eq. (2.3), we denote the wavefunction $\psi_p(q) \coloneqq \langle q|p\rangle$ of the momentum eigenstates in position representation

$$\mathsf{P}\psi_p(q) = -i\hbar\partial_q\psi_p(q) = p\psi_p(q) \quad \Leftrightarrow \quad \psi_p(q) = Ne^{i\,qp/\hbar} \tag{2.5}$$

where $N = 1/\sqrt{2\pi\hbar}$ is the normalisation set by the orthonormality. With this relation, one finds that the wavefunction in momentum representation $\psi(p) \coloneqq \langle p|\psi\rangle$ [4] of a state $\psi \in \mathcal{H}$

$$\psi(p) = \int \frac{dq}{2\pi\sqrt{\hbar}} e^{-i\,\frac{qp}{\hbar}}\psi(q). \tag{2.6}$$

It is the Fourier transform (cf. Eqs. (C.8) for definitions and conventions regrading Fourier transformation) of the wavefunction in position representation. This shows that both representations are related one-to-one by a Fourier transform, and it makes it explicit that both eigenbasis are different.

This implies that the quantum state of the object is completely described by knowledge of its position state *or* its momentum state: i.e. the wavefunction $\psi(q)$ in position representation is a complete description of the state and, equally, the momentum wavefunction $\psi(p)$ is a complete description as well.[5] Said otherwise, position

3. It is the conserved quantity under translational invariance symmetry, which is not always the same as the *kinetic momentum* (mass times velocity). In this document, unless stated otherwise, we consider canonical momenta.

4. It is the argument that distinguishes the basis/representation, cf. Fourier transform conventions and notations Eqs. (C.8).

5. For observables with degenerate eigenbasis (like angular momentum), a complete set of commuting observables (e.g. J_z and J^2 for angular momentum) and quantum numbers are necessary to specify a state [CTDL05].

and momentum are not independent in quantum mechanics – they relate to each other via the Fourier transform, cf. Eq. (2.5). This is in contrast to classical kinematics where both position *and* momentum of an object must be specified independently to describe its state entirely.

The interdependence of (operator) observables leads to relationships between what is known and what is knowable from their associated measurements. An insightful characterisation of these relationships is provided by the commutation relations of observable operators; the *commutator* of operators A and B is defined as $[A, B] \coloneqq AB - BA$. Hermitian operators are diagonal in the same basis if and only if they commute (commuting observables are called *compatible*). Position and momentum have different eigenbasis and thus have non-trivial *canonical commutation relation*

$$[Q, P] = i\hbar\mathbb{I} \tag{2.7}$$

where $\mathbb{I}$ is the identity operator (which we will not indicate further, as is customary). The commutation relation Eq. (2.7) is associated with *boson statistics*. In this thesis, we deal only with bosons and we need not describe their possible spin degrees of freedom. This relation is central to our work [6]: we argue in the next section that they are the fundamental basis for the quantum interpretation of the phenomenon of Gaussian entanglement that we study.

2.2 UNCERTAINTY RELATIONS

Finite commutation relations between observables set constraints on how well one can know them relative to each other: this is the result of what is sometimes called [Gri17, Ch. 3.5] *generalised uncertainty relations*. [7] Given that the "uncertainty of an observable" is characterised by its standard deviation $\mathrm{std}[A] \coloneqq \sqrt{\mathrm{var}[A]} \coloneqq \sqrt{\langle A^2\rangle - \langle A\rangle^2}$, then the (quantum) uncertainty of observables A and B are related by [8]

$$\mathrm{std}[A]\,\mathrm{std}[B] \geqslant \left|\frac{\langle [A, B]\rangle}{2i}\right|. \tag{2.8}$$

If A and B commute (are compatible), then there is no limit on how precisely they might be known simultaneously. If they are incompatible, then their commutator scales how much they prevent each

6. In [Hal13, Ch. 12], they explain that, given this commutator, one can formally derive the physical properties of the operators forming it, and it turns out that they *must* correspond to the physical notion of canonically conjugated position and momentum.

7. Historically, it is a result due to Robertson [Rob29] and Schrödinger [Sch30].

8. This formula is not as general as one would wish (I least I would!) and does not capture correctly certain tricky cases involving bounded and unbounded operators, see [Hal13, Ch. 9] for details; they are irrelevant for the purpose of this thesis where we deal exclusively with quadrature operators (e.g. like position and momentum).

other from being known better. When the observables are position and momentum, the result is the well-known *Heisenberg uncertainty relation*

$$\mathrm{std}[Q]\,\mathrm{std}[P] \geqslant \hbar/2. \tag{2.9}$$

From the perspective of the states, described by wavefunctions $\psi(q)$ and $\psi(p)$ in position and momentum representations, their std scales the spread of the measurement results of position and momentum, respectively. The uncertainty relation Eq. (2.9) sets a fundamental quantum limit on what a state can be – it constrains how $\psi(q)$ and $\psi(p)$ can look like. See also our discussion of squeezed states in Sec. A.4 for a pictorial depiction of this concept.

From the perspective of measurements, uncertainty relations set constraints on how an observer's knowledge about the system can be updated by a measurement result. In the context of repeated measurements on the same quantum object, relevant in this work, they prescribe (quantitatively) how the knowledge of one observable is lost when gaining information about another non-commuting quantity; this is what we mean by "measurement disturbance". If one measures a state in a very well defined position q so that its position uncertainty $\mathrm{std}[Q]$ is much smaller than $\hbar/2$, then the uncertainty in momentum $\mathrm{std}[P]$ must accordingly be much larger than $\hbar/2$. Consequently, the broader distribution of momenta will drive the (modelled) dynamics so that the object might be relatively far away at the time of the next measurement. In the extreme (and unphysical) case of a perfect projective measurement on a position eigenstate (i.e. perfectly certain position state after the measurement) $\mathrm{std}[Q]\,(t) \to 0$ and the momentum must be accordingly completely uncertain with $\mathrm{std}[P]\,(t) \to \infty$.[9] (This state has infinite energy which is unphysical.[10])

2.3 DENSITY OPERATORS

We briefly introduce *density operators*[11] usually denoted ρ – unfamiliar readers are advised to consult sections of standard references that present the formalism, for example [CTDL05; NC10; WM09].

Density operators describe generally *indefinite* quantum states – i.e. imprecisely or imperfectly known. This formalism is necessary to model the interaction of quantum systems with an unknowable environment: the so-called open systems introduced and discussed in Ch. 4.

9. An effect well-known from PhD students with evasive quantum supervisors: prolonged observation of the supervisor in their office puts them in a state with large random momentum fluctuations; almost surely the supervisor will be gone for the next student observation attempt.

10. And indeed, position and momentum eigenstates *are not* physical and are not elements of the Hilbert space [CTDL05; Hal13] – they are on its boundary.

11. Also called *density matrices*, mostly in the context of finite-dimensional systems.

The key concept in this section is the distinction between two forms of lack of definite knowledge about the state, leading to probabilistic predictions: the fundamental quantum *uncertainty* of a state and technical (non-fundamental) *indeterminacy*. The term "uncertainty" to qualify quantum indefiniteness should remind ourselves of the uncertainty relations Eq. (2.8), which are a consequence of the quantum formalism. The choice of "indeterminacy" to qualify technical indefiniteness is arbitrary. We stick to these terms as markers of the type of indefiniteness we are talking about. Both forms of indefiniteness are encoded in the density operator describing a state.

The ratio of quantum uncertainty to the total indeterminacy of a state is quantified by its purity $\langle\rho\rangle$: *pure states* have purity one and are exactly the elements of the Hilbert space; states with sub-unit purity are called *mixed* and the lesser their purity, the more (technical, in principle avoidable) indeterminacy it encodes.

Density operators are Hermitian, of trace 1 (trace-class operator), and semi-positive definite. These properties determine whether a certain ρ is a well-defined quantum state. The (quantum mechanical) expectation value of an observable O, given a state ρ, is given by

$$\langle O\rangle = \mathrm{Tr}[O\rho] \tag{2.10}$$

where $\mathrm{Tr}[\square]$ is the trace operation.

2.4 QUANTUM DYNAMICS

The unitary quantum dynamics of an operator A in Heisenberg picture is given by [BP07]

$$\frac{d}{dt}A(t) = \frac{i}{\hbar}[H, A(t)] + (\partial_t A)(t) \tag{2.11}$$

where H is the Hamiltonian and the last term accounts for the explicit time dependence of the operator A in Schrödinger picture. The derivations and results in the following are in the Heisenberg picture, unless otherwise stated. [12]

2.5 QUANTUM HARMONIC OSCILLATORS

It is hard to overstate the importance of the harmonic oscillator in physics and the diversity of models that rely on it. The optomechanical dynamics we are interested in are described by the interplay of two harmonic oscillators: a harmonic mechanical motion and a mode of light; see Ch. 5 where we introduce optomechanical devices. The full

12. In the Schrödinger picture the (unitary) evolution of a state ρ is given by the *Liouville–von Neumann equation* [BP07].

quantum treatment of the harmonic oscillator can be solved exactly [CTDL05, Ch. V]. We list and discuss here the results most relevant for our study of entanglement in optomechanical systems.

Consider a massive (quantum) object, whose centre-of-mass motion is associated with the observables position Q and momentum P (as introduced in Sec. 2.1 above), and suppose that it is trapped in a quadratic confining potential $V(Q) = Q^2 k/2$ (of strength k).[13] The restoring force deriving from this potential is linear[14] in Q, which is the definition of a harmonic motion. Our object is thus a mechanical harmonic oscillator and its Hamiltonian H is

$$H_{HO} = \frac{1}{2m} P^2 + \frac{m\omega^2}{2} Q^2 \tag{2.12}$$

where m is the object's mass and $\omega = \sqrt{k/m}$ is the oscillator's natural frequency (or resonance frequency).

From fundamentally different considerations, the Hamiltonian of a mode of the electromagnetic field (in the absence of charges) can be put in the same form as Eq. (2.12); this is the result of the so-called *quantisation of the electromagnetic field*; see details in [CTDRG97, Ch. II. and III.] for example. In this formalism (in the Coulomb gauge), one finds that the conjugated variables (playing the role of Q and P) are the cosine and sine components of the complex transverse electric field; we denote them X and Y and call them "amplitude" and "phase" *quadratures* of the light mode.[15] Importantly, X and Y are Hermitian and they have the same bosonic canonical commutation relation as Q and P Eq. (2.7)

$$[X, Y] = i\hbar. \tag{2.13}$$

Consequently, modes of light in a cavity or from the free field in a laboratory are formally equivalent to harmonic oscillator modes.

The quantisation of the electromagnetic field finds that the free electromagnetic field is a collection of infinitely many (harmonic oscillator) modes characterised by a transverse-mode profile, a direction of propagation, a polarisation, and a (natural) frequency. In that model, one understands light propagating in a certain state as the corresponding excitation of the oscillators (modes) making out the light's state.

13. In the limit of small displacements, there are many general potentials of practical interest that are approximately quadratic close to their minima.

14. A note on jargon: quadratic (or harmonic) potentials are sometimes called "linear" in reference to the equations of motion driven by that force, which is linear in the operator (or classical dynamical variable) Q.

15. They are *not* the physical amplitude and (relative) phase of electromagnetic waves. For coherent light, they approximate phase and amplitude fluctuations (relevant in the quantum treatment with homodyne or heterodyne measurements) in the large intensity (or displacement) limit and with appropriately chosen phase reference (or measurement basis) so that, indeed, X and Y correspond to amplitude and phase of the state; see [Lou00, Sec. 5.3].

Hermitian operators, commuting to $i\hbar$ as above, for a system with a Hamiltonian of the form of Eq. (2.12), are called *quadratures* – independently of the nature (mechanical or electromagnetic) of the harmonic oscillator mode.

The first step in our study of the quantum harmonic oscillator is to rescale the (mechanical [16]) quadratures as follows

$$Q = \sqrt{2} q_{zpf} q \quad \text{with } q_{zpf} \coloneqq \sqrt{\frac{\hbar}{2m\omega}} \tag{2.14a}$$

$$P = \sqrt{2} p_{zpf} p \quad \text{with } p_{zpf} \coloneqq \sqrt{\frac{\hbar m\omega}{2}} \tag{2.14b}$$

where scaling factors q_{zpf} and p_{zpf} carry the units of their respective variables, and the operators q and p are dimensionless. [17] The subscript "zpf" stands for *zero-point fluctuations* which will be clarified in a few paragraphs.

For dimensionless quadratures u, v, where u is q for a mechanical (oscillating) mode or x for a light mode (and v is the respective conjugated quadrature p or y), the commutation relation is

$$[u, v] = i \tag{2.15}$$

and Heisenberg uncertainty relation Eq. (2.9) becomes

$$\mathrm{std}[u]\,\mathrm{std}[v] \geqslant 1/2. \tag{2.16}$$

The Hamiltonian of Eq. (2.12) becomes

$$H_{HO} = \frac{\hbar\omega}{2}\left(u^2 + v^2\right). \tag{2.17}$$

We introduce *ladder operators* a and $a^\dagger$ defined as

$$\begin{aligned} a &\coloneqq \frac{u + i v}{\sqrt{2}} & \qquad u &\coloneqq \frac{a + a^\dagger}{\sqrt{2}} \\ a^\dagger &\coloneqq \frac{u - i v}{\sqrt{2}} & \qquad v &\coloneqq \frac{a - a^\dagger}{i\sqrt{2}}. \end{aligned} \tag{2.18}$$

16. The electromagnetic field treatment is a little different and there, X and Y have the same units $[\sqrt{\hbar}]$ so that $X = \sqrt{\hbar}x$ (and similarly for y); as for example in [GAC10, Ch. 4]. Conveniently, their definition is independent of the frequency or the quantisation volume (which enter the electric field amplitude of a single excitation of the mode $\sqrt{\hbar\omega_k/(\epsilon_0 V)}$; see also [Lou00, Secs. 4.1-4.4].

17. Two comments on the conventions: first, the factor $\sqrt{2}$ at the denominators is the "optomechanical convention" (cf. [AKM14; Hof15]) and it differs from certain references (e.g [CTDL05; Lou00]). We will see shortly that this leads to q_{zpf} and p_{zpf} being the std of the oscillator's ground state wavefunctions, which is a reference of choice in the optomechanical context. Second, references to eigenvalues q and pure eigenstate $|q\rangle$ will be explicitly indicated (and they are rare in the Heisenberg picture).

Contrary to the quadratures, they are not Hermitian and therefore correspond to non-measurable quantities. Their commutation relation is

$$\left[a, a^\dagger\right] = 1. \tag{2.19}$$

The Hamiltonian of a harmonic oscillator (mode) in terms of the ladder operators is

$$H_{\mathrm{HO}} = \frac{\hbar\omega}{2}(a^\dagger a + a a^\dagger) = \hbar\omega(a^\dagger a + 1/2). \tag{2.20}$$

Because H is not explicitly time dependent, solving the Schrödinger equation amounts to solving an eigenvalue problem of the form $H|\psi\rangle = E|\psi\rangle$. The solution of the time evolution and most properties of the quantum harmonic oscillator can be found from purely algebraic consideration, see [CTDL05, Ch. V] for example. The Hamiltonian Eq. (2.20) is the system's energy observable and its eigenvalues are

$$E_n = \hbar\omega(n + 1/2), \quad n \in \mathbb{N}. \tag{2.21}$$

They come in discreet fashion – in energy quanta – with fixed energy difference $\hbar\omega$ between consecutive eigen-energies. This is different from the classical treatment of the harmonic oscillator where, given the stiffness ω of the potential, the possible energy of the oscillator is a continuum. The Hermitian operator $a^\dagger a$, called the *number operator*, has eigenstates $|n\rangle$ [with eigenvalue n in Eq. (2.21)]. $\{|n\rangle : n \in \mathbb{N}\}$ are also the eigen-energy states of the harmonic oscillator and they form an orthonormal basis of a Hilbert space $\mathcal{H}$ called *Fock space*; the $|n\rangle$ are called *number-* or *Fock- states*.

The state with minimal eigenvalue $|n = 0\rangle$ is the state with the least energy; it is called *ground state* or *vacuum state* because it corresponds to the absence of energy quanta. The minimal energy of the quantum harmonic oscillator $E_0 = \hbar\omega/2 > 0$ is finite, which is another feature of the quantum treatment that departs from the classical picture. One identifies the origin for the additive factor $\hbar\omega/2$ in Eq. (2.20), where it emerges from the non-zero commutation relation between the ladder operators.

The effect of this leftover energy of the ground state is best understood when looking at the state's wavefunction: it is found by solving the differential equation $a|0\rangle = 0$, e.g. in position representation. The modulus squared of the solution $|\psi_0(Q)|^2$ is [Gri17; CTDL05]

$$\begin{aligned} |\langle Q|0\rangle|^2 &= \left(\frac{m\omega}{\pi\hbar}\right)^{1/2} e^{-\frac{m\omega}{\hbar}Q^2} \\ &\sim \mathcal{N}\left(0, q_{\mathrm{zpf}}^2\right) \end{aligned} \tag{2.22}$$

here in terms of the dimensionful position variable Q of a massive oscillator. It is a normal distribution $\mathcal{N}(0, q_{\mathrm{zpf}}^2)$ [MH18, Ch. 6]. This

means that the ground state of a harmonic oscillator is a coherent superposition of position eigenstates, normally distributed around the origin of positions ($Q = 0$), which is the local minimum of the potential. The ground state is spread – delocalised – by a standard deviation $\mathrm{std}[Q] = \sqrt{\hbar/(2m\omega)} = q_{\mathrm{zpf}}$, where we recognised the scaling factor from Eq. (2.14) which we had called "zero-point fluctuation". One sees that it characterises the size of the ground state of a mechanical (harmonic) oscillator in terms of its std in position space. Using that the Fourier transform of the wavefunction gives the momentum representation Eq. (2.6), and that the Fourier transform of a Gaussian is again a Gaussian with inverse variance, one finds for the conventions adopted here that

$$|\psi_0(P)| \sim \mathcal{N}\left(0, p_{\mathrm{zpf}}^2\right). \tag{2.23}$$

We clarify here that the model we study describes the centre-of-mass motion of a massive harmonic oscillator, so that we are speaking about the position of the single point corresponding to the object's centre-of-mass. We just established that in its state of absolute minimal energy the centre of mass is normally distributed and delocalised in position and momentum.

Converting the exponent of the Gaussian functions of Eqs. (2.22) and (2.23) to dimensionless units with Eqs. (2.14) yields the same Gaussian distribution of both dimensionless position and momentum eigenstates forming the ground state

$$|\langle q|0\rangle|^2 = |\langle p|0\rangle|^2 \sim \mathcal{N}(0, 1/2). \tag{2.24}$$

In dimensionless units, all the results above apply formally whether one speaks of harmonic oscillators that are of (massive) mechanical nature or of (massless) electromagnetic nature.

In terms of the Heisenberg uncertainty relation Eq. (2.9), the standard deviation of the ground state of the harmonic oscillator are $\mathrm{std}[Q] = q_{\mathrm{zpf}}$ and $\mathrm{std}[P] = p_{\mathrm{zpf}}$ and one finds that it saturates the bound

$$\mathrm{std}[Q]\,\mathrm{std}[P] = q_{\mathrm{zpf}} p_{\mathrm{zpf}} = \hbar/2. \tag{2.25}$$

And similarly in dimensionless units $\mathrm{std}[q]\,\mathrm{std}[p] = 1/2$, cf. Eq. (2.16). This means that the uncertainty in position and momentum are minimised simultaneously – in this sense, the ground state is a minimal uncertainty state.

2.6 ENTANGLEMENT

We introduced mechanical and electromagnetic harmonic oscillators, which are the systems forming the optomechanical devices we study.

The second ingredient at the centre of our attention is entanglement, more specifically *opto–mechanical* entanglement that can exist between light and mechanical motion. Entanglement entails superpositions of correlations between two or more systems; these correlations emerge from the formalism of quantum mechanics and they lead to observable effects that are, in general, incompatible with classical theories.

In this work we consider *bi-partite entanglement*, that is entanglement between exactly two systems. [18] The two entangled systems can themselves have some internal structure and be composed of several sub-systems; we do not treat or assess entanglement within these sub-systems.

Bi-partite entanglement is defined as follows [Wer89; GT09; ARL14; Hor+09]. Consider two systems, labelled 1 and 2, with respective Hilbert spaces $\mathcal{H}_1$ and $\mathcal{H}_2$. A (joint) state of the two systems is a density operator ρ_{12} on the joint Hilbert space $\mathcal{H}_{12} = \mathcal{H}_1 \otimes \mathcal{H}_2$ (tensor product of Hilbert spaces). The state ρ_{12} is called *separable* if there exists $c_m \geqslant 0$ and states $\rho_1^m \in \mathcal{H}_1,\ \rho_2^m \in \mathcal{H}_2$, with $m = 1, \ldots, M$ and $\sum_{m=1}^{M} c_M = 1$, such that

$$\rho_{12} = \sum_{m=1}^{M} c_m \rho_1^m \otimes \rho_2^m. \tag{2.26}$$

ρ_{12} is *entangled* if it cannot be written in this way. Note that M is not related to any parameter of these systems, in particular, not to the dimensions of the Hilbert spaces.

It is useful to distinguish a sub-class of separable states called *product states*: they are those states where $c_1 = 1$ and all other coefficients are zero. Physically, product states describe uncorrelated systems, e.g. where both ρ_1 and ρ_2 were produced independently, thus encoding no information in their joint state. The more general separable states (with several different and non-zero c_ms) encode some non-fundamental (classical) correlations; e.g. quantifying which pairs of separable states ρ_2^m and ρ_1^m are most probable.

Given a state, it is hard in general to check whether it is entangled or not [GT09]. Rather than demonstrate that a certain state can or cannot be written as Eq. (2.26), one uses *entanglement tests*. It is (typically) a function f of the (joint) state ρ that returns a real number. When this number is below a certain threshold s – called *separability bound* – then the state is entangled

$$f(\rho) < s \implies \text{ent.} \qquad \text{(sufficient test)} \tag{2.27}$$

$$f(\rho) < s \iff \text{ent.} \qquad \text{(necessary and sufficient test).} \tag{2.28}$$

18. Entanglement among more than two parties – multi-partite entanglement – has a rich but complicated structure that we do not touch upon. The interested reader can have a look at [GT09; Hor+09; HE06; EG06] for example.

An example of entanglement test is the so-called *positive partial transpose* (PPT) criterion that was first proposed for finite-dimensional systems (like spins) by A. Peres and the Horodecki family [Per96; HHH96; Hor+09; GT09]; it was generalised later to continuous variables by R. Simon [Sim00; WW01; ARL14] which is relevant for our work and which we will present in detail in Sec. 3.4.

If the function f fulfils certain salient mathematical features (see [GT09, Sec. 4] for details) so that it provides an ordering of the entangled states, then it is called a *measure* of entanglement. With such a measure function, one can rank states as being more or less entangled compared to each other so that it makes sense to speak of the *amount* of entanglement in a certain state [GT09; Hor+09]. In this work, we use the *logarithmic negativity*, which is an *entanglement monotone* [Ple05], to quantify Gaussian entanglement [VW02]; it is particularly simple to use and to compute (being a tremendous advantage) and works fine as an entanglement quantifier for our purposes.

Tests and measure functions, as in Eq. (2.27), require full knowledge of the state ρ. In practice, one might have an idea about the state in an experimental setup (e.g. because it has been modelled, its preparation is well known, etc.), but it is rarely true that one knows it for sure – unless one characterises it completely with a "full-state tomography", which is not always possible and/or experimentally difficult. Alternatively, one can use *entanglement witnesses*, which are tests explicitly based on a set of measurements (that do not fully characterise the state). An entanglement witness is an observable W constructed in such a way that a state ρ is entangled whenever the expectation value of W is less than a separability bound s, similar to Eq. (2.27) above. Formally, one writes

$$w = \langle W \rangle = \mathrm{Tr}[\rho W] < s \implies \text{ent.} \tag{2.29}$$

and we call the number w the *witness value*. They take the form of a sufficient test. Importantly, they are not based on the knowledge of ρ because $\langle W \rangle$ is the result of the measurement procedure specified by W. For instance, the CHSH inequality, used to demonstrate Bell non-locality with entangled states, is a witness test of entanglement [GT09]. In the following, will study the EPR-variance, which is a witness based on second moments [HE06], see Sec. 3.4.

3

ELEMENTS OF CONTINUOUS-VARIABLES FORMALISM

A *continuous-variable system* is characterised by observables with infinitely many possible outcomes – the measurable variable is thus "continuous". An operator with infinitely many eigenvalues operates on a Hilbert space of correspondingly infinite dimensions. Position and momentum observables – i.e. quadratures – have continuous spectra of eigenvalues; they are continuous variables. The harmonic oscillator is thus an example of an infinite-dimensional continuous variable system, and the Hilbert space is the Fock space; cf. Sec. 2.5. More details can be found in standard reviews like [BL05; AI07; Wee+12] or textbooks like [Sch01].

3.1 QUANTUM PHASE SPACE

infinite-dimensional systems are conveniently described via the phase space formulation of quantum mechanics – which is a consistent quantisation method [CFZ14]. [1] States in the infinite-dimensional Hilbert space of a single, continuous-variable system (mode) are mapped onto the space of 2-dimensional real functions. This representation of quantum states shares striking similarities to classical statistical physics in phase space: in this sense, this looks like a simplification.

In classical physics, the phase space (or configuration space) of a 1-dimensional degree of freedom is $\mathbb{R}^2$ with axis corresponding to the dynamical variables (e.g. position and momentum); a point in phase space thus corresponds to a configuration of the system. The phase space also supports a probability distribution of configurations that models some lack of knowledge about the state (indefiniteness). As mentioned in Ch. 1, in classical models there is nothing fundamental in the probabilistic description of a state (i.e. its *indeterminacy*) in the sense that there is no limitation to how well one can know the configuration/state of the system in principle – a single point in phase space (or its generalisation to a Dirac-delta distribution) is a valid classical state. Quantum states, on the other hand, are fundamentally *uncertain* and (quantum) phase space provides a useful formalism to represent this indefiniteness – which is at the centre of this work.

1. Finite dimensional systems can also be described on an appropriate phase space, see for example [Til+16; Run+19].

Consider a continuous-variable system of M (bosonic) modes described by the tensor product of Hilbert spaces $\mathcal{H} = \bigotimes_{j=1}^{M} \mathcal{H}_j$, where $\mathcal{H}_j$ is the Fock space of mode j. The dimensionless[2] canonically conjugated quadratures of each mode are arranged in a $2M$-vector

$$\mathbf{r} \coloneqq (q_1, p_1, q_2, p_2, \ldots, p_M)^T \tag{3.1}$$

so that the canonical commutation relations take the form[3]

$$\left[\mathbf{r}_j, \mathbf{r}_k\right] = i\,\Omega_{jk}, \quad \Omega \coloneqq \bigoplus_{k=1}^{M} \begin{pmatrix} 0 & 1 \\ -1 & 0 \end{pmatrix}. \tag{3.2}$$

Ω is a $2M$-by-$2M$ matrix called the *symplectic form*.

Any state ρ is represented in phase space by the *Wigner function*

$$W(\mathbf{r}) \coloneqq \frac{1}{(\pi\hbar)^M} \int_{-\infty}^{\infty} d^M\mathbf{q}'\, \left\langle \mathbf{q} - \mathbf{q}' \right| \rho \left| \mathbf{q} + \mathbf{q}' \right\rangle e^{i\frac{2}{\hbar}\mathbf{q}'\cdot\mathbf{p}}. \tag{3.3}$$

It is a particular Wigner-Weyl map [CFZ14; AI07; Sch01] between the space of density operators on $\mathcal{H}$ and functions on phase space $\mathbb{R}^{2M}$. The map is faithful so that W is a complete and unambiguous representation of ρ, for all ρ. The Wigner function is not the only possible faithful representation of states on $\mathbb{R}^{2M}$: other well-known representations are the Glauber–Sudarshan P-function and the Husimi Q-function; see [GZ00, Ch. 4] for details. We stick to the Wigner function in the following because it was constructed to mimic probability distributions of (classical) statistical mechanics [GZ00].

Wigner functions (and actually all state representation functions in phase space) are *quasi-probability distribution*; this makes clear that, in general, a quantum state representation in phase space is not comparable to a classical probability distribution in phase space. Nevertheless, they have three mathematical properties that motivate the association with probability distributions, although they are not. Firstly, they are normalised

$$\int d^{2M}\mathbf{r}\, W(\mathbf{r}) = 1. \tag{3.4}$$

Second, the marginals $m(r_j)$ of W along any phase space coordinate r_j, $j = 1, \ldots, 2M$, are probability distributions, just like the marginals of a multi-variate probability distribution. They provide the probability of measurement outcomes of the observable r_j given the state ρ

$$m(r_j) = \int d^{2M-1}\mathbf{r}'\, W(\mathbf{r}', r_j) = \left\langle r_j \right| \rho \left| r_j \right\rangle. \tag{3.5}$$

2. For mechanical oscillator modes, recall the scaling factors from Eqs. (2.14).

3. Many conventions are possible here: we use those introduced in Ch. 2, they are the same as in [Sim00] for example.

Lastly, (quantum) expectation values are obtained from W in formally the same way as mathematical expectations are defined from a probability distribution: for an observable A

$$\langle A \rangle = \int \mathrm{d}^{2M}\mathbf{r}\, A(\mathbf{r}) W(\mathbf{r}) \tag{3.6}$$

where $A(\mathbf{r})$ is the operator's Wigner representation (replace ρ by A in Eq. (3.3)). For example, expectation values of quadratures are

$$\langle r_j \rangle = \int \mathrm{d}^{2M}\mathbf{r}\, r_j W(\mathbf{r}) \tag{3.7}$$

where r_j is an operator on the lhs and a real number (phase space coordinate) in the integral. The Wigner representation is associated with the symmetric [4] ordering of non-commuting operators [AI07]: for instance, the Wigner representation of the operator $A = q_j^2 p_j p_k$ is the symmetrised $A(\mathbf{r}) = (q_j^2 p_j p_k + q_j p_j q_j p_k + p_j q_j^2 p_k)/3$.

Importantly, quantum mechanics *is not* equivalent to statistical mechanics and this is partly encoded in the mathematical properties of W: prominently, W can take negative values, which is incompatible with it being a probability distribution. In fact, except for the important class of Gaussian states introduced in the next section, the Wigner function of all other pure states is negative-valued [Hud74]; for mixed states, the Wigner function can be positive and non-Gaussian in general.

3.2 GAUSSIAN STATES

Gaussian states are the class of states whose Wigner function is a multivariate Gaussian

$$W(\mathbf{r}) = \frac{\exp\left(-(\mathbf{r}-\boldsymbol{\mu})^{\mathsf{T}} \sigma^{-1} (\mathbf{r}-\boldsymbol{\mu})/2\right)}{(2\pi)^M \sqrt{\det|\sigma|}} \sim \mathcal{N}(\boldsymbol{\mu}, \sigma). \tag{3.8a}$$

Here $\boldsymbol{\mu}$ is the 2M-vector of means and σ is the 2M-by-2M matrix of *symmetrised (co-)variances* [5]

$$\boldsymbol{\mu} \coloneqq \langle \mathbf{r} \rangle \tag{3.8b}$$

$$\sigma \coloneqq \left\langle \mathbf{r}\mathbf{r}^{\mathsf{T}} \right\rangle_{\mathrm{sym}} - \boldsymbol{\mu}^2, \quad \text{with } \left\langle r_j r_k \right\rangle_{\mathrm{sym}} \coloneqq \frac{1}{2} \left\langle r_j r_k + r_k r_j \right\rangle. \tag{3.8c}$$

σ is a central quantity to the coming developments and we call it the *covariance matrix*. As in probability theory, σ is symmetric and positive definite. A normal distribution is entirely characterised by $\boldsymbol{\mu}$ (1st moments) and σ (2nd moments); hence, Gaussian states are entirely

4. The P-representation is associated with normal ordering and the Q-function with anti-normal ordering [AI07].

5. Mind that in the literature, σ is often the std of a variable (with variance σ^2); cf. [MH18, Sec. 6.7].

defined by $2M + 2M(2M-1)$ real numbers – a rather economical way of describing infinite-dimensional states.

Gaussian states are those states that are most accessible in practice. In Fig. 3.1, we plot the Wigner function of some relevant ones, namely: thermal, coherent, vacuum, and squeezed states. Examples of non-Gaussian states are Fock states $|n > 0\rangle$; see Fig. A.2. Appendix A provides details on states particularly useful for the considerations in this work.

Because the Wigner function of Gaussian states is positive, it is a (true) probability distribution, directly comparable to a distribution describing states in (classical) statistical mechanics.[6] In this sense, Gaussian quantum states are formally not different from indeterminate classical states. Because we aim at demonstrating entanglement – which, by all accounts, requires a genuinely quantum correlation between the systems – it is important to clarify what is "quantum", what is "classical", and why.

In Sec. 2.2, we related quantum state uncertainty to the non-commutation of observables Eq. (2.8). In the phase-space representation, uncertainty relations imply that the marginals of the Wigner function for incompatible variables cannot be too narrow simultaneously. The uncertainty relations are expressed as a constraint on the covariance matrix [Sim00; AI07]

$$\sigma \geqslant -\frac{i}{2}\Omega \tag{3.9}$$

where Ω is the symplectic form defined in Eq. (3.2). The uncertainty relation Eq. (3.9) is general and applies to any state – also to non-Gaussian states with higher moments.

The Wigner functions in Fig. 3.1 provide a pictorial account for the uncertainty relation of Gaussian states in phase space: the symmetric spread (in dimensionless units) of the coherent (including the vacuum) states saturates the uncertainty bound, hence it is the smallest achievable spread of both conjugated quadratures at once (i.e. minimal uncertainty states). The squeezed state on the other hand is a trade-off where more accuracy along one direction *must* be compensated by more uncertainty along an orthogonal direction.[7] Classically indeterminate states are not restricted in that way and can be arbitrarily peaked – corresponding to the classical assumption that a state (or configuration) can be certain.

The uncertainty constraint Eq. (3.9) thus limits the set of Wigner functions of Gaussian quantum states to a sub-set of all possible classical states with normal distributions. This situation is at odds with

6. In fact, all phase space representation functions (P or Q for example) of Gaussian states are normal distributions [AI07].

7. The volume of the Gaussian blob is fixed: like a closed tube of mayo, if you squish it one way, it must expand the other way.

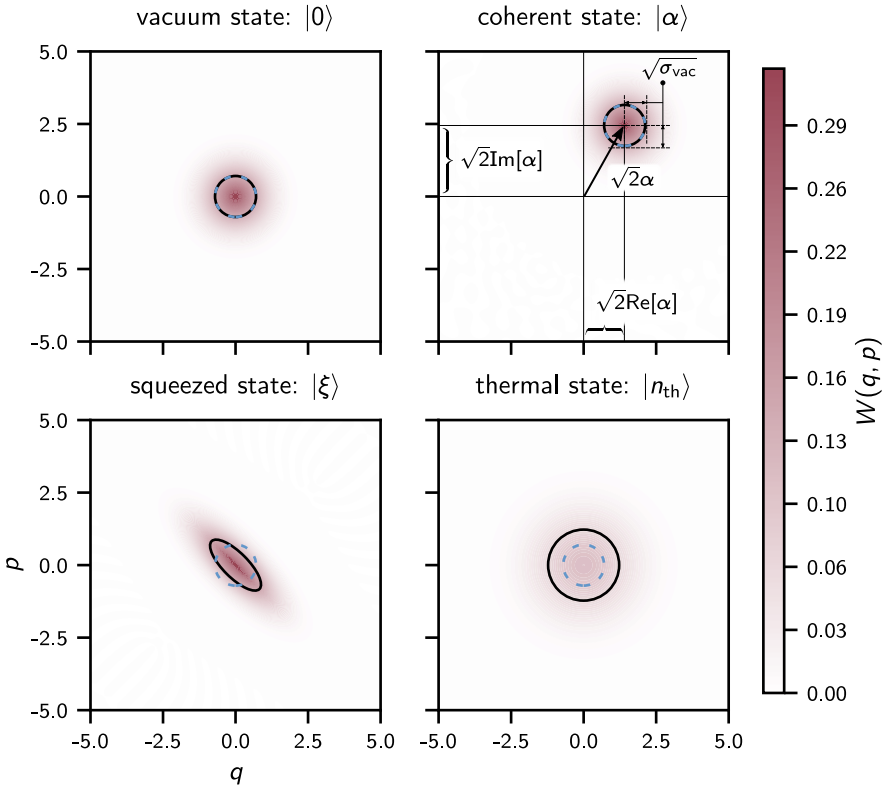

Figure 3.1 A collection of Gaussian states represented by their Wigner function $W(q, p)$. In black are the std ellipses of the corresponding bi-variate distribution; the dashed blue circle is the std of the vacuum for comparison. The coherent state's displacement is $\alpha = 2\,e^{i\,\pi/3}$, the squeezing parameter is $\xi = 0.5\,e^{i\,\pi/2}$ and the occupation of the thermal state is $n_{\text{th}} = 1$. The colour scale is the same for all plots. The Wigner functions were generated with the Python library Qutip [JNN12; JNN13].

the expectation that quantum mechanics is the more general theory from which classical mechanics "emerges" in some limit. This is one of the reasons why it is hard to argue that observing a certain feature of a Gaussian state is the witness of a quantum phenomenon: one can always come up with a classical statistical model that reproduces that result.

We are now in a position to make a statement about what is quantum and what is not in this work: the marker of quantumness for Gaussian states is that the variance of a generalised quadrature be less than that of the vacuum state (or a coherent state) – i.e. squeezing corresponding to quantum correlations between quadratures. Quantumness comes from acknowledging the fundamental uncertainty relation between non-commuting observables Eq. (2.8). Importantly, while there are works that support this definition in rigorous and quantitative terms, see [RSV17] for instance, other works, like [Cat+23], have a different stance and will say that classicality is equivalent, roughly, to

local-realism and there are local-realistic theories with mechanisms reproducing uncertainty relations.

3.3 GAUSSIAN DYNAMICS

We turn now to the physical processes that leave Gaussian states Gaussian – they are called Gaussian maps. These maps describe unitary evolution, fluctuations and dissipation, and measurements; see [EP03; Wee+12; Hol21].

Unitaries preserving the Gaussian character of states are generated by Hamiltonians that are at most second order in the operators

$$H = \mathbf{r}^\mathsf{T} A \mathbf{r} + \mathbf{b}^\mathsf{T} \mathbf{r} + c. \tag{3.10}$$

For M modes, $\mathbf{r}$ is the $2M$-vector of Hermitian quadratures Eq. (3.1), A is a $2M$-by-$2M$ Hermitian matrix, $\mathbf{b}$ is a real $2M$-vector, and c is a real constant. At the level of phase space representations, these unitaries are exactly the linear transformations S (square $2M$ matrices) that leave the symplectic form Eq. (3.2) invariant: $S^\mathsf{T} \Omega S = \Omega$. This is the defining property of *symplectic transforms* that leave Gaussian states Gaussian.

The dynamics in Heisenberg picture are given by the Heisenberg–von Neumann equation Eq. (2.11), whose equations of motion for quadratic Hamiltonians Eq. (3.10) are linear in the operators.[8] The constant term c commutes with the operators, hence it has no (direct) influence on the dynamics. The linear term $\mathbf{b}^\mathsf{T} \mathbf{r}$ leads to generalised displacement dynamics that shifts the $2M$ first moments of the state; see App. A.3 for details on the displacement operator. In the following, one will assume that the trajectories of the first moments are known (or have been computed already) and we place ourselves in a *displaced frame* that is constantly shifted with the opposite displacements so that, effectively in our description, the state's first moments remain zero at all times [AI07; AKM14]. In this frame, the Wigner function remains centered at the origin and Gaussian states are entirely described by their covariance matrix. For that reason, we will often refer to the covariance matrix of a Gaussian state as being *the state*. Therefore, only the quadratic terms in Eq. (3.10) are relevant for Gaussian unitary dynamics in what follows.

The quadratic Hamiltonian terms $\mathbf{r}^\mathsf{T} A \mathbf{r}$ describe two physical operations on the state's 2nd moments: *beam splitters* and *squeezers*.

8. See also [BYZ94] for an interesting and detailed comment on the difference between classical and quantum dynamics in phase space. Especially, they clarify that Ehrenfest theorem relates the quantum trajectories (that is the evolution of the first moments) to those of a definite (Dirac-delta) classical state. They argue that it is more relevant to compare time-evolved (measurable) moments of classical probability distributions (according to Liouville's equation) and of the Wigner function.

They are conventionally defined in the ladder operator basis (use Eq. (2.18) to convert $\mathbf{r}$ into a vector of ladder operators). For M modes, $j, k = 1, \dots, M$:

- **beam splitter (BS)** interaction Hamiltonian

$$H_{BS} \coloneqq \eta a_j a_k^\dagger + \eta^* a_j^\dagger a_k \tag{3.11}$$

  coherently distributes the excitations (energy) between each mode [VW94; GAC10]. The beam splitter applied to coherent states famously yields a separable output.[9] The transformation is *passive* because it does not change the total number of excitations in the system. It describes physical beam splitter devices [HOM87; VW94] which is an essential building block of (quantum) optical experiments. When acting on the same mode $j = k$, then the operation is a phase shift on mode j – which is the free evolution of the corresponding harmonic mode Eq. (2.20).
- **two-mode squeezer (TMS)** interaction Hamiltonian

$$H_{TMS} \coloneqq \xi a_i a_j + \xi^* a_i^\dagger a_j^\dagger \tag{3.12}$$

  creates and annihilates excitations on modes j and k simultaneously; see for example the form of the two-mode squeezed state Eq. (A.23) [CS85; SC85]. This transformation is called *active* because it changes the total number of excitations in the system (cf. Sec. A.4). When acting on the same mode $j = k$, then the operation is a single-mode squeezer.

In Sec. 5.3.1, we will see that both of these unitary operations arise in the linearised optomechanical interaction, and our scheme to detect optomechanical entanglement uses them. For now, we simply highlight that the "quantum" operation (or resource), when working with Gaussian states, is the squeezing operation [WEP03; EP03]. Of particular interest to us, the two-mode squeezing operation generates an entangled Gaussian state from the separable vacuum state [AI07; EP03]. This is in essence "where" entanglement comes from; see also [Kim+02] where they find that (roughly speaking) if the degree of squeezing below the vacuum level compensates the degree of thermal mixedness, then the output is entangled. The limit of an infinitely two mode squeezed state is the famous EPR-state [EPR35].

Non-unitary, open dynamics from the interaction of the (Gaussian) system with one or more environments lead to fluctuations and dissipation; see Ch. 4 where we discuss and model open systems. Under the general condition that the coupling to the bath is at most quadratic and that the state of the bath leads to a normal distribution underlying the associated fluctuations, then the state of the system will remain Gaussian [Wee+12; SC07].

9. This is the only example I know of unitary multi-mode dynamics of pure states that remains separable. In Ref. [Kim+02] they treat more general cases of squeezed and thermal inputs on a beam splitter.

Measurements affect states, and we restrict ourselves to only those measurements that leave Gaussian states Gaussian. These are the measurements of linear combinations of quadratures [Wee+12; SC07] like homodyne or heterodyne detection; see App. F for details of these detection methods.

3.4 BI-PARTITE GAUSSIAN ENTANGLEMENT TESTS

The prototypical (bi-partite) entangled pure Gaussian state is the two-mode squeezed state and Gaussian entanglement is essentially (single mode) squeezing distributed over the parties [EP03; Wee+12]; see also Appendix A.5 where we give details about two-mode squeezed states. Therefore, in the context of this thesis, testing for entanglement amounts to finding squeezing of the uncertainty of generalised quadratures below the reference uncertainty of the system's vacuum state [HE06]. We introduce here the entanglement tests used in the following.

The theoretical description and model of the protocol presented in Part II consider entanglement between exactly two modes: this is termed the $1+1$-modes bi-partite configurations. In the analysis of experimental data (discussed in Part III) it is possible to account for the more complex $M_1 + M_2$ bi-partition, i.e. where one partition contains M_1 modes and the other M_2 modes. Call $M = M_1 + M_2$ the total number of modes. Denote $\mathbf{r}$ the 2M-vector of quadrature coordinates Eq. (3.1). The $2M_1$ quadratures of the first party come first and the $2M_2$ quadratures of the second party come second, which defines the bi-partition of the state.[10] Gaussian entanglement is entirely characterised by the 2M-by-2M covariance matrix of the states [AI07; HE06].

3.4.1 *EPR-variance*

The EPR-variance[11] test is defined for $1+1$-mode systems and takes the form of

$$\Delta_{\text{EPR}} \coloneqq \text{var}\left[x_1 + x_2^\theta\right] + \text{var}\left[p_1 - p_2^\theta\right] \tag{3.13}$$

with

$$\mathbf{r}_2^\theta = \begin{pmatrix} x_2^\theta \\ p_2^\theta \end{pmatrix} = \begin{pmatrix} \cos(\theta) & \sin(\theta) \\ -\sin(\theta) & \cos(\theta) \end{pmatrix} \begin{pmatrix} x_2 \\ p_2 \end{pmatrix} = U(\theta)\mathbf{r}_2$$

10. This is the convention in the references used here.

11. Named in reference to the measurement and the state introduced in Einstein, Podolski, and Rosen's important article [EPR35] on the completeness of the quantum theory.

where $U(\theta)$ is a local rotation on the second mode. It is a sufficient (but in general not necessary) test for entanglement:

$$\Delta_{\text{EPR}} < 2 \implies \text{ent.} \tag{3.14}$$

The separability bound is 2 here so that the (joint) vacuum state saturates it; cf. Sec. 2.5 and App. A.1.

The EPR-variance is a sum of correlators of observables, hence it belongs to the class of *witnesses based on second moments* [HE06]. Formally, it can be written in a form strongly evocative of standard entanglement witnesses [cf. Eq. (2.29)], in terms of the covariance matrix σ of a state

$$\Delta_{\text{EPR}} = \text{Tr}[W_{\text{EPR}}\sigma] \,. \tag{3.15}$$

W_{EPR} is a real matrix that describes how the (measurable) second moments are combined to form the witness. The EPR-variance is a special case of the *Duan-criterion* [Dua+00]. In its necessary and sufficient formulation,' the witness matrix of the Duan-criterion $W_{\text{Duan}}(\sigma)$ depends on the state – in this sense, it is not a witness. On the other hand, W_{EPR} is fixed, up to a parameter ϕ that can be tuned, but not in a way that Δ_{EPR} becomes necessary for entanglement.

Δ_{EPR} is a well-known entanglement test with an interpretation in the spirit of the EPR-argument [EPR35]: it assesses whether the positions of both parties are anti-correlated [thus reducing the first term on the rhs in Eq. (3.13)] and the momenta correlated [thus reducing the second term on the rhs in Eq. (3.13)].[12] Effectively, the EPR-variance checks whether, in the 2-dimensional sub-space spanned by $(x_1 + x_2^\theta)$ and $(p_1 - p_2^\theta)$, the state is squeezed below the vacuum state extension *along both directions*. The entanglement test recognises that this is a special thing by acknowledging the fundamental limit in quantum uncertainty.[13] See also Fig. A.5 for a (nice) depiction of EPR-entanglement and testing. In our work, the advantage of using the EPR-variance is its mathematical simplicity, allowing us to compute explicit expressions analytically.

3.4.2 *Optimised witnesses based on second moments*

The Duan-criterion can be extended to states involving more than two modes. In [HE06] they demonstrate that, given the covariance

12. In [EPR35] they considered the correlated positons and anti-correlated momenta corresponding to the case $\theta = \pi/2$ in our definition Eq. (3.13).

13. In their famous argument against the completeness of quantum mechanics [EPR35] Einstein, Podolski, and Rosen did not question the existence of these correlations. They used such a two-system (EPR-) correlated state to show that their definition of "being and element of reality" was incompatible with the assumption that the wavefunction provides a complete description of a state.

matrix of a state (not necessarily Gaussian) with bi-partite $M_1 + M_2$-modes structure, it is possible to efficiently [14] find the *optimal witness* matrix W_{opt} that minimises $\text{Tr}\left[W_{\text{opt}}\sigma\right]$; and when the result of this expectation value is below the associated separability bound (e.g. 2, like in the Δ_{EPR}) then this implies entanglement. For $M_1 + M_2$-modes Gaussian states, this test is also necessary for entanglement.

It is thus the test one uses in the analysis of experimental data in Part III where the $M_1 + M_2$ structure is relevant for the so-called *multi-mode evaluation* procedure we used. Entanglement tests that are optimised for a given state can introduce to biases (e.g. due to imperfection of the state estimation). We adapt the optimisation and testing to mitigate that bias; discussions and details are provided in Sec. H.8.

3.4.3 *PPT-criterion for continuous variables*

The positive partial transpose (PPT) criterion testing for entanglement in finite-dimensional systems [Per96; HHH96; Hor+09; GT09] can be extended to infinite-dimensional (continuous-variables) systems [Sim00]. The test consists in taking the *partial transpose* of a bi-partite state with respect to one of the parties and then checking whether the resulting operator is still a "bona fide" state. If it is not, then this is sufficient (but in general not necessary) for entanglement. For a $M_1 + M_2$-mode continuous-variable system, with covariance matrices σ, the partially transposed state with respect to the first party is [Sim00; AI07]

$$\sigma^{\tau_1} = \theta_1 \sigma \theta_1, \text{ with } \theta_1 = \text{diag}(\underbrace{1, -1, 1, \ldots, -1}_{2M_1 \text{ entries}}, \underbrace{1, 1, \ldots, 1}_{2M_2 \text{ entries}}). \quad (3.16)$$

The partial transposition with respect to the second party is defined analogously. σ^{τ_1} is a ("bona fide") state if it fulfils the Heisenberg uncertainty relation Eq. (3.9): if it does not, then it is bi-partite entangled [Sim00]. Formally, we write

$$2\sigma^{\tau_k} < -i\,\Omega \implies \text{ent.} \quad (3.17)$$

for $k = 1$ or 2. The one directional arrow indicates that the PPT-criterion is only sufficient in general, but if the bi-partition structure is $M_1 = 1$ and $M_2 = M - 1$, then it is necessary and sufficient for entanglement [WW01; AI07]. [15]

The PPT entangelment test Eq. (3.17) can be expressed in terms of *symplectic eigenvalues*. Every covariance matrix can be diagonalised by

14. Semi-definite optimisation problem with polynomial complexity.

15. If the state has additional symmetries, there are cases with $M_1, M_2 > 1$ for which the criterion is also necessary and sufficient [AI07]. These cases are not relevant to our analysis.

the symplectic transformations (recall that they correspond to the unitaries that leave Gaussian states Gaussian, cf. Sec. 3.3). The diagonal elements of the thus diagonalised matrix are the *symplectic eigenvalues* denoted $\{\nu_j\}_{j=1}^{2M}$: they are the regular eigenvalues of $|i\,\Omega\sigma|$.[16] The Heisenberg uncertainty bound implies that the symplectic eigenvalues (their magnitude) of states are $\geqslant 1/2$ (also for non-Gaussian states).

Call $\{\nu_j^\tau\}_{j=1}^{2M}$ the symplectic eigenvalues of the partially transposed σ^τ and the smallest eigenvalue of that set $\nu_-^\tau \coloneqq \min_j\left[\nu_j^\tau\right]$. Then Eq. (3.17) is equivalent to

$$\nu_-^\tau < 1/2 \implies \text{ent.} \tag{3.18}$$

In the $1 \times M-1$-mode scenario, where the PPT-criterion is necessary and sufficient, at most one of the ν_j^τ can be less than $1/2$ [AI07].

3.4.4 *Logarithmic negativity*

When $M_1 = 1$ (or $M_2 = 1$) so that the PPT-criterion is necessary and sufficient, it seems intuitive to associate "more entanglement" with states with smaller symplectic eigenvalues. It makes ν_-^τ a good candidate for ranking entanglement states and building an entanglement measure. The *logarithmic negativity* function (logneg for short) is defined as [VW02; AI07]

$$\text{logneg}[\sigma] \coloneqq \max\left[0, -\ln\left(2\nu_-^\tau\right)\right]. \tag{3.19}$$

It is an entanglement monotone (and not a measure) [Ple05; AI07] but for all practical purposes in this thesis, we use it to quantify entanglement.

The relation between the PPT-criterion and the logarithmic negativity (via the minimal symplectic eigenvalue) suggests that larger violations of a separability bound in other tests or witnesses (like Δ_{EPR}) are associated with stronger quantum correlations or "more entanglement". Generally speaking, it is discouraged to think this way because measures (or monotones) must fulfil mathematical properties that enable quantitative statements. However, when dealing with Gaussian states, the violation of the optimal witness is a lower bound on the logarithmic negativity, so that a larger violation of the witness might involve more entanglement in that sense [HE06, Sec. 6.3]. For non-Gaussian states, the matter is more complicated, but the reasoning remains valid, and as they put it in [HE06, sec. 6.3]: "a state that very much violates this criterion [the optimised witness] is also very much entangled".

16. Symplectic eigenvalues come in pairs, so that there are at most M different ones. They are different from the (regular) eigenvalues of the matrix in general. $|\square|$ is the absolute value of the eigenvalues and not the determinant of the matrix.

4

ELEMENTS OF OPEN-SYSTEMS DYNAMICS

In the framework of this thesis, we can agree that the "interesting" systems are observable in some way (which is a rather positivist view point). Then, an observer is in a position to provide a description of a system based on observations. [1] Observation/measurement of the system updates the information the observer has about the state, and, according to the quantum formalism, the update looks like a disturbance of the state, in general. In this sense, from the point of view of an observer, a quantum system is disturbed (in the most general case) because the observer is aware of its existence through observations. [2]

More generally, the effect of noise on a quantum system can be interpreted as updates of the observer's knowledge about the system – its state. And similarly, measurement results update the observers' knowledge according to the rules of quantum mechanics. It is the same in classical statistical mechanics or thermodynamics. The difference from the quantum description are the updating rules. Prominently, in classical mechanics there are no tread-off requirements upon gaining information about a certain observable – in principle, measurements in classical physics always lead to improved overall information about the system.

Noise and disturbances affecting a quantum (or a classical) system (from the outside) are often modelled as interactions with external systems that form an *environment*. These environmental systems are characterised by the limited knowledge and control an operator has of them. The interactions with the (partially) unknown and uncontrolled environment affect the system in a partly unknown manner that we call noise. A system interacting with an environment is called *open*. In the quantum case, perturbations or noises of two distinct nature need to be accounted for: the ones resulting from measurements and those resulting from interactions with uncontrolled and unknowable other systems.

1. A lecturer at a the VCQ summer school 2020 asked the audience if they could think of a method to "detect", in some sense, a system that is not interacting at all (the context was a lecture on quantum gravity and dark-matter). They said they would be interested in such a scheme. Someone mentioned detection via the absence of signal.

2. I should clarify that in many relevant situations (theoretical or experimental) isolated system model provide accurate and useful predictions. Moreover, in certain cases, quantum measurements do not disturb the state (e.g. when the system is already in an eigenstate of the observable, which is common in protocols involving finite-dimensional systems).

In this work, the close link between measurement and noise is understood according to the theory of *decoherence* [Sch05; Sch07; Sch19; Zur81; Zur03; Zeh70; Zeh73; JZ85]. Decoherence is a mechanism that prevents the observation and experience of most states of a Hilbert space at our human scale; it explains the loss of quantum features (e.g. coherence) and the emergence of classical (i.e. non-quantum) behaviours. A decoherence model is essentially an open-system model; and depending on how information flows with respect to an observer, it models noise or measurement.

Central in mainstream models of decoherence, the system under consideration becomes entangled with systems of its environment. The information in these correlations is either obliterated (in the description), thus corresponding to noise, or it is channelled (transported and amplified) to the observer in the form of a measurement result [VN96; Zur81; Zur82; WM09; Lam18]; recall also our introductory discussion of an optomechanical position sensor in Sec. 1.4. [3] I personally like to think of measurements as "controlled decoherence" where some knowledge about the system is obtained (or saved from obliteration); or, conversely, decoherence is a set of measurements whose outcomes are ignored. Seen as an environment, a measurement apparatus is actually known and controlled (well enough).

Optomechanical cavity devices are coupled to two different environments: one for the mechanical oscillator mode and one for the cavity mode. The typical mechanical oscillators we have in mind in this work are mirco- or nano- fabricated devices whose elastic deformations/vibrations form the harmonic mode [Cle03; Gä20; Ber22; EBK24]. [4] These vibrating devices are clamped to a bulk substrate which corresponds to the mechanical environment. A description of the bulk – its precise state and its interaction with the mechanical mode of interest – is prohibitively complex to provide fully and we resort to a simplified open-system model that leads to accurate theoretical predictions in all the regimes we treat in this document [AKM14].

The environment of the cavity is the free electromagnetic field outside of it. Contrary to bulk matter, the state of the free light field can be derived from first principles (it is the quantisation of the electromagnetic field without charges; see [CTDRG97, Ch. II and III] for example), we thus have an analytical model for that environment. In our model, the cavity and its environment are part of the measurement apparatus

3. Note that the theory of decoherence provides explanations for several deep and important questions relating the quantum description to human everyday-life experience of the macroscopic (classical) world. Importantly, it does so within the quantum framework using the dynamics and Born rule [Sch05; Sch19].

4. Many of the results and considerations in this thesis apply to macroscopic devices like the suspended mirrors of LIGO and Virgo. But massive, low-frequency, mechanical oscillators are typically subject to non-Markovian correlated noises, which are not treated in this work. See for example our study of optomechanical entanglement in LIGO-like devices subject to coloured noise in [Dir+24].

that monitors the position of the mechanical oscillator. A particular set of modes of the cavity environment are measured by a photodetector – here, photodetection corresponds to retrieving information from the environment. Then the free-field state and dynamics allow us to draw a comprehensive picture of what happens in this quantum measurement (up to the point where the light itself is measured); recall Fig. 1.5 of a position sensor where the Heisenberg–von Neumann cut is in front of the photodetector.

From this perspective, the two environments of cavity optomechanical devices have different roles. On the one hand, the mechanical environment is hard to model and must be approximated; it is also inaccessible and all information shared with it must be considered lost. The environment of the cavity, on the other hand, bears a well established model and it is (partly) measured so that it is part of the quantum measurement apparatus monitoring the mechanical motion.

In the remainder of this chapter, we introduce a formalism to model the optomechanical state in the presence of the two environments. We provide equations of motion for the quadratures of the cavity and a mechanical mode in Heisenberg picture. These equations are called *quantum Langevin equations* (QLE) because they have the same form as the classical ones [GZ00].[5] The QLE are well suited to describe the protocol we propose and lead to exactly solvable dynamics.

4.1 SYSTEM–ENVIRONMENT PARADIGM

Consider a system of interest and its corresponding Hilbert space $\mathcal{H}_S$. Then consider an appropriately chosen environment with Hilbert space $\mathcal{H}_E$. In this work, we assume environments coupled weakly to the system and that are large (i.e. with effectively infinitely many degrees of freedom and dense energy spectrum) [GZ00, Sec. 3] [BP07, Sec. 3.1]. Such environments are also called *baths*, as in thermodynamics. In that limit, one can assume that the interaction with the system leaves the state of the bath unchanged [BP07, Sec. 3.3.1] and that the latter has no memory: i.e. all excitations or information from the system is "carried away rapidly into the environment and never comes back" – this is the obliteration of information mentioned above. This memoryless property of the environment is mathematically characterised by the limit of arbitrarily short correlation times

5. We note the important alternative approach in the Schrödinger picture that leads to a *master equation*. Its derivation traces out the environmental degrees of freedom, which makes the obliteration of the environment particularly explicit. For derivations and usage of the master equations, the reader is directed to [BP07; WM09]. There are convenient and accessible software to perform computations, for instance the python library Qutip [JNN12; JNN13] or the library QO in Julia [Krä+18].

within the environment [BP07, Sec. 3.3.1]: an operator e of a bath is delta-correlated in time

$$\langle e(t)e(t')\rangle \propto \delta(t-t'). \tag{4.1}$$

They lead to uncorrelated perturbations of the system in the form of white-noise, and we call such environments *Markovian*.

In this work, the systems will be a cavity and a mechanical mode, i.e. continuous-variable bosons, cf. Ch. 3. Similarly, we assume bosonic baths: e.g. the phonons (quanta of vibrations) of the substrate holding the mechanical oscillator and the photons of the free light field around the cavity. Finally, we assume that the baths are in thermal states characterised by Bose-Einstein distributions of energies; see Sec. A.6 for details on thermal states. Then we speak of *thermal baths* [BP07, Sec. 3.1.3].

We associate internal Hamiltonians H_S and H_E to both system and environment, respectively. The interaction between them is modelled with a Hamiltonian H_I. Importantly, we restrict to linear interactions: that is, H_I must be of the form $\sum_j g_j s_j \otimes e_j$, where g_j are scalar couplings, the s_j operators act on the system states and the e_j operators act on the environment states. Along with the assumption that the bath's state is Gaussian (thermal), this guaranties that the resulting fluctuations and dissipation form a Gaussian dynamical map, as discussed in Sec. 3.3. The compound dynamics is thus dictated by the total Hamiltonian

$$H = H_S + H_E + H_I. \tag{4.2}$$

4.2 QUANTUM LANGEVIN EQUATIONS

This section provides the (quantum) Langevin equations (QLE) of an optical cavity mode, a clamped mechanical oscillator, and a nanoparticle levitated in an optical tweezer. Although they are rather different systems, it turns out that their model and resulting open-dynamics are similar. As explained in Sec. 4.1, they lead to Gaussian, Markovian noise affecting the system.

Physically, the environment of an optical cavity is the collection of harmonic oscillators forming the modes of the free field that couple to it [GC85]. At optical frequencies, the state of the free field at room temperature (300 K) is the ground state, to a good approximation; cf. App. A.6. The bulk matter substrate, on which a mechanical oscillator is clamped, can be seen as a collection of masses bound harmonically to the mechanical resonator [FV63; CL83; GZ00]. The state of this environment is thermal at the temperature of the substrate (e.g. cryogenic temperatures of a few kelvins or less if it is placed in a dilution refrigerator). Levitated systems are affected by the tweezers'

photons scattering off it and by residual gas molecules in a thermal state at the temperature of the walls of the vacuum chamber.

The QLE are equations of motion of operators in the Heisenberg picture. For a dimensionless bosonic system operator z, the QLE have the following structure in this document

$$\dot{z} = \frac{i}{\hbar}[z, H_S] - \gamma z + \sqrt{2\gamma}\xi. \tag{4.3}$$

The commutator specifies the unitary evolution of the system under the Hamiltonian H_S [cf. Eq. (2.11)]; γ is the energy decay rate of the system into the environment and it gives the system–environment interaction strength; ξ is a stochastic process that implements the noise and the factor $\sqrt{\gamma}$, partly scaling its strength, reflects the fluctuation-dissipation theorem [Kub66; CW51; CG52].

The presence of both fluctuation and dissipation in the QLE is crucial for the dynamics to be meaningful quantum mechanically. In the absence of fluctuations, the dissipation would cause the operator z to decay to zero, which would make its commutator (with any other non-commuting system operator) Eqs. (2.15) and (2.19) decay to zero accordingly. But the commutator relates to the bosonic nature of z, which must not change in the course of the dynamics. It is the input noise fluctuations that ensure that the commutation relations are fulfilled at all times [CW51; CG52].

We note in passing that, in the presence of a cavity, a red detuned drive ($\Delta < 0$) also effectively damps the motion of the particle as well [AKM14]. In terms of Langevin equations, this mechanism is included in the unitary dynamics (commutator term) – in particular, the exact computation for a single mechanical mode devised in Ch. 9 includes this effective passive cavity cooling effect. In the broad cavity limit Eq. (8.4) we consider in this work, this effect is inefficient. [6]

4.2.1 *Cavity mode*

Consider a cavity mode with ladder operators c and $c^\dagger$ (cf. Sec. 2.5) coupled to the free field outside the cavity. The coupling strength κ is the cavity decay rate. We assume that the mode is at optical frequencies ω_{cav}, much larger than the optomechanical dynamics we are interested in (in particular $\omega_{cav} \gg \kappa$ or ω_m the mechanical frequency). In that regime, one performs a rotating-wave approximation so that the cavity–bath interaction is of the form of a beam splitter Eq. (3.11). We work

6. But it is not clear that it is unimportant because we find that, in certain parameter regimes, it improves entanglement detection with our protocol; see Sec. 10.1 and App. G.

in a frame rotating at ω_{cav} so that the integrals in the continuum limit of bath modes extend to $-\infty$. The QLE are [GC85, Sec. II]

$$\dot{c}(t) = -\frac{i}{\hbar}[c, H_S] - \frac{\kappa}{2}c(t) + \sqrt{\kappa}c_{in}(t) \tag{4.4}$$

and its Hermitian conjugate. The second term models viscous friction and yields exponential damping at a rate $\kappa/2$ – in frequency space this corresponds to the Lorentzian lineshape with full width at half-maximum (FWHM) κ of a cavity. The input operator c_{in} in the last term models fluctuations (noise) induced by the bath.

The statistic of the input noise process is given by the state of the bath, which is the vacuum at optical frequencies (cf. Sec. A.6). Therefore, c_{in} is Gaussian and characterised by its first two moments [GC85, Sec. II]

$$\langle c_{in} \rangle = 0 \tag{4.5a}$$

$$\left\langle c_{in}^\dagger(t)c_{in}(t') \right\rangle_{sym} = \left\langle c_{in}(t)c_{in}^\dagger(t') \right\rangle_{sym} = \frac{\delta(t-t')}{2} \tag{4.5b}$$

and all other correlators are zero. The delta-correlation reflects the assumption that the environment is Markovian.

4.2.2 *Clamped mechanical oscillator*

The derivation of QLE for a massive mechanical oscillators clamped to a substrate is provided in [GZ00, Ch. 3]. The bath is modelled by an ensemble of massive harmonic oscillators and the interaction is the product of the positions of the system's oscillator with the bath's oscillators [FV63; CL83] – we call it an "qx-coupling". Differently from the cavity case above, the coupling is not of the form of a beam splitter because the rotating-wave approximation cannot be performed, and there is no appropriate rotating frame that allows to extend the integrals to $-\infty$. The QLE for the dimensionless quadratures of the mechanical mode are [Hof15, Sec. 1.3.1]

$$\dot{q}(t) = -\frac{i}{\hbar}[q(t), H_S] \tag{4.6a}$$

$$\dot{p}(t) = -\frac{i}{\hbar}[p(t), H_S] - \gamma p(t) + \sqrt{2\gamma}\xi(t) \tag{4.6b}$$

where γ is the damping rate (FWHM) and ξ is a Hermitian input noise operator. Contrary to the QLE for the cavity Eqs. (4.4), these equations are asymmetric: i.e. fluctuations and dissipation affect the momentum quadrature only. This relates well to the intuition that the disturbance from the mechanical environment in the form of uncontrolled vibrations are like momentum kicks. In the decoherence vocabulary, the form of the (qx-)interaction with the bath determines the preferred

(pointer) basis being measured by the bath; and subsequently forgotten (obliterated) to appear like pure noise [Zur81; Zur82]. The noise ξ affects the position q via the internal (unitary) dynamics H_S (typically) connecting q and p.

As c_{in} for the cavity, ξ is a process whose statistics are dictated by the state of the bath. We assume that it is a thermal state at the temperature T of the substrate; therefore xi is a Gaussian process. The modes of the bath coupled to the mechanical oscillator are in the frequency range of ω_m. In this work, we will consider ω_m of a few tens of kHz up to GHz, therefore the thermal state of the bath has large occupation number n_{th} of the order 10^4 or more (see Sec. A.6 for details). The first two moments of ξ are then [Hof15, Sec. 1.3.1]

$$\langle \xi \rangle = 0 \tag{4.7a}$$

$$\left\langle \xi(t)\xi(t') \right\rangle_{sym} \approx \frac{k_B T}{\hbar\omega_m}\delta(t-t') \approx n_{th}(\omega_m)\delta(t-t'). \tag{4.7b}$$

Both approximations hold in the high temperature limit $k_B T \gg \hbar\omega_m$ where $n_{th} \gg 1$. The first states that the process is approximately Markovian in that limit [GV01]; contrary to the cavity case above, that is Markovian for a bath at zero temperature, i.e. with $n_{th} = 1/2$. $n_{th}(\omega_m)$ is the mean occupation number from a Bose-Einstein distribution Eq. (A.26) and the second approximation relates it to $k_B T/(\hbar\omega_m)$ according to Eq. (A.27).

4.2.3 *Levitated nano-particle*

In the final Part III of this thesis we study data from two setups where the mechanical oscillator is implemented by a nano-particle levitated at the tight focus of an intense laser field (called an optical *tweezer*[7]) [Del19; Mag21; Del+20b; Mag+21]. Quantum Langevin equations can be derived similarly to those for the cavity and the clamped mechanical systems.

The dominating noise mechanism in optically levitated systems is *photon recoil*: this is the random momentum exchange of the intense tweezer light with the particle. It is precisely the *radiation pressure* at the core of optomechanical devices. In the open-dynamics model, the electromagnetic field – tweezer + (free) field around the levitated particle – forms the bath associated to the photon recoil noise. Radiation pressure interaction is introduced in Sec. 5.3 where we find that, in the limit of large intensity of the light, the linearised coupling is of qx-type.[8] That it involves the particle's position reflects again

7. To be distinguished from magnetic levitation [Hof+23; Chi+17], which we do not treat in this work.

8. As for the the clamped mechanical systems above, no rotating wave approximation is possible.

that it is the degree of freedom being measured (by the environment here).[9] Similarly to the cavity above, we move to a rotating frame at the frequency of the tweezer ω_{tw} and the integrals over the bath energy levels can be extended to $-\infty$, because optical frequencies are so much larger than the optomechanical dynamics of interest. In this approximation, the terms that led to dissipation vanish identically – i.e. the QLE are frictionless(!?), which is at odds with the fluctuation–dissipation theorem. Radiation damping is expected in the form of Doppler cooling but its rate γ_{rad} is very small[10]; see [KFM08; Jai+16; Nov17] for discussions and theoretical expressions. Therefore, one writes the QLE for the dimensionless quadratures of the particle in the template form of Eq. (4.3) as

$$\dot{q} = -\frac{i}{\hbar}[q, H_S] \tag{4.8a}$$

$$\dot{p} = -\frac{i}{\hbar}[p, H_S] - \gamma_{rad} p + \sqrt{2\gamma_{rad}}\xi_{rad}. \tag{4.8b}$$

The statistics of the photon recoil process ξ is derived from the state of the environment it forms: an intense coherent state and the vacuum. Hence ξ is a Gaussian process. In a suitably displaced frame, the first moment is zero

$$\langle \xi_{rad}(t) \rangle = 0. \tag{4.9a}$$

Equations (4.8) explicitly enforce the template form of the Langevin equations Eq. (4.3) (and the fluctuation–dissipation theorem): given the damping rate γ_{rad}, the fluctuation strength is given by the noise process correlator

$$\left\langle \xi_{rad}(t)\xi_{rad}(t') \right\rangle_{sym} \approx n_{rad}\delta(t-t'). \tag{4.9b}$$

Markovianity is a consequence of the electromagnetic field model, as for the cavity in Sec. 4.2.1 above. In practice, γ_{rad} is too small to be measured[11] and it is the (re)heating rate $\Gamma_{rad} = \gamma_{rad} n_{rad}$ that is measurable [Jai+16]; because γ_{rad} is (very) small, n_{rad} is (very) large.

9. As far as I can tell, the use of the amplitude x of the light in the interaction model is a convention. It relates to the classical intuition that, in a sensor as in Fig. 1.3, the position of the object is encoded on the (physical) phase of the reflected light (it difference with send light actually). Here, the quantum dynamics Eq. (2.11) lead to position information being encoded onto the phase *quadrature* y. We explained in Sec. 2.5 that physical and quadrature phases are *different* physical things in general.

10. To my understanding, it is indeed the approximate extension of frequency integrals to $-\infty$ that misses the necessary finite damping. But the approximation at optical frequencies is quite good, which is consistent with the damping being quite small.

11. To my knowledge, radiation damping has not been measured directly yet. But with more and more levitation setups operating in ultra-high vacuum and the improvement of control to stabilise them, I can't wait to read about an experimental characterisation.

In the systems considered in this document, Γ_{rad} is the dominating noise [Del+20b; Mag+21].

In the setups studied in Part III, additional noises are relevant. We add them to Eqs. (4.8) in an ad hoc manner [following the template Eq. (4.3)] as

$$\dot{q} = -\frac{i}{\hbar}[q, H_S] \tag{4.10a}$$

$$\dot{p} = -\frac{i}{\hbar}[p, H_S] - \sum_j \gamma_j p + \sqrt{2\gamma_j}\xi_j. \tag{4.10b}$$

where j labels the different (and independent) baths connected to the levitated system.

Concretely, the additional dissipation and fluctuation mechanisms relevant for later are residual gas damping and feedback damping. The former is typically modelled in the same way as the thermal input noise ξ for a clamped mechanical oscillator [cf. Eqs. (4.6) and (4.7)] [Del+20a; Del19; Mag+21; Mag21; Jai+16]. The damping rate γ_{gas} can be expressed empirically with respect to the remaining gas pressure and average velocity of the molecules, see for example [Del19, Sec. 2.3.1] and references therein. The fluctuations are modelled by a Gaussian white-noise process $\sqrt{2\gamma_{\text{gas}}}\xi_{\text{gas}}$ with amplitude relating to the average kinetic energy of the gas at temperature T: in the thermodynamic limit, the average kinetic energy of the molecules is $k_B T$, corresponding to $n_{\text{gas}} \approx k_B T/(\hbar\omega_m)$ phonons at the frequency of the mechanical oscillator. We write the now familiar first and second moments

$$\langle \xi_{\text{gas}}(t) \rangle = 0 \tag{4.11a}$$

$$\langle \xi_{\text{gas}}(t)\xi_{\text{gas}}(t') \rangle_{\text{sym}} \approx n_{\text{gas}}\delta(t - t') \tag{4.11b}$$

where the approximation symbol reminds us that this is a classical (high temperature) limit.

Most levitation experiments in vacuum have some *feedback damping* implemented. It typically uses the knowledge of the particle's position (from prior measurements) and actuates the system (e.g. the trap) in order to decrease the particle's motional amplitude. This leads to an effective damping at rate γ_{fb} [Wil+15]. It (must!) come with an associated noise ξ_{fb} accounting, fundamentally, for the quantum noise in the measurement, and also for technical imperfection of the feedback mechanism. Depending on the feedback strategy, ξ_{fb} can be non-Markovian and non-Gaussian. For the practical cases studied in this thesis, the fluctuations due to feedback can be neglected compared to the photon recoil, while the feedback damping is large enough to stabilise the particle in the trap [Del+20b; Mag+22] (and possibly cool to its ground state [Mag+21; Teb+21]); in that limit, γ_{rad} can be neglected compared to γ_{fb}.

4.3 MEASURABLE OUTPUT LIGHT

Central to the aim of this work, we want to demonstrate optomechanical entanglement based on measurable quantities. Therefore, we need to specify what is measured: the light coming out of an optomechanical device forms the *output mode*, which is monitored (possibly continuously) by (linear) photodetectors that define the *detected mode*. Output and detection modes might have some mismatch (imperfect visibility) or photons from the output mode might not reach the detector (imperfect efficiency); (at optical frequencies) these are so-called *passive losses* and they are discussed in detail in Sec. F.2.

The presence of a cavity in the device defines the output mode: it is the mode of the free field outside the cavity (its bath, cf. Sec. 4.2.1) that couples to it at rate of the cavity linewidth κ (FWHM). Moreover, in the case where only one of the mirrors transmits light, then the input and output modes of the light overlap. Then, the quadratures x, y of the cavity mode – which relate to the mechanical oscillator via the optomechanical interaction (left unspecified in H_S here) – are encoded on the cavity output according to the so-called *input-output relations* [GC85]

$$x_{\text{out}} = \sqrt{\kappa} x - x_{\text{in}} \tag{4.12a}$$

$$y_{\text{out}} = \sqrt{\kappa} y - y_{\text{in}}. \tag{4.12b}$$

All quantities here relate to the QLE for the cavity Eqs. (4.4) transformed to the quadrature representations with Eqs. (2.18). The input–output equations for ladder operators take the exact same form.

In the absence of a cavity, the output mode is defined by some other property of the device. In a scattering picture model, the input light scatters form the optomechanical device and the scattered light forms the output mode. The relevant case here is when the optomechanical device is solely a nano-particle (in back-scattering configuration) held at the focus of an intense optical laser (tweezer). One writes [Mag21, Sec. 5.1.3]

$$x_{\text{out}} = x_{\text{vac}} \tag{4.13a}$$

$$y_{\text{out}} = y_{\text{vac}} + \sqrt{\Gamma_{\text{rad,j}}}\, q_j \tag{4.13b}$$

where $\Gamma_{\text{rad,j}}$ here is to be interpreted as the scattering rate into the output mode [in the same way the cavity decay rate is the coupling rate between cavity mode and detected mode of the output field in Eq. (4.12)]. Because the photon recoil bath is a coherent state (plus the vacuum), the input operators in a suitably displaced frame (cf. Sec. 3.3) are the vacuum state; and in these equations, x_{vac} and y_{vac} operate on the output mode exactly [12]

12. This shortcut from the full description where the input mode is different form the output one is possible precisely because the input are vacuum fluctuations (in

In general, and in the dipolar scattering case in particular, not all the scattered light is detected. In the back-scattering configuration, the lens (focussing the tweezer) is also the one (re-)collecting the (back-scattered) light and channelling the light towards the detector – i.e. it defines (theoretically speaking) the detection mode. The mode mismatch between output and detected modes leads to photon losses modelled by passive losses [13]; cf. App. F.2. We introduce the *collection visibility* $\nu_{\mathrm{coll}} (= n_{\mathrm{det}}/n_{\mathrm{in}})$ that quantifies the ratio of detected photons to total scattered photons. We call "orthogonal" the mode that is detected but not populated by the scattered light, and it is associated to the quadrature operators denoted $x^{\perp}_{\mathrm{out}}$ and $y^{\perp}_{\mathrm{out}}$. [14] It is in the vacuum state. We write the detected quadratures as [Mag21, Sec. 5.1.3]

$$x_{\mathrm{det}} = \sqrt{\nu_{\mathrm{coll}}} x_{\mathrm{vac}} + \sqrt{1-\nu_{\mathrm{coll}}} x^{\perp}_{\mathrm{out}} \tag{4.13c}$$

$$y_{\mathrm{det}} = \sqrt{\nu_{\mathrm{coll}}} \left[y_{\mathrm{vac}} + \sqrt{\Gamma_{\mathrm{rad},j}} q_j \right] + \sqrt{1-\nu_{\mathrm{coll}}} y^{\perp}_{\mathrm{out}}. \tag{4.13d}$$

The $\Gamma_{\mathrm{rad},j}$ enter the dynamical equations with two different roles. In the input-output relations Eqs. (4.13) they are a coupling rate that scales how well the particle's position is encoded on the detected channel – i.e. how much information an observer obtains about the particle. But in the QLE for the particle Eqs. (4.8) it is a noise term disturbing the particle's momentum. Both mechanisms are what we will call (measurement) *back-action* in Sec. 5.3.1. For this reason, $\Gamma_{\mathrm{rad},j}$ is also denoted by Γ^{ba}_j [Mag21; Mag+21]. For imperfect collection efficiency $\nu_{\mathrm{coll}} < 1$, it is common to denote $\Gamma_{\mathrm{meas},j} \coloneqq \nu_{\mathrm{coll}} \Gamma^{\mathrm{ba}}_j$ as the *measurement rate*.

The scattering picture is a neat example of how measurement and noise are both related in terms of gain and loss of information (with respect to the observer that updates their knowledge accordingly). Importantly, both measurement and noise are decoherence mechanisms. Here, observed and unobserved photons disturb (and decohere) the particle's motion: the detected photons lead to position localisation, while the undetected ones lead to recoil heating. Both are detrimental in the preparation of states in general; but certain Gaussian entangled states are robust to the passive losses decoherence (in the sense that they remain entangled for arbitrary finite losses) [Bar+11].

---

the displaces frame). See [Mag+21, Suppl. S.5] for the rigorous derivation and [Del19; Del+20b; GB+19] for the (more general) treatment of the coherent scattering configuration where the input and output modes do not overlap.

13. In the language of decoherence, the undetected scattered photons carry away information about the system and are "lost to the environment".

14. It is painful for me as well...

5

ELEMENTS OF CAVITY OPTOMECHANICS

This chapter describes the concrete physical optomechanical systems studied in this work, where a light mode is coupled via radiation pressure to some oscillatory-motion mode of a solid. They are modelled as quantum harmonic oscillators of different natures.

5.1 MECHANICAL MODE

In the context of this work, mechanical oscillators are vibrating massive objects. There are many ways to engineer mechanical oscillators and it heavily depends on what is their purpose. For most of them, the vibrating mode is a particular deformation of some solid: e.g. the cantilever or guitar-string motion of a nanorod [Ber22; Dos+19], the drum modes of a membrane [Gä20; Tsa+17], the breathing mode of a micro-torus [SK10] or of a helium droplet [Chi+17], the bulk or surface acoustic waves in a solid [O'C+10; Chu+18; Gus+14; Mod+20]; while for other mechanical oscillators, it is the entire solid body that is moving, for instance levitated nano-particles [Del19; Mag21] or suspended mirrors [Aas+15; Ber+21]. Detailed studies of every type of device lead to optimised and engineered properties such as reduction of losses (lower damping), engineering of the frequencies of the modes, and improvement of the coupling to light with better reflectivity and smaller interaction volumes.

A mechanical oscillator with effective mass m of the moving part and resonance frequency ω_m is associated to quadrature operators Q (position) and P (momentum). They relate to the corresponding dimensionless operators q and p via zero-point fluctuations factors q_{zpf} and p_{zpf} Eq. (2.14) that give (in absolute units) the ground state extension of the oscillator in phase space; cf. Secs. 2.5 and 3.1. The spread q_{zpf} and p_{zpf} are the typical scale of the fundamental uncertainty associated with the quantumness of a harmonic oscillator. The (non-Hermitian) ladder operators b and $b^\dagger$ relate to q and p via Eqs. (2.18) and the unitary dynamics of a harmonic oscillator is given by the Hamiltonian of Eq. (2.20)

$$H_{HO} = \frac{\hbar\omega_m}{2}\left(p^2 + q^2\right) = \hbar\omega_m\left(b^\dagger b + 1/2\right). \tag{5.1}$$

See Sec. 2.5 for details on quantum harmonic oscillators.

The technological advances in nano-fabrication of the last years allowed to produce mechanical oscillators with smaller masses and

larger frequencies thereby increasing q_{zpf} and making that typical "quantum scale" more accessible. Moreover, mechanical resonators with small masses are more susceptible to tiny forces, which makes them precise sensors.[1] Also, higher frequencies are favourable in terms of sensing because there are fewer possible sources of noise that could mask a signal at higher frequencies. This is relevant in this work where we study mechanical oscillators above 50 kHz so that the only relevant sources of noise are stationary (over the relevant time scales of the dynamics of the system), Markovian, and Gaussian (e.g. associated to a thermal bath model as in Ch. 4).

Another important property of mechanical oscillators is their amplitude decay or damping rate γ_m. In the open-system model of Ch. 4, the damping is due to the coupling to an environment and γ_m quantifies both how much energy is dissipated into the bath and how much the bath disturbs the system as a consequence of the fluctuation–dissipation theorem. Here again, technological developments in (micro-/nano-) fabrication made it possible to reach tiny decay rates, thus decoupling certain mechanical modes from their substrate/bath.[2] The usual figure of merit is the mechanical *quality factor* Q which compares γ_m to the mechanical frequency

$$Q := \frac{\omega_m}{\gamma_m}. \tag{5.2}$$

Q is the number of oscillations before the amplitude decreased significantly (by 1/e). Nowadays it is common to have systems with Q above 10^5 and some even reach 10^{10} [Ber22; Tsa+17; Gä20]; in this work, we always assume large $Q \gg 1$ so that we are deep in the underdamped regime.

5.2 CAVITY MODE

A cavity singles out a certain mode of the electromagnetic field. According to its quantisation, this field mode is described by a harmonic oscillator: cf. Sec. 2.5. We assign to it ladder operators c and $c^\dagger$, associated to dimensionless observable quadratures x (called "amplitude")

1. It is worthwhile noting that the nature of the force to be detected is also relevant in the choice of the oscillator's mass: for instance the LIGO/Virgo collaboration opted for very heavy masses because the mechanical oscillator acts as a low frequency noise filter rather than a resonant amplifier. Also, in an experiment measuring the gravitational force between small masses, they opted for a relatively large source mass with appreciable gravitational field strength and a relatively large test mass to have a sensitive acceleration sensor [Wes+21].

2. This reasoning is particularly suited for vibrational modes of solids clamped to a bulk substrate (like the membranes we will study later). In the case of optically levitated systems, decoupling from the bath amounts to losing control and measurement rate, therefore isolation as optimisation target is no longer suitable.

and y (called "phase"). The dynamics of the cavity mode is also given by the harmonic oscillator Hamiltonian Eq. (2.20)

$$H_{cav} = \frac{\hbar\omega_{cav}}{2}\left(y^2 + x^2\right) = \hbar\omega_{cav}\left(c^\dagger c + 1/2\right). \tag{5.3}$$

ω_{cav} is the resonance frequency of the cavity and we assume that it is at optical frequencies.

There are many possible implementations of electromagnetic resonators; for optical frequencies, we use here the prototypical Fabry-Pérot cavity in order to highlight typical relationships between key physical quantities (relations might be different for different implementations, but the underlying logic and principles remain the same). A Fabry–Pérot cavity consists of two perfectly parallel mirrors facing each other so that propagating light bounces back and forth between them. ω_{cav} is resonance of the cavity, that is, there must be a positive integer n such that $\omega_{cav} = \pi n c/L$, where L is the distance between the mirrors and c is the speed of light. We want to detect the light outside the cavity, and we assume that one of the mirrors has finite reflectivity and the other is (asymmetrically) perfectly reflective. The average number of times light bounces on the mirror before it is leaves is called *finesse* $\mathcal{F}$ and is large but fixed by the nature of the mirrors.

In Sec. 4.2.1 when we modelled the coupling of a cavity mode to the fields outside, we introduced the cavity decay rate κ in the QLE Eqs. (4.4). It is the decay rate of the mode quadratures. κ relates to the cavity finesse as

$$\kappa = \frac{\pi c}{\mathcal{F} L}. \tag{5.4}$$

Because the finesse is fixed, κ is tuned by changing the separation between the mirrors. From the perspective of the cavity field, κ scales the time light stays in the cavity; and the trapped light the mirrors corresponds to a build-up of intensity compared to free propagating light. This effect is quantified by the circulating power in the cavity: if $\dot{n}_{in}$ is the rate of photons [3] at the cavity input, we get for a resonant drive [HO17]

$$\dot{n}_{cav} = n_{cav}\frac{c}{2L} = \frac{2}{\pi}\mathcal{F}\dot{n}_{in}. \tag{5.5}$$

This is an enhancement of the circulating power by a factor proportional to the finesse.

Similarly to γ_m, κ is the coupling of the cavity mode to its thermal bath. But, as we stressed in Ch. 4, the role of the cavity environment is different from that of the mechanical oscillator because it is measured (or part of the measurement apparatus). Depending on the purpose of the optomechanical device, one chooses κ large or small compared

3. Multiply by $\hbar\omega_{cav}$ to get the power.

to the mechanical frequency ω_m: the narrow cavity regime where $\kappa < \omega_m$ (called "sideband resolved") is useful to tailor and enhance the optomechanical interaction and mitigate the noise input from the cavity environment. It is also helpful to efficiently cool the mechanical oscillator passively (possibly to its ground state) [AKM14]. The broad cavity linewidth regime $\kappa > \omega_m$ (called "sideband unresolved") corresponds to the case where light exits the cavity quickly so that the information it contains about the mechanical state is not delayed much; this is the regime we are interested in.

5.3 LINEAR OPTOMECHANICAL HAMILTONIAN

The optomechanical interaction considered in this work is radiation pressure between a cavity mode (or free space) and a mechanical mode (typically a vibrating deformation of a piece of matter or a swinging solid body). Radiation pressure is predicted (classically) by Maxwell's equations (through the Poynting vector of energy flux). Quantum mechanically, radiation pressure interaction is modelled by the following Hamiltonian [AKM14]

$$H_{int} = \sqrt{2} g_0 c^\dagger c q \tag{5.6}$$

where g_0 is the single photon coupling. In essence, this interaction couples the cavity mode intensity (or circulating power) $g_0 c^\dagger c$ to the mechanical position q. In the limit of strong drive (i.e. input power), the cavity average occupation is large $n_{cav} \gg 1$ and the interaction can be linearised to [Hof15; AKM14]

$$H_{int,lin} = 2\hbar g x q \tag{5.7}$$

where x is the cavity amplitude quadrature and g is the "dressed" optomechanical coupling

$$g \coloneqq g_0 \sqrt{n_{cav}/2}. \tag{5.8}$$

In a frame rotating at the frequency ω_d of the electromagnetic field driving the cavity, and displaced so that the first moments of the (cavity and mechanical modes) operators are zero at all times (cf. discussion of displaced frames in Sec. 3.3), the optomechanical Hamiltonian takes the following form

$$H_{OM,lin} = -\hbar\Delta c^\dagger c + \hbar\omega_m b^\dagger b + 2\hbar g x q. \tag{5.9}$$

We introduced the *detuning* $\Delta \coloneqq \omega_d - \omega_{cav}$ between the drive and the cavity (with the same sign convention as in [Hof15; AKM14]). If $\Delta < 0$ one speaks of *red detuning*, and one speaks of *blue detuning* when $\Delta > 0$.

5.3.1 *Unitary dynamics*

The linearised qx-optomechanical interaction Eq. (5.7) in the ladder operator representation is

$$H_{\text{int,lin}} = \hbar g(c^\dagger b + c b^\dagger) + \hbar g(c^\dagger b^\dagger + c b). \tag{5.10}$$

It contains two distinct mechanisms:

- The first bracket describes the swap of quanta from one mode to the other: $c^\dagger b$ annihilates a phonon and creates a cavity photon, and its Hermitian conjugate does the opposite. In Sec. 3.3 we had called this term *beam splitter* (BS) because it models the behaviour of a physical beam splitter, distributing excitations from two input channels across two outputs coherently.
- The second bracket creates (and annihilates) quanta in both modes simultaneously. We had called it *two-mode-squeezer* (TMS) in Sec. 3.3. When operating on a two modes Gaussian state where one mode is in the vacuum state and the other is in an (arbitrary!) thermal state, it generates an entangled state [MMS03; Bar+11]; this is the state we expect for the optomechanical systems we have in mind. This is essentially how the optomechanical entanglement that we aim to verify is created.

The two-mode squeezing interaction generates down-scattered (Stokes) photons at frequency $\omega_d - \omega_m$ (in the non-rotating laboratory frame) [AKM14] [Hof15, Sec. 1.2]. In the frequency spectrum[4] of the detectable light emitted by the cavity, these photons form a *sideband*. Because it is below the main component from the drive, it is called the *red sideband*; see Fig. 5.2. Similarly, the beam splitter interaction generates up-scattered light (anti-Stokes) at $\omega_d + \omega_m$ that appears as an upper sideband in a detection spectrum; therefore, this is called the *blue sideband*.

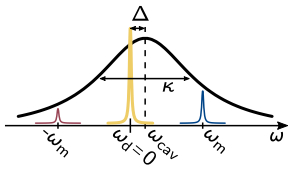

Fig. 5.2 Schematic of the three Lorentzian spectral components of the cavity output light: the driving field in yellow at $\omega_d = 0$ (in the rotating frame); the red (at $-\omega_m$) and blue (at $+\omega_m$) sidebands form the scattering with the mechanical oscillator according to $H_{\text{int,lin}}$ and transmitted by the cavity (broad black Lorentzian).

Relating the sidebands to the different interactions is a central guide for thoughts when devising the protocol to detect stationary entanglement in the coming Part II. Specifically, the components $\omega_d \pm \omega_m$ designate, in measurement records, which process produced the light (in that spectral component). The two-mode-squeezing interaction generates an entangled state of the cavity light and the mechanics, hence the photons on the red sideband contain information about the optical part of this entangled state. The beam splitter swaps coherently the mechanical state of the mechanics onto the light, hence the light in the blue sideband contains information about the mechanical state. This reasoning is at the core of our specific proposal of an experimental protocol to verify stationary optomechanical entanglement; see Ch. 6.

4. For example, monitoring the light in the stationary regime allows to determine the power spectral density (PSD) of the output light that tells how much intensity there is in different frequency bins.

5.4 SUMMARY OF OPTOMECHANICAL MODEL

In the previous sections, we provided a heuristic and, hopefully, intuitive picture of the optomechanical dynamics. In this section, we provide a rigorous treatment of cavity optomechanical devices as open systems where both the cavity and the mechanical modes are coupled to thermal baths, cf. Ch. 4. We present the scenario where two mechanical modes interact optomechanically with the cavity; this is a generalisation of the habitual treatment and it allows to introduce the notation used in the next parts. We combine here the material introduced so far: the quantum harmonic oscillator from Sec. 2.5, the linearised optomechanical interaction from Sec. 5.3 above, and the quantum Langevin equations (QLE) with their associated Gaussian white-noise models presented in Ch. 4. The continuous-variables formalism of Ch. 3 binds everything together in the compact picture of Gaussian dynamics with powerful tools to study states, dynamics, and (later) entanglement.

The solution for the detectable output light field is provided and discussed: it is the basis for the original work presented in the rest of the thesis. The derivation of the solution is well known; see [Gen+08] for instance. Nevertheless, we present it in App. C because there are several subtle points and notation (and Fourier transform conventions!) that deserve to be highlighted for anyone to reproduce or use the method. The symbolic calculations are implemented in a Mathematica notebook available in [Gut24, Theoretical predictions derivation .nb][5].

We want to describe cavity optomechanical devices that couple an optical mode of light to two mechanical oscillator modes via radiation pressure. On their own, cavity and mechanics are harmonic oscillators with frequencies ω_{cav}, ω_j ($j = 1, 2$). The mechanical frequencies relate to each other according to

$$\omega_2 = (1 + D)\omega_1 = \omega_1 + \Delta\omega \tag{5.11}$$

with $1 > |D| > 0$ – we expect $D \sim 1$ to 30% for the cases treated in this thesis. Cavity and mechanical modes are described by dimensionless Hermitian bosonic quadrature operators x, y, q_j, p_j, respectively. The quadratures are associated with non-Hermitian ladder operators c, $c^\dagger$ for the cavity mode, and b_j, $b_j^\dagger$ for the mechanical modes. They relate to each other according to [cf. Eqs. (2.18)]

$$\begin{aligned} b_j &= \frac{q_j + i\,p_j}{\sqrt{2}} & q_j &= \frac{b_j + b_j^\dagger}{\sqrt{2}} \\ b_j^\dagger &= \frac{q_j - i\,p_j}{\sqrt{2}} & p_j &= \frac{b_j - b_j^\dagger}{i\sqrt{2}} \end{aligned} \tag{5.12a}$$

5. File path:
`Thesis_CGut_StationaryOptomechanicalEntanglement/chapter_structure/9ch_TheoreticalPredictions/TheoreticalPredictions_derivation.nb`

and similarly for the cavity operators

$$\begin{aligned} c &= \frac{x + i y}{\sqrt{2}} & x &= \frac{c + c^\dagger}{\sqrt{2}} \\ c^\dagger &= \frac{x - i y}{\sqrt{2}} & y &= \frac{c - c^\dagger}{i\sqrt{2}}. \end{aligned} \tag{5.12b}$$

In the Heisenberg picture, they obey equal-time canonical bosonic commutation relations [cf. Eqs. (2.15) and (2.19)]

$$\left[q_j(t), p_j(t)\right] = i\,\delta_{jk} \qquad \left[b_j(t), b_k^\dagger(t)\right] = \delta_{jk} \tag{5.13a}$$

$$\left[x(t), y(t)\right] = i \qquad \left[c(t), c^\dagger(t)\right] = 1. \tag{5.13b}$$

The open-system dynamics in Heisenberg picture is given by the quantum Langevin equations (QLE) [Hof15, Sec. 1.3]

$$\dot{x} = -\frac{\kappa}{2}x - \Delta y + \sqrt{\kappa}x_{\text{in}} \tag{5.14a}$$

$$\dot{y} = \Delta x - \frac{\kappa}{2}y - 2g_1 q_1 - 2g_2 q_2 + \sqrt{\kappa}y_{\text{in}} \tag{5.14b}$$

$$\dot{q}_j = \omega_j p_j \tag{5.14c}$$

$$\dot{p}_j = -\omega_j q_j - \gamma_j p_j - 2g_j x + \sqrt{2\gamma_j}\xi_j. \tag{5.14d}$$

They are valid in the limit where the cavity is driven strongly, so that the optomechanical interaction can be linearised. In addition, they are expressed in a frame rotating at the drive frequency ω_d (detuning by Δ from the cavity resonance) and suitably displaced so that the operators have zero first moments. The mechanical modes interact only with the cavity at rates g_j (i.e. they are independent), and we assume that $g_1 > g_2$ (in the sense that the device is designed so that one mechanical mode is better readable by the light).

The environment of the cavity is the free electromagnetic fields outside. They are coupled at the rate of the cavity linewidth κ. At optical frequencies, the free fields are in an (almost) unoccupied thermal state (i.e. almost the vacuum) and the input noise is a Gaussian white-noise process characterised by its first two moments [cf. Eqs. (4.5)]

$$\langle x_{\text{in}}(t)\rangle = \langle y_{\text{in}}(t)\rangle = 0 \tag{5.15a}$$

and

$$\begin{aligned} \left\langle x_{\text{in}}(t) y_{\text{in}}(t')\right\rangle_{\text{sym}} &= \left\langle x_{\text{in}}(t) y_{\text{in}}(t')\right\rangle_{\text{sym}} = 0 \\ \left\langle x_{\text{in}}(t) x_{\text{in}}(t')\right\rangle_{\text{sym}} &= \left\langle y_{\text{in}}(t) y_{\text{in}}(t')\right\rangle_{\text{sym}} = \delta(t - t')/2. \end{aligned} \tag{5.15b}$$

The environments of the mechanical resonators are independent thermal baths. They couple at rate $\gamma_j \ll \omega_j$ so that both modes have high quality factors. It will be convenient for later to define a matrix of ratios of mechanical frequencies and decay rates

$$Q_{jk} \coloneqq \frac{\omega_j}{\gamma_k} \gg 1 \tag{5.16}$$

with $j, k = 1, 2$; the quality factors form the diagonal $Q_{jj} \equiv Q_j$ (we will use both notations). All the elements of the matrix are large for mechanical frequencies that are spaced by a few tens of percent [cf. Eq. (5.11)]. We assume that both baths are highly populated $n_j \gg 1$ (high temperature limit) and, for the systems we have in mind (e.g. clamped mechanical oscillators or levitated nano-particles), we expect that their temperatures are the same $T_1 = T_2 = T$. For mechanical frequencies differing by a few tens of percents, we have

$$n_j \approx k_B T_j/(\hbar\omega_j) \approx n_{k\neq j}. \tag{5.17}$$

The input noise operators are thus white-noise Gaussian processes as well, with statistics [cf. Eqs. (4.7)]

$$\langle \xi_j(t) \rangle = 0 \tag{5.18a}$$
$$\langle \xi_j(t)\xi_k(t') \rangle_{\text{sym}} \approx n_j \delta_{jk} \delta(t - t'). \tag{5.18b}$$

We assume that the dynamics are stable (see App. C.2 and/or [Gen+08]) with a unique steady state [Hof15]. In all subsequent analysis, we assume that this steady state has been reached.

We write the QLE Eqs. (5.14) in a compact matrix form as

$$\dot{\mathbf{r}}(t) = M\mathbf{r}(t) + N\mathbf{n}(t). \tag{5.19}$$

In control theory, one says that they form a *state-space model*, where the 6-vector of quadratures

$$\mathbf{r} \coloneqq (x, y, q_1, p_1, q_2, p_2)^T \equiv (x, y, q_j, p_j)^T \tag{5.20}$$

is called the *state vector*. The real 6-by-6 matrix M is called *system matrix* and it encodes the deterministic part of the dynamics. The 6-vector

$$\mathbf{n} \coloneqq (x_{\text{in}}, y_{\text{in}}, 0, \xi_j)^T \tag{5.21}$$

encodes the input stochastic fluctuations from the environments and is called the *input vector*. The 6-by-6 real matrix N is called *input matrix* and it encodes the coupling strengths of the input noises.

The solution to the linear system of ordinary differential equations Eq. (5.19) amounts to inverting a linear transformation in Fourier space [Gut24; Gen+08]

$$\mathbf{r}(\omega) = -(M + i\,\omega\mathbb{I})^{-1} N\mathbf{n}(\omega). \tag{5.22}$$

This form is the same regardless of whether one uses ladder or quadrature operator representations, but the explicit form of the matrices and vectors in terms of the system parameter must be adapted; see App. C for details.

The detectable light is the output of the cavity given by (cf. Sec. 4.3)

$$\mathbf{r}_{\text{out}}(\omega) = \begin{pmatrix} x_{\text{out}} \\ y_{\text{out}} \end{pmatrix} = \left[N_{\text{out}}(-1)(M + i\,\omega\mathbb{I})^{-1} N_{\text{in}} + N_{\text{fdtr}} \right] \mathbf{n}(\omega). \quad (5.23a)$$

In the vocabulary of state-space models, N_{out} is the *output matrix* and N_{fdtr} is the so-called *feed-through matrix*. Because $\mathbf{r}_{\text{out}}$ is a 2-vector,[6] N_{out} and N_{fdtr} must be rectangular 2-by-6. Moreover, their explicit form depends on the choice of ladder or quadrature representation as well; see App. C.

It is instructive to have a look at the explicit expression of the output light quadratures for the simpler but relevant undetuned case $\Delta = 0$ [Gut+20] (this calculation his carried out and checked in [Gut24, Theoretical predictions derivation .nb][7])

$$x_{\text{out}}(\omega) = \mathcal{S}(\omega) x_{\text{in}}(\omega) \quad (5.23b)$$

$$\begin{aligned} y_{\text{out}}(\omega) = \mathcal{S}(\omega) y_{\text{in}}(\omega) \\ + \sum_{j=1,2} 4\, g_j^2 \chi_{\text{opt}}(\omega)^2 \chi_j(\omega) x_{\text{in}} \\ - \sum_{j=1,2} 2\, g_j \sqrt{2\gamma_j}\, \chi_{\text{opt}}(\omega) \chi_j(\omega) \xi_j(\omega). \end{aligned} \quad (5.23c)$$

We introduced the *mechanical susceptibilities*

$$\chi_j(\omega) \coloneqq \frac{2\omega_j}{\omega_j^2 - \omega^2 - i\,\gamma_j \omega} = \frac{2\omega_j}{(\omega - \omega_j^+)(\omega - \omega_j^-)} \quad (5.23d)$$

with roots $\omega_j^{\pm} = (\pm\sqrt{4\omega_j^2 - \gamma_j^2} - i\,\gamma_j)/2$; the *optical susceptibility*

$$\chi_{\text{opt}}(\omega) \coloneqq \frac{\sqrt{\kappa}}{\kappa - 2i\,\omega} \quad (5.23e)$$

and the *reflection phase*

$$\mathcal{S}(\omega) \coloneqq \frac{\kappa + 2i\,\omega}{\kappa - 2i\,\omega}. \quad (5.23f)$$

The phase quadrature of the light is affected by the optomechanical interactions, while the amplitude quadrature encodes only the input noise of the cavity; this is a particular feature of the zero detuning case. For non-zero detuning, both quadratures encode the mechanical motion. We see that, in the displaced frame, the dynamics is driven by the environmental input fluctuations x_{in}, y_{in} and ξ_j. We distinguish three types of driving noises: *shotnoise*, *back-action noise*, and *thermal noise*.

6. Because we ignored the inaccessible output modes of the mechanical bath.
7. File path: see footnote 5.

SHOTNOISE The only term in x_{out} and the first one in y_{out} is the so-called shotnoise contribution. It corresponds to the (fundamental) vacuum fluctuations of the environmental mode supporting the output field. The phase $\delta(\omega)$ is due to the cavity that delays the output field compared to the input. Importantly, this shotnoise contribution does not depend on the presence of the mechanical oscillator; it is always present when detecting modes of light. When a sensing device is limited in sensitivity by this noise source it is called *shotnoise limited* – it is the best possible precision for measuring both quadratures of the light simultaneously. It is achievable with homodyne or heterodyne detection (discussed in App. F), which is considered a standard tool in quantum optics laboratories nowadays. Shotnoise in the detection of light is unavoidable, but it can be mitigated using squeezed states for the drive. This method is an example of quantum non-demolition methods used for improved sensing [GLM06; GLM11; Yu+20]. The shotnoise is a (fundamental) form of so-called "sensing noise", that is noise affecting the measurement probe on top of any signal (as opposed to the "force noise" below). An example of (non-fundamental) sensing noise is the thermal motion of the mirror's coating of the LIGO/Virgo interferometers. We do not include sensing noise explicitly in our model because it is not relevant for the micro-/nanomechanical devices we are primarily interested in. However, we discuss *passive losses* of imperfect detection in App. F.2, which are also a form of sensing noise.

BACK-ACTION NOISE The terms in the second line of the expression of y_{out} are the back-action contributions. Back-action originates from the amplitude quadrature x_{in} of the electromagnetic bath that enters the QLE Eqs. (5.14) as a drive of the cavity amplitude in Eq. (5.14a). Subsequently, it affects the mechanical momenta in Eq. (5.14d), which corresponds to the radiation pressure interaction of strength g_j. Then, the harmonic motion transfers the effect onto q_j via Eq. (5.14c). Finally, in Eq. (5.14b) a second optomechanical interaction encodes the fluctuations from q_j into the cavity's phase quadrature. This is how the input noise x_{in} "acts back" onto the output y_{out} through the optomechanical interaction twice (leading to the factor g_j^2). The mechanical susceptibilities χ_j describe the transduction of a drive by the mechanical modes. The cavity also transfers the back-action (twice), as encoded by the optical susceptibility χ_{opt}^2. With a suitable choice of correlation between x_{in} and y_{in}, the back-action term in Eq. (5.23c) can be reduced and, in principle, eliminated [Lei+16; Sho+19].

THERMAL NOISE The last terms in Eq. (5.23c) are the contributions from the mechanical baths via the operators ξ_j. They appear linear in g_j because they interact with the cavity mode only once. The effect of this driving noise is transmitted by the mechanical oscillators

and the cavity, hence the factors χ_j and χ_{opt}. It is an instance of what is sometimes called a "force noise" – i.e. a perturbation acting on the centre-of-mass motion of the mechanical oscillator and being transduced by it. From this point of view, our QLE model here is restricted to white force noises that are more common for oscillators at relatively high frequencies (typically above 10kHz). Low frequency mechanical modes are usually subject to non-Markovian noises such as structural damping [Fed+18; Grö+15; Cri+19] or seismic noise filtered by several suspension layers like in LIGO/Virgo [Aas+15; Ber+21]; see also our work on optomechanical entanglement in the presence of non-Markovian noise [Dir+24].

In this discussion of the different noises driving an optomechanical cavity, we see that shotnoise and back-action are related to the very fact of observing/measuring mechanical motion through the cavity bath in the vacuum state, while thermal noises are pure noise channels. It is useful to characterise the rate at which information is "read-out" from the system in the detection channel and the rate at which it is lost due to the noise channel. We introduce heuristically the *readout rates* and the *thermal noise rates*

$$\Gamma_j^{\mathrm{ro}} \coloneqq \frac{4g_j^2}{\kappa} \tag{5.24a}$$

$$\Gamma_j^{\mathrm{th}} \coloneqq \gamma_j n_j. \tag{5.24b}$$

Arguably, their meaning and origin from the QLE or the output field Eqs. (5.23b) and (5.23c) is not obvious; but they will come in handy later in the calculations and results of Part II. Γ_j^{ro} relates to the coherent optomechanical interaction rate, as observed at the cavity output – the factor $1/\kappa$ describes the transduction by the cavity, in the unresolved sideband limit $\kappa \gg \omega_j$. On the other hand, Γ_j^{th} are the thermal noise rates that would give the strength of the jumps operators in a Lindbald master equation: they are the product of the system–bath coupling γ_j with the strength (or number) n_j of incoherent excitations from the bath (typically associated to its temperature).

In the optomechanical literature, it is common to introduce the dimensionless *(quantum) cooperativity* C, which effectively quantifies how well mechanical motion is knowable, i.e. how well the mechanical mode is coherently coupled to the detectable output mode, as compared to the undetectable noise channel. The cooperativity is defined as the ratio of readout to thermal noise rates

$$C_j \coloneqq \frac{\Gamma_j^{\mathrm{ro}}}{\Gamma_j^{\mathrm{th}}} = \frac{4g_j^2}{\kappa\gamma_j n_j}. \tag{5.24c}$$

This definition (second term) also applies to devices without cavity; for a levitated particle in back-scattering configuration (treated in Part III) Γ^{ro} is the photon recoil rate Γ_{rad} (or back-action rate Γ_{ba}) from Sec. 4.2.3 [Mag21]. The right most term is the expression for cavity

optomechanical systems [AKM14]. [8] Cooperativity larger than 1 is a typical marker that one operates at the quantum limits; the cooperativity is closely related to the possibility of cooling the mechanical state to its ground state [AKM14; HH15].

It is surprising how little our results below relate to C and to the regime $C > 1$. Instead, the quantity that appears often in the coming study is what we call the *total dynamical rate*

$$\Gamma_j^{\text{tot}} := \Gamma_j^{\text{ro}} + \Gamma_j^{\text{th}}. \tag{5.24d}$$

We will see that it relates to the detection of entanglement in temporal modes of light, as prescribed by our protocol – so far we cannot attribute more physical meaning or interpretation to it.

8. It differs from the definition in [Hof15] where the thermal rate is $\gamma_j(n_j + 1)$. Our study is relevant only in the high temperature limit $n_j \gg 1$ where both definitions are equivalent.

Part II

A PROTOCOL TO DETECT STATIONARY OPTOMECHANICAL ENTANGLEMENT

PREFACE TO PART II

This part describes the details of a scheme to demonstrate stationary optomechanical entanglement experimentally. The main procedure and results were published in: C. Gut, K. Winkler, J. Hölscher-Obermaier, S. G. Hofer, R. Moghadas Nia, N. Walk, A. Steffens, J. Eisert, W. Wieczorek, J. A. Slater, M. Aspelmeyer, and K. Hammerer, Physical Review Research **2**, 033244 (2020) [Gut+20]. We also present subsequent analyses and extend the study to a second mechanical mode in the model. The developments presented here are for cavity optomechanical devices. It turns out that a similar derivation can be undertaken for devices without cavity; the derivation and study of this case is the work of my colleague Klemens Winkler, who will report on them elsewhere.

The theoretical description of stationary entanglement between a measurable light field and a mechanical oscillator was provided already in 2008 [Gen+08]. The experimental demonstration of optomechanical entanglement was performed in the pulsed regime in 2013 [Pal+13] and it remains an open challenge to demonstrate it in the stationary regime. Examples of proposals to do so [MDC10; Mia+10a; Mia+10b] are based on the deduction of the state of the mechanical oscillator from measurements of the light. This is possible by means of a state-space model (e.g. a Kalman filter) [Wie+15; Mag+21; Ros+19]. Entanglement in the thus deduced (filtered) joint state of the mechanics and the light can in principle be assessed. For the state-space model to provide accurate state estimations, the system parameters entering the model (e.g. mechanical frequency, couplings, decoherence rates, etc.) must be accurately characterised, which can be a challenging experimental task. The added value of our protocol presented in the following lies here: in principle, the parameters of the device need not be known (at all) to certify optomechanical entanglement. In the stationary regime, if one observes entanglement in particular temporal modes of the light coming out of the cavity, then this is enough to conclude the presence of stationary optomechanical entanglement. In practice, knowledge of the system parameters is useful for making model-based predictions.

ORGANISATION OF PART II

Chapter 6 presents the ideas at the core of the protocol, based on the physical understanding of optomechanics developed throughout Part I. It introduces the building blocks of our understanding and

interpretation, which guided more or less all subsequent choices, treatments, and derivations. The next chapters are devoted to a rigorous and systematic presentation of the protocol.

The generality of our approach relies on an entanglement verification "theorem"[9] that we present and prove in Ch. 7. It allows to infer optomechanical entanglement from the observation of entanglement between temporal modes of the light coming out of the device – but not vice versa. The theorem has two prerequisites that are agnostic of the system (neither the parameters nor the details of the dynamics need to be specified). As far as I can tell, in principle, all optomechanical devices can be operated in a way that satisfies these prerequisites; however, we do not expect that entanglement can be demonstrated in all systems with our approach.

Being sufficient – but not necessary – for optomechanical entanglement, the theorem is informative only when one successfully observes entanglement (in temporal modes of the output light). Moreover, it applies to any system, therefore it is not helpful to determine parameter regimes (or the type of devices) where entanglement can successfully be observed. In order to target systems that can succeed in demonstrating optomechanical entanglement, it is useful to specify a model and make theoretical predictions. This corresponds to making choices specifying some parameter regimes we think are favourable, as well as a particular procedure: in Section 8.1 we present the parameter regime we restrict ourselves to; in Section 8.2 we define particular temporal modes to test for entanglement; and in Section 8.3 we explain how entanglement can be tested given a certain measurement.

The resulting dynamical model is precisely that presented in Sec. 5.4 and the theoretical predictions for the protocol are presented in Ch. 9. Interestingly, the model is simple enough that we can determine the exact symbolic expression of the covariance matrix of the temporal modes of the light in Sec. 9.1.1. Moreover, in Sec. 9.2 we derive an approximate formula for the EPR-variance entanglement test, as a function of the system parameters, that is concise enough to be interpreted; with this formula we gain a better understanding of which devices can demonstrate stationary optomechanical entanglement and why.

SUMMARY OF RESULTS

The results of this part are:

9. We call it a "theorem" because it is essentially a mathematical statement – that comes with premises, conclusion, and a rigorous proof – which is central to our work. In the broader context of quantum information science, it would probably not bear the status of a theorem.

- An entanglement verification theorem providing general circumstances under which optomechanical entanglement can be inferred from measurements of the light only, see Ch. 7.
- The formulation of a concrete protocol applicable to a wide range of parameter regimes; see Ch. 8.
- The symbolic integral form for the covariance matrix of the temporal modes σ^{tm} Eq. (9.11) according to the protocol, as well as its exact integration (when $T_{\mathrm{sep}} = 0$); see Sec. 9.1.2 and [Gut24].
- An approximate expression of the EPR-variance entanglement test Eq. (9.27).
- Systematic comparison of the accuracy of the approximate formula with the exact result; see Sec. 9.3.

Various limiting cases are discussed, and we find that, for practical purposes:

- The temporal modes bandwidths must be larger than the total dynamical rate (i.e. the sum of readout and thermal noise rates): $\Gamma > \Gamma_1^{\mathrm{tot}}$ Eq. (9.35) is necessary for entanglement detection with the EPR-variance.
- Larger cooperativity leads to larger separability violations: see Eq. (9.45) in Sec. 9.4.1.
- Whenever effects from a spectator mode are not relevant, a sufficient condition for entanglement detection with the EPR-variance is $\Gamma_1^{\mathrm{tot}} < 2\,\omega_1/(3\,\sqrt[3]{2\,Q_{11}})$ Eq. (9.46a).
- Finite delay $T_{\mathrm{sep}} > 1/\kappa$ between the temporal modes does not prevent entanglement detection. Moreover, when $T_{\mathrm{sep}} = \pi/(2\,\omega_1)$ entanglement detection is more robust; see Sec. 9.4.3.
- The uncertainty of the mechanical frequency $\delta\omega$ (reflecting the uncertainty of the demodulation frequency of the temporal modes) must fulfil $\delta\omega < \Gamma/\sqrt{n_1(C_1+1)}$ Eq. (9.48). This a (stringent) constraint on the stability of the mechanical frequency over a measurement.
- When the spectator mode contribution dominates, Eqs. (9.50) give a sufficient condition for entanglement detection

$$3\,\Gamma_1^{\mathrm{tot}} < \frac{g_1}{g_2}\frac{\Delta\omega}{\sqrt{3\,n_2(C_2+1)}}.$$

6

HEURISTIC IDEAS AND BASIC INTUITION

Optomechanical devices are prototype position sensors: the (mechanical) surface reflecting the light is the *object being measured*; the light inside and outside the cavity with the detector form the *measurement apparatus*. (Unitary) quantum dynamics lead to entanglement between the output light and the mechanical motion: these (quantum) correlations between measured object and measurement apparatus are the way information is encoded, amplified, and transported in a von Neumann measurement model – and this is precisely the optomechanical entanglement we want to detect. Recall our introductory discussion in Sec. 1.4.

In order to certify entanglement between two parties, one must characterise (maybe not fully) both parties separately. This is the difficulty here because the state of the mechanical oscillator is not directly accessible. It is accessible via the measurement with the light (the apparatus) – which is indeed the reason for developing the position sensor in the first place! Concretely, we have to establish entanglement between mechanics and light with access only to the light; the scheme is thus necessarily indirect. This is a fundamental problem when studying apparatus–object entanglement in a von Neumann measurement model, namely, the apparatus *is* the mean of extracting information about the object so that one must look for correlations of the apparatus *with itself*. This calls for being careful as one might observe strong correlations that are actually trivial (like autocorrelation of the apparatus with itself for instance). Explicitly, we must extract from the out-coming light the relevant information about its own state and the relevant information about the mechanical oscillator's state. Then we must look for the appropriate correlations.

Our solution to this difficulty is based on the heuristic picture of the optomechanical dynamics presented in Sec. 5.3.1 and is a natural extension of the logic of the theoretical proposal to demonstrate optomechanical entanglement in non-stationary pulsed regime [Hof+11b] (which led to the experimental demonstration [Pal+13]). We explained there that the optomechanical interaction has two parts: the two-mode squeezer and the beam splitter, cf. Eq. (5.10). The former entangles the cavity light with the mechanical motion. The cavity state is mapped onto the output field so that the output mode and the mechanics are entangled. The beam splitter interaction, on the other hand, coherently maps the state of the mechanical oscillator and the cavity onto each other. After this operation, the cavity mode encodes part of the state

of the mechanics. Therefore, the cavity mode is entangled with the output light at earlier times. The state of the cavity is subsequently mapped onto the output field as well so that the entangled state, originally formed by the mechanical oscillator and the cavity, has been mapped onto the measurable output light at different times. It is worth emphasising the temporal ordering of the operations: first optomechanical two-mode squeezing generates the entangled state of the mechanics and the light (escaping the cavity and propagating away in the output mode); then the beam splitter interaction maps the state of the mechanics onto the light, which ultimately also propagates away from the cavity into the output mode. This suggests that selecting temporally ordered modes of the continuous output light allows to reveal (indirectly) the entanglement that existed between mechanics and light.

In the stable steady-state, this cycle happens continuously in time, hence the stationary nature of the entanglement. Also, for constant and continuous driving (necessary for stationarity), both beam splitter and two-mode squeezing processes happen simultaneously (and continuously), hence the sequence we depicted is a particular one, happening in parallel to all other possible sequences of these interactions in the continuous dynamics.

In Section 5.3.1, we saw that two-mode squeezer and beam splitter scatter light at frequencies $\mp\omega_{\mathrm{m}}$ (respectively) from the drive's frequency, thus forming the red and blue sidebands (respectively). We know that the photons on the lower sideband were produced by the two-mode squeezing interaction – and are entangled with the mechanics – and the photons in the upper sideband were produced by the beam splitter interaction and encode the state of the mechanical oscillator. Therefore, the first – or early – temporal mode of the output field should extract information about the red sideband, while a subsequent – later – temporal mode should extract information about the blue sideband. We expect these two modes to share the entanglement originally existing between the early optical mode and the mechanical mode. In other words, the mechanical oscillator *mediated* the entanglement between the early and late temporal modes of light. This logic, in the stationary regime and involving temporal modes of the output light retrieving information in both sidebands, was first formulated by Jason Hölscher-Obermaier in his thesis [HO17].

One must make sure that it is true that observing entanglement between temporal modes of the light is enough to infer optomechanical entanglement and what are the conditions under which this inference is possible. This is in essence the role of the entanglement verification "theorem" presented in Ch. 7: it formalises these ideas and rigorously guarantees that we can infer optomechanical entanglement from the observation of entanglement in the light, whenever its premises are fulfilled. This theorem is the core of the protocol.

To motivate the necessity for this general theorem, we mention the rather subtle – and daunting – phenomenon of "entanglement mediation, without entanglement of the mediator". Consider three systems A, B, and M; assume that they are originally in a separable state; A and B never interact with each other, but they both interact with the mediator M – this is a strict pairwise interaction between the mediator and the other two systems. A and B can become entangled via their interaction with the mediator in such a way that the mediator is never entangled with either A or B. Refs. [Cub+03; MK08] provide explicit protocols for this phenomenon, and experimental realisations are reported in Refs. [Fed+13; Peu+13; Vol+13].

The logic we proposed above is the same: the early and late temporal modes are systems A and B that do not interact with each other, and the mechanical oscillator is the mediator; we propose to observe entanglement between the temporal modes to infer entanglement between the early light mode and the mediator. The phenomenon just described is a particular case where the inference would be wrong: because it is possible to entangle the early and late temporal modes via their interaction with the mechanics, without the mechanics ever becoming entangled with any of the temporal modes. We must make sure that this situation is excluded. We will see that this requires assuming that the three parties are in an uncorrelated product state initially rather than in a separable state.

7

A THEOREM TO INFER ENTANGLEMENT FROM MEASUREMENTS

The following entanglement verification theorem applies to a scenario where two systems (call them E for early and L for late) interact pairwise and sequentially with a third system (call it M for mechnaics or mediator). It relates entanglement between the parties E and L to the entanglement between the mediator and the early system that interacted first. First, we state and prove the theorem, and then relate it to optomechanical scenarios of interest.

THEOREM Suppose the initial state (before any interaction) of the three parties E, L, and M is uncorrelated (i.e. it is a product state). Suppose also that system E interacts first with M, and only afterwards does system L interacts with M – this a strict sequential and pairwise interaction pattern. Then observing that E and L are entangled implies that E and M must have been entangled after their interaction. The panel at the bottom of Fig. 7.1 summarises this scenario.

PROOF The first requirement is that the initial state is an *uncorrelated product state*

$$\rho_{EML}^{init} = \rho_E \otimes \rho_M \otimes \rho_L. \tag{7.1}$$

The interaction between E and M can be described, in general, by a quantum channel $\mathcal{E}_{EM}$ [NC10] that acts non-trivially on E and M only – this is the second requirement that the interactions are sequential and pairwise. If this quantum channel *does not* generate entanglement between E and M, then

$$\begin{aligned}(\mathcal{E}_{EM} \otimes \mathbb{I}_L)\rho_{EML}^{init} &= \mathcal{E}_{EM}(\rho_E \otimes \rho_M) \otimes \rho_L \\ &= \sum_j p_j \rho_E^j \otimes \rho_M^j \otimes \rho_L.\end{aligned} \tag{7.2}$$

In this case, any subsequent channel $\mathcal{E}_{ML}$ acting on M and L cannot generate entanglement between E and L: the final state is

$$\begin{aligned}\rho_{EML}^{fin} &= (\mathbb{I}_L \otimes \mathcal{E}_{ML})(\mathcal{E}_{EM} \otimes \mathbb{I}_L)\rho_{EML}^{init} \\ &= \sum_j p_j \rho_E^j \otimes \mathcal{E}_{ML}(\rho_M^j \otimes \rho_L)\end{aligned} \tag{7.3}$$

and the reduced state of E and L is

$$\rho_{EL}^{fin} = \mathrm{tr}_M\left[\rho_{EML}^{fin}\right] = \sum_j p_j \rho_E^j \otimes \tilde{\rho}_L^j \tag{7.4}$$

where $\tilde{\rho}_{\mathrm{L}}^{\mathrm{j}} = \mathrm{tr}_{\mathrm{M}}\left[\mathcal{E}_{\mathrm{ML}}(\rho_{\mathrm{M}}^{\mathrm{j}} \otimes \rho_{\mathrm{L}})\right]$. The state $\rho_{\mathrm{EL}}^{\mathrm{fin}}$ is manifestly separable. This is essentially a consequence from the fact that entanglement cannot be created via local operations. It is the contraposed statement which is useful to us: if $\rho_{\mathrm{EL}}^{\mathrm{fin}}$ is entangled, then $\mathcal{E}_{\mathrm{EM}}$ must have entangled parties E and M. This terminates the proof. [1]

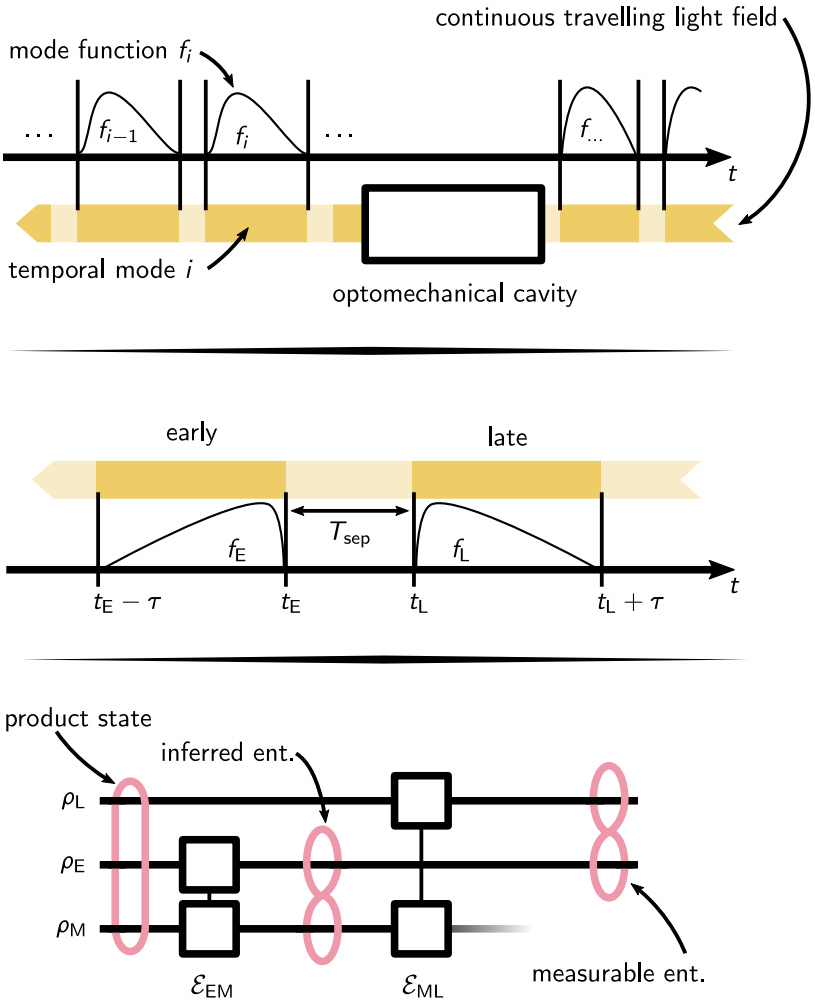

Figure 7.1 (top) The continuous light field (travelling to the left because the time axis points to the right) can be decomposed into temporal modes via an abstract modulation by mode functions f_i. In general, the temporal profile at the input of the device) is different than at the output. The shaded area is a temporal separation between the modes. (middle) Two temporal modes are considered: an early pulse (E) and a late pulse (L) defined by the mode functions f_{E} and f_{L}. (bottom) The quantum circuit corresponding to the dynamics. The mechanical oscillator (M); the early and the late pulses are initially in an uncorrelated state. M interacts sequentially with E and then L according to the quantum channels $\mathcal{E}_{\mathrm{EM}}$ and $\mathcal{E}_{\mathrm{ML}}$, respectively. Figure adapted from [Gut+20].

1. This proof is due to Klemens Hammerer. We also point out the critical contribution from Nathan Walk, who clarified for us that the initial state *must* be uncorrelated, and that assuming separability (involving possible classical correlations) was not strict enough.

7.1 DISCUSSION OF THE THEOREM

The physical nature of the three parties is irrelevant for the proof; also no assumptions about the form or effect of the channels $\mathcal{E}_{\mathrm{EM}}$ and $\mathcal{E}_{\mathrm{ML}}$ is necessary, so that any dynamics is allowed – not only stationary optomechanical processes. Hence, details of device parameters are not necessary. The restrictions are the two premises of the theorem: uncorrelated initial state and strict sequential pairwise interactions.

The conclusion of the theorem is an implication, i.e. entanglement between E and L is sufficient to infer entanglement between E and M, but the converse is not true in general and this theorem says nothing about the case when E and L are separable.

As explained in Ch. 6, the phenomenon of "mediated entanglement without entanglement with the mediator" [Cub+03; MK08; Fed+13; Peu+13; Vol+13] prevents from concluding the presence of optomechanical entanglement from detecting entangled light modes after interaction, in general. The premises of the theorem provide circumstances in which it is possible. In the references above, the initial state of E, M and L is separable but, crucially, it is (classically) correlated – i.e. it is not a product state as required by the theorem; it is because we require that the initial state is uncorrelated that we can write in general that the action of $\mathcal{E}_{\mathrm{EM}}$ yields a separable state in Eq. (7.2). On the other hand, in [Bar+19; Che+20] they observe entangled tones of the output field, but cannot conclude the presence of entanglement of a tone with the mechanics. In the light of our theorem, this is because they look at simultaneous tones, thus not fulfilling the strict sequential pairwise interaction constraint. Lastly, in the non-stationary pulsed protocol [Hof+11a; Pal+13], the interaction between entangling and readout pulses is strictly pairwise and the three parties are uncorrelated so that the theorem applies – in this sense, the pulsed protocol is a particular procedure using the theorem.

7.2 APPLICATION OF THE THEOREM TO OPTOMECHANICS

A general protocol to demonstrate optomechanical entanglement goes as follows. Take any optomechanical device and choose sequential and temporally non-overlapping modes E and L of the driving cavity input field: these temporal modes and the mechanical mode must be uncorrelated originally, and the temporal modes must interact strictly pairwise and one after another with the mechanical oscillator. For example, these modes could be sequential pulses sent to the device as in the pulsed protocol of [Hof+11a; Pal+13], or they can be an abstract temporal mode basis of the stationary continuous field, as we used in [Gut+20] and in this thesis. Then, measure the transmitted temporal light modes and test whether they are entangled: if they are,

then the E mode was entangled with the mechanical motion; if they are not, one can say nothing.

The choice of measurement depends on the entanglement test. In the most common situation where the dynamics and the states are Gaussian, tests like the Duan-criterion [Dua+00] or Simon's PPT criterion [Sim00] require measuring correlations of quadratures of the temporal modes which can be achieved by homodyne detection.

In the stationary regime, where an optomechanical device is driven by a continuous and constant light field, it is possible to decompose the state of the driving field into a basis of orthonormal temporal modes – that is modes with an explicit time dependence. This basis has infinitely many elements and we can choose two of these elements and call them ρ_E and ρ_L – they are the early (E) and late (L) temporal modes we study. Mathematically, they are characterised by temporal profiles described by functions $f_E(t)$ and $f_L(t)$ chosen so that the premises of the entanglement verification theorem are fulfilled. In particular, we can choose them strictly causal and non-overlapping, insuring that they interact one after the other with the mechanical mode ρ_m. Figure 7.1 (top) illustrates this idea. Additionally, the joint state of the mechanics and any two non-overlapping temporal modes of light is initially (i.e. far in the past, before interactions) in a product state.[2] These abstract pulses eventually come out of the device and one can perform appropriate measurements to test whether they are entangled. The transmitted temporal modes will, in general, be different from the input modes because they are transduced by the cavity and the mechanical oscillator. The output light is still a continuous field and the choice of the temporal modes can be performed at the level of the measurement: either by physical shaping and filtering of the light or in postprocessing of continuous measurement data.

In the presence of a cavity, strict pairwise interaction based (only) on causal and non-overlapping temporal modes is not strictly possible: once the cavity is populated by the first temporal mode, the photon population in the cavity will decay exponentially (at the rate κ of the cavity linewidth), but it will (mathematically speaking) never be *exactly* zero. Therefore, in this strict mathematical sense, there is always some light from the early mode left in the cavity when the late mode enters – this invalidates the sequential interaction requirement of the theorem. We thus introduce a separation time $T_{sep} > 0$ between the temporal modes. We choose $T_{sep} \gtrsim \kappa^{-1}$ such that the photons from the early mode have almost entirely left the cavity when the late mode enters the cavity. Another way, arguably cleaner, to ensure the strict sequential pairwise interaction is to restrict ourselves to devices without cavities where the mechanical mode interacts directly with the

2. Note that the driving laser coherence time/length is a statement about the phase of the coherent state, not about the correlation of second moments of the state.

detected mode of the free field. Klemens Winkler showed that this is possible and that the treatments and results are similar to what will be presented in the next chapters.[3] All the derivations and results in this Part II of the document focus on optomechanical devices including a cavity.

Defining the temporal modes in postprocessing is a flexible and convenient technique, but we must point out an important (theoretical) loophole: it relies on some knowledge of the device at hand. Given the output temporal modes chosen in postprocessing, one must check that the corresponding input modes fulfil the requirements of the entanglement verification theorem, i.e. one must know how the latter are transmitted by the device. Therefore, this technique cannot be entirely agnostic of the device's working and parameters. The scheme we propose in the following uses this technique (Ch. 8).

If the dynamics and the states are Gaussian, a most versatile approach is to measure both quadratures of the output field continuously, thus characterising its state fully. Then, the choice of temporal modes can be performed flexibly on the measured data in postprocessing. In practice, this corresponds to applying mode functions f_E and f_L to the continuous records of both quadratures, thus defining records of quadratures of the temporal modes. One can then estimate all the entries of the covariance matrix of these temporal modes, which is a complete description of their state (cf. Sec. 3.2). Finally, one can test for entanglement with any known criterion, witness, or measure; cf. Sec. 3.4 on Gaussian entanglement tests.

3. The details will be presented elsewhere. We consider a cavity-free device in Part III of this work, where we discuss real setups and analyse experimental datasets.

8

PROPOSAL OF AN EXPLICIT EXPERIMENTAL PROCEDURE

In Section 7.2, we sketched how a general protocol for detecting optomechanical entanglement using our entanglement verification theorem might look like. In this chapter, we make some choices and trade generality for definiteness that allows us to model the procedure and make theoretical predictions on the feasibility of the protocol – the derivation and presentation of these predictions are presented in the next chapter.

We want to describe a wide variety of optomechanical devices operating in broad parameter regimes. Also, we aim for an accurate model that remains simple enough to be solved; even better, we would like efficiently computed solutions for fast parameter sweep. In the best case, we can extract general behaviour of the protocol and physical insights of how entanglement is being detected. It turns out that all of these points can be met simultaneously.

8.1 RESTRICTION OF PARAMETER REGIMES

To the best of our understanding, the most favourable parameters for the stationary entanglement detection are exactly those of our open-system model of cavity optomechanical devices in Sec. 5.4. We review them quickly here, emphasising how they serve the logic of entanglement detection of Ch. 6 and with respect to the theorem.

Because it has not been demonstrated yet, we target stationary optomechanical entanglement. We thus restrict ourselves to *stable* parameter regimes, ensuring the existence of a stable steady state, and we assume that the system has reached it. Stability is assessed using the Routh-Hurwitz criterion; see [Hof15, Sec. 1.3.1] and [Gen+08] or the discussion in App. C.2. In terms of time-dependent operators in the Heisenberg picture subject to fluctuations (open-system dynamics), we speak of a *stationary regime* when their statistics are invariant under time translation. In this work, the stationary regime also means that all the parameters entering the dynamics are fixed: i.e. no modulations of the parameters like drive power or frequency.

To minimise noise due to coupling to an environment (cf. Ch. 4), we target mechanical oscillators that are well decoupled from their environment, i.e. with high mechanical quality factor [cf. Eqs. (5.2)]

$$Q_1 = Q_{11} \coloneqq \frac{\omega_1}{\gamma_1} \gg 1. \tag{8.1}$$

This is the multiple-mechanical modes notation of Eq. (5.16); in a first approach, we do not think about additional mechanical modes.

In Sec. 5.4, assuming high temperature of the mechanical bath(s) Eq. (5.17) leads to associated Markovian noise on the oscillator [GV01], which greatly simplifies the calculations. For this reason and also because it is a realistic and more accessible (i.e. wide-spread regime for experiments) experimental regime, we assume a highly populated thermal bath of the targeted mode

$$n_1 \approx \frac{k_B T_1}{\hbar \omega_1} \gg 1. \tag{8.2}$$

In [Gen+08; MDC10], it has been shown that stationary optomechanical entanglement persists for high bath occupations – in this sense it is "robust" against thermal decoherence – and it is reasonable to expect to detect it in this regime. [1]

Strong coherent optomechanical interaction is an intuitive requirement for generating entanglement, e.g. in the sense that it leads to larger cooperativities Eq. (5.24c). As in Sec. 5.3, we assume that the dressed coupling g_1 Eq. (5.8) is much larger than the single photon coupling $g_{0,1}$ of the targeted mechanical mode

$$g_1 \gg g_{0,1}. \tag{8.3}$$

This corresponds to driving the device with an intense laser, which is common in practice. In that regime, the linearised optomechanical interaction Hamiltonian Eq. (5.9) is accurate and the dynamics are Gaussian (which is an important simplification).

In Section 7.2, we introduced a delay $T_{sep} \gtrsim \kappa^{-1}$ to mitigate the optomechanical interaction overlap of early and late modes due to the cavity. On the other hand, we expect entanglement to diminish in time as a result of decoherence. Partly for that reason, we restrict ourselves to broad linewidth cavities, so that κ^{-1} is the shortest time scale of the dynamics. Consequently, T_{sep} can be accordingly short. In this broad cavity limit, the temporal modes at the input of the optomechanical

1. As commented in Sec. 5.3.1, light and mechanics can become entangled, although the mechanical state is highly thermal, because applying the two-mode squeezing on a joint thermal and vacuum state leads to an entangled state for any finite squeezing and independently of temperature of the thermal state; see [MMS03] and our calculation in [Gut24, TMS passive losses .nb] (file path: `Thesis_CGut_StationaryOptomechanicalEntanglement/chapter_structure/Happ_AnalysisPipeline/TMS_passiveLosses.nb`).

device are not significantly altered after their transmission by the device. Therefore, one can define the temporal modes on the recorded data in postprocessing (i.e. at the output) and assess whether they satisfy the entanglement verification theorem's requirements (which is on the modes at the input). Lastly, as we argued in Ch. 6, we intend to extract information about both sidebands, therefore the cavity linewidth must be large enough for a significant part of the sidebands to be present at the output; see Fig. 5.2. This corresponds to working in the *sideband unresolved regime* where [2]

$$\kappa \gg \omega_1. \tag{8.4}$$

Non-zero detuning Δ of the drive compared to the cavity enhances one sideband or the other [AKM14]. But with our reasoning, there is a priori no reason to enhance one sideband compared to the other, [3] hence we consider the zero detuning case so that red and blue sidebands have equal contributions in the output mode (see Fig. 5.2)

$$\Delta = 0. \tag{8.5}$$

In that case, the system is unconditionally stable [Hof15, Sec. 1.3.1]. $\kappa \gg \omega_1$ and $\Delta = 0$ is the typical operation regime of a position sensor.

We note that in the narrow cavity linewidth regime, one could study a drive with two frequencies (tones), one on each sideband, with the optomechanical interaction scattering light at the cavity resonance. Then one would look at the temporally separated modes at that frequency and assess their entanglement, similar to the pulsed protocol for optomechanical entanglement [Hof+11a; Pal+13] and the stationary entanglement between temporal modes of the output light [Bar+19; Che+20]. We have not studied this scenario.

8.2 CHOICE OF TEMPORAL MODE FILTERS

We present here a choice of two temporal profile functions that we call f_E and f_L; they define the early (E) and late (L) modes introduced in Ch. 7. They are two elements of a basis of time-dependent modes that can express the output light mode given by the annihilation

2. Note how, in the QLE Eqs. (5.14), κ and γ_1 have the same dissipation role. Yet we choose here that they are the shortest and longest time-scales of the system. This relates nicely to the different nature of their baths as discussed in Ch. 4: one is pure noise, while the other is measured and delivers information to the observer. Additionally, this limit looks counter-productive according to the intuition that cooperativity should be large (or maximised). I suggest that this is an early indicator that this intuition is not particularly useful in terms of entanglement detection with our protocol.

3. The exact calculation says otherwise: in App. G, we will see that some red detuning improves the EPR-variance and the logarithmic negativity detection sensitivity. We have currently no (heuristic or rigorous) insight as to why it is the case.

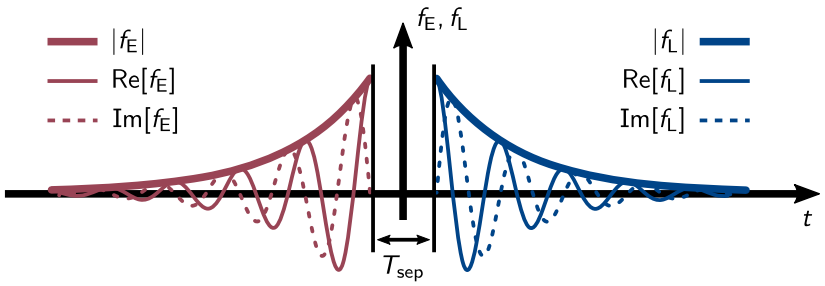

Figure 8.1 Mode functions of Eqs. (8.7): they are temporally ordered and non-overlapping as required by the entanglement verification theorem of Ch. 7. They are orthonormal as required by Eq. (8.12), and they are pulse-shaped to account for decoherence. The early pulse (in red) has a raising exponential time envelope and is resonant with the red sideband at $-\bar{\omega} = -\omega_1$. The late pulse (in blue) has an exponentially decaying envelope in time and is resonant with the blue sideband at $+\bar{\omega} = +\omega_1$. Figure reproduced from [Gut+20].

operator $c_{out}(t)$ (Heisenberg picture). We define the annihilation operator of a temporal mode, specified by a mode function $f_\alpha(t)$, $\alpha = E, L$, as

$$c_\alpha \coloneqq \int_{-\infty}^{\infty} dt\, f_\alpha(t) c_{out}(t) \tag{8.6}$$

This is essentially a weighted sum of $c_{out}(t)$ at different times. We choose the following explicit form for f_E and f_L, with three parameters $\bar{\omega}$, Γ, and T_{sep},

$$f_E(t) \coloneqq N e^{-i\omega_E t}\Theta(-t - T_{sep}/2) \tag{8.7a}$$
$$f_L(t) \coloneqq N e^{-i\omega_L t}\Theta(t - T_{sep}/2) \tag{8.7b}$$

with

$$\omega_E \coloneqq \bar{\omega} + i\Gamma \tag{8.7c}$$
$$\omega_L \coloneqq -\bar{\omega} - i\Gamma = -\omega_E \tag{8.7d}$$

where

$$N \coloneqq \sqrt{2\Gamma} e^{\Gamma T_{sep}/2} \tag{8.7e}$$

is the normalisation constant, and Θ is the Heaviside step function. They are hulls that decay exponentially at rate Γ, for demodulations at frequencies $-\bar{\omega}$ and $+\bar{\omega}$, and spaced by a duration T_{sep}; they are depicted in Fig. 8.1.

As we argued in Ch. 6, we will choose $\bar{\omega}$ close to ω_1 to demodulate the sidebands of the output field. In practice however, one should expect that ω_1 is not known perfectly so that

$$\bar{\omega} = (1 + d)\omega_1 = \omega_1 + \delta\omega \tag{8.8}$$

where we expect $|d| \ll 1$. Both modes have equal duration scaled by Γ. The inter-mode delay $T_{sep} > 0$ addresses the issue of light

trapped in the cavity preventing the strict pairwise interaction required by the entanglement verification theorem to infer optomechanical entanglement; see Sec. 7.2. Because we assume a stationary output field, one can choose an arbitrary reference for time: here, we chose the origin at $t = 0$ and the mode functions are symmetric around it so that $f_E(-t) = f_L(t)$. These mode functions were first proposed and discussed by Jason Hölscher-Obermaier in his Ph.D. thesis [HO17, Ch. 5.3].

f_α are orthonormal, which implies that c_α can be interpreted as the annihilation operator of the temporal mode α satisfying canonical commutation relations Eq. (2.19), $\alpha = E, L$,

$$\left[c_\alpha, c_\alpha^\dagger\right] = 1. \tag{8.9}$$

See also Eq. (8.12) below and the discussion of orthonormality that leads to it. This is a crucial property of the temporal mode operators that allows to use the continuous-variable formalism and the associated toolbox of Ch. 3 to describe states and test for entanglement.

In the broad cavity limit, where κ is the fastest time scale of the dynamics, the temporal profiles at the input of the optomechanical device are almost the same; as discussed above Eq. (8.4). The Heaviside function ensures that they are non-overlapping and ordered in time so that they interact sequentially and pairwise with the mechanical oscillator. Disjoint temporal modes of light are uncorrelated before the interaction. Therefore, the requirements of the theorem are met.

Because of decoherence, we expect entanglement between time bins to decrease with the duration of their separation, hence the f_αs give more weight to parts of the mode functions that are close in time. Among all possible forms of decay, we chose an exponential with decay rate Γ for both modes E and L; it is the same for both modes for mathematical convenience only. Γ is a free parameter that we can adjust and optimise in the procedure. It scales the effective duration of the temporal modes and, in frequency space, it is associated with a Lorentzian bandwidth (HWHM); see Eqs. (8.10a) below. This choice of exponential hull is consistent with the natural decay response of a cavity. Moreover, in [MDC10] (and partly in [Dir+24]) they derive the temporal mode of light sharing maximum amount of entanglement with the mechanical mode: it turns out to be the same as f_E above.

Generally speaking, we do not know how good our mode functions Eqs. (8.7) are: from experience we know that some choices are much worse, but we also know that other mode functions yield larger violations of particular entanglement witnesses (e.g. we discuss that multi-mode evaluations of experimental data are systematically better and show examples in Ch. 11). Ultimately, our theoretical predictions are that entanglement can be detected with these temporal modes, but they are probably not optimal. As of this day, we are not aware of any

way to find (or decide) what are the modes that are best for detecting entanglement with our scheme, and this question is actively being studied.

In Sec. 5.4 we expressed the solutions of the QLE model in frequency space [see our conventions for the Fourier transform Eqs. (C.8)], hence we give here the Fourier transform of the mode functions for later reference

$$f_\alpha(\omega) = \mathcal{F}[f_\alpha]_\omega = \frac{N_\alpha(\omega)}{\omega - \omega_\alpha} \tag{8.10a}$$

with

$$N_E(\omega) := -i\sqrt{\Gamma/\pi}\, e^{i(\bar{\omega}-\omega)T_{sep}/2} =: -N_L(-\omega) \tag{8.10b}$$

and ω_E, ω_L are as in Eqs. (8.7). They have symmetry $f_E(\omega) = f_L(-\omega)$. Their modulus squared are Lorentzian [4] with first moments $\pm\bar{\omega}$, respectively, and HWHM Γ. In this frequency representation of the temporal modes, we think of them as (Lorentzian) *filters* at frequencies $\pm\bar{\omega}$ and with bandwidth Γ.

8.2.1 *Multi-mode temporal filters*

In principle, one can choose a set of (infinitely many) temporal profiles $\{f_\alpha : \alpha = 1, 2\ldots\}$ and corresponding operators of the field outside the cavity c_α, given by Eq. (8.6). The set $\{c_\alpha\}_{\alpha=1}^{\infty}$ of temporal modes spans the Hilbert space of the output light field so that, at each time t, there are coefficients $c_t(\alpha)$ such that one can express the output field operators in terms of the c_α

$$c_{out}(t) = \sum_\alpha c_t(\alpha) c_\alpha. \tag{8.11}$$

Choosing (or changing) temporal modes corresponds to choosing a new set to express c_{out}. In selecting one (or more) temporal modes, we pick particular components of the output field. Notice how the time t is a label for states, but the underlying basis of temporal modes is fixed.

If we want to interpret c_α as the annihilation operator of the temporal mode labelled α, they must fulfil canonical commutation relations Eq. (2.19)

$$\left[c_\alpha, c_\beta^\dagger\right] = \delta_{\alpha\beta} \qquad \left[c_\alpha, c_\beta\right] = \left[c_\alpha^\dagger, c_\beta^\dagger\right] = 0. \tag{8.12a}$$

This amounts to requiring that the mode functions are orthonormal with respect to the L^2 inner product

$$f_\alpha \cdot f_\beta = \int_{-\infty}^{\infty} dt\, f_\alpha^*(t) f_\beta(t) = \delta_{\alpha\beta}. \tag{8.12b}$$

4. Also termed Cauchy probability density function.

If the set $\{f_\alpha\}$ of orthonormal functions also spans the space of functions L^2, then it forms a basis. Because ladder operators are not Hermitian, the mode functions can be complex.

With these considerations, we can generalise the mode functions to account for several components of the light split between a collection of early and late modes, with the only constraint of being orthonormal. This was explored in [HO17, Sec. 5.6] where they proposed additional early and late modes to incorporate setups with multiple mechanical modes. We used this technique to study experimental data and we will discuss the effect in Sec. H.4 and show examples in Ch. 11. Importantly, although more than two temporal modes are involved in such a generalisation, it is still bi-partite entanglement between the set of early and late modes that needs to be characterised.

8.3 CHOICE OF ENTANGLEMENT TESTS

As a last step in designing a specific protocol, we discuss tests for detecting entanglement in the measurable light. That is, the bipartite entanglement between the early (E) and late (L) temporal modes introduced in the entanglement verification theorem and completely specified by the functions f_E and f_L in Eqs. (8.7). In general, the choice of entanglement test specifies what information must be obtained by the experimental procedure, i.e. what measurement(s) must be performed. Technologies in quantum optics laboratories allow to measure both quadratures of light continuously and simultaneously at level of their vacuum fluctuations – thus characterising a stationary state of light completely. This is *not* prohibited by the Heisenberg uncertainty relation Eq. (2.9), as long as the bound is satisfied by the measurements results (or the estimable state) [WM09]; see App. F.3 for a discussion and an example of implementation called "dual-rail homodyne detection".

We thus assume that the full state of the light is continuously measured. Because the initial states (of the mechanics and the light), the noise processes, and the dynamics are Gaussian, the output field and its associated temporal modes are Gaussian too; cf. Sec. 3.3 on Gaussian maps. This means that the bi-partite state of the temporal modes is completely characterised by its covariance matrix σ^{tm} (in the displaced frame where the first moments are zero at all times); in particular, entanglement of the state is completely determined by σ^{tm}. See Appendix H or [HO17, Ch. 5] for an explicit description of how to compute σ^{tm} from a record of continuous quadratures-measurements. Because we have access to the entire covariance matrix of temporal modes, we can choose any bi-partite test of Gaussian entanglement – for instance those discussed in Sec. 3.4 or more generally in [ARL14].

Before we discuss which tests are best in the scenarios we are interested in, we take a step back and comment on the type of statements we can make about optomechanical entanglement from observing entanglement in σ^{tm}. The entanglement verification theorem provides a sufficient inference: entanglement between the temporal modes of light implies optomechanical entanglement. Therefore, using a necessary and sufficient criterion to determine whether the temporal modes are entangled or not does not transfer to the entanglement between the mechanics and the light. In particular, demonstrating that the temporal modes are not entangled does not allow to conclude that the mechanical mode and the light were not entangled. Similarly, any quantitative measure of entanglement in σ^{tm} does not allow to make (direct) quantitative statements about optomechanical entanglement. In this sense, there is no informational gain in using a powerful (and typically complicated) measure to characterise entanglement in the light versus using a less powerful (and relatively simple) sufficient criterion. From an experimental point of view, however, it is advantageous to use the most powerful or sensitive test possible in order to detect as many entangled states of the temporal modes as possible – thus increasing the probability of success. Moreover, tests leading to large violations of their separability bound leave more margin for unavoidable experimental imperfections. In addition, theoretical quantitative information about the *amount* of detectable entanglement in the light is useful to optimise the regime of operation and the parameters of the protocol.

In our work, we looked at the three tests introduced in detail in Sec. 3.4: the *EPR-variance*, a state-dependent *optimised witness*, and the *logarithmic negativity*.

The EPR-variance (Δ_{EPR}) was defined in Eq. (3.13); it is a witness based on second moments that is sufficient for entanglement in σ^{tm}. Its (relatively simple) mathematical form leads to expressions that we will work out analytically in Ch. 9. Under some simplifying assumptions, we provide in Sec. 9.2 an explicit approximate expression for Δ_{EPR} that is concise enough to be interpreted. Because it is (only) sufficient for entanglement, the predictions from this model underestimate the experimental capabilities of a given system.

Given the state σ^{tm}, one can compute an optimal witness that determines whether it is separable or not; see Sec. 3.4.2 and Ref. [HE06]. The optimisation is numerical, therefore it is not directly useful in the analytical treatments of Ch. 9. Because it is of the same nature as Δ_{EPR}, we compare them in Sec. 9.2 and assess the sub-optimality of Δ_{EPR}. In Part III, where we discuss the application of the protocol to study real experimental setups, we prefer to use the optimised witnesses because it is also necessary and sufficient when the temporal modes have internal structure (multi-mode evaluation). Moreover, our data analysis pipeline involves witness cross-validation to mitigate biases

from statistical errors, and the bootstrap method to estimate errorbars: both were developed for the optimal witness. Details are provided in Secs. 11.1,H.8, and H.9.

Finally, we also use the logarithmic negativity (cf. Sec. 3.4.4) to predict the amount of entanglement for the parameters of candidate experimental setups in Chs. 10, 11, and App. G. For Gaussian states, the separability violation of an optimised witness is an upper bound on the logarithmic negativity [HE06], hence we treat them as equivalent, which is not necessary in principle, but facilitates the numerical study.

9

THEORETICAL MODEL AND PREDICTIONS

This chapter presents a theoretical model of the protocol described and specified by the choices made in Ch. 8. We solve that model and present its predictions in terms of detectable entanglement. The main results are the theoretical demonstration of feasibility for broad realistic experimental parameter and noise regimes, as well as insightful formulae providing physical understanding and general limits on parameters to detect entanglement.

All relevant symbolic and numerical calculations in this chapter are also performed in a Mathematica notebook [Gut24, Theoretical predictions derivation .nb] [1]. Importantly, all exact mathematical simplifications and reformulations of expressions were systematically verified in the notebook. Approximations were systematically tested numerically for those set of parameters deemed relevant. In the following, we present an overview of the derivation with a focus on concepts, results, and interpretations; necessary technical details are given in App. E.

The structure of this chapter is as follows. From the explicit symbolic expression for the light output operators in frequency space Sec. 5.4 we compute its covariance matrix $\sigma^{\text{out}}(\omega)$. We then express the covariance matrix of the temporal modes σ^{tm} as an exact analytical integral over frequency. Under certain circumstances, this integral has an exact closed-form mathematical expression with finitely many symbols. We approximate σ^{out} and perform the integral by hand with the residue method to find a concise closed-form approximate formula for the EPR-variance, which can be interpreted physically. We study the predictions and limits of this formula in detail and establish constraints on the parameter regimes where entanglement can be detected with our protocol.

1. A PDF printout of the notebook and a parsable plain text file are available for readers who cannot use Mathematica. File path:
`Thesis_CGut_StationaryOptomechanicalEntanglement/chapter_structure/9ch_TheoreticalPredictions/TheoreticalPredictions_derivation.nb`

9.1 STATE OF MEASURABLE TEMPORAL MODES

9.1.1 *Exact symbolic expression*

Our starting point is the solution for the output light operators $\mathbf{r}_{\text{out}}(\omega)$ Eqs. (5.23) for the open-system optomechanical model of Sec. 5.4; the details of the solutions along with important conventions are given in App. C.2.

We define *early* (E) and *late* (L) temporal mode operators of the output light Eq. (8.7). The time overlap of $\mathbf{r}_{\text{out}} = (c_{\text{out}}, c_{\text{out}}^\dagger)^\mathsf{T}$ with the mode profiles f_α Eqs. (8.6), $\alpha = \mathrm{E}, \mathrm{L}$, is converted to an overlap in frequency with Plancherel's theorem

$$c_\alpha = \int \mathrm{d}\omega\, f_\alpha(-\omega) c_{\text{out}}(\omega), \qquad c_\alpha^\dagger = \int \mathrm{d}\omega\, f_\alpha^*(\omega) c_{\text{out}}^\dagger(-\omega). \tag{9.1}$$

We changed variables $\omega \to -\omega$ so that the argument of $c_{\text{out}}^\dagger$ is $-\omega$, complying with our convention on the operator adjoints in Fourier space Eq. (C.8c). These relations are true for any function f_α (provided it has definite L^2-norm and can be Fourier transformed).

The temporal mode filter functions f_E and f_L retrieve information about the first mechanical mode at ω_1 – we call it the *target* mode.[2] The mode functions considered here are not designed to extract information about the second mode at ω_2; hence, it is basically not taken into account in the analysis, and we call it the *spectator* mode.

Ideally, ω_1 is known perfectly and the filter functions can be tuned to it perfectly with

$$\bar{\omega} = \omega_1 \tag{9.2}$$

in Eqs. (8.7). In practice, we expect finite accuracy on ω_1, possibly limited by a combination of finite measurement statistics and drifts of the mechanical resonance over the course of a measurement run. This is modelled by imperfectly tuned filters with $\bar{\omega} = \omega_1 + \delta\omega$, where $\delta\omega = \omega_1 \mathrm{d}$ and $|\mathrm{d}| \ll 1$; cf. Eq. (8.8). We want to model a situation where the filters still extract information about the sidebands; hence we assume $\delta\omega < \Gamma$, so that the sidebands still fall in the bandwidth of the Lorentzian filters.

We define 2-by-2 *mode functions matrices* F_α ($\alpha = \mathrm{E}, \mathrm{L}$)

$$F_\alpha(\omega) = \begin{pmatrix} f_\alpha(\omega) & 0 \\ 0 & f_\alpha^*(-\omega) \end{pmatrix}. \tag{9.3}$$

They are diagonal in the ladder operator representation, but not in the quadrature representation. Taking advantage of the diagonal form,

2. This target mode is typically defined by the property $g_1 > g_2$ – in the sense that it is the one best coupled to the light. But there could be other considerations involved like the decoherence rate for example.

we label both entries $F_{\alpha,a}$, with $a = 1, 2$. Using Eq. (9.1), the 2-vector describing a temporal mode is

$$\mathbf{r}_\alpha \coloneqq \begin{pmatrix} c_\alpha \\ c_\alpha^\dagger \end{pmatrix} = \int d\omega\, F_\alpha(-\omega)\mathbf{r}_{\text{out}}(\omega). \tag{9.4}$$

The minus sign in the argument of the mode functions reminds us of the underlying Fourier transform conventions Eqs. (C.8).

We extend the definition of the mode-function matrix Eq. (9.3) to early and late modes. The joint state of both modes is a 4-vector $\mathbf{r}_{\text{tm}}$, hence the matrix of mode functions acting on the 2-vector of (cavity) output operators $\mathbf{r}_{\text{out}}$ must be of rectangular 4-by-2 type: we define

$$F^{\text{tm}}(\omega) \coloneqq \begin{pmatrix} F_E(\omega) \\ F_L(\omega) \end{pmatrix} = \begin{pmatrix} f_E(\omega) & 0 \\ 0 & f_E^*(-\omega) \\ f_L(\omega) & 0 \\ 0 & f_L^*(-\omega) \end{pmatrix} \tag{9.5}$$

where we stacked the 2-by-2 matrix of each mode function. Using the explicit matrix form Eq. (5.23a) for $\mathbf{r}_{\text{out}}$, the 4-vector of ladder operators of the E and L temporal modes is thus given by

$$\mathbf{r}_{\text{tm}} = \int d\omega\, F^{\text{tm}}(-\omega) \underbrace{\left[-N_{\text{out}}(M + i\,\omega\mathbb{I})^{-1}N_{\text{in}} + N_{\text{fdtr}}\right]}_{\coloneqq M(\omega)} \mathbf{n}(\omega). \tag{9.6}$$

The rectangular 2-by-6 matrix M, mapping the input on the output fields, is a short-hand notation for later. The form of this expression is valid for both ladder and quadrature representations, but the explicit form of all the matrices must be adapted accordingly; see Sec. C.1 for details.

We are now in a position to compute the 4-by-4 covariance matrix σ^{tm} of the state of the E and L modes. The Gaussian nature of the state is unaltered by expressing it in a particular basis of temporal modes. Hence, the joint state of temporal modes is Gaussian, with zero means in the displaced frame in which we are working. Then, the state is entirely determined by its second moments that form the covariances, and we say that σ^{tm} *is* the state of the temporal modes of light. From the definition of the covariances Eq. (3.8c) we write

$$\sigma^{\text{tm}} = \left\langle \mathbf{r}_{\text{tm}}\mathbf{r}_{\text{tm}}^{\mathsf{T}} \right\rangle_{\text{sym}} \tag{9.7}$$

where $\langle \square \rangle_{\text{sym}}$ is the symmetrised quantum mechanical expectation value. From Eq. (9.6) we find

$$\begin{aligned} \sigma^{\text{tm}} &= \int d\omega\, d\omega'\, F^{\text{tm}}(-\omega)M(\omega) \overbrace{\left\langle \mathbf{n}(\omega)\mathbf{n}^{\mathsf{T}}(\omega') \right\rangle_{\text{sym}}}^{\coloneqq D(\omega,\omega')} \\ &\qquad\qquad \times M^{\mathsf{T}}(\omega')F^{\text{tm}\,\mathsf{T}}(-\omega') \\ &= \int d\omega\, d\omega'\, F^{\text{tm}}(-\omega)\sigma^{\text{out}}(\omega,\omega')F^{\text{tm}\,\mathsf{T}}(-\omega'). \end{aligned} \tag{9.8}$$

We defined the 2-by-2 covariance matrix of the output light

$$\sigma^{\text{out}}(\omega,\omega') \coloneqq M(\omega)D(\omega,\omega')M^{\mathsf{T}}(\omega') \tag{9.9}$$

with the correlation matrix of the baths operators

$$D(\omega,\omega') = D\,\delta(\omega+\omega') \tag{9.10}$$

that encodes the white-noise models of the mechanical environments Eqs. (5.18) (valid when $n_1, n_2 \gg 1$) and of the cavity environment Eqs. (5.15); see App. C.4 for the derivation of $D(\omega,\omega')$. We replace the latter in Eq. (9.8) and integrate over the Dirac delta to find

$$\sigma^{\text{tm}} = \int d\omega\, F^{\text{tm}}(-\omega)\sigma^{\text{out}}(\omega,-\omega)F^{\text{tm}\,\mathsf{T}}(\omega). \tag{9.11}$$

The matrix product $\sigma^{\text{out}}(\omega,-\omega)$ can be computed explicitly and we find

$$\begin{aligned}\sigma^{\text{out}}(\omega) = S(\omega)\begin{pmatrix}0&1\\1&0\end{pmatrix} + [C(\omega)+X(\omega)]\begin{pmatrix}-1&1\\1&-1\end{pmatrix}\\ + R(\omega)\begin{pmatrix}1&0\\0&-1\end{pmatrix} + I(\omega)\begin{pmatrix}0&-1\\1&0\end{pmatrix}\end{aligned} \tag{9.12}$$

with

$$S(\omega) \coloneqq \frac{|\mathcal{S}(\omega)|^2}{2} = \frac{1}{2} \tag{9.13a}$$

$$\begin{aligned}C(\omega) \coloneqq 4\sum_{j=1}^{2} g_j^2\left[4\,g_j^2\left|\chi_{\text{opt}}(\omega)\right|^2 + \gamma_j n_j\right]\\ \times \left|\chi_{\text{opt}}(\omega)\right|^2\left|\chi_j(\omega)\right|^2\end{aligned} \tag{9.13b}$$

$$\begin{aligned}R(\omega) &\coloneqq 4i\sum_{j=1}^{2} g_j^2\left|\chi_{\text{opt}}(\omega)\right|^2 \operatorname{Re}\left[\chi_j(\omega)\right]\\ &= 2i\sum_{j=1}^{2} g_j^2\frac{(\omega_j^2-\omega^2)}{\omega_j}\left|\chi_{\text{opt}}(\omega)\right|^2\left|\chi_j(\omega)\right|^2\end{aligned} \tag{9.13c}$$

$$\begin{aligned}I(\omega) &\coloneqq 4\sum_{j=1}^{2} g_j^2\left|\chi_{\text{opt}}(\omega)\right|^2 \operatorname{Im}\left[\chi_j(\omega)\right]\\ &= 2\sum_{j=1}^{2} g_j^2\frac{\gamma_j\omega}{\omega_j}\left|\chi_{\text{opt}}(\omega)\right|^2\left|\chi_j(\omega)\right|^2\end{aligned} \tag{9.13d}$$

$$\begin{aligned}X(\omega) &\coloneqq 16\,g_1^2 g_2^2\left|\chi_{\text{opt}}(\omega)\right|^4 \operatorname{Re}[\chi_1(\omega)\chi_2^*(\omega)]\\ &= 8\frac{g_1^2 g_2^2}{\omega_1\omega_2}\left[(\omega^2-\omega_1^2)(\omega^2-\omega_2^2)+\gamma_1\gamma_2\omega^2\right]\\ &\qquad\times\left|\chi_{\text{opt}}(\omega)\right|^4|\chi_1(\omega)|^2|\chi_2(\omega)|^2.\end{aligned} \tag{9.13e}$$

These expressions are also valid for a single mechanical mode: in that case $g_2 = 0$ and only those terms with index $j = 1$ contribute. In particular, the function X is zero. The constant S is the sum of the cavity input noise in the output channel and its reflection by the cavity – it is the shotnoise contribution discussed at the end of Sec. 5.4. It is a white-noise component to the output state (i.e. a constant in frequency space), which leads to unphysical infinity when integrated over all frequencies;[3] we will see later how the finite bandwidth of the filtering mode functions regularise this behaviour. The function X combines contributions from both modes. It appears because both mechanical modes interact with the same cavity mode – in particular, this term does not appear in cases without cavity.[4]

In the ladder operator representation, the expression for σ^{tm} is given compactly with four tensor indices: $\sigma^{tm}_{\alpha\beta,ab}$, where $\alpha, \beta = E, L$ and $a, b = 1, 2$. The Greek indices indicate the four 2-by-2 blocks of the full 4-by-4 σ^{tm} matrix. They correspond to the different sectors of combinations of temporal modes. For example, σ^{tm}_{EE} refers to the top left block of the covariance matrix and corresponds to "intra"-temporal mode correlations of the early mode (it is the "early mode sector"), and σ^{tm}_{LE} is the bottom left block corresponding to "inter"-mode correlations between late and early modes (it is the "late–early sector"). The indices a, b determine the entry of each 2-by-2 sector and are directly related to the entries of the output field covariance matrix σ^{out} from Eqs. (9.9) and (9.12). For example, $\sigma^{tm}_{LL,22}$ is the entry $(4, 4)$ of σ^{tm} and $\sigma^{tm}_{EL,21}$ is the entry $(2, 3)$. We write Eq. (9.11) as

$$\sigma^{tm}_{\alpha\beta,ab} = \int d\omega \, F^{tm}_{\alpha,a}(-\omega)\sigma^{out}_{ab}(\omega,-\omega){F^{tm}_{\beta,b}}^{T}(\omega) \tag{9.14}$$

where

$$F^{tm}_{\mu,m}(\omega) \coloneqq \mathrm{diag}\big[f_\mu(\omega), f^*_\mu(-\omega)\big]_m = \begin{cases} f_\mu(\omega) & \text{if } m = 1 \\ f^*_\mu(-\omega) & \text{if } m = 2 \end{cases} \tag{9.15}$$

according to Eq. (9.3). This notation works with a single index $m = 1, 2$ because the matrices F_μ are diagonal in the ladder operator representation.

σ^{out} given by Eq. (9.12) is an exact closed-form expression for the state of the output light field. σ^{tm} given by Eq. (9.14) [or Eq. (9.11)] is an exact symbolic expression for the state of the temporal modes. It is not in closed form because the solution of the integral might not be;[5] this integration prevents further exact analytical calculations

3. Indeed, white-noise processes are necessarily unphysical models with infinite energy distributed as, equal, finite contributions at each frequency component.

4. This was derived by my colleague Klemens Winkler and the corresponding developments will be made available elsewhere.

5. We use a somewhat customised jargon here: a "closed-form" expression is composed of a finite number of symbols that can be evaluated to a numerical value

in general. In the next section, we discuss how the integration can be performed analytically and how the result bears a closed-form symbolic expression.

9.1.2 *Symbolic integration over frequencies*

The integrand $F^{tm}(-\omega)\sigma^{out}(\omega)F^{tm\,T}(\omega)$ of Eq. (9.11) is a 4-by-4 matrix where each entry is of the form

$$\int_{-\infty}^{\infty} d\omega \, \frac{g(\omega)}{h(\omega)} e^{-i\,\omega\,T_{sep}} \tag{9.16}$$

with g and h polynomials in ω of order N_g and N_h, respectively. Under certain conditions on the form and order of g and h, this integral has a closed-form analytical solution ([GZ15, entry 3.11.2, 8th edition] or [Hof15, app. B.5]). Details and usage are presented in App. D.1; see also our implementation in [Gut24, Theoretical predictions derivation .nb] [6]. Here, it is enough to say that it applies to all configurations treated in this thesis, whenever $T_{sep} = 0$. This is how we obtain the *exact symbolic expression* of σ^{tm} in the following. The resulting symbolic expression is too large and cumbersome to be interpreted, but it can be efficiently evaluated with numerical values of the system parameters. We make five comments on the usage and results of this exact integration formula.

First, the limitation $T_{sep} = 0$ implies that this method is useful (in the context of our protocol) only in the limit where the cavity decay κ^{-1} is the fastest time scale (cf. Sec. 7.2). Then, the detectable entanglement does not change appreciably for small but finite $T_{sep} \gtrsim \kappa^{-1}$ (or larger); we see in Sec. 9.4.3 that it is the case for the EPR-variance.

Second, the exact integration is a mathematical formula for the symbols forming the integrand. In this sense, the integration is agnostic of the value or meaning of the parameters and it applies whenever the mathematical constraints are met. It is thus on us to make sure that we use parameters consistent with the derivation that led to the integral (cf. Ch. 8): in particular, the dynamics must be stable, the linearised Hamiltonian must be accurate (strong drive such that $g_j \gg g_{0,j}$), the Markovian bath model must be accurate ($n_j \gg 1$), etc.

Third, in order to keep expressions concise in this document, we present only the case of resonant drive ($\Delta = 0$). Therefore, the expression of σ^{out}, derived in Sec. 9.1.1 in terms of S, C, R, I, and X [Eqs. (9.13)], is not valid when $\Delta \neq 0$. Nevertheless, it is possible to set $\Delta \neq 0$ in the system matrix M and obtain the corresponding σ^{out}

relatively easily – e.g. it contains no integrals, infinite sums, or operation that cannot be computed directly efficiently on a computer.

6. File path: see footnote 1.

Eq. (9.9). Integrating σ^{tm} Eq. (9.11) with the formula thus yields the exact symbolic expression for a detuned drive.

Fourth, other choices of mode functions would still comply with the formula, as long as their Fourier transforms are polynomials of order -1/2 at most; see App. D.

Lastly, the symbolic results from the formula are, in our experience, very large and cumbersome expressions; their size prevents extracting information or physical understanding from them directly. This is why we make approximations in the next section and derive a concise but approximate formula for the EPR-variance, testing entanglement in σ^{tm}. We use the exact integration to give quantitative estimations of the accuracy of the approximate results in Sec. 9.3.

The complex analysis residue integration method (see standard textbooks like [Mar19, Ch. 9]) offers another systematic way to perform the integrals in $\sigma^{\mathrm{tm}}_{\alpha\beta,ab}$ Eq. (9.14) analytically; details and comments on how we use it are given in App. D.2. For all the cases treated below (including finite $T_{\mathrm{sep}} > 0$), every integral $\sigma^{\mathrm{tm}}_{\alpha\beta,ab}$ Eq. (9.14) is

$$\sigma^{\mathrm{tm}}_{\alpha\beta,ab} = \int_{-\infty}^{\infty} \mathrm{d}\omega\, I_{\alpha\beta,ab} = 2\pi \mathrm{i} \sum_{p_+} \mathrm{Res}\left[I_{\alpha\beta,ab}, p_+\right] \tag{9.17}$$

where p_+ are the poles of the integrand I with positive imaginary parts (the integration contour is always a half-circle in the upper complex plane), they are all of order one, and their residue is $\mathrm{Res}\left[I_{\alpha\beta,ab}, p_+\right]$; cf. Eq. (D.6). These are closed-form symbolic expressions that are possibly very large and unusable for direct (physical) interpretation (just like with the integration formula we just discussed). Although we have not done so, we believe that it is possible to implement an algorithm that preforms the residue method for any of the integrands we treat in this work – and even for more general ones (e.g. for $T_{\mathrm{sep}} > 0$ or mode functions with non-polynomial numerators in frequency) thus being more versatile than the integration formula. This point will become clear in Sec. 9.2 (see also Sec. D.2 and Sec. E.2) where we integrate, by hand, approximate forms of σ^{tm} with the residue technique.

9.1.3 *Approximate symbolic expressions*

In order to obtain concise expressions that can be interpreted, we make some simplifying approximations in σ^{out} Eq. (9.9) before integration. For large mechanical quality factors $\omega_j \gg \gamma_j$, the poles of the mechanical susceptibilities χ_j Eq. (5.23d) are well approximated by

$$\omega_j^{\pm} = \frac{1}{2}\left(\pm\sqrt{4\omega_j^2 - \gamma_j^2} - \mathrm{i}\,\gamma_j\right) \approx \pm\omega_j - \mathrm{i}\,\gamma_j/2 \tag{9.18a}$$

for $j = 1, 2$. We thus approximate

$$\chi_j(\omega) \approx \frac{1}{\omega - \omega_j^-} - \frac{1}{\omega - \omega_j^+}. \tag{9.18b}$$

This approximation leaves out terms with scaling $\mathcal{O}\left(Q_{jj}^{-2}\right)$. We approximate $\left|\chi_j\right|^2$ as

$$\begin{aligned}
\left|\chi_j(\omega)\right|^2 &\approx \left|\frac{1}{\omega - \omega_j^-} - \frac{1}{\omega - \omega_j^+}\right|^2 \\
&\approx \left|\omega - \omega_j^-\right|^{-2} + \left|\omega - \omega_j^+\right|^{-2} && (9.19a) \\
&=: \left|\chi_j^-(\omega)\right|^2 + \left|\chi_j^+(\omega)\right|^2. && (9.19b)
\end{aligned}$$

The first approximation is that from Eqs. (9.18) and the second neglects cross terms that scale like $\mathcal{O}\left(Q_{jj}^{-2}\right)$ relative to the ones we keep, close to the resonances $\pm\omega_j$ of $\chi_j(\omega)$ where they are peaked. Mechanical oscillators with large Q_{jj} efficiently enhance terms at frequencies in a narrow band around the mechanical resonance, which is the physical origin of the approximations here.

The modulus of the optical susceptibility $\chi_{\text{opt}}(\omega)$ Eq. (5.23e) is largest at $\omega = 0$ where it is $1/\sqrt{\kappa}$. Close to $\pm\omega_j$, where the other terms in σ^{out} are enhanced by $|\chi_j(\omega)|^2$, the optical susceptibility is $\approx 1/\sqrt{\kappa}$ in the sideband unresolved regime $\kappa \gg \omega_j$ Eq. (8.4). At higher frequencies, it becomes smaller, and so do the mechanical susceptibilities. Therefore, it is in the region near $\pm\omega_j$ that the σ^{out} has its largest contributions as integrand in Eq. (9.11). We thus approximate the optical susceptibility with

$$\chi_{\text{opt}}(\omega) \approx \frac{1}{\sqrt{\kappa}}. \tag{9.20}$$

The functions S, C, R, I and X in σ^{out} Eqs. (9.13) are approximated as

$$\begin{aligned}
S(\omega) &= \frac{1}{2} && (9.21a) \\
C(\omega) &\approx \sum_j \Gamma_j^{\text{ro}} \Gamma_j^{\text{tot}} \left|\chi_j(\omega)\right|^2 && (9.21b) \\
R(\omega) &\approx i \sum_j \Gamma_j^{\text{ro}} \frac{(\omega_j^2 - \omega^2)}{2\,\omega_j} \left|\chi_j(\omega)\right|^2 && (9.21c) \\
I(\omega) &\approx \sum_j \Gamma_j^{\text{ro}} \frac{\gamma_j \omega}{2\,\omega_j} \left|\chi_j(\omega)\right|^2 && (9.21d) \\
X(\omega) &\approx \Gamma_1^{\text{ro}} \Gamma_2^{\text{ro}}\, \text{Re}[\chi_1(\omega)\chi_2^*(\omega)] \\
&= \frac{\Gamma_1^{\text{ro}} \Gamma_2^{\text{ro}}}{2\,\omega_1 \omega_2} [(\omega^2 - \omega_1^2)(\omega^2 - \omega_2^2) + \gamma_1 \gamma_2 \omega^2] && (9.21e) \\
&\qquad \times |\chi_1(\omega)|^2 |\chi_2(\omega)|^2.
\end{aligned}$$

where we use the rates from Eqs. (5.24) characterising the optomechanical dynamics: $\Gamma_1^{\mathrm{ro}} \coloneqq 4g^2/\kappa$, $\Gamma_1^{\mathrm{th}} \coloneqq \gamma_1 n_1$, and $\Gamma_1^{\mathrm{tot}} \coloneqq \Gamma^{\mathrm{ro}} + \Gamma^{\mathrm{th}}$.

In App. D, we show that the thus approximated integrals converge. Polynomials in the denominator of the integrands are always suitable for integration with the residue method discussed above. The poles of

$$\left|\chi_j^{\pm}\right|^2 = \frac{1}{(\omega - \omega_j^{\pm})(\omega - \omega_j^{\pm *})}$$

are $\{\omega_j^{\pm}, \omega_j^{\pm *}\}$, all of order one, appearing in all four quadrants of the complex plane. Note how we wrote the denominator as $(\omega - \omega_j^{\pm})(\omega - \omega_j^{\pm *})$ and not $|\omega - \omega_j^{\pm}|^2$; this is to avoid mistakes when promoting ω to the complexes when using the residue integration technique. In Eq. (9.11), the mode functions contribute two poles of order one; they are either in the same complex half-plane or one on each side. Due to the symmetry $\omega_E = -\omega_L$ [cf. Eqs. (8.10a)], when both poles are in the same complex half-plane, they form a pole of order two. Given a distribution of the poles in the complex plane, a clever choice of integration contour can reduce the number of poles to evaluate (and avoid the increased complexity of poles of order two). The choice of integration contour depends on the numerator of the integrand. In the cases encountered in this derivation, the best choice is always the contour along the real line with a closing half-circle in the upper complex plane, and no poles of order two need to be computed; see App. D.2 and [Gut24, Theoretical predictions derivation .nb][7] for details.

9.2 APPROXIMATE FORMULA FOR EPR-VARIANCE

In the previous section, we explained how to compute the exact and approximated symbolic expression for the state σ^{tm} of the temporal modes of measurable light. In principle, any entanglement test can be applied to σ^{tm}, in particular, entanglement measures that are most informative. Here we focus on the EPR-variance (Δ_{EPR}): a particular, sub-optimal, entanglement witness based on second moments introduced in Sec. 3.4.1. The goal is to obtain concise expressions that can be interpreted physically in order to understand how entanglement is being detected in this protocol. It is the mathematical simplicity of Δ_{EPR} (compared to the logarithmic negativity, for example) that dictates its choice here.

7. File path: see footnote 1.

The EPR-variance was defined in Eq. (3.13) in the quadrature representation; in the ladder operator representation we get

$$\begin{aligned}\Delta_{\mathrm{EPR}} &= 2\left\langle a_{\mathrm{E}} a_{\mathrm{E}}^{\dagger}\right\rangle_{\mathrm{sim}} + 2\left\langle a_{\mathrm{L}} a_{\mathrm{L}}^{\dagger}\right\rangle_{\mathrm{sim}} + 2\left\langle e^{i\Phi} a_{\mathrm{E}} a_{\mathrm{L}} + \mathrm{H.c.}\right\rangle_{\mathrm{sim}} \\ &= 2\left(\sigma^{\mathrm{tm}}_{\mathrm{EE},12} + \sigma^{\mathrm{tm}}_{\mathrm{LL},12} + e^{i\Phi}\sigma^{\mathrm{tm}}_{\mathrm{EL},11} + e^{-i\Phi}\sigma^{\mathrm{tm}}_{\mathrm{EL},22}\right) \end{aligned} \tag{9.22}$$

where we used the tensor notation of Eq. (9.14). It is thus the sum of four entries of σ^{tm} – this is what we call "mathematical simplicity".

In Appendix E.1, we demonstrate the following symmetries that reduce the number of necessary integrations. One finds that that $\sigma^{\mathrm{tm}}_{\mathrm{EL},11}$ is the complex conjugate of $\sigma^{\mathrm{tm}}_{\mathrm{EL},22}$ so that

$$\begin{aligned}e^{i\Phi}\sigma^{\mathrm{tm}}_{\mathrm{EL},11} + e^{-i\Phi}\sigma^{\mathrm{tm}}_{\mathrm{EL},22} = 2\,\mathrm{Re}\Bigg[e^{i\Phi}\int \mathrm{d}\omega\, \mathsf{f}_{\mathrm{E}}^2(-\omega)\,[-\mathsf{C}(\omega) \\ +\mathsf{R}(\omega) - \mathsf{X}(\omega)]\Bigg]. \end{aligned} \tag{9.23}$$

Also, the sum

$$\sigma^{\mathrm{tm}}_{\mathrm{EE},12} + \sigma^{\mathrm{tm}}_{\mathrm{LL},12} = 1 + 2\int \mathrm{d}\omega\, \mathsf{f}_{\mathrm{E}}(-\omega)\mathsf{f}_{\mathrm{E}}^{*}(-\omega)(\mathsf{C}(\omega) + \mathsf{X}(\omega)) \tag{9.24}$$

because the I terms [cf. Eq. (9.12)] cancel out.

The factor 1 in Eq. (9.24) arises from the integration over the constant $S = 1/2$ (we had called this contribution shotnoise). In the absence of mode functions, the integral over this term in Eq. (9.11) would diverge as a consequence of the white-noise model (with infinite energy).

Only five integrals (three in the single mechanical mode case) must be computed to obtain Δ_{EPR}. We introduce the following notation: the integrands are sans-serif uppercase l's; the integrals are uppercase I's; we supplement them with the tensorial notation of Eq. (9.14) $\square_{\alpha\beta,ab}$, with $\alpha, \beta = \mathrm{E}, \mathrm{L}$ and $a, b = 1, 2$; and a superscript $A = S, C, R, I, X$ that indicates the function involved, either from the exact Eqs. (9.13) or from the approximated Eqs. (9.21)1. This notation is best understood with an example: from Eq. (9.24) we need to compute

$$\begin{aligned}\int_{-\infty}^{\infty} \mathrm{d}\omega\, \mathsf{f}_{\mathrm{E}}(-\omega)\mathsf{f}_{\mathrm{E}}^{*}(-\omega)\mathsf{C}(\omega) =: \mathrm{I}^{\mathrm{C}}_{\mathrm{EE},12} \\ = \int_{-\infty}^{\infty} \mathrm{d}\omega\, \mathsf{I}^{\mathrm{C}}_{\mathrm{EE},1,2}(\omega). \end{aligned} \tag{9.25}$$

The EPR-variance takes the form

$$\begin{aligned}\Delta_{\mathrm{EPR}} = 2 + 4\,\mathrm{I}^{\mathrm{C}}_{\mathrm{EE},12} + 4\,\mathrm{I}^{\mathrm{X}}_{\mathrm{EE},12} \\ + 4\,\mathrm{Re}\left[e^{i\Phi}\left(-\mathrm{I}^{\mathrm{C}}_{\mathrm{EL},11} + \mathrm{I}^{\mathrm{R}}_{\mathrm{EL},11} - \mathrm{I}^{\mathrm{X}}_{\mathrm{EL},11}\right)\right]. \end{aligned} \tag{9.26a}$$

When only one mechanical mode is modelled, it is

$$\Delta_{\mathrm{EPR}} = 2 + 4\,\mathrm{I}^{\mathrm{C}}_{\mathrm{EE},12} + 4\,\mathrm{Re}\left[e^{i\Phi}\left(-\mathrm{I}^{\mathrm{C}}_{\mathrm{EL},11} + \mathrm{I}^{\mathrm{R}}_{\mathrm{EL},11}\right)\right]. \tag{9.26b}$$

These expressions are exact if one uses the exact expressions of C, R, I, and X from Eqs. (9.13). Explicit closed-form expressions can be obtained with the integration techniques of Sec. 9.1.2 above.

We proceed with the simpler approximate forms of C, R, I, and X Eqs. (9.21) and compute only those entries entering the expression of Δ_{EPR} in Eq. (9.26). We thus derive an approximate concise expression of the EPR-variance.

In Section E.2, we explain how we performed (by hand) the integration of the five terms in Eq. (9.26) with the method of residues; see also [Gut24, Theoretical predictions derivation .nb][8]. The result of the integration of the approximate terms is still too cumbersome for interpretation. We thus approximate them further with the following procedure (performed and documented in [Gut24, Theoretical predictions derivation .nb][9]). For each integral in Eq. (9.26):

- sum the residues of the different poles and put them in the simplest form without approximation (e.g. using Mathematica's function `FullSimplfy`)[10];
- neglect γ_j against ω_k, $j,k=1,2$ under the assumption that $Q_{kj} \gg 1$ [cf. Eq. (5.16)] and neglect the mismatch between filter demodulation and target mechanical frequency d against unity [cf. Eq. (8.8)];
- finally, take the real part of the expressions, whenever explicitly required in Eq. (9.26).

The contributions from cross-term X can be neglected in the high-Q limit Eq. (5.16) and assuming that the spectator mode is well outside the filtering bandwidth $\Delta\omega \gg \Gamma$ [cf. Eq. (5.11)]; see Sec. E.6 for the detailed justification.

We find the following expression for the EPR-variance

$$\Delta_{\mathrm{EPR}} \approx 2 + G\,[E + \mathcal{N}_0 + \mathcal{N}_1 + \mathcal{N}_2] \tag{9.27}$$

where the complexity is hidden in the notation. We define and explain each term step by step in the next paragraphs.

We define

$$G \coloneqq 4\frac{4\Gamma_1^{\mathrm{ro}}\Gamma_1^{\mathrm{tot}}}{(2\Gamma+\gamma_1)^2} \tag{9.28}$$

which is a positive quantity. The EPR-variance detects entanglement when $\Delta_{\mathrm{EPR}} < 2$, which only happens when the term in the square bracket is negative. In this sense, G scales the amplitude of the separability violation. We will argue below that the only term that contributes significantly to entanglement detection is E, while the $\mathcal{N}$-terms are typically detrimental.

8. File path: see footnote 1.
9. File path: see footnote 1.
10. Simplifying the sum of residues of a single integral has the virtue of keeping terms real before further approximations.

In the limit of no interactions when $g_j = 0$, then $\Gamma_j^{ro} = 0$ and $\Delta_{EPR} = 2$.[11] We can trace back the factor of 2 [1st term in Eq. (9.27)] to the shotnoise contribution in the output field, i.e. the term related to $\mathcal{S}$ in Eqs. (5.23), and to S in Eq. (9.12). It is the noise of the cavity environment – the inherent (quantum) fluctuations in the detection channel. From the quantum measurement perspective, this is the fundamental quantum sensing-noise of the probe itself.

We rescale the temporal filter bandwidth Γ by the mechanical frequency of the target mode

$$\nu \coloneqq \frac{\Gamma}{\omega_1}. \tag{9.29}$$

On the one hand, we expect that the temporal modes must be shorter than the mechanical loss of coherence due to the influence of the thermal bath: here, the thermal noise rate is $\Gamma^{th} = \gamma_1 n_1 \gg \gamma_1$ in the high bath temperature limit Eq. (8.2). Hence, it is physically meaningful to restrict the analysis to bandwidths significantly larger than the mechanical decay rate $\Gamma \gg \gamma_1$. On the other hand, based on our physical (but somewhat heuristic) understanding of the role of the temporal modes as "filters extracting the relevant information from the output field", we expect that the amplitude of temporal modes should not decay faster than a mechanical oscillation. If $\Gamma > \omega_1$, the demodulation is effectively suppressed and it is not clear how (and what) information is retrieved from a partial oscillation; see depiction of the mode functions in Fig. 8.1. Hence, it is also physically sensible to restrict ourselves to $\Gamma < \omega_1$. In terms of the newly defined ν, these limitations mean that

$$1 > \nu \gg \frac{1}{Q_{11}}. \tag{9.30}$$

We go further and assume $\Gamma^2 \ll \omega_1^2$, so that the mode functions demodulate several mechanical oscillations.[12] This implies $\nu^2 \ll 1$. The reason for pushing the left bound of Eq. (9.30) to that limit is because it allows to obtain the clearest mathematical and physical expressions for Δ_{EPR} below. Relaxing these limitations on Γ makes the study of Eq. (9.27) (and in fact all other expressions derived below) harder and less insightful.

11. We will see below that if $g_1 = 0$ and $g_2 \neq 0$, then Γ_1^{ro} in G cancels with $1/\Gamma_1^{ro}$ from $\mathcal{N}_2$ and there is a finite contribution from the latter (associated to the spectator mode).

12. This is a technicality and it is the ordering of the squares that is formally needed for the approximations we make below; which is less demanding than assuming $\Gamma \ll \omega_1$.

We define the following functions:

$$E \coloneqq A - \frac{\Gamma}{\Gamma_1^{\mathrm{tot}}} N_0 \tag{9.31}$$

$$A \coloneqq \frac{4 + 2\nu^2}{4 + 4\frac{d^2}{\nu^2} + \nu^2} \tag{9.32}$$

$$N_0 \coloneqq \left[\frac{\nu^2 - d^2}{\nu^2 + d^2} \cos(\phi) - \frac{2d\nu}{\nu^2 + d^2} \sin(\phi) \right] e^{-\gamma_1 T_{\mathrm{sep}}/2}. \tag{9.33}$$

Recall that d and $\delta\omega$, defined in Eq. (8.8), quantify imperfect tuning of f_E and f_L. We assumed that each sideband is still inside the Lorentzian mode filter, which means $d < \nu$. For real numbers a, b, we have [13] $a^2 + b^2 > 2ab$, and $(a^2 - b^2)\cos(x) \pm 2ab \sin(x) \leqslant a^2 + b^2$. Also, if $\nu^2 > 2d > 0$, then we have the following important restrictions [14]

$$1 < A < 2 \tag{9.34a}$$

$$|N_0| \leqslant 1. \tag{9.34b}$$

Taking for granted (for now) that E is the only term that can become significantly negative, these restrictions lead to the important necessary condition to detect entanglement

$$\Gamma > \Gamma_1^{\mathrm{tot}} \Longleftarrow \text{ ent.} \tag{9.35}$$

It will come up repeatedly in the following. In the high bath occupation limit Eq. (5.17), we have $\Gamma_j^{\mathrm{tot}} \gg \gamma_k$, for $j, k = 1, 2$, so that $\Gamma \gg \gamma_k$ is necessary for entanglement – compatible with Eq. (9.30). In terms of the factor G Eq. (9.28), this implies that $G < 4(1 - \Gamma_1^{\mathrm{th}}/\Gamma_1^{\mathrm{tot}}) = 4\,[1 - 1/(C_1 + 1)]$.

Related to A and N_0 we define

$$\mathcal{N}_0 \coloneqq \frac{2\Gamma}{\gamma_1}(A - N_0). \tag{9.36}$$

Because of the limits in Eqs. (9.34), this term can never be negative [15] so that it is always detrimental to the detection of entanglement in Eq. (9.27). Moreover, we just saw that Eq. (9.35) implies $\Gamma/\gamma_1 \gg 1$; in the following, this will be the reason to choose the free parameters that minimise $A - N_0$ in priority, i.e. before optimising any other term.

13. We used Mathematica to check and do not have a proof ourselves...

14. This is again a technicality. It is compatible but more restrictive than $\nu > d$ above. Allowing $d \to \nu$ (from below) can make $A < 1$ which makes the argumentation later more complex.

15. If we had used $\nu > d$ instead of $\nu^2 > 2d$ above, then A can become less than 1 and $\mathcal{N}_0$ is not detrimental. We did not study that regime.

We defined

$$\mathcal{N}_1 \coloneqq \frac{\Gamma^3}{2\gamma_1\omega_1^2}\left(1+\frac{\gamma_1}{2\Gamma_1^{\mathrm{tot}}}\right)N_1 \tag{9.37}$$

$$N_1 \coloneqq \left[\frac{4-\nu^2}{4+\nu^2}\cos\left(\phi+2T_{\mathrm{sep}}\omega_1\right) + \frac{4\nu}{4+\nu^2}\sin\left(\phi+2T_{\mathrm{sep}}\omega_1\right)\right] e^{-\gamma_1 T_{\mathrm{sep}}/2} \tag{9.38}$$

and just like N_0, we have $|N_1|<1$. N_1 can become negative so that $\mathcal{N}_1$ can contribute positively to the detection of entanglement. We could not prove that it can make Eq. (9.27) less than 2 without negative E, nor could we exclude it in general. Its prefactor $\propto \nu^2\Gamma/\gamma_1$ is less than that of $\mathcal{N}_0$ by a factor $\nu^2 \ll 1$, so its contribution is typically much less; therefore, we prioritise the optimisation of N_0 over that of N_1 in the following.

Finally, we defined

$$\mathcal{N}_2 \coloneqq \frac{\Gamma^3}{2\gamma_1\omega_1^2}\frac{4\omega_1^2}{\Gamma^2+\Delta\omega^2}W^2\left[1+\frac{\gamma_2}{2\Gamma}+\left(1+\frac{\gamma_2}{2\Gamma_2^{\mathrm{tot}}}\right)N_2\right] \tag{9.39}$$

$$N_2 \coloneqq \left[\frac{D^2-\nu^2}{D^2+\nu^2}\cos\left(\phi-T_{\mathrm{sep}}\Delta\omega\right) - \frac{2D\nu}{D^2+\nu^2}\sin\left(\phi-T_{\mathrm{sep}}\Delta\omega\right)\right] e^{-i\,T_{\mathrm{sep}}\gamma_2/2} \tag{9.40}$$

$$W^2 \coloneqq \frac{g_2^2}{g_1^2}\frac{n_2}{n_1}\frac{C_2+1}{C_1+1} = \frac{\gamma_1}{\gamma_2}\frac{\Gamma_2^{\mathrm{ro}}}{\Gamma_1^{\mathrm{ro}}}\frac{\Gamma_2^{\mathrm{tot}}}{\Gamma_1^{\mathrm{tot}}}. \tag{9.41}$$

This contribution is due to the spectator mode – indeed, if $g_2 = 0$ it vanishes.[16] D and $\Delta\omega$ defined the frequency of the spectator mechanical mode relative to the target mode Eq. (5.11). The integrals that deliver these terms are the same as those providing the contribution due to imperfect tuning of the filters – with D playing the role of d and $\Delta\omega$ the role of $\delta\omega$. However, in the approximate expression of Eq. (9.27) they contribute differently: we assumed $\delta\omega < \Gamma$ with $|d| \ll 1$ and $\Delta\omega > \Gamma$ with $|D| < 1$ so that we cannot neglect D against unity, contrary to d. This translates the idea that the imperfect filtering still performs approximately as expected and the sidebands fall *within* the filter bandwidths. On the other hand, we expect that additional mechanical modes are detrimental, and one chooses mechanical systems where the second mode is well *outside* the filters so as to minimise their effect. Like N_0 and N_1 we have $|N_2|<1$. We used the cooperativities of both modes $C_j = \Gamma_j^{\mathrm{ro}}/\Gamma_j^{\mathrm{th}}$ Eq. (5.24c) in the dimensionless term W. In the regime we have in mind, where the occupations of the mechanical baths are similar $n_1 \approx n_2$ [cf. Eq. (5.17)] and where $g_1 > g_2$, then $W < 1$. In the limit where the second mechanical mode interacts very

16. The limit $g_1 \to 0$ is well defined because W comes as a product with G Eq. (9.28) that has a g_1^2 in Γ_1^{ro} at the numerator.

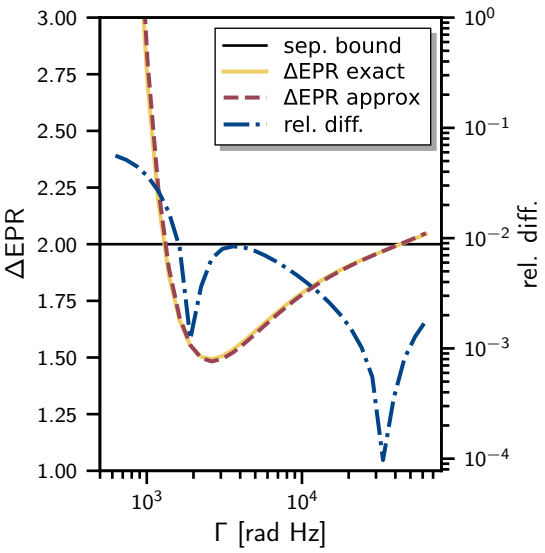

Fig. 9.1 For a single mechanical mode, the exactly integrated Δ_{EPR} is the continuous yellow line; the dashed red curve is Δ_{EPR} from the approximated formula Eq. (9.27). The parameters are those of Tab. 9.1. The dot-dashed blue curve provides the relative accuracy of both (right ordinate). The abscissa is the temporal mode filter bandwidth Γ.

little with the light compared to the target mode $g_1^2 \gg g_2^2$, then $W \ll 1$ and the contribution from $\mathcal{N}_2$ is reduced accordingly. In the regime $\Gamma > \Gamma_1^{tot}$ – expected for entanglement Eq. (9.35) – and $\Gamma_1^{tot} > \Gamma_2^{tot}$ (when $g_1 > g_2$), then $\mathcal{N}_2$ can become negative when $\mathcal{N}_2$ approaches -1: in that limit we get $\mathcal{N}_2 = \frac{\gamma_2}{2\Gamma}\left(1 - \frac{\Gamma}{\Gamma_2^{tot}}\right)$, a form similar to E above. As for $\mathcal{N}_1$, we could not prove that this term can yield entanglement detection without $E < 0$, nor could we exclude it.

9.3 ACCURACY OF APPROXIMATE FORMULA

The approximate formula of Eq. (9.27) above is the starting point for the coming analytical analysis of how our scheme detects entanglement. We assess its accuracy compared to the exact result based on the state σ^{tm} integrated exactly as described in Sec. 9.1.2. The set of parameters for the comparison presented here are given in Tab. 9.1. They are realistic and not particularly optimistic.[17] They are the basis for all numerical studies in this Chapter 9: in the following we make relatively small changes of certain parameters to explore and illustrate interesting features.

Figure 9.1 shows the approximate formula from Eq. (9.27) (dashed red) for a single mechanical mode (i.e. with $g_2 = 0$) against the exact Δ_{EPR} (continuous yellow). The blue dash-dotted line gives the relative accuracy of the approximated formula (right ordinate). The worst agreement with 6 percent error is far from the entangled regime; in

17. In terms of experimental resource, sub-kelvin temperature probably makes the scenario more demanding because it is lower than liquid helium requiring more sophisticated cryogenic techniques.

Physical property	**Symbol**	**Value**	**Units**
mech. frequencies	ω_1	$10^6 \times 2\pi$	[rad Hz]
	ω_2	$(1 + 0.05)\,\omega_1$	[rad Hz]
drive detuning	Δ	0	[rad Hz]
cavity linewidth (FWHM)	κ	$10\,\omega_1$	[rad Hz]
optomech. couplings	g_1	$16.5 \times 10^3 \times 2\pi$	[rad Hz]
	g_2	$g_1/5$	[rad Hz]
mech. linewidths (FWHM)	γ_1	$0.01 \times 2\pi$	[rad Hz]
	γ_2	$\approx 10\,\gamma_1$	[rad Hz]
mech. quality factors	Q_1	10^8	[]
	Q_2	$Q_1/10$	[]
mech. baths temp.	T_1	0.5	[K]
	T_2	T_1	[K]
baths' occupation numbers	n_1	10^4	[]
	n_2	$\approx n_1$	[]

Table 9.1 Parameters inspired by experiments where the mechanical oscillators is a drum mode of a thin membrane, as described in Sec. 10.1 and App. G.1, see also [Che+20; Ros+19; Tsa+17; MN17]. The cooperativity of the target mode is slightly above 1 $C_1 \approx 1$, and that of the spectator is much less than 1 $C_2 \approx 4 \times 10^{-3}$. These parameters for the target modes were used in or publication [Gut+20].

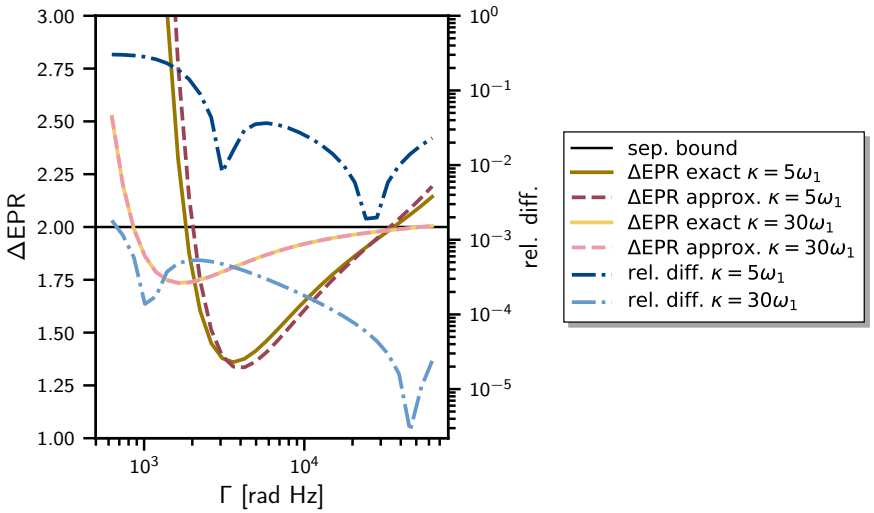

Figure 9.2 Approximate vs exact Δ_{EPR} for different cavity linewidth κ leading to different accuracy: light colours are for the accurate largely unresolved sidebands and dark colours are for the less accurate one. Yellow continuous lines are the exact calculations and dashed red are the approximated results. The relative differences are the blue dash-dotted lines referring to the left ordinate axis. x-axis is the filter function's bandwidth.

the entangled regime, the agreement is better than a percent. This is evidence that the approximation is correct.

As far as we call tell, it is the approximation that relies on the unresolved sideband regime Eq. (8.4) that is the most inaccurate in this parameter regime. In Figure 9.2 we show how the accuracy changes depending on the sideband resolution. In light colours, κ is three times larger than in Tab. 9.1 and the curves overlap very well with a relative difference below a percent. In dark colours, κ half its value from Tab. 9.1 and the discrepancy between exact and approximate curves is visible.

Figure 9.3 shows the results accounting for a spectator mode (i.e. with g_2 as in Tab. 9.1). The agreement between exact and approximate EPR-variance is better than a few percent. This is evidence that our calculations are correct also in this more involved case.

We systematically varied all parameters from 0.1 to 10 times their values in Tab. 9.1 (picking 20 different values in that interval). Only ω_1 was kept the same, while the bandwidth Γ was swept from 1 to 10^6 rad Hz (60 values). We find that the relative difference between the exact and the approximate EPR-variance, where it detects entanglement, is between $+6\%$ and -33%. This means that, tendentiously, the approximated formula Eq. (9.27) underestimates the correct value of Δ_{EPR} – this is a possible non-conservative bias to be aware of. We also compared the predictions on the largest separability violation (i.e. we find the minimal Δ_{EPR} with respect to the temporal mode bandwidth

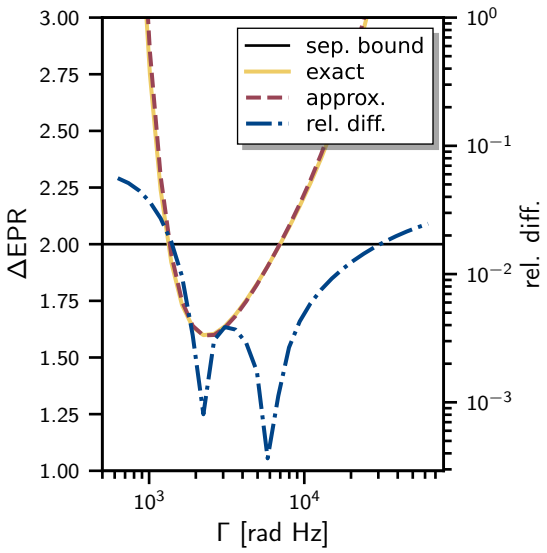

Fig. 9.3 Approximate (dashed red) vs exact (continuous yellow) Δ_{EPR} including a spectator mode 5% away from the target mode; cf. Tab. 9.1. Blue dot-dashed curve gives the relative accuracy (right ordinate).

Γ for each configuration) and found that the relative error is between 3% and -21%. These results were computed with Python and are available in the Zenodo repository [Gut24]. [18]

The spectator mode scenario is numerically more demanding, so we performed the same broad parameter sweep but with only 5 different points per parameter range (except Γ). We found that, in the region where entanglement is detected, the approximate formula deviates by 5% up to -41% from the exact results; in terms of largest separability violation, the accuracy is between 3 and -41%.

9.4 LIMIT SCENARIOS

An explicit and relatively concise formula describing the functional role of the parameters in detecting entanglement is a powerful opportunity to understand and optimise the protocol efficiently. Although Equation (9.27) is much more concise than the exact symbolic expression, [19] it remains quite bulky and hard to interpret at once. Our strategy for understanding the various parts is to look at relevant

18. The evaluation of the symbolic formula with numerical parameters is efficient and our barely optimised code produced the evaluation of the exact EPR-variance for this large sweep in less than 5 minutes on my personal computer.

19. Seen as a string – where the variables are `omega1`, `gamma2`, etc. – the exact symbolic expression of σ^{tm} has a little more than 132 million characters. Tolkien's trilogy *The Lord of the Rings* has approximately 480×10^3 words according to this website. Assuming an average of five characters per word [BSS15] and adding one more character for the white spaces, the three books contain a little less than 3 millions symbols, which is 44 times less than our exact expression. It is probably more appropriate to compare this opaque formula to some comparably opaque texts: I found that the Swiss penal code [RS 311.0 le code pénal (CP)] has a little less than half a million characters, that is less than half a percent of the exact expression of the covariance matrix. Meta/Facebook's privacy policy has about 170×10^3 characters

limits. The free parameters that are not set by the experimental setup are d (or $\bar{\omega}$), ν (or Γ), ϕ, and T_{sep}. We saw that the first two are small – or we expect them to be small – while the last two are more or less free – but we also expect them to be small relative to their typical scale. In a first analysis, we restrict ourselves to the case of a single mechanical mode to better isolate the role of the spectator mode: that is, we set g_2 to zero so that $\mathcal{N}_2 = 0$ in Eq. (9.27). The global strategy is to start with tuned filters $\delta\omega = 0$ and look first at the limit $\nu \to 0$. Then, we study the regime $1 \gg \nu^2 > 0$. Subsequently, we optimise ϕ and T_{sep}. We will establish that, in the limit of finite $T_{sep} \gtrsim 1/\kappa > 0$, entanglement can still be retrieved, which is crucial for the consistency and soundness of our argument; see discussion in Sec. 7.2 about the strict pairwise interaction requirement of the entanglement verification theorem and the delay induced by the cavity. Then we allow for imperfect tuning of the mode function $\delta\omega \neq 0$, which is important in practice, as the mechanical frequency is not known perfectly and is subject to possible drifts during a measurement run. Lastly, we explore the spectator mode scenario with finite g_2.

9.4.1 *Limit of narrow filter bandwidths:* $\Gamma^2/\omega_1^2 \to 0$

In the limit where ν^2 is so small that it can entirely be neglected, we get

$$\Delta_{EPR} \approx 2 + G\left[\left(1 - \frac{\Gamma}{\Gamma_1^{tot}} N_0\right) + \frac{2\Gamma}{\gamma_1}(1 - N_0)\right] \tag{9.42}$$

with

$$N_0(d = 0) = \cos(\phi)\, e^{-\gamma_1 T_{sep}/2}. \tag{9.43}$$

It is the expression that we had derived in our published work presenting the protocol [Gut+20]. This expression is minimised when $N_0 = 1$, which happens when $T_{sep} = \phi = 0$.

The filter bandwidth that minimises Eq. (9.42) is

$$\Gamma_{opt} = 2\,\Gamma_1^{tot} + \gamma_1/2 \approx 2\,\Gamma_1^{tot} \tag{9.44}$$

where the approximation holds when $n_1 \gg 1$. Γ is the (inverse) duration of each temporal mode and the relevant temporal scale is the duration of both pulses $2/\Gamma_{opt}$, hence the factor of 2 in Eq. (9.44). Γ_1^{tot} is the sum of the coherent "readout" rate Γ_1^{ro} – which relates to the rate at which entangled light exits the cavity – and the (thermal) noise rate Γ_1^{th} that sets the time scale at which coherence of mechanical motion is lost. This expression states that one should verify the presence of entanglement:

[estimate obtained from the printable version of the privacy policy at that url on 2024-05-01], which is one per mil.

- *faster than the decoherence rate*

and

- *as fast as the readout rate allows.*

The former sets the minimal necessary requirement to observe entanglement: $\Gamma > \Gamma^{\text{th}}$. And the latter is an optimisation measure that minimises the probability of decoherence. The existence of an optimum implies that being "too fast" becomes detrimental. Intuitively, if the pulses are faster than the dynamics generating entanglement, then less entanglement can be retrieved. In the limit of very short temporal modes, Γ becomes large and ν^2 cannot be neglected, so that Eqs. (9.42) and (9.44) become inaccurate.

We replace the optimal bandwidth in Eq. (9.42), and obtain the optimal violation of the EPR-variance (in the limit $\phi = T_{\text{sep}} = 0$ and when ν^2 can be neglected)

$$\Delta_{\text{EPR}}^{\text{opt}} = 2\frac{(2\Gamma_1^{\text{tot}} - \Gamma_1^{\text{ro}} + \gamma_1)}{2\Gamma_1^{\text{tot}} + \gamma_1} \approx 1 + \frac{1}{C_1 + 1} \tag{9.45}$$

where we ignored terms of order 1 against n_1, and $C_1 = \Gamma_1^{\text{ro}}/\Gamma_1^{\text{th}}$ is the cooperativity Eq. (5.24c). The limits $C_1 \to 0$ and $C_1 \to \infty$ in Eq. (9.45) are remarkable and we study them in Fig. 9.4. For any (however small) finite cooperativity $C_1 > 0$, this formula predicts $\Delta_{\text{EPR}}^{\text{opt}} < 2$, so that the scheme seemingly *always* detects entanglement – for any parameters compatible with the limits we consider here. To interpret this point correctly, it is important to remind ourselves that $\Gamma_1^{\text{tot}} < \Gamma$ must necessarily hold for entanglement and that $\Gamma^2 \ll \omega_1^2$ must hold as well so that ν^2 can be neglected: these two conditions are in opposition limiting rather strictly their span of common validity (we will see the details of this process with the sufficient condition for entanglement Eqs. (9.46) later on).

In the left panel of Fig. 9.4 we show how the particularly concise expression of Eq. (9.45) (continuous red line) compares to the exact results (yellow circles): the parameters are those of Tab. 9.1 where $C_1 \approx 1$, then we vary g_1 to sweep various cooperativity regimes. We see good agreement for moderate cooperativities – in particular, it confirms the unexpected feature of detectable entanglement at low cooperativity. As g_1 increases, Γ_1^{tot} increases and so does the temporal mode bandwidth (in order to maintain the necessary condition $\Gamma_1^{\text{tot}} < \Gamma$) up to the point where neglecting ν^2 becomes inaccurate: this is when the circles depart from the continuous line. The exact Δ_{EPR} values eventually become larger than 2 for $C_1 > 10$ and the scheme does not detect entanglement in this regime. It is well understood in terms of the sufficient condition Eqs. (9.46) presented below. It remains astonishing that larger cooperativity leads to undetected entanglement. Given exact covariance matrices σ^{tm}, we compute their optimal witness introduced in Sec. 3.4.2: they are the blue dots in the figure. The separability bound of the optimal witness is rescaled to 2 so

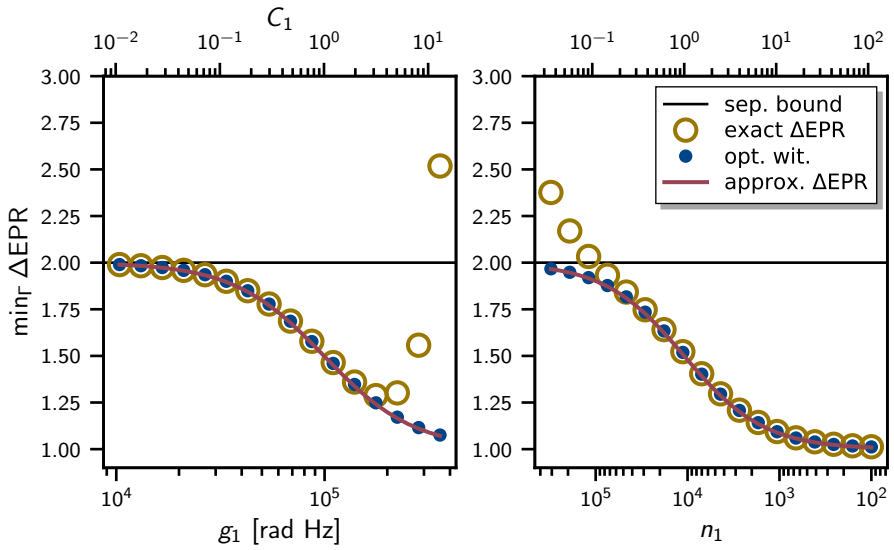

Figure 9.4 (left) Minimal value of Δ_{EPR} over the filter bandwidth Γ as a function of cooperativity via coupling to the target mode g_1. Solid red line is the approximated $\Delta^{\text{opt}}_{\text{EPR}}$ Eq. (9.45), yellow circles are the result from the exact integration, and the blue dots are the optimal witness values for the exactly integrated σ^{tm} (with same separability bound as Δ_{EPR}). (right) Same but with the cooperativity changed via the mechanical bath occupation n_1 (that increases to the left). These plots are adapted reproductions of those in [Gut+20].

that it can be plotted on the same y axis as Δ_{EPR}. The optimal witness is a necessary and sufficient test and shows a monotonically increasing separability violation with increasing C_1, as intuition dictates. This means that it is the choice of the EPR-variance as entanglement test that prevents the detection of entanglement at large values of g_1. Interestingly, the approximate formula for the optimal Δ_{EPR} (red line) and the optimal witness agree well with each other: we have no explanation for this fact and experience showed that it is the case as well in other parameter regimes.

From the base parameters of Tab. 9.1, one can reach the high cooperativity limit, while satisfying $\Gamma_1^{\text{tot}} < \Gamma$ and $\Gamma^2 \ll \omega_1^2$, by decreasing n_1 but remaining in the regime $n_1 \gg 1$. In Figure 9.4 (right panel), g_1 is that of Tab. 9.1 so that $C_1 \approx 1$ for $n_1 = 10^4$. In the large cooperativity regime, the concise formula of Eq. (9.45) (red line) agrees well with the exact Δ_{EPR} (yellow circles): there, Γ_{opt} decreases with n_1 so that ν^2 becomes smaller and smaller. When n_1 increases, the circles first depart from the solid line when ν^2 cannot be neglected anymore, and then they stop revealing entanglement when the sufficient condition Eqs. (9.46) (below) stops being satisfied, just as in the left panel. The optimal witnesses computed from the exact states again match well the formula Eq. (9.45): in particular, it saturates at 1, which is half of the (mathematically) possible separability violation. This limitation is unexpected, and because it seems to be a limit for the optimised

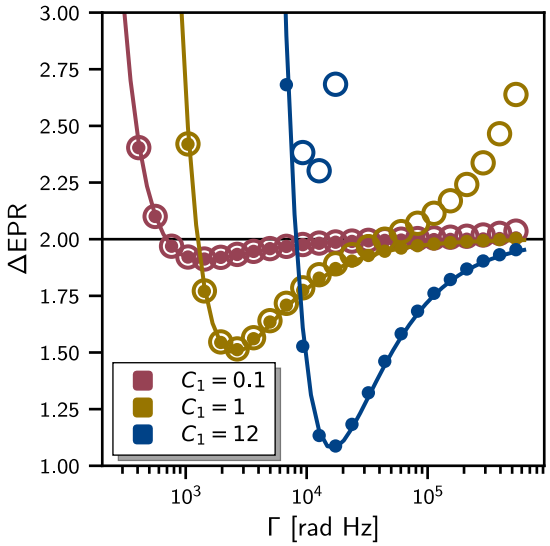

Fig. 9.5 EPR-variance against Γ for different cooperativities: $C_1 = 0.1$ (red), 1 (yellow), and 12 (blue). The solid lines are from the approximate formula Eq. (9.42), the circles are from the exact calculation, and the dots are the optimal witness values computed from the exact σ^{tm} (with the same separability bound as Δ_{EPR}). This is an adapted reproduction from [Gut+20].

witness as well, it is not due to the choice of entanglement test.[20] Hence, it seems that "half the available entanglement" (in the large cooperativity limit) is not encoded in the temporal modes we look at. We do not have an explanation for this fact. In Ref. [MDC10], where they study optomechanical entanglement between the oscillator and an optimised temporal mode of the light (which is the same as our early mode), they find no limit on the amount of entanglement; i.e. their expression for the logarithmic negativity is not bounded. This prompts us to think that it is the late mode that does not retrieve all the correlations (after all, the beam splitter interaction might not swap the whole mechanical state exactly). It would be interesting to investigate if another late filtering mode can do better.

The behaviour of Eq. (9.42) for different cooperativities is shown in Fig. 9.5; the parameters are those of Tab. 9.1, where g_1 is chosen to set the cooperativities indicated in the legend. We see in more detail how well (or not) the rough approximations leading to Eq. (9.42) (solid lines) compare to the exact Δ_{EPR} (circles). The discrepancies occur consistently with the understanding developed in the previous paragraphs. Here again, the approximated formula and the optimal witness overlap quite well.

9.4.2 *Limit of finite filter bandwidth:* $\Gamma^2/\omega_1^2 > 0$

In the limit of ν small but finite $1 \gg \nu^2 > 0$ Eq. (9.30), it is still best to set $N_0 = 1$ with $\phi = 0$ and $T_{sep} \to 0$. Details are presented in App. E.3 and in [Gut24, Theoretical predictions derivation .nb][21].

20. The logarithmic negativity that measures entanglement also saturates to a finite value in this limit.

21. File path: see footnote 1.

We find the following necessary and sufficient condition for detecting entanglement (with the EPR-variance, in the presence of a single mechanical mode)

$$\Gamma_1^{\mathrm{tot}} < \Gamma < \frac{2}{3}\frac{\omega_1}{\sqrt[3]{2\,Q_{11}}}. \tag{9.46a}$$

The first inequality corresponds to the necessary condition Eq. (9.35) and we refer to the second inequality as the sufficient condition. In the limit of large mechanical quality factors the sufficient condition is compatible with $\nu^2 \ll 1$, which we used to derive this result. Remarkably, it relates Γ_1^{tot} to the mechanical frequency in a way that forms a stringent constraint on the bath temperature [22]

$$n_1^3(C_1+1)^3 < (3\,n_1(C_1+1))^3 < (2\,Q_{11})^2. \tag{9.46b}$$

We also give the explicit dependence of the different parameters independently

$$\frac{4g_1^2}{\kappa\sqrt[3]{\gamma_1}} + n_1\gamma_1^{2/3} < \frac{(2\omega_1)^{2/3}}{3}. \tag{9.46c}$$

This sufficient condition for entanglement is essentially the same as Eq. (25) in our published work [Gut+20]. This regime is rather unexpected: given a high mechanical bath occupation and a large quality factor, the cooperativity C_1 should not be too large in order to detect entanglement. Importantly, Eqs. (9.46) is not a statement about the amplitude of the violation of the separability bound, hence we expect that small cooperativity will lead to rather small violations of the bound reflecting weak correlations; as illustrated in Fig. 9.4 and Eq. (9.45). Small violations in turn make an experimental realisation more challenging because it leaves less room for uncertainties and error bars.

We test this sufficient condition for entanglement in Fig. 9.6. Starting from the parameters in Tab. 9.1, we reduce the mechanical frequency by a factor 7 and, accordingly, increase n_1 by the same factor (thus keeping the bath temperature constant), we also keep Q_{11} constant so that the cooperativity remains approximately 1. In that regime, the sufficient condition Eqs. (9.46) is not met and entanglement is not detected in Fig. 9.6 (left). At unit cooperativity, the coherent contribution Γ_1^{ro} in Γ_1^{tot} and the incoherent contribution Γ_1^{th} contribute equally. Hence, one can attempt to restore the sufficient condition by reducing either of these rates. Because it is counter-intuitive (and experimentally easier), we decrease the optomechanical coupling g_1 by a factor 2 (thus dividing the cooperativity by 4). The result is shown in the right panel of Fig. 9.6 where entanglement is detected again, but the separability bound violation is small, reflecting the decreased

22. We often use that $\Gamma_j^{\mathrm{tot}} = \gamma_j n_j(C_j+1)$.

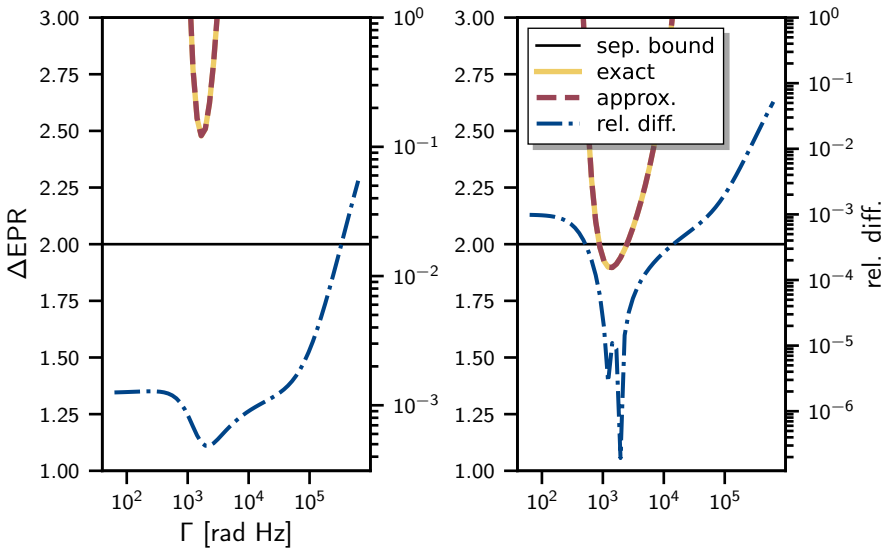

Figure 9.6 EPR-variance from exact σ^{tm} as continuous yellow lines, from the approximated formula Eq. (9.27) as dashed red, and their relative difference in dot-dashed blue. (left) The mechanical frequency from parameters from Tab. 9.1 is reduced (at fixed C_1 and Q_{11}) so that the sufficient condition Eqs. (9.46) is not satisfied. (right) Optomechanical coupling g_1 is decreased by half so that the sufficient condition is satisfied and entanglement is detected again.

cooperativity. Both plots in Fig. 9.6 show exact and approximated results, and their relative accuracy is better than the percent level (in the region where Δ_{EPR} is smallest).

The results from the optimised witnesses in Figs. 9.4 show that the limitation set by the sufficient condition Eqs. (9.46) is being overcome by a better entanglement test – hence the limitation set by this sufficient condition is not fundamental. In fact, in our experience, necessary and sufficient entanglement tests *always* detect entanglement when only a single mechanical mode is included. This is an illustration of the *universality* of optomechanical entanglement, as demonstrated in [MDC10] and extended in [Dir+24]. In practice, this led to the situation where the theoretical model was not very helpful in understanding why the analysis of experimental data would not succeed.

Experience also shows that the entangled states detected by necessary and sufficient tests typically require large Γ (typically $> \omega_1$) consistent with [MDC10]. This is also consistent with the intuition that on time scales shorter than the incoherent noise channel rate Γ_1^{th}, the temporal modes necessarily encode (some) quantum correlations. But short temporal modes are broad frequency filters that are limited in practice by other (incoherent) processes in the associate bandwidth; see Part III where we discuss real experimental setups.

We also point out a result from [Bar+11] showing that states detected by EPR-variance-like criteria are robust against passive losses. This is

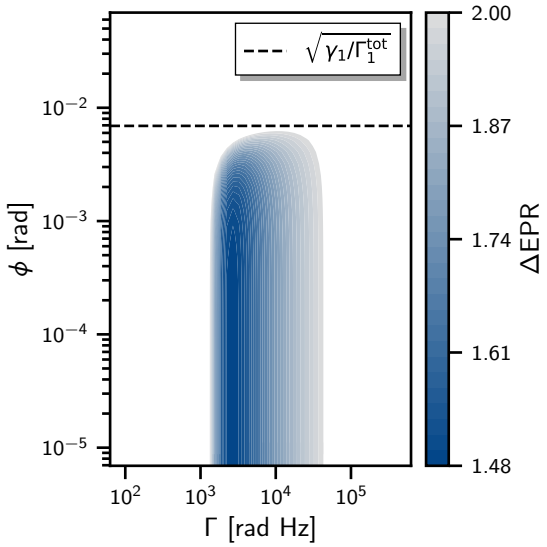

Fig. 9.7 Contour plot of exact $\Delta_{\mathrm{EPR}} < 2$ (the darker the smaller) for varying Γ and ϕ. The dashed line is the accuracy condition on ϕ Eq. (9.47b). All axis' scales are logarithmic.

an argument for targeting the parameter space characterised by our sufficient condition Eqs. (9.46) – and still using a more powerful test in paractice.

9.4.3 *Limit of finite* ϕ *and* T_{sep}

Remaining in the limit $\nu^2 \ll 1$ with the perfectly tuned filters ($\delta\omega = 0$), we now discuss how the approximate formula for Δ_{EPR} Eq. (9.27) changes when ϕ and T_{sep} are finite – the latter is of crucial importance for cavity optomechanical devices where we saw that T_{sep} must be $> 1/\kappa$ for the entanglement verification theorem to hold in good approximation; cf. Sec. 7.2. The case $\phi \neq 0$ simulates, for example, the effect of imprecision in the optimised witness matrix; we did not study this point, but it could be a starting point to describe statistical effects of the state reconstruction in the computation of the optimal witness; see also Sec. H.9 on the estimation of confidence intervals. In the present case, the witness matrix W_{EPR} defining Δ_{EPR} is set in advance and there is no uncertainty on ϕ.

In the broad cavity regime $\omega_1^{-1} \gg T_{\mathrm{sep}} \gtrsim \kappa^{-1}$ [cf. Eq. (8.4)], when $\nu < 1$, and when the necessary and the sufficient conditions for entanglement Eqs. (9.46) are met, one finds the following approximate sufficient conditions for entanglement detection (details in Sec. E.4)

$$0 \leqslant T_{\mathrm{sep}} < \frac{1}{\Gamma_1^{\mathrm{tot}}} \tag{9.47a}$$

$$|\phi| < \sqrt{\frac{\gamma_1}{\Gamma_1^{\mathrm{tot}}}}. \tag{9.47b}$$

In Figure 9.7, we see that entanglement is no longer detected when ϕ is greater than $\sqrt{\gamma_1/\Gamma_1^{\mathrm{tot}}} \approx 7 \times 10^{-3}$ rad (for the parameters of

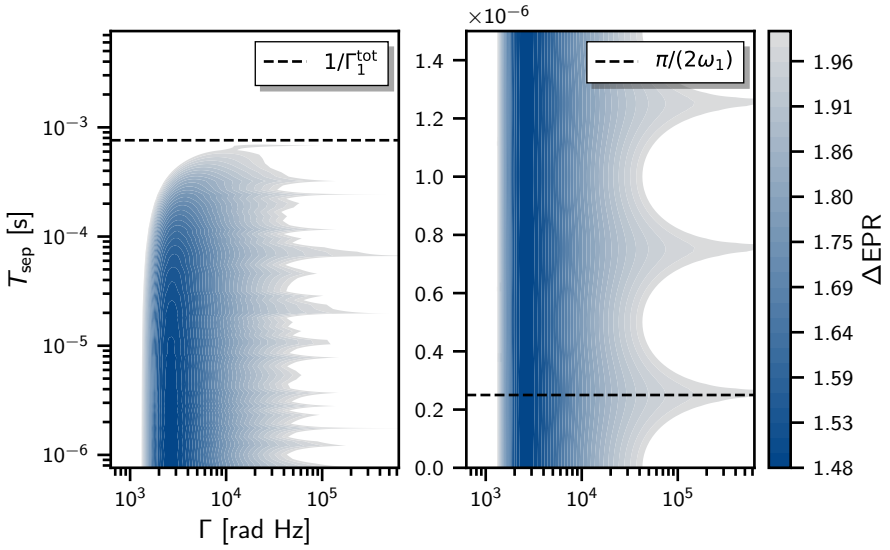

Figure 9.8 (left) Contour plot of the exact $\Delta_{\mathrm{EPR}} < 2$ for varying Γ and T_{sep}. The dashed line is the accuracy condition on T_{sep} Eq. (9.47a). (right) A zoom along the y-axis. The dashed line is the optimised value for T_{sep} that minimises N_1.

Tab. 9.1). And in Fig. 9.8 (left), we see that entanglement is no longer detected when $2\pi\, T_{\mathrm{sep}}$ is larger than $2\pi/\Gamma_1^{\mathrm{tot}} \approx 7 \times 10^{-4}$ s. This is much longer than $2\pi/\kappa = 10^{-7}$ s, which leaves an ample margin to choose a finite separation between the temporal modes – so as to satisfy the strict pairwise interaction required to use the verification theorem – and still detect entanglement between the temporal modes.

We see features towards larger filter bandwidths in the left panel of Fig. 9.8. A zoom (right panel) reveals a regular structure, where the domain of entanglement detection is periodically extended by an order of magnitude (albeit with small separability violations). This improved entanglement sensitivity happens when N_1 Eq. (9.38) becomes negative. In Section E.4, we expand N_1 close to its minimum attempting to keep N_0 Eq. (9.33) close to its maximum. The smallest values for Δ_{EPR} are then with $\phi = 0$ and $T_{\mathrm{sep}} = \pi(2n+1)/(2\omega_1)$ with $n \in \mathbb{N}$. In that case, the sufficient condition for entanglement is $n_1\,(C_1+1) < 2\,Q_1^2$ Eq. (E.21), which is much less stringent than Eq. (9.47a), and $\Gamma_1^{\mathrm{tot}\,2} < \Gamma^2 \ll \omega_1^2$ must hold too, reflecting the necessary condition for entanglement Eq. (9.35) and the assumption $\nu^2 \ll 1$ used to derive the results.

We illustrate this effect in Fig. 9.9 where we use the same parameter regime as for Fig. 9.6 (ω_1 7 times smaller, n_1 7 times smaller, $C_1 \approx 1$ and $Q_{11} = 10^8$). As we had seen in Fig. 9.6 (left), no entanglement is detected at $T_{\mathrm{sep}} = 0$. As T_{sep} increases, entanglement becomes periodically detectable, corresponding to the relaxation of the sufficient condition. The first occurrence occurs at $T_{\mathrm{sep}} = \pi/(2\omega_1) \approx 1.75$ µs.

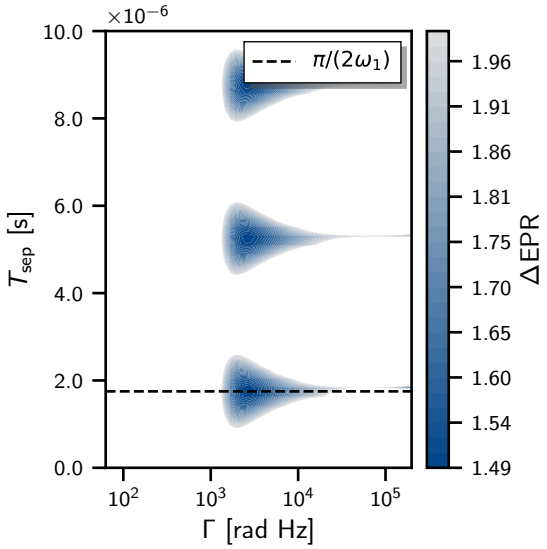

Fig. 9.9 As Fig. 9.8, contour plot of the exact $\Delta_{\mathrm{EPR}} < 2$ of varying Γ and T_{sep}. The parameters are as in the left panel of Fig. 9.6 and no entanglement is detected when $T_{\mathrm{sep}} = 0$; then periodic detection for $T_{\mathrm{sep}} = \pi(2n+1)/(2\omega_1)$, $n \in \mathbb{N}$.

See also quantitative expressions and qualitative discussions on the required precision on T_{sep} to see this effect in Sec. E.4

9.4.4 *Limit of imperfectly tuned temporal filters:* $|\delta\omega| > 0$

We motivated our protocol arguing that it is, in principle, agnostic of the system parameters. This statement is true at the abstract level of the entanglement verification theorem of Ch. 7 to infer optomechanical entanglement from unspecified temporal modes. We went on specifying a particular protocol implementation in Ch. 8: in particular, we chose a specific functional form of the temporal modes involving demodulations of the sidebands of the detectable cavity output light; cf. Eqs. (8.7). That particular choice requires knowing the frequency of the targeted mechanical mode ω_1, which is possible up to some finite accuracy, limited by finite statistics or because ω_1 varies in the course of a measurement run due to uncontrolled and/or unknown processes.

We study here the expression of Δ_{EPR} from Eq. (9.27) for $1 \gg |d| > 0$, which defined the demodulation mismatch between $\bar{\omega}$ and ω_1 Eq. (8.8). We also assume that the mismatch is much less than the filter bandwidth, so that $\Gamma \gg \delta\omega \;\Rightarrow\; \nu \gg d$.[23] In Section E.5 and in [Gut24, Theoretical predictions derivation .nb][24] we derive a sufficient condition Eqs. (E.23) on the temporal mode detuning for detecting entanglement

$$\delta\omega < \frac{\Gamma}{\sqrt{n_1(C_1+1)}} \qquad \Longrightarrow \qquad \delta\omega < \frac{\sqrt{\gamma_1 \Gamma_1^{\mathrm{tot}}}}{2} \tag{9.48}$$

23. Compatible with $\nu^2 > 2d$ assumed to obtain Eqs. (9.34).
24. File path: see footnote 1.

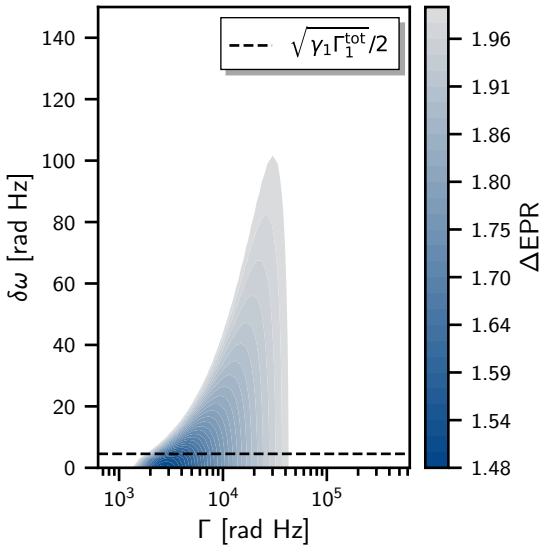

Fig. 9.10 Contour plot of the exact $\Delta_{\rm EPR} < 2$ for varying Γ and filter detuning $\delta\omega$. The dashed line is the bound Eq. (9.48) on the filter mistuning $\delta\omega$ combined with the necessary condition on Γ to detect entanglement.

where we used the necessary condition $\Gamma_1^{\rm tot} < \Gamma$ to obtain the implied stricter condition.

Figure 9.10 illustrates how entanglement is lost as accuracy on the demodulation frequency decreases. With the parameters of Tab. 9.1 $\sqrt{\gamma_1\Gamma_1^{\rm tot}}/2 \approx 5$ rad Hz, meaning that the mechanical resonance must be known (or stabilised) at the level of one part per million(!) – to my knowledge, this is a very stringent requirement. The less strict condition (on the left) indicates that $\delta\omega$ can be at most 1% of Γ, as a consequence of the high mechanical bath temperature.

9.4.5 *Spectator mode scenario*

We now turn to the study of the effect of the term $\mathcal{N}_2$ in Eq. (9.27) and set $g_2 > 0$. We recall that the spectator mode has frequency Eq. (5.11)

$$\omega_2 = (1+D)\omega_1 = \omega_1 + \Delta\omega$$

where $1 > |D| > 0$ (roughly expected to be at least a percent and at most 30%). We assume that the Lorentzian filters are narrow enough not to resolve the spectator mode: that is, $\Gamma < \Delta\omega$. In fact, in this section, it will be useful to assume a little more, namely that $\Gamma^2 \ll \Delta\omega^2 \;\Rightarrow\; \nu^2 \ll D^2$. We work with filter functions that are perfectly tuned to the target mode and set $\bar{\omega} = \omega_1$, and we set $\phi = T_{\rm sep} = 0$ that maximise $\mathcal{N}_0$.

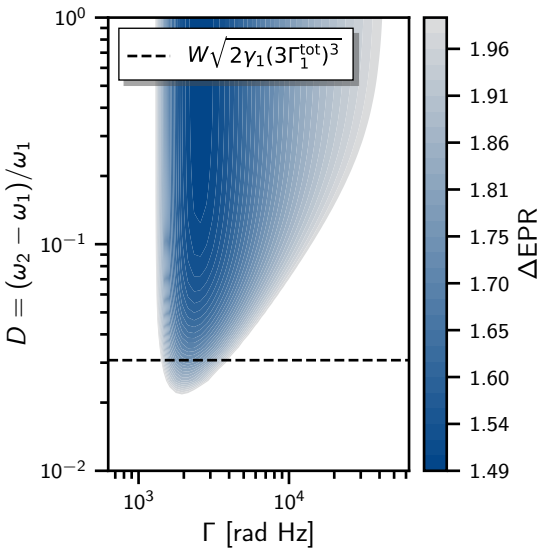

Fig. 9.11 Exact $\Delta_{\mathrm{EPR}} < 2$ against Γ and D. The dashed line is the bound on the spectral separation between the mechanical modes from the sufficient condition Eqs. (9.50).

We find in Sec. E.6 (see also [Gut24, Theoretical predictions derivation .nb][25]) that the effects from the spectator mode dominate if [cf. definition of W Eq. (9.41)]

$$\frac{(2W\omega_1)^2}{\Delta\omega^2} \gg 1 \quad \Longleftrightarrow \quad 4\,W^2 = 4\frac{\gamma_1}{\gamma_2}\frac{\Gamma_2^{\mathrm{ro}}}{\Gamma_1^{\mathrm{ro}}}\frac{\Gamma_2^{\mathrm{tot}}}{\Gamma_1^{\mathrm{tot}}} \gg \mathrm{D}^2. \tag{9.49}$$

(In the opposite case, the effects from the target mode dominate and the results from the previous sections provide the main behaviour.) In that case, a sufficient condition for entanglement is

$$(3\,\Gamma_1^{\mathrm{tot}})^3 < \gamma_1 \frac{\Delta\omega^2}{W^2} \tag{9.50a}$$

$$\Leftrightarrow \Gamma_1^{\mathrm{tot}} < \Gamma < \frac{g_1}{g_2}\frac{\Delta\omega}{3\sqrt{3\,n_2(\mathrm{C}_2+1)}}. \tag{9.50b}$$

We inspect numerically what this bound means in terms of the parameters in Tab. 9.1. We find $W \approx 0.14$. With $\mathrm{D} = 5\%$, Eq. (9.49) indicates that the spectator mode is relevant, albeit perhaps not quite the dominant contribution to Δ_{EPR}. With Eqs. (9.50), we find that $\Delta\omega$ should be more than 3% of ω_1 to detect entanglement (consistent with entanglement detection in Fig. 9.3). Figure 9.11 shows a map of the evaluation of the exact EPR-variance, where it detects entanglement. The dashed line is the approximate bound on D from Eqs. (9.50). The estimate is conservative apparently, probably because we used an upper bound of $\mathcal{N}_2$ thus overestimating the effect of the spectator mode; see [Gut24, Theoretical predictions derivation .nb][26] for details.

The sufficient condition for entanglement detection with Δ_{EPR} in the single mechanical mode scenario Eqs. (9.46) has a form analogous

25. File path: see footnote 1.
26. File path: see footnote 1.

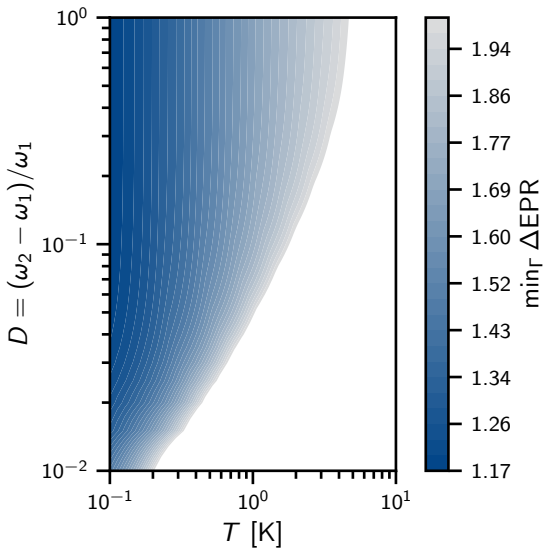

Fig. 9.12 Exact $\Delta_{\mathrm{EPR}} < 2$ minimised with respect to Γ. T is the substrate temperature and we assume $n_1 \approx n_2 \gg 1$ Eq. (8.2).

to Eqs. (9.50) with $\Delta\omega$ taking the place of ω_1 and the prefactor W. Similarly to Eqs. (9.46), one should acknowledge the strong effect of temperature on the detectability of entanglement. In Figure 9.12 we show Δ_{EPR} minimised over the bandwidth Γ. We find that the temperature of the substrate [assuming $n_2 \approx n_1 \approx k_B T/(\hbar\omega_1)$] plays a crucial role: below a kelvin, 5% spectral separation between the mechanical modes is enough to observe entanglement. While above 5 kelvins, no entanglement is detectable, even for a spectator mechanical mode 100% away from the target mode.

Part III

APPLICATIONS: THEORETICAL STUDY OF SPECIFIC EXPERIMENTAL SETUPS AND ANALYSIS OF THEIR DATA

PREFACE TO PART III

We are now in the position to use the model and theoretical machinery exposed thus far to study candidate experimental devices. First, we assess the feasibility of the protocol in light of the theoretical results of Ch. 9, for the parameters of five existing setups that are different implementations of optomechanics: two membranes, one hard-clamped [Gä20; HO17; MN17] and one soft-clamped [Tsa+17; Ros+19; Che+20]; two levitated nano-particles, one in coherent-scattering configuration [Del+19; Del19; Del+20b] and the other in back-scattering configuration [Mag+21; Mag21; Mag+22]; and a photonic crystal [GNG19]. A physical description of each of these devices will be provided prior to their study and will clarify the naming. Except for the back-scattering levitated particle, all the devices couple the mechanical mode to a cavity mode, which is subsequently detected (i.e. they are cavity optomechanical devices). My colleague Klemens Winkler worked out the theoretical formulation of the protocol for such levitated cavityless systems and showed that it works analogously to what was presented in Part II (his work will be presented elsewhere). The photonic crystal was an experiment at Delft University of Technology in the group of Simon Gröblacher and operated by Jinkun Guo; the soft-clamped membrane was implemented at the University of Copenhagen in the group of Albert Schliesser; the remaining three devices where in my group at the University of Vienna, the hard-clamped membrane was fabricated by Claus Gärtner and operated by Jason Hölscher-Obermaier, Ramon Moghadas Nia, Joshua Slater, and Witlef Wieczorek; Manuel Reisenbauer, Kahan Dare, Aisling Johnson, and Uros Delic operated the coherent-scattering particle; and Lorenzo Magrini, Aisling Johnson, and Victor A. Camarena-Chávez operated the back-scattering particle. We processed and studied the data from four of these devices, while the treatment of the soft-clamped membrane was performed independently of us by the group operating it in Copenhagen.

ORGANISATION OF PART III

Chapter 10 presents the theoretical predictions based on the parameters of the hard-clamped membrane and the back-scattering levitated particle as examples of how to use the theoretical apparatus of Ch. 9. The parameter study of the remaining three cavity devices is exposed in App. G. All the results (raw data and codes) are available on [Gut24].

In Chapter 11, we synthesise the results of the analysis of four different experimental datasets. The hard-clamped membrane was the first device we studied and the results are presented and discussed in [HO17, Ch. 5] and [MN17, Part. V]. The subsequent analyses of the other three devices lead to essentially similar results, therefore we present here only [27] the latest – most mature and arguably best understood – data analysis of the levitated particle in back-scattering configuration. We make sure to highlight the most relevant features and behaviours observed in all four data analysis. In applying the protocol to the different datasets, we refined certain choices in the postprocessing procedure. Appendix H documents the differences and updates compared to the data processing originally devised and described in [HO17, Ch. 5] and in [MN17, Part. V].

We could not demonstrate convincingly stationary optomechanical entanglement in the data analysis of any of the four devices. To our knowledge, the protocol performed (independently from us) on the soft-clamped membrane did not demonstrate entanglement either. For the four cavity devices (hard/soft-clamped membranes, photonic crystal and coherent-scattering particle) the spectator mode model provides a partial explanation for the reason why it did not work; this is discussed in Ch. 10 and in App. G.

Different from the theoretical model of Ch. 9, the data evaluation can account for more than one mechanical mode in the early and late temporal mode filters; this is the so-called *multi-mode* data evaluation procedure already described in Jason Hölscher-Obermaier's thesis [HO17, Sec. 5.6]. Because our theoretical model cannot make predictions for multi-mode evaluations, we do not have an explanation for why the multi-mode evaluation of the cavity devices failed.

In the absence of a cavity, in the levitated nano-particle in back-scattering configuration, Klemens Winkler was able to compute the exact symbolic expression of the early–late state of the light detected; his model assumes arbitrary many mechanical modes and – crucially – it accounts for up to two modes in each temporal party (i.e. both early and late parties have an internal structure with two modes each). [28] Therefore, Klemens' exact analytical simulation can do more than what is possible with the results of Ch. 9 for cavity devices. The thus more advanced theoretical predictions can be compared to multi-mode evaluations of numerical simulations and experimental data; this is the reason for presenting the back-scattering device in Chs. 10 and 11. We shall see excellent agreement between analytical and numerical

27. I want to emphasis that it was an immense privilege and potent opportunity to receive so many datasets from so diverse setups. The processing of each dataset relied on substantial experimental work (e.g. re-producing entire measurements, characterising parameters, preprocessing data, etc.), intense collaborations, and exchange of insights.

28. Derivations and details will be presented by Klemens elsewhere.

simulations – in contrast to the extensive numerical simulations study of the hard-clamped membrane in [HO17, Secs. 5.4-5.11]. This was an important aspect for us to check that the data evaluation was correct. Some encouraging similarities to the results with experimental data are also highlighted.

SUMMARY OF RESULTS

The main results of this part are:

- Evaluation of experimental data from four different experiments by ourselves – plus one independent attempt on another setup – did not demonstrate optomechanical entanglement.
- The single mechanical mode model always predicts detectable entanglement between the temporal modes of the light when one uses a necessary and sufficient entanglement test (i.e. not the EPR-variance). This makes it difficult to determine how experiments should be chosen (or improved) to be successful based on the model.
- The addition of a spectator mode to the model explains why single-mode evaluations of all cavity devices did not succeed as a result of the presence of the spectator mode. The important lesson is that the presence of stationary processes, even relatively far detuned compared to the temporal mode filter bandwidth Γ, can affect entanglement detection significantly. The spectator mode model does not explain why the multi-mode evaluation failed as well.
- The data evaluation of the three cavity devices that we performed ourselves led to similar behaviours as already documented in [HO17, Ch. 5] and [MN17, Part V]. Therefore, we only report that they appear similarly in different setups. Most relevant to highlight are the systematic improvements when using the multi-mode protocol, in the sense that the witness values are always smaller then. This effect is observed in analytical and numerical simulations as well.
- An argument that the data-processing must be "conservative", i.e. it must mitigate possible *false-positive detection of entanglement*. To this end we propose slight changes in the calibration and passive-losses compensation procedure originally proposed in [HO17, Sec. 5.3.3]. Additionally, we describe a *cross-validated entanglement test* that conservatively mitigates finite statistical effects.
- The comparison of exact analytical simulations, numerical simulations, and the evaluations of experimental data. The good overlap of analytical and numerical simulation results indicates that the data evaluation implementation does correctly what we intended (and modelled). Simulations and experimental data display similar behaviours, which indicates that the former capture some relevant physics.

10

THEORETICAL PREDICTIONS FOR CANDIDATE EXPERIMENTS

This chapter applies the results of the protocol model discussed in Ch. 9 to the specific parameter regimes of two existing devices: a hard-clamped membrane in an optical cavity and a levitate nanoparticle in back-scattering detection without a cavity. The feasibility of entanglement detection with our protocol is discussed in light of the derived theoretical results. Similar analyses of three additional existing experimental setups are provided in App. G.

10.1 HARD-CLAMPED MEMBRANE

Membranes are a thin layer of material that vibrates like a drum. The light (of a cavity mode) is shone perpendicular to the membrane so that the drum-mode deformations form the moving mechanical part of the optomechanical device. The thin membrane is clamped to some substrate that can be patterned to form a *phononic shield*: that is, a bandgap for phonons at frequencies around several modes of the membrane. Phonons at frequencies in the bandgap cannot propagate (radiate) to/from the membrane, thus isolating the modes in the bandgap; see for instance [Gä20, Ch. 4] for details. When the phononic shield pattern is thick and stiff (i.e. it is the substrate that is patterned), we say that the membrane is *hard-clamped* (as opposed to soft-clamped ones, see App. G.1).

A hard-clamped membrane was designed by W. Wieczorek, J. Hölscher-Obermaier and K. Gärtner, and fabricated by K. Gärtner at Delft University of Technology. An optical cavity was built around that membrane in a device that could be placed in a small liquid-helium flow cryostat for relatively fast characterisation but limited time at low temperature. This setup was built to test stationary optomechanical entanglement with the protocol. The experimental work and inconclusive attempts to perform the protocol were documented in [HO17; MN17]. The parameters of this setup are given in Tab. 10.1. The PSD of all six time traces of a typical measurement is shown in Fig. 10.1.

The model devised in Sec. 5.4 was primarily designed to describe clamped nano/micro-resonators subject to radiation pressure – precisely like the membrane setup at hand [Hof15]. The mechanical bath model is the substrate on which the membrane is clamped. It is a

Physical property	Symbol	Value	Units
mech. frequencies	ω_1	$1.19 \times 10^6 \times 2\pi$	[rad Hz]
	ω_2	$1.86 \times 10^6 \times 2\pi$	[rad Hz]
cavity linewidth (FWHM)	κ	$5 \times 10^6 \times 2\pi$	[rad Hz]
detuning (red)	Δ	$-200 \times 10^3 \times 2\pi$	[rad Hz]
optomech. couplings	g_1	$205 \times 10^3 \times 2\pi$	[rad Hz]
	g_2	$13/40\, g_1$	[rad Hz]
mech. linewidths (FWHM)	γ_1	$0.16 \times 2\pi$	[rad Hz]
	γ_2	$1.03 \times 2\pi$	[rad Hz]
mech. quality factors	Q_1	7.3×10^6	[]
	Q_2	10^6	[]
mech. baths temp.	T_1	10	[K]
	T_2	T_1	[K]
bath occupation numbers	n_1	1.76×10^5	[]
	n_2	1.11×10^5	[]

Table 10.1 Parameters of a hard-clamped membrane operated in my group at the University of Vienna [MN17, Tab. 9.2].

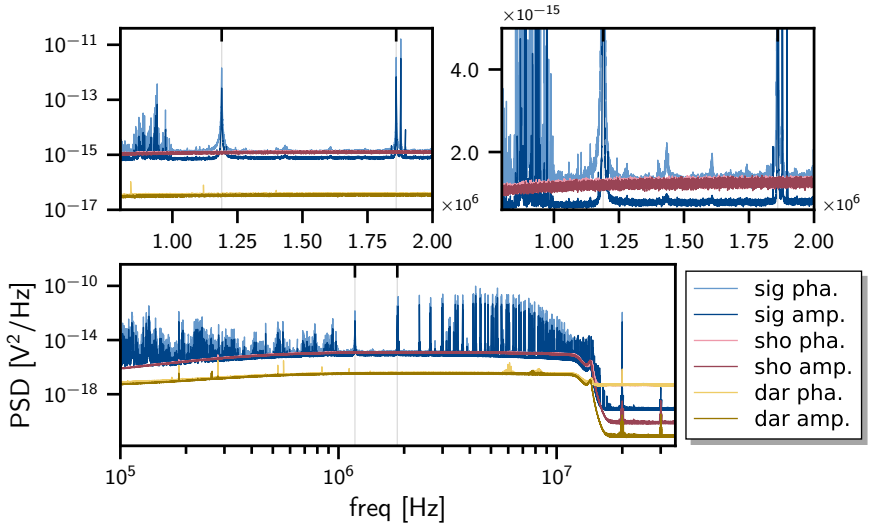

Figure 10.1 Power spectral density (PSD or NPS) of the hard-clamped membrane device described in [HO17; MN17]. The upper plots are zoom of the same frequency interval around the first two mechanical modes (indicated with ticks on the upper axis); mind the different logarithmic and linear scales of the ordinate. All six time traces are plotted: amplitude (dark colours) and phase (light colours) of signal (blue), shotnoise (red), and darknoise (yellow).

thermal environment at temperature $T_1 = T_2$ that is set by implementing a certain cryogenic environment (or not) for the system. [1]. The theoretical results from Ch. 9 apply, and we make some predictions.

Equations (9.46) provide a sufficient condition for entanglement being detectable with the protocol outlined in Sec. 7.2. Plugging the parameters from Tab. 10.1 we find that $\Gamma^{\text{tot}} \approx 390 \times 10^3$ Hz and $\frac{2}{3}\frac{\omega}{\sqrt[3]{Q_1}} \approx 20 \times 10^3$ Hz so that the condition is not satisfied by a factor of 19. Therefore, our protocol cannot detect entanglement. This looks like a bad start: in order to reduce Γ^{tot} by a factor 19 [without changing the rhs of Eqs. (9.46)], one needs to decrease both the driving power *and* the environmental temperature by 2×19 each. While reducing the power is counter-intuitive, it is readily feasible; reducing the temperature on the other hand is experimentally more demanding/expensive because it requires sub-Kelvin temperatures.

The derivation of the sufficient condition Eqs. (9.46) assumed resonant driving of the cavity $\Delta = 0$ Eq. (8.5). In practice, it is not easy to operate exactly in this regime; this is because the blue detuned case (when the drive frequency is larger than the cavity resonance and $\Delta > 0$) is unstable [2] already at relatively small values of Δ (small compared to how well it can be controlled). Therefore, experiments with small detunings usually operate in the slightly red detuned regime ($\Delta < 0$) [Gut+20]. Section 9.1.2 explains that the exact symbolic expression for the state σ^{tm} of the early–late temporal modes of the light can be computed on a computer; moreover, this expression can be obtained for any detuning. We plotted in Fig. 10.2 (left) the exact Δ_{EPR} for the finite detuning in Tab. 10.1. There, the protocol detects entanglement between the light modes, contrary to the resonant case. This goes against the intuition developed (heuristically) in Ch. 6 where we argued that it is best to work on resonance to maximise the strength of both sidebands in the detected light. We do not have a physical or mathematical explanation for this effect.

Because we have access to the exact full state, we can compute the logarithmic negativity (which is a measure of entanglement) instead of Δ_{EPR} (which is only a sufficient test). The result, with and without detuning, is plotted in the right panel of Fig. 10.2. In both cases the logarithmic negativity detects entanglement: this illustrates that Δ_{EPR} is a sub-optimal entanglement test. This reflects the behaviour of Fig. 9.4 where the optimised witnesses reveal more entangled states

1. For the theorist readers, there are essentially three reference temperatures for bulk environments: room temperature at about 300K; liquid Helium temperature at about 4 K; tens of milli-kelvins (and below) that require dilution refrigerators. Roughly speaking, room temperature down to 10-4 K requires comparatively little experimental effort

2. Physically, this is when the two-mode squeezing process exciting the mechanical oscillator, dominates over the beam splitter process cooling it down. Mathematically, the stability threshold is given by the Ruth-Hurwitz criterion, cf. Sec. 5.3.1, [Gen+08], and [Hof15, Sec. 1.3.1].

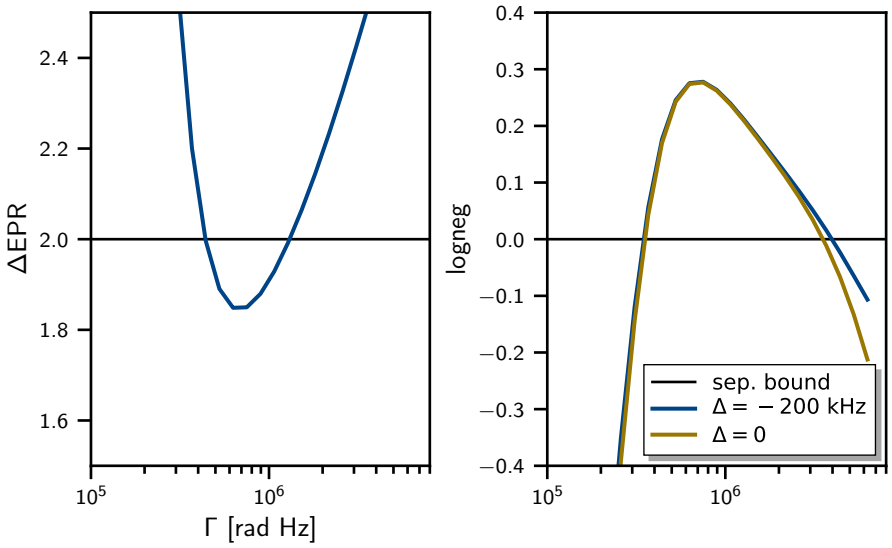

Figure 10.2 (left) Exact EPR-variance for the parameters of Tab. 10.1. The temporal modes are entangled when $\Delta_{\mathrm{EPR}} < 2$. Δ_{EPR} for resonant drive $\Delta = 0$ is far above and not visible here. (right) Logarithmic negativity (logneg) entanglement measure obtained from the exactly computed covariance matrix. The temporal modes are entangled when the logneg is > 0.

than the exact EPR-variance. The logarithmic negativity varies little depending on the detuning [3]: the maximal *amount* of entanglement is the same and at the same temporal mode bandwidth Γ. In the detuned case, more entangled states are detected as Γ varies.

Figure 10.2 indicates that one can expect to successfully detect entanglement with this setup. It turns out that for all parameters we ever looked at – and in particular for the parameters of the four cavity devices we studied in detail – the logarithmic negativity always detects entanglement for some bandwidth Γ. This reminds us of the particularly concise expression Eq. (9.45) for Δ_{EPR} predicted entanglement detection for any finite cooperativity. In particular, on Fig. 9.4 the optimised witness (that detects all entangled states like the logarithmic negativity) would detect entanglement at very low cooperativity. This behaviour echoes – and most probably is a consequence of – the "universality of optomechanical entanglement" (in the absence of sensing noise) demonstrated in [MDC10]. [4] From an experimental point of view however, it is a little too good to be true... and, indeed, the

3. Strictly speaking, only positive logarithmic negativity is well defined in terms of entanglement; standard definitions in the literature identifies negative values to zero, see [AI07, Eq. (68)] for example. We still plot the negative values because, when no entanglement is detected, the negative values are a heuristic indicator of how far we are from entanglement – this follows the convention from [HO17, App. C.1].

4. For more on this phenomenon, we recommend the work of Haixing Miao, Helge Müller-Ebhardt, Stefan Danilishin, and Yanbei Chen [Mia+10a; Mia+10b; MDC10; DK12], for instance. Also the more recent (and coming up) works of Su Direcki picks up on that concept in more general terms [Dir+24].

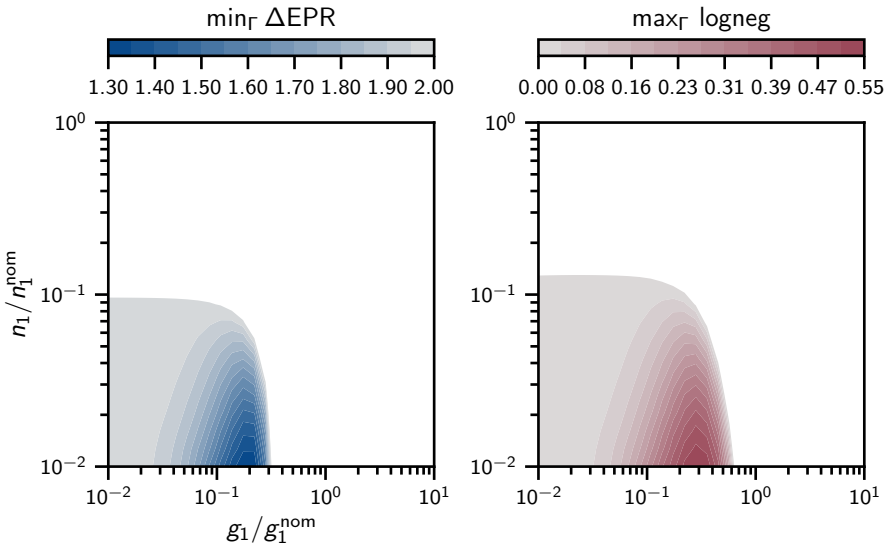

Figure 10.3 (left) Exact EPR-variance, minimised over the temporal filter bandwidth Γ between 1kHz and 10MHz. Optomechanical couplings g_1 (with fixed ratio to g_2) and thermal bath occupation number $n1$ (with fixed ratio to n_2) are varied; both axes are ratios to the nominal value in Tab. 10.1. The results from the approximate Δ_{EPR} Eq. (9.27) are not shown but they are close to the exact ones here. (right) Logarithmic negativity maximised with respect to the temporal filter bandwidth Γ.

model is too simplistic and in reality additional phenomena must be accounted for to make accurate predictions.

In Section 9.4.5 we studied the effect of a second mechanical mode which is not taken into account by the temporal mode filtering. In other words, the analysis does not attempt to extract information about this mode from the associated sidebands in the detected light. We had called this mode a *spectator* mode. Eqs. (9.50) provides a sufficient condition for entanglement detection with the protocol (using Δ_{EPR}). The modes of the hard-clamped membrane are relatively far apart (compared, for example, with the soft-clamped membrane treated in App. G.1): in Tab. 10.1, the spectator mode is some 700 kHz above the target mode, i.e. a relative spectral distance D $\approx$ 58%. We get $\sqrt[3]{\gamma_1 \Delta\omega^2/(27W^2)} \approx 28.8 \times 10^3$ Hz, a factor 13 less than Γ_1^{tot}, so that the theoretical model again predicts that there is no detectable entanglement with Δ_{EPR}. Numerical evaluations also reveal no entanglement with the logarithmic negativity. [5]

We sweep over some parameters to establish "how far" the system is from detectable entanglement in this spectator mode scenario. The inter-relation between the parameters in membranes are: the relative couplings between the modes relate to the geometry of the vibration pattern and its overlap with the light mode [Gä20; HO17; MN17],

5. Recall that, in the spectator mode scenario, we could not incorporate the finite detunings to the exact calculation (nor spacing Γ_{sep} between the temporal modes).

hence we keep the ratio $g_2/g_1 = 13/40$ fixed as in Tab. 10.1; similarly, the quality factors are fixed by the design (e.g. material properties, stress, bandgap, mode shape); lastly, the bath of each mode is at the same temperature T of the substrate, which can be changed, but maintaining the ratio n_1/n_2 given by $\omega_2/\omega_1 = 1 + D$ (in the high temperature limit). Under these constraints, we varied drive power (g_1) and temperature (n_1) to see when entanglement is detected. The results are plotted on Fig. 10.3. As already clear from Eqs. (9.50), lower temperatures are necessary: presently, a reduction by a factor 10 or more is needed. Less intuitive, it appears necessary to decrease g_1; and there seems to be an optimum at 20-30% of the nominal value from Tab. 10.1. Figure 10.3 shows the contour plot for both the EPR-variance and the logarithmic negativity. Both coutours are relatively similar (although the logarithmic negativity detects more entangled states, as it should), so that Δ_{EPR} is almost as informative as a necessary and sufficient test in this regime – and the sufficient condition Eqs. (9.50) applies approximately to necessary and sufficient tests. The result with the approximate Δ_{EPR} formula Eq. (9.27) is not shown but it captures well the exact behaviour; cf. [Gut24].

Figure 10.4 shows the EPR-variance and logarithmic negativity minimised over Γ for different coupling strengths (g_1/g_2 fixed) and spectator mode spectral distance, for a substrate temperature 10 times less than in Tab. 10.1 (i.e. ≈ 1 K). Apparently, even at this low bath temperature, the constraint on the mode spectral distance remains quite stringent and one cannot afford a much closer spectator. The result with the approximate Δ_{EPR} formula Eq. (9.27) is not shown but it captures well the exact behaviour. We decrease the temperature of the substrate by another factor of 2 (i.e. to 0.5 K) and show the results in Fig. 10.5. Exact logarithmic negativity, exact Δ_{EPR}, and approximates Δ_{EPR} (not displayed) yield similar results. Some entanglement is detected with the spectator mode below the target mode ($\omega_2 < \omega_1$), which was not the case in Fig. 10.4. We do not have a clear understanding for the asymmetry between spectator mode above or below the target, but it could be studied from Eq. (9.27) which reproduces the effect.

The model here is for a spectator that is a harmonic mechanical mode, but I think it can be interpreted as a prototype model for any process with a component in the measured light. From my experience with experimental data, strong low-frequency signals in long time traces are usually typically present in the records. The asymmetry making low frequency spectator modes seemingly more detrimental is an incentive to select (or design) the setup with accordingly quiet (or flat) low frequency components.

Lastly, we fixed g_1 (and accordingly g_2) to 10% of its nominal value in Tab. 10.1, which is close to the best operating regime in Fig. 10.3. We then swept over ω_2 and the substrate temperature n_1, keeping the ratio with n_2 fixed and independent of ω_2 (which is not too inaccurate

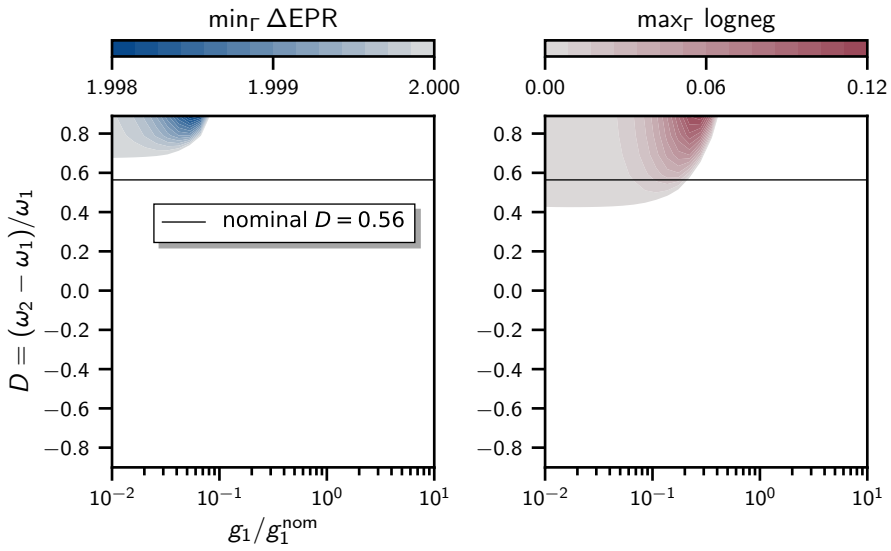

Figure 10.4 (right) Exact Δ_{EPR}, minimised over Γ (1kHz to 10MHz), with a substrate 10 times colder than in Tab. 10.1. Results from the approximate Δ_{EPR} Eq. (9.27) are close to the exact ones here. We draw the attention of the reader on the rather modest separability violation of the EPR-variance test. (right) Exact logarithmic negativity maximised over Γ. It detects entanglement in this case for about 10 times less driving power. No entanglement is detect for spectator modes at lower frequency than the target (when $\mathrm{D} < 0$).

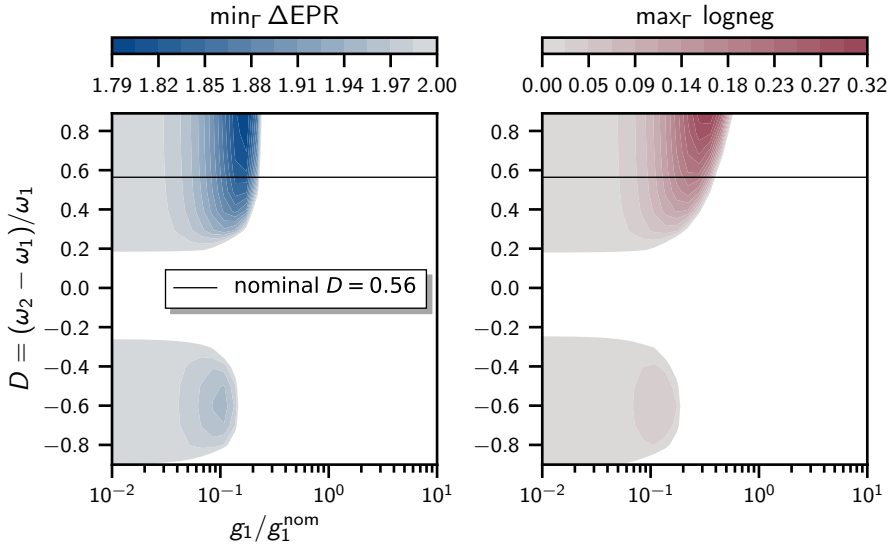

Figure 10.5 (right) Exact Δ_{EPR}, minimised over Γ between 1 kHz and 10 MHz, with a thermal bath 20 times colder than in Tab. 10.1. Again, the result from the approximate Δ_{EPR} are very similar. (left) Exact logarithmic negativity maximised over Γ. Entanglement is detected when the spectator modes has lower frequency than the target (i.e. where $\mathrm{D} < 0$), albeit in smaller amounts.

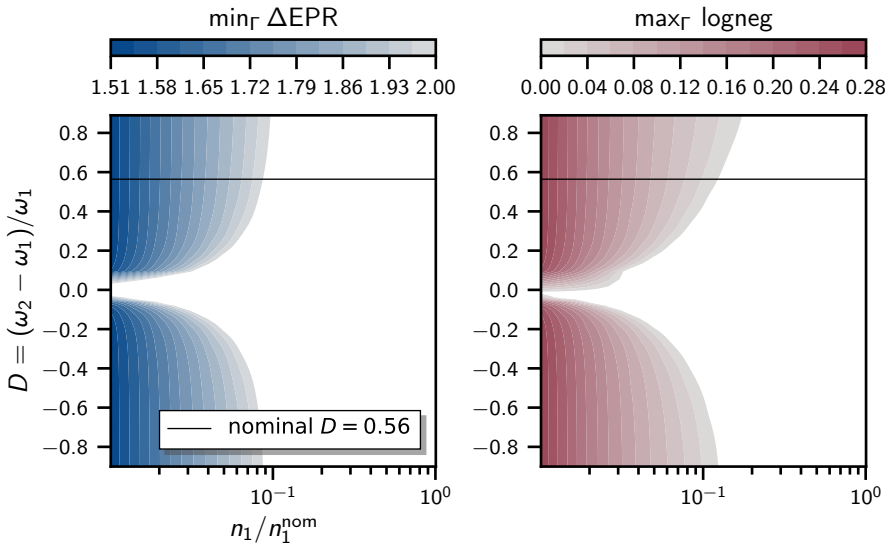

Figure 10.6 (right) Exact Δ_{EPR}, minimised over Γ between 10 Hz and 1 MHz, with g_1 10 times less than in Tab. 10.1. The approximate formula for Δ_{EPR} gives similar results. (left) Exact logarithmic negativity maximised over Γ. Possible numerical instability at small positive D.

in the large occupation limit $n_1, n_2 \gg 1$ and for $|D| < 1$). The results are displayed in Fig. 10.6. The requirement on temperature is decisive. The asymmetric nick at lower D in the logarithmic negativity is not understood and looks like a numerical problem.

10.1.1 *Summary of predictions for cavity devices*

In Appendix G, we present a similar analysis of the three additional cavity optomechanical devices: a soft-clamped membrane, a soft-clamped photonic crystal, and a coherent-scattering levitated nanoparticle. The results of the analysis of all four parameter regimes can be summarised as follows: the single mechanical mode model always predicts detectable entanglement with a necessary and sufficient test, but never with the EPR-variance (in the resonant case). This is the apparent "triviality" of entanglement with the single mechanical model discussed above. In some cases, red detuning can lead to entanglement detection with the EPR-variance, as we saw in Fig. 10.2.

On the other hand, for all devices, the addition of a spectator mode leads to no entanglement detection, even with logarithmic negativity. Similarly to the hard-clamped case, logarithmic negativity and by Δ_{EPR} detect almost the same entangled regimes (within the span of our numerical exploration). As a consequence, the sufficient condition for entanglement in the presence of a spectator mode Eqs. (9.50) is informative on how to modify the parameters to be able to detect entanglement. In all cases (except for the coherent-scattering levitation

system), reducing the mechanical bath temperature is most effective, and reducing the driving power is necessary in some cases.

The case of the levitated nano-particle in coherent-scattering configuration is quite different from that of the clamped systems, for which the code was originally designed. Moreover, my understanding of the inter-relations of the different parameters did not lead to meaningful or insightful parameter sweeps. [6]

10.2 LEVITATED PARTICLE IN BACK-SCATTERING CONFIGURATION

We study the parameters of a levitated particle in back-scattering configuration [Mag21, Chs. 4 & 5]. The nano-particle is held in the tight focus of an optical tweezer, similar to the coherent-scattering setup of Sec. G.3. The detection channel of this device are the modes of light recollected by the lens focusing the tweezer (see Sec. 4.3); mainly, it is the light that is scattered back (reflected) by the particle. Importantly, no cavity is involved in this setup (contrary to the coherent-scattering configuration). The decoherence mechanisms are the same in both levitation setups in the considered operation regime: photon recoil dominates and gas scattering is second.

In the absence of a cavity, the optomechanical model of Ch. 5 and the theoretical results of Ch. 9 do not apply. A rigorous description and modelling of the protocol for cavityless scenarios was thoroughly derived by my colleague Klemens Winkler, and it will be presented elsewhere. For the purpose of the presentation in this document, it is enough to say that the theory and mechanisms described in Ch. 9 are similar, and the intuition remains analogous – in fact, the mathematical complexity is slightly less. Klemens produced a code that computes the exact analytical state of the light's early and late temporal modes, for arbitrarily many mechanical modes. Moreover, he extended the theoretical derivation to 2-mode evaluation, where early and late temporal parties account for two modes each (cf. Sec. 8.2.1); Klemens' software is a Mathematica code available on [Gut24, cavless anaSim .nb] [7] (with Klemens' generous permission). The theoretical model for the 2-mode evaluation in the presence of a cavity is not

6. In private communications with some colleagues (that are levitation experts), I was explained that, in principle, the spectator modes coupling can be attenuated significantly (see also [Del19; GB+19]), to the point that their effect is not important according to Eq. (9.49). This means that the spectator mode study may not be relevant then. Nevertheless, it could be another process that disturbs entanglement detection and the spectator mode model provides a first approximation on the bandwidth next to the target mechanical mode that should be free of noise. In my experience, the necessary band without noises or mechanical modes is broader than one expects.

7. File path:
`Thesis_CGut_StationaryOptomechanicalEntanglement/chapter_structure/10ch_CandidateExp/Processing_and_data/backScattLev/cavless_anaSim.nb`

Physical property	Symb.	Value	Units
(z,x,y)-mech. modes	ω_j	$(76.6, 177.8, 228.5) \times 10^3 \times 2\pi$	[rad Hz]
meas. back-action	Γ_j^{ba}	$(5, 0.62, 0.24) \times 10^3 \times 2\pi$	[rad Hz]
effective heating	$\Gamma_{th,j}$	$(2.7, 1.1, 0.9) \times 10^3 \times 2\pi$	[rad Hz]
effective damping	$\gamma_{eff,j}$	$(90, 0.5, 0.5) \times 2\pi$	[rad Hz]
detection efficiency	$\eta_{det,j}$	$(0.11, 0.006, 0.003)$	[]

Table 10.2 Levitated nano-particle in backward-scattering detection configuration without a cavity [Mag+22], with $j = z, x, y$. Parameters generously provided and commented for us by Lorenzo Magrini, Aisling Johnson, and Victor Camarena-Chávez.

available (yet), hence this cavityless system has a more advanced analytical description. In addition to the automated analytical exact results, we also had access to numerical simulations of the system, which had been successfully used to obtain the results in [Mag+21; Mag+22] – the simulation implemented in Python is the work of Lorenzo Magrini and the code is available on [Gut24, cavless numSim .py] [8] (with Lorenzo's generous permission). We are thus in a position to assess our implementation of the protocol also in the multi-mode evaluation case. Checking that the postprocessing method is sound became an important point that is relevant to present here. Indeed, after the failed attempts to observe entanglement in three different datasets, we became suspicious that the data analysis method and/or implementation might not do what we had intended or modelled.

The QLE of the cavityless scenario are those from Eqs. (4.10) with the system Hamiltonian being only the mechanical harmonic evolution (and without cavity). The radiation pressure force that implements the optomechanical interaction is the photon recoil force ξ_{rad} and the coupling rate is the photon recoil heating rate Γ_{rad}. The (coupling) rate at which photons are emitted in the output modes in the input–output formalism is also Γ_{rad} Eqs. (4.13c). From the perspective of the detected light, Γ_{rad} corresponds to the measurement back-action and is denoted by Γ_j^{ba} ($j = z, x, y$) in the following [Mag+21, Suppl. S.5] and/or [Mag21, Ch. 5].

Table 10.2 lists the parameters of the experimental setup; the parameters are those of the dataset that demonstrated ponderomotive squeezing reported in [Mag+22]. The target mode is the z-motion along the tweezer beam axis – intuitively, it is the motion which is best encoded in the back-scattered detected mode. The effective damping rates $\gamma_{eff,j}$ are the sum of all damping along the direction j and it is dominated by feedback damping in the z-direction and by gas damp-

8. File path:
`Thesis_CGut_StationaryOptomechanicalEntanglement/chapter_structure/10ch_CandidateExp/Processing_and_data/backScattLev/cavless_numSim.py`

ing in the transverse directions. The effective heating rates $\Gamma_{\mathrm{th},j}$ are the noise contributions from the processes not related to measurement and they are mainly due to the residual gas collisions acting like a thermal bath for the different mechanical frequencies. Finally, the detection efficiency η_{det} incorporates the collection visibility ν_{coll} [from Eqs. (4.13c)] and all the passive losses in the detection channel; see App. F.2 for details on passive losses in homodyne detection. It is the large collection efficiency of the z-motion, compared to the collection efficiency of the transverse modes, that designate it as the target mode.

In the following, we consider quite a few configurations and it is worth introducing a naming convention. One speaks of $\mathfrak{m}$-*modes analytical or numerical simulations* when $\mathfrak{m}$ mechanical modes (at frequencies ω_j) are included in the dynamical model (i.e. in the QLE Sec. 5.4). An $\mathfrak{n}$-*modes evaluation* has $\mathfrak{n}$ filtering mode functions in both the early and the late party: they account for sidebands at $\mathfrak{n}$ different frequencies (say $\bar{\omega}_j$) thus producing $4\mathfrak{n}$-by-$4\mathfrak{n}$ reconstructions of covariance matrices, as explained in Sec. H.4.1.

Below we refer to *1- and 2- sided evaluations*: the latter is a particular form of multi-mode evaluation where the early mode also demodulates the blue sideband (additionally to the red one) and the late mode demodulates the red sideband. The technique was proposed by Klemens Hammerer and is described in [HO17, Sec. 5.8] (see also our comments in Sec. H.4.2).

With this nomenclature one speaks of "$\mathfrak{m}$-modes analytical or numerical simulations, with $\mathfrak{n}$-modes, 1- or 2- sided evaluations".

10.2.1 *Analytical and numerical simulations*

In the following we call *analytical simulation* the exact symbolic expression of the covariance matrix of the early–late temporal modes of the light; the computation is analogous to the cavity scenario; cf. Sec. 9.1.2. The symbolic covariance matrix is evaluated with the numerical values of the device parameters and tested for entanglement with the EPR-variance, the logarithmic negativity, or an optimised witness; cf. Sec. 3.4. The analytical code was extended to account for a second mode in the evaluation and compute the exact state, which is an 8-by-8 matrix. That means that the exact analytical calculation can compute the 2-mode 1-sided evaluation or the 1-mode 2-sided case. In the following, the number of simulated modes is 2 or 3. [9]

9. A technical subtlety regarding the orthonormalisation of the second mode: the shape of the orthonormalised mode functions depend on the orthonormalisation method (cf. [HO17, App. C.2], Secs. 8.2.1, and H.4.1), hence the method must be the same in the analytical simulation as in the data postprocessing procedure. In the analytical code it is calculated by hand with the Gramm-Schmidt algorithm, while we preferred using Matlab's `qr()` decomposition function (based on Housholder reflections) in the data evaluation code for stability (e.g. numerical accuracy). Whenever

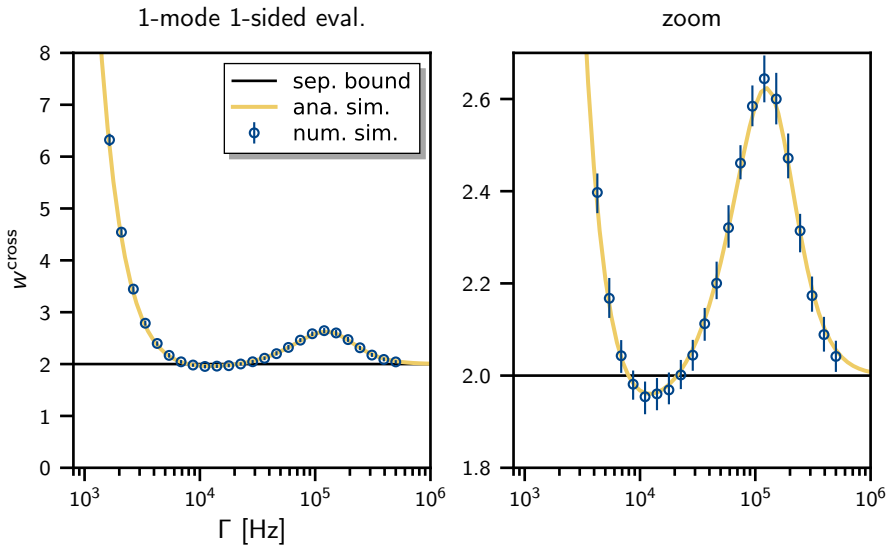

Figure 10.7 Cross-validated optimised witness values for different filtering temporal mode bandwidths Γ. The simulations are for one mechanical mode and the evaluation procedure is 1-mode 1-sided. The exact analytical results is the continuous yellow line and numerically generated time traces post-processed like experimental data are the blue markers. The error bars are the 5/95th percentile of the bootstrap distribution of witness values. Entangled states are below the separability bound at 2. The right panel is a close up zoom on the entanglement detection. One recognises a "trough+bump" shape.

The *numerical simulations* approximately integrate the QLE evaluated with the experimental parameters. The output is simulated time traces of both quadratures of the light being detected. It is an artificial dataset that mimics the output of a real experimental run. Then, one processes these numerically simulated time traces according to the protocol, just like experimental time traces: apply the mode functions and produce traces of pulse pairs, then reconstruct the corresponding temporal parties' covariance matrix according to the cross-validation optimised entanglement test, and bootstrap over reconstructed covariance matrices. See [HO17, Ch. 5] for the details of the protocol data analysis, but also Sec. 11.1 and Appendix H.

We draw the reader's attention on the important difference between both simulations and approaches: the analytical method provides the state of the temporal modes directly (and exactly) as a result of our modelling of the protocol; the numerical simulation and subsequent postprocessing (also named evaluation) mimic the way experimental data are generated and processed. The output of both procedures are covariance matrices and witness values that should (must!) match, but, importantly, they were obtained in very different ways. In fact, if they are not the same (up to statistical fluctuations and inaccuracy

comparing analytical and numerical simulations, one uses the Gramm-Schmidt method (and checks that it remained accurate enough in the cases at hand).

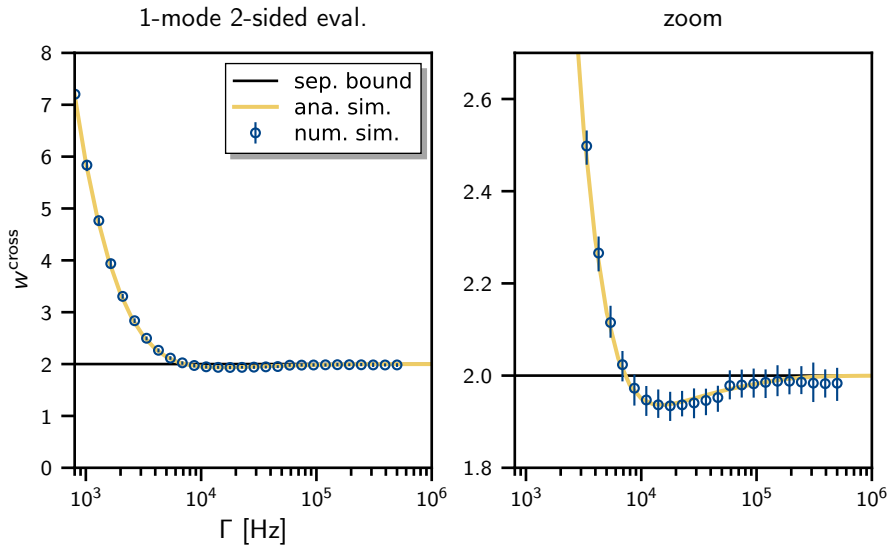

Figure 10.8 1-mode analytical (continuous yellow line) and numerical (blue markers) simulations and 1-mode 2-sided evaluation. The separability bound violation is larger compared to the 1-sided evaluation in Fig. 10.7 (the ordinates are the same across the figures).

of the approximate numerical method), this signals a problem in the postprocessing (e.g. its implementation, etc.) – assuming that both simulations are correct.

10.2.2 *1-mode simulations, 1-mode 1&2-sided evaluations*

This is the basic scenario of the protocol described in Part II and originally discussed in [Gut+20]. The witness plots of the exact analytical calculation and that of the numerically simulated time traces evaluated with the protocol are displayed on top of each other in Fig. 10.7, for the parameter of Tab. 10.2. The numerically simulated data (blue discontinuous markers) were studied just like real experimental data: the error bars are the 5/95th percentile confidence interval of the bootstrap distribution (cf. Sec. H.9) and the dot is centred on the cross-validated witness values w^{cross} Eq. (11.1); see details in Sec. H.8. The analytical result (continuous yellow line) overlaps well with the numerical one, and hence both methods make similar predictions, which is a first evidence that the procedure and our implementation of it are correct.

We draw the reader's attention to the shape of the curves, specifically the "trough" at filter bandwidths Γ just above 10 kHz and a "bump" just above 100 kHz. We will see in the next chapter that we recover it in the experimental data as well (in Fig. 11.3 below); for that reason we give this feature the (highly imaginative) name of "trough+bump" shape.

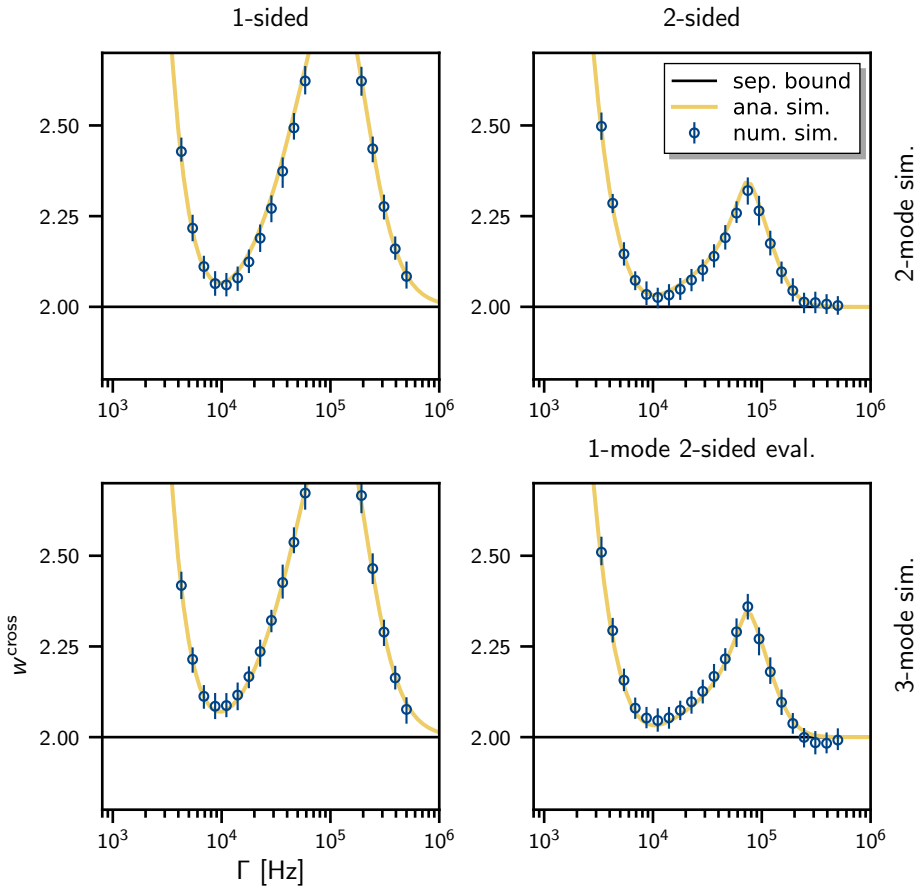

Figure 10.9 2&3-mode simulations (analytical is the continuous yellow line and numerical are the blue markers) for 1-mode 1&2-sided evaluations. The first row of plots is for 2-mode simulations and the second row is for 3-mode simulations. The columns are for 1- or 2- sided evaluations.

Figure 10.8 shows how the 2-sided evaluation improves the witness plot compared to the 1-sided case of Fig. 10.7, in the sense that the separability violation is greater. This is a general effect observed in the study of all the datasets as explained in Sec. 11.1 below. Qualitatively, one recognises at least the trough from the characteristic "trough+bump" shape.

10.2.3 *2&3-mode simulation, 1-mode 1&2-sided evaluations*

We add some complexity to the simulations and introduce additional mechanical modes at 178 kHz (transverse x-motion) and 229 kHz (y-motion); cf. Tab. 10.2. We keep the evaluation single-mode. The result of 2&3-mode simulations, 1-mode 1&2-sided evaluations is summarised in Fig. 10.9. Again, analytical and numerical results overlap well, indicating that the method and its implementation are correctly doing what we expect it to. Comparison of upper and lower

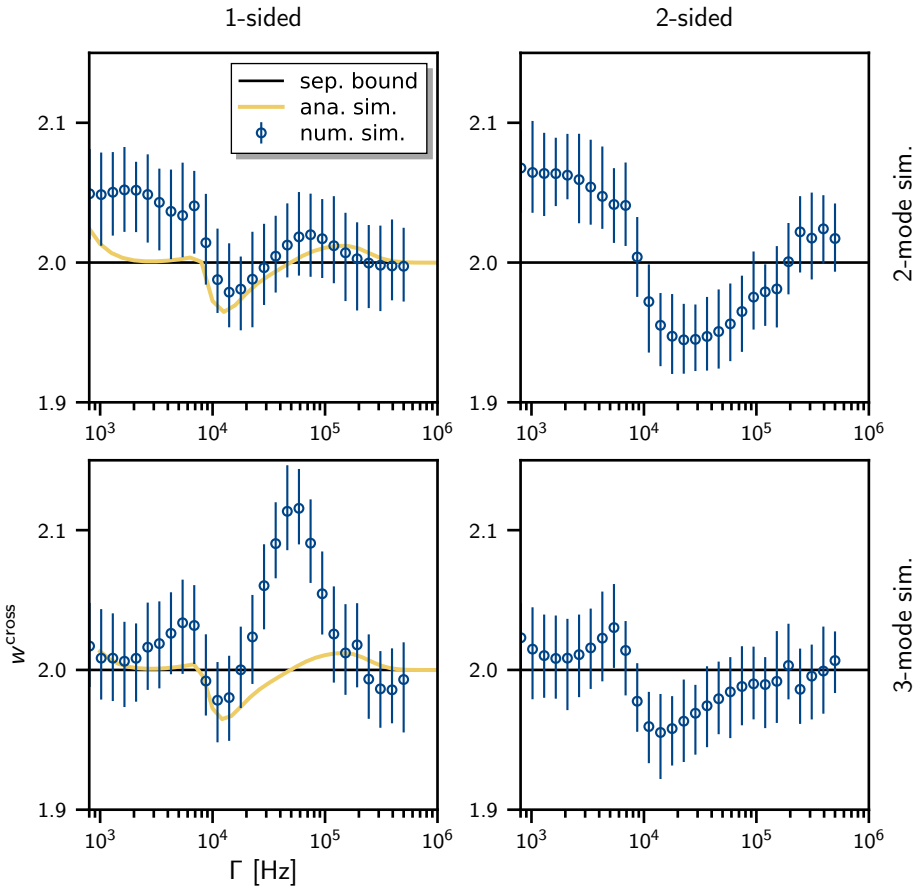

Figure 10.10 2&3-mode simulations (analytical is the continuous yellow line and numerical are the blue circles) for 2-mode 1&2-sided evaluations. Demodulating the y-motion in these 2-mode evaluation recovers entanglement that was not detected in the 1-mode evaluations of Fig. 10.9. The first row of plots is for 2-mode simulations and the second row is for 3-mode simulations. The columns are for 1- or 2- sided evaluations. The analytical code cannot treat more than two modes per party, hence no continuous line in the second column.

plots shows that the presence of a third mechanical mode does not make a significant difference. Comparison of left and right columns confirms that 2-sided evaluations perform (slightly) better (in the sense that the witness values are smaller) in this configuration as well. The "trough+bump" shape is well recognisable.

The 1-sided evaluation on the top left is essentially the spectator mode scenario treated analytically in Sec. 9.4.5. The addition of spectator mode(s) prevents the detection of entanglement, which is analogous to what we had found for all cavity devices; cf. Sec. 10.1 and App. G. 2-sided evaluation is not enough to retrieve the entanglement.

10.2.4 *2&3-mode simulations, 2-modes 1&2-sided evaluations*

In the more complex situations involving several mechanical modes, one can use the multi-mode evaluation method, which accounts for the additional mode(s); see [HO17, Sec. 5.6], Secs. 8.2.1, and H.4.1. Currently, the cavityless exact symbolic calculation is possible for two modes per temporal parties, i.e. it can simulate 1-mode 2-sided or 2-mode 1-sided evaluations.

The result of evaluations accounting for 2-modes (z and x) are summarised in Fig. 10.10. The overlap between analytical and numerical simulations is less good at low pulse bandwidths compared to what we saw above. Interestingly, entanglement is detected according to both simulations, which indicates that the multi-modal approach is a possible way to cope with additional mechanical modes.[10] This is consistent with our observation that multi-mode evaluations of experimental datasets lead systematically to smaller witness values; cf. Sec. 11.1. The 2-sided evaluation leads to larger separability violations.

Adding a third mechanical (spectator) mode in the y-direction makes little difference to the analytical result. The overlap with the numerical simulation is significantly less good. The qualitative trough+bump shape, at $\Gamma \approx 10$ and 100 kHz respectively, remains discernible however.

10. With longer numerical simulations – or with the technique of Sec. H.9.1 – the error bars of the numerical simulations are smaller.

11

ANALYSIS OF EXPERIMENTAL DATA

We analysed experimental data from the hard-clamped membrane, the photonic crystal, and the levitated particle in coherent-scattering configuration. The analysis of the former is presented in the theses of Jason Hölscher-Obermaier [HO17, Ch. 5] and Ramon Moghadas Nia [MN17, Part V]. The analysis of the other two cavity devices is a modified version of the original procedure; the relevant details of the analysis pipeline are provided in App. H. The analysis of all three cavity devices did not yield qualitatively different results. A summary of the evaluation is provided in Sec. 11.1 below, where we highlight the relevant features and link to the considerations in App. H. In Section 11.2, we present the evaluation of the dataset used in [Mag+22] to demonstrate ponderomotive squeezing in a back-scattering levitation setup without a cavity; see also [Mag21, Chs. 4 & 5].

11.1 DATA EVALUATION PROCEDURE AND RESULTS FOR CAVITY DEVICES

The detailed study of experimental datasets from three cavity optomechanical devices remained unsuccessful in demonstrating stationary optomechanical entanglement. Data, results, and codes are available upon request. We make the following comments.

Because testing for Gaussian entanglement amounts to determining if the state is squeezed below the vacuum noise level, it is of crucial importance to characterise the latter accurately but also conservatively to avoid "false positive" entanglement detection – i.e. apparent positive detection of entanglement while the "true" state is actually separable. The logic we follow is that proposed by Jason Hölscher-Obermaier [HO17, Sec. 5.3.3] where the data are calibrated to units of vacuum fluctuation amplitudes (interchangeably called *shotnoise units* in this document) based on a measurement thereof. The goal is to express the covariance matrix of the temporal modes of the light in dimensionless units where squeezing along the (generalised) quadrature r corresponds to $\langle r^2 \rangle_{\mathrm{sym}} < 1/2$, as in the theoretical development of Parts I and II. Detailed discussion of the calibration is provided in Sec. H.6.

The optimised witness method (cf. Sec. 3.4.2 and [HE06]) is the preferred entanglement test because it detects more entangled states than the EPR-variance. Moreover, we prefer it over the logarithmic

negativity because, when the temporal modes themselves are constituted of several modes, it remains necessary and sufficient [HE06], contrary to the PPT-criterion. This is relevant for the multi-mode evaluation method; see [HO17, Sec. 5.6] for details, as well as our comments in Secs. 8.2.1 and H.4.1.

The reconstructed covariance matrices of the temporal modes are necessarily imprecise, at least due to the finite statistics of the datasets. It is then possible that the optimisation algorithm identifies statistical fluctuations as quantum correlations, leading to lower witness values than for the true state. This is a bias towards entanglement that can lead to false positive detection of entanglement. To alleviate this caveat, Jason Hölscher-Obermaier (with inputs form Sebasitan Hofer, Adrian Steffens, Ramon Moghadas Nia, Joshua Slater, Witlef Wieczorek and the present author) devised a *cross-validation* scheme that goes as follows: estimate the state once with half of the data (call it the *training* covariance matrix $\varpi_{\text{sig}}^{\text{train}}$) and compute the optimal witness $W_{\text{opt}}^{\text{cross}}$ from it; then use the second half of the data to reconstruct the state a second time, denote it $\varpi_{\text{sig}}^{\text{cross}}$, and obtain its *cross-validated optimal witness value*

$$w^{\text{cross}} := \text{Tr}\left[W_{\text{opt}}^{\text{cross}} \varpi_{\text{sig}}^{\text{cross}}\right]. \tag{11.1}$$

This method is (conservatively) biased towards separability [1] as is shown in Fig. H.1. The technique was used in the results presented in [MN17].Section H.8 various practical considerations of choosing the entanglement test, as well as the bias of the logarithmic negativity and EPR-variance.

We compute the confidence intervals on the witness values deduced from the estimated covariance matrix with the *bootstrap* statistical method [ET94]. The witness matrix $W_{\text{opt}}^{\text{cross}}$ obtained from half the data is computed once, while the bootstrap is used to repeatedly reconstruct the state $\varpi_{\text{sig}}^{\text{cross}}$ from the second half of the data (resample by drawing samples with replacement, according to the bootstrap's prescription); see Sec. H.9 for details.

A direct measurement of vacuum fluctuations (shotnoise) is necessary for the calibration outlined above. With the available shotnoise data, we can perform the following sanity check: there must be no entanglement between early–late temporal modes of vacuum noise. Moreover, the state of temporal modes of vacuum is the vacuum state again, hence saturating the separability bound; see Sec. H.6. Henceforth, we systematically compute the (cross-validated) witness values of temporal modes of shotnoise data. In practice, one typically observes that shotnoise witness values "dive" significantly below the separability threshold at large Γ, i.e. for broad filters in frequency. An

1. This is because $W_{\text{opt}}^{\text{cross}}$ is not optimal for $\varpi_{\text{sig}}^{\text{cross}}$ in general. It follows that the cross-validated witness test is no longer necessary

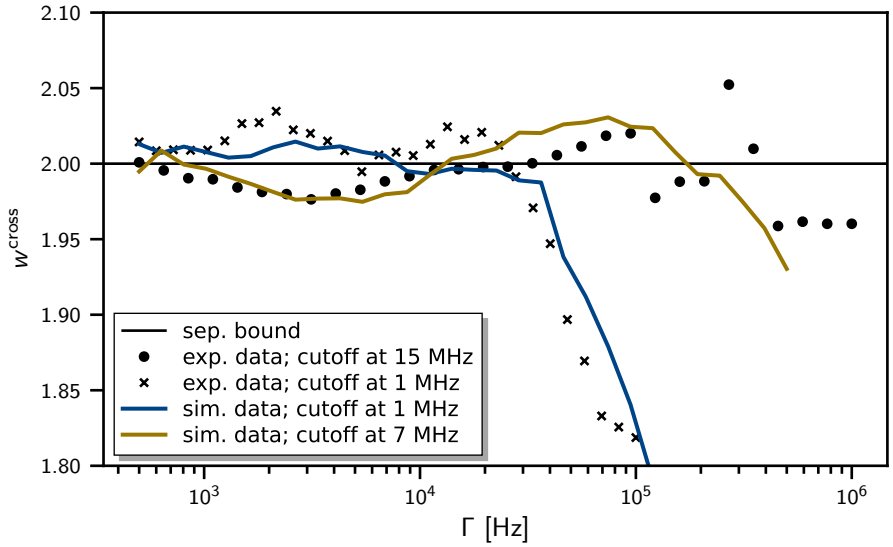

Figure 11.1 We simulated white noise and applied the same (Butterworth, forward and backward) lowpass filter as in the experimental data from the back-scattering levitated particle. The a corner frequencies applied to the simulation are 1 and 7 MHz. We then evaluate the lowpass filtered simulated white-noise and the continuous lines are the resulting witness values. At higher corner frequency the witness values "dive" at larger bandwidths Γ. In black are witness values of experimental shotnoise data with filter corner at 1 MHz (crosses) and 15 MHz (dots). The confidence intervals from the bootstrap are not shown for clarity; it is less than 0.05 above and below the dots and crosses.

example is shown by the black crosses in Fig. 11.1, which should make clear what we mean by "diving witness values". The interpretation is that the reconstructed temporal modes of vacuum encode correlations that should not be there. The possibility of this caveat highlights the difficulty of certifying quantum correlations in Gaussian states. At the level of the physical states, squeezing below vacuum noise *is* a purely quantum feature that cannot be faked (or accidentally created by some disturbance)[2]; but at the level of the amplified signal (recorded in the memory of a computer) any sort of fluctuations (be it electronic or of statistical nature, possibly introduced by the data processing) might make the state look like it is squeezed.

If no better solution is available to cope with the "diving shotnoise" witness, one practical way forward is to reconstruct states only for those filter bandwidths that do not incorporate significant correlations; that would be up to $\Gamma \approx 30$ kHz for the black crosses in Fig. 11.1.

In the case of the back-scattering levitation setup, we could relate the diving behaviour (black crosses in Fig. 11.1) to the lowpass filter at

2. I often heard (and I used to think like that too) that entanglement (or squeezing) is the quantum resource, hence it is the "hard thing" which is inimitable – i.e. it cannot be faked. Somewhat in the spirit of quantum cryptography and key distribution where the quantum nature of the state makes it "uncounterfeitable".

1 MHz that was applied in postprocessing of the data to avoid aliasing. Consulting with the experimentalists, we increased the lowpass corner frequency to 15 MHz. The corresponding shotnoise witness values are the black dots in Fig. 11.1. Although the lowpass was relatively far from the targeted mechanical mode in frequency, we see that it affects strongly the entanglement detection for filter bandwidth $\Gamma > 30$ kHz (much less than the lowpass corner frequency at a MHz). This is yet another instance of strong effects from processes spectrally far from the targeted mechanical mode. The experimental traces were additionally filtered with a highpass at about 2-3 kHz (to reduce the effect of low-frequency noises); see PSD in Fig. 11.2. The high-pass is spectrally much closer to the mechanical mode than the lowpass. Simulations do not show that this filter affects the shotnoise witness values much. My current conjecture is that there are far fewer data points at these low frequencies, hence they affect the temporal mode states estimations much less.

The same effect of high- and low- pass filtering had already been observed and identified by Jason Hölscher-Obermaier in his thesis [HO17, Sec. 5.11]. Tobias Westphal proposed to inverse the effective band-pass and effectively "flatten" the PSD. This technique has been used to analyse the hard-clamped membrane data and is documented in the thesis of Ramon Moghadas Nia [MN17, Sec. 10.4 and fig. 10.4].

We saw theoretically in Sec. 10.2 that extending the temporal mode basis to extract information from more sidebands of the detected light (the so-called *multi-mode evaluation*) is advantageous in terms of entanglement detection; multi-mode evaluation is described in detail in [HO17, Sec. 5.6] (see also our comments in Secs. 8.2.1 and H.4.1). In all four experiments we studied, the multi-mode evaluation led systematically to smaller witness values. In the next section, we will see how it affects the results of the experimental data analysis for the back-scattering levitated particle.

The apparently beneficial effect of accounting for more mechanical sidebands in the early–late state led us to try systematically many combinations (whenever possible, we tried them all) in all the experimental data we studied. In our experience, including more than 6 modes (i.e. 3 mechanical modes in 2-sided configuration) leads to instabilities of the optimised witness and its values can become very large (several hundreds or thousands) or even negative; these "wild" witness behaviours are, as far as we can tell, impossible to interpret meaningfully.

In principle, it is possible to compensate for unavoidable passive losses (i.e. inefficiency and mode mismatch) in the detection of the light. This is explained in Sec. F.3 where we derive the *inefficiency compensation formula* Eq. (11.2) below from a model of dual-rail homodyne detection, under the assumption that the losses and amplification in

both arms are the same; see also Sec. H.7. The formula relates the estimated covariance matrix of the temporal modes $\sigma^{\mathrm{tm}}_{\mathrm{sig}}$ (after darknoise correction and shotnoise calibration) to the ideal one $\sigma^{\mathrm{tm}}_{\mathrm{sig}}$

$$\sigma^{\mathrm{tm}}_{\mathrm{sig}} \approx \underline{\sigma}^{\mathrm{tm}}_{\mathrm{sig}} := \frac{1}{\eta_{\mathrm{det}}} \left[\sigma^{\mathrm{tm}}_{\mathrm{sig}} - (1-\eta_{\mathrm{det}})\, \sigma^{\mathrm{tm}}_{\mathrm{sn}} \right]. \tag{11.2}$$

Where $\sigma^{\mathrm{tm}}_{\mathrm{sn}} = \sigma_{\mathrm{vac}} = \mathbb{I}/2$ and the (total) effective detection losses $0 < \eta_{\mathrm{det}} \leqslant 1/2$ cannot exceed one-half as a consequence of measuring both quadrature simultaneously with a dual-rail homodyne detection scheme; see Sec. F.4 for a comment on heterodyne detection that has the same limitation. This formula is similar to that in [HO17, Sec. 5.3.3] and the difference is that, there, they use the estimated state of shotnoise $\sigma^{\mathrm{tm}}_{\mathrm{sho}}$ where we use the ideal matrix $\sigma^{\mathrm{tm}}_{\mathrm{sn}}$ which is diagonal; see our comments and explanations in Sec. H.7.

In our exploratory approach of the datasets, we tried a large range of variations and extensions of the data-processing. Among other things, we used half-Gaussian temporal mode profiles (partly proposed by Lorenzo Magrini) in order to restrict the filters' extension in frequency space. This did not improve the results. The most successful attempt was to use asymmetric decay rates for the temporal modes demodulating first and second mechanical modes; see Sec. H.11.

Not knowing precisely how to best perform the data analysis and optimising the analysis, there is a risk of introducing an over-fitting bias. This needs to be assessed and, if there are reason to suspect it, it must be excluded in some way. The best option is to apply the procedure (decided prior the data-processing) on a new or independent dataset. When additional datasets are not available, one can attempt to explain and cross-check the experimental results with theoretical predictions. Also, one can modify the analysis (slightly) in order to exhibit some other (theoretically) expected behaviour. The idea is to show that the wanted feature is not an artefact of the analysis.

11.2 DATA EVALUATION OF BACK-SCATTERING LEVITATED NANOPARTICLE

This section presents the results of the protocol applied to the data from [Mag+22] (back-scattering levitation). It is our latest and most mature entanglement analysis of experimental data applying all the considerations mentioned above $\sigma^{\mathrm{tm}}_{\mathrm{sn}}$; the details are described in App. H. Moreover, the comparison with the analytical and numerical simulation from Sec. 10.2 is the most informative compared to the other experimental devices.

The noise power spectra of the six time traces are displayed in Fig. 11.2. The light is measured with a heterodyne detector and quadratures are obtained with suitable extraction of the orthogonal

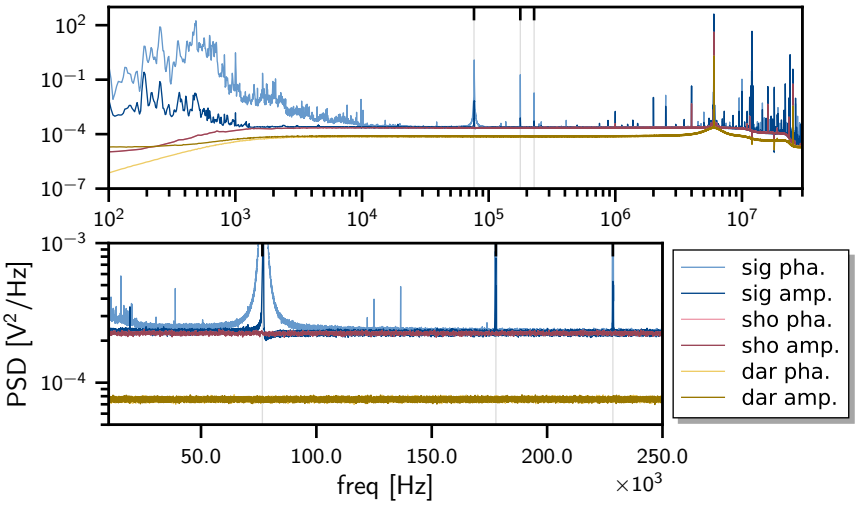

Figure 11.2 Power spectral density of 500 seconds long time traces. The target mode (z-motion) at 76 kHz is indicated by the left most tick on the top axis. The first spectator mode (x-motion) is at about 177 kHz, i.e. more then 100% apart from the target mode. Therefore, it is the low frequency (noisy) features that are spectrally closest to the target mode. The y-mode is at about 229 kHz. The dip of the signal amplitude on the right of the z-peak (visible in the lower panel) is ponderomotive squeezing of the light [Mag+22].

sine and cosine components via a Hilbert transform; see [WM09, Ch. 4], [Hof15, App. B.1.1], [LP95], and our comments on heterodyne detection in App. F.4. Therefore, the noise floor of both quadratures is the same by construction. The shotnoise level is slightly below that of the signal time traces in Fig. 11.2 (lower panel), hence it can be used as unit calibration reference, as explained in Sec. H.6.

The witness plots for different evaluation configurations are summarised in Fig. 11.3. Unfortunately, none of them shows entanglement. The top left configuration (1-mode 1-sided evaluation) is the worst and hardly comparable to the analytical and numerical simulations results of the previous Section 10.2.[3] The top right and bottom left panels show witness curves with a "trough" between 10 and 20 kHz and a "bump" just below 100 kHz, similarly for the 2-mode 1&2-sided evaluations of Fig. 10.10. The "trough+bump" shape is analogous to the simulated results (albeit shifted towards larger witness values), which we interpret as a strong sign that model and data processing capture some of the relevant physics in the experimental data.

As mentioned in the previous section, using asymmetric bandwidths for the temporal filters demodulating the first two modes lead to improved results. With a suitable optimisation we obtained a witness

3. A similar behaviour can be reproduced with the analytical simulation by setting the 3rd mechanical mode at several hundreds of hertz with relatively large effective heating rate $\Gamma_{\mathrm{th},3}$. This simulates heuristically the low frequency noises in the spectrum Fig. 11.2.

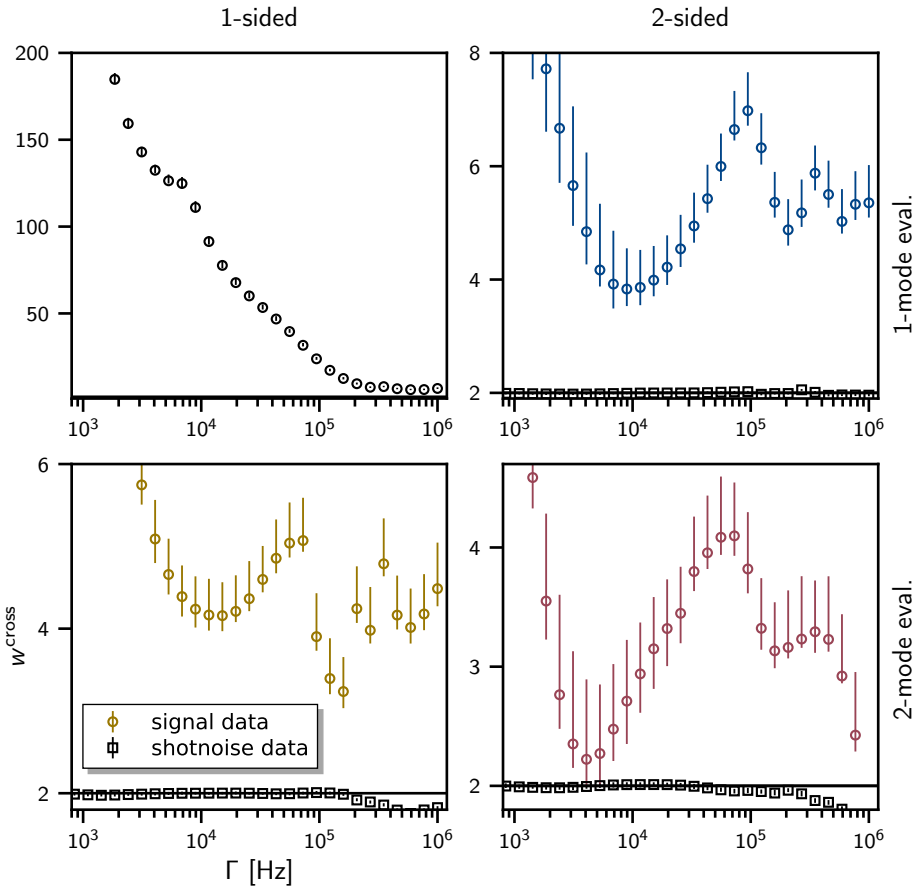

Figure 11.3 Cross-validated witnesses of 1&2-mode 1&2-sided evaluations (rows and columns resp.) of experimental data. The separability bound is at 2 with entangled states below it. All plots have different y-axis but they have the same x-axis. The black squares are the witnesses of the shotnoise data (not shown on the top right figure for clarity). The amplitude of the trough+bump behaviour here cannot be compared directly with the simulations in Figs. 10.9 and 10.10, because the latter are not compensated for inefficiencies.

curve showing entanglement; see Fig. H.4 and the details in Sec. H.11. But, as we explain in Sec. H.11, the optimisation led to unexpectedly specialised and sensitive analysis settings; especially, changing them in relatively small amount or attempting to retrieve some other (theoretically) expected behaviour, yielded no detectable entanglement. Therefore we could not exclude that the optimisation introduced a bias towards the wanted result (i.e. a form of over-fitting).

12

CONCLUSION

Our protocol for certifying stationary promising entanglement was designed to be applicable to a wide range of currently existing devices and for minimal experimental effort [Gut+20]. Practically, this is reflected by the four different experimental datasets that we were given the opportunity to study. None revealed entanglement, but the experience gathered in the analyses led to a number of additional insights on how entanglement is detected with this protocol.

Firstly, the theoretical model was extended to incorporate several mechanical modes in order to describe the physics of real devices more accurately. The comparison between analytical and numerical simulations in Sec. 10.2, and their close similarity to the experimental results, strongly indicates the success of this approach. Although the analytical calculations in Ch. 9 are for EPR-variance, the derived sufficient condition for entanglement detection applied well to necessary and sufficient entanglement tests in the examples we studied. This contrasts with the single-mechanical-mode scenario, where necessary and sufficient tests seemingly always detect entanglement.

Specifically, we found that the necessary condition Eq. (9.35) and the sufficient condition (in the presence of a spectator mode) Eqs. (9.50) form an interval of possible bandwidths Γ for the early–late temporal modes

$$\gamma_1 n_1(C_1+1) < \Gamma < \frac{g_1}{g_2}\frac{\Delta\omega}{3\sqrt{3\,n_2(C_2+1)}}. \tag{12.1}$$

This expression emphasises the role of the occupation numbers of the mechanical baths and makes their detrimental roles explicit; especially in the (challenging) high temperature limit $n_j \gg 1$ we considered.

Strictly speaking, our spectator mode model applies to harmonic mechanical modes interacting with the light via radiation pressure. I conjecture that it is also an indicator for the detrimental effect on entanglement detection from other processes with spectral features in the detected temporal modes of light: e.g. low-frequency noise or filters applied on the data.

In Section 9.4.4, we saw that the demodulation frequency of the temporal modes must be chosen with great accuracy:[1] the discrepancy $\delta\omega = \bar{\omega} - \omega_1$ must be no larger than $\sim \Gamma/\sqrt{n_1}$ Eq. (E.22). The scaling with the bath temperature is severe and, in the (relevant) regime $\Gamma <$

1. Equivalently, the mechanical frequency must stable during the measurement run.

ω_1, this corresponds to a precision at least of $\frac{\delta\omega}{\omega_1} < \frac{1}{\sqrt{n_1}}$. Combined with the upper bound of the sufficient condition for entanglement in Eq. (12.1) above, one obtains the stringent bound

$$\delta\omega < \frac{g_1}{g_2}\frac{\Delta\omega}{3\sqrt{3\,n_2 n_1(C_2+1)}}. \tag{12.2}$$

In all five parameter regimes studied, the presence of a spectator mode prevented entanglement detection; see Secs. 10.2, 10.1, and App. G. However, this is only a partial explanation because the data analysis can account for multiple mechanical modes, which is not described by the model presented in this thesis. In all four experimental datasets we analysed, the multi-mode evaluation performed better in the sense that it systematically led to lower witness values; cf. Ch. 11. [2]

The experience we gained in applying the protocol to analyse various datasets led to an update of the original postprocessing procedure proposed by Jason Hölscher-Obermaier in [HO17, Ch. 5]. The main differences are: the use of a cross-validated witness method [3] to mitigate bias of the entanglement test (cf. Secs. 11.1 and H.8); confidence intervals estimated with the bootstrap method [4] (cf. Sec. H.9); conservative units calibration (cf. Sec. H.6); and a modified compensation of passive losses (cf. Secs. 11.1 and H.7). Mainly, these modifications aim to mitigate the possibility for false positive entanglement detection – and thus increase confidence/trust of a successful attempt.

We highlight that the difficulty in certifying Gaussian entanglement is false-positive detection due to postprocessing steps meant to improve the visibility of the correlations. It is a matter of confidence/trust in the final result and our conservative choices are one way of establishing trust. [5] We encountered the risk of false positive detection from over-specialising the analysis procedure by rounds of optimisations on a particular dataset and possibly introducing a bias towards the wanted result; see Sec. H.11.

12.1 HOW TO MAKE IT WORK

The refined analysis of the levitated particle in back-scattering configuration showed very promising results, with the reserve that it might have been an artefact due to over-fitting. Applying the ana-

2. With Klemens Winkler's exact analytical model for cavityless levitation systems, we confirmed that the multi-mode analysis indeed yields larger violation of the separability bound (and larger logarithmic negativities); cf. Sec. 10.2. This is in contrast to passive losses that can decrease the witness values of a separable state.

3. Used in Ramon Moghadas Nia in [MN17, Part V].

4. Used in Ramon Moghadas Nia in [MN17, Part V].

5. Sebastian Hofer often suggested that it would be more informative to devise an adequate statistical estimate of the confidence intervals that accounts for calibration and inefficiency compensation and quantifies the trustworthiness of results.

lysis procedure that led to Fig. H.4 to a new dataset, with similar mechanical frequency stability, can settle the question.

The insights on how to choose the parameters, provided by the theoretical derivations, set two and a half constraints: they are the necessary and sufficient boundaries in Eq. (12.1) above, and the half constraint is the single mechanical mode sufficient condition $\Gamma \lesssim \frac{\omega_1}{\sqrt[3]{Q_1}}$ Eqs. (9.46) (it is only half a constraint, because necessary and sufficient entanglement tests are not subject to it, as far as we can tell). [6]

Equation (12.1) makes explicit that lower temperatures of the mechanical baths efficiently broaden the range of Γ that lead to entanglement detection. Moreover, it relaxes the constraint on $\delta\omega$, and possibly increase the separably violation associated to larger cooperativity (cf. Sec. 9.4.1). Increasing the mechanical frequency of the target mode has the same effect. Note that the derivations in this work hold in the large thermal occupation regime Eq. (8.2), hence one must interpret "reduction of the temperature" in the sense that n_1, n_2 remain large (compared to 1).

One might insist on operating at the temperatures and mechanical frequencies treated here. Then, the requirements for entanglement detection are requirements of more control on the processes contributing to the detected signal, in the spectral vicinity of the sidebands of the target mode. For example, mechanical modes can be engineered spectrally farther apart; or the design leads to genuinely single-mode structures (like drum-head capacitors [Teu+11; Kot+21]); or the devices allow parameter tuning such that the spectator coupling g_2 is strongly attenuated (like levitated systems in coherent-scattering configuration [Del19; GB+19]).

It is not excluded that different choices than those we motivated in Sec. 8 lead to better protocols. For instance, for optimised separation $T_{sep} = \pi/(2\omega_1)$ between the temporal modes, the (single-mode) sufficient condition Eqs. (9.46) becomes significantly less stringent (cf. Sec. 9.4.3). Red detuned driving enabled entanglement detection with Δ_{EPR} in certain cases (cf. Sec. 10.1 and App. G). The multi-mode evaluations with more complex filtering temporal modes systematically improved the results. Asymmetric decay rates for different demodulations led to a potentially decisive enhancement as well. A systematic study and/or optimisation [7] of the temporal profiles is an interesting theoretical aspect that can help the identification of the quantum correlations in the output light. In addition, it remains intriguing that, in

6. It is worth pointing out that entangled states not detected by Δ_{EPR} typically require short temporal filters unlikely to work out in practice due the spectral features not included in the model. Moreover, entangled states detected by the EPR-variance are robust against passive losses [Bar+11].

7. Preliminary expression of the mathematical problem as a quadratic optimisation problem with semi-definite constraints was formulated [Gut+20, App. B.2], but no interesting result were found yet.

the larger coherent coupling regime (large cooperativity), the violation of the separability bound is limited to half its range; cf. Sec. 9.4.1.

One might also consider alternative approaches. While our protocol is (fairly) agnostic of the details of the optomechanical device (cf. Ch. 8), some experimental setups nowadays are very well characterised, to the point that an accurate state-space model and conditional knowledge of the state (e.g. with a Kalman filter) can be used to estimate the mechanical state accurately [HH15; Wie+15; Ros+19; Mag+21]. With such a technology, one can afford not to use the entanglement verification theorem and test directly whether the joint optomechanical state (estimated with the Kalman filter) is entangled. The best temporal mode of light after interaction was derived in [MDC10]; see also [Mia+10b; Mia+10a]. This method also suffers from trust issues because the bi-partite state is reconstructed from measurements of a single party – the light. An option is to use the data in a sequential fashion, as we propose with the early–late temporal partition: first, use light measurement data from $t = 0$ to T to define the light mode (which interacted with the mechanics; see the time ordering logic from [MDC10; Dir+24]), and then use data from T to $T + T_{sep} < 1/\Gamma_1^{tot}$ Eq. (9.47a) (assuming that this is enough) to estimate the mechanical state at $T + T_{sep}$. Alternatively, the state of the oscillator at time T can be "retrodicted" without (theoretical) constraints on the amount of data [Lam18; LH24; Ros+19]. This defines the joint state of the (early) temporal mode of light and the (conditional) mechanical state. Sampling long enough allows to estimate the state (covariance matrix) of the unconditional stationary optomechanical state, which can be tested for entanglement. [8]

12.2 OUTLOOK

Inspired by exquisite sensors such as LIGO, Virgo, KAGRA and GEO600, one naturally wonders how the concepts presented in this thesis apply as the mass of the mechanical oscillator increases to truly macroscopic [9] scales. LIGO and Virgo operate now with squeezed light [Yu+20; Aba+11; BHS19; Tse+19; Ace+19] and their description in quantum terms is relevant. Consequently, entanglement between the heavy mirrors and the light probing their positions must be encoded in the measured information. The (quantum) position sensor paradigm is how we introduced and motivated the search for optomechanical

8. In that case, the entanglement verification theorem is not necessary to conclude. But the accuracy of the state-space model and the reconstructed mechanical state must be demonstrated [Wie+15; Mag+21].

9. The interferometer with four suspended mirrors is equivalent to a single rubber-cavity optomechanical device, as in Fig. 1.2, with an effective mechanical degree of freedom weighing $\approx 40/4 = 10$ kg; this is the so-called "scaling law" derived for LIGO in [BC03].

entanglement in Sec. 1.4. Our entanglement verification theorem applies in exactly the same way in these cases. However, the open system optomechanical model from Sec. 5.4, at the basis of our study, is not accurate to describe a gravitational wave detector; typically because several of the noises affecting the suspension mode are non-Markovian and we did not model squeezed driving light.

In a recent collaboration with Su Direkci and Yanbei Chen from Caltech, we studied entanglement in stationary optomechanical systems subject to Gaussian non-Markovian noises [Dir+24], building on and generalising the work from [MDC10]. That work focused on massive low-frequency oscillators that are typically affected by correlated noises. With the mathematical and numerical tools developed, we could ask whether the mechanical oscillator and the measured light of a LIGO-like device are entangled (theoretically). The numerical evaluation with parameters close to LIGO's was too demanding for our computational resources (the computer must distinguish deviations of order one or less between terms of order 10^{20}). But for seismic noise 12 orders of magnitude less than measured, we found that the optomechanical state is separable. Because we do not expect that it becomes entangled at higher levels of noise, we consider this a strong evidence that Advanced LIGO's optomechanical state was separable. Our model did not include the current (frequency dependent) squeezed input, for which it has been claimed that the massive mechanical state shares "quantum correlations" with the light field [Yu+20]. Our result is a first indication that these quantum correlations might not be entanglement.

The questions around macroscopic quantum correlations in extremely precise (quantum) position sensors sparked a lot of thrilling discussions among us – mainly because of their close connection to this work on stationary optomechanical entanglement. We wondered if one can formulate a quantitative relationship between (precise) measurements and entanglement? Klemens Winkler was able to formulate an answer to this question that will be presented elsewhere.

Another outstanding aspect, in my opinion, is the question of what exactly would be entangled in a sensor like LIGO? On the one hand, the mechanical oscillator in gravitational wave interferometers is the effective result of the seismic noise isolation technique by (multi-stage) suspension. The associated quantum mode (i.e. the single bosonic system) defined by the resonance frequency (about 1 Hz in LIGO) is strongly driven by seismic forces (and correspondingly damped actively, so that its effective quality factor is relatively low). In the end, it is the motion at frequencies between 40 Hz and 10 kHz that is unprecedentedly quiet – but not the (bosonic) swinging once per second. On the other hand, the technique in [Dir+24; MDC10] provides the explicit temporal shape of the (unique) light mode which is entangled with the mechanical oscillator. Such a temporal profile for LIGO-like para-

meters is shown in fig. 9 of [Dir+24]. It is well fitted by an exponential decaying hull at rate $\Gamma \approx 25$ Hz for a demodulation at frequency $\bar{\omega} \approx 40$ Hz – just like the early temporal mode of our analysis and the functional form originally obtained in [MDC10]. The corresponding Lorentzian is not centred on the mechanical sideband, but it is at the lower boundary of the quiet region of the noise spectrum (compatible with the findings in [MDC10, cf. p. 4] in the analogous free-mass limit). To my understanding, this hints at the fact that modelling the mechanical degree of freedom as a single-frequency mode might not be suited in that case. In the free-mass limit, where the mechanical oscillation at ω_m is the second slowest process (after energy dissipation so that the Q remains high), the mechanical state is described by an (almost) freely propagating wave packet. In that picture, it corresponds to excitations of a mechanical field, with time (or frequency) as labels for different modes of that field – like electromagnetic radiation. I owe this picture to Yanbei Chen and Roman Schnabel. Then one can ask which temporal modes of the mechanical field (i.e. which superposition of modes at different times) are entangled with the temporal mode of the light after interaction. The covariance matrix of that state is infinite (while it was "only half infinite" when treating the mechanical part at a single specific time $t = 0$ in [Dir+24; MDC10]). This brings up several complications, the most important being the lack of an easily computable necessary and sufficient entanglement test. In addition to trying with the usual tests (like Δ_{EPR} or the PPT-criterion), one could fix the light mode to be the one found when the mechanical mode was treated as a single mode (as in [Dir+24, fig. 9]). In that case, the situation is again a bi-partite Gaussian configuration with one single-mode party for which the PPT-criterion is necessary and sufficient. For numerical approaches with truncated temporal modes, one can use the witness optimisation procedure (cf. Sec. 3.4.2 and [HE06]) to test for entanglement, but probably not to discover which modes are entangled.

Lastly, Klemens Hammerer once proposed to me the picture of stationary optomechanical entanglement as a spatial region in front of the mechanical oscillator (or pointing out of the cavity). This reflects the fact that, in the stationary regime, entanglement between the oscillator and the travelling light is continuously generated while the mechanical state continuously decoheres. Therefore, the entangled region is the path of the travelling light as long as it is entangled with the mechanics; and it stops probably once the light has travelled a distance $\sim c/\Gamma^{th}$ corresponding to the mechanical decoherence time. Varying the shape, duration, the separation T_{sep}, etc. of our temporal modes construction, one can imagine mapping the features of this entanglement region in front of the oscillator. With control over the light in that region, one can further speculate the possibility to actuate, prepare, and steer the mechanical (quantum) state.

APPENDIX

A

A ZOO OF STATES

In this appendix, we summarize the properties of several harmonic oscillator states relevant to this thesis: the ground state, Fock states, coherent states, squeezed states, thermal states, and two-mode squeezed states. Our objectives are twofold. Firstly, we introduce and provide context for several standard mathematical tools and concepts used in the main text, such as the displacement operator and the thermal distribution of bosonic excitations. Secondly, we discuss the properties of these states to differentiate between quantum and classical characteristics of a system or process. Loosely speaking, we argue that the thermal states are a quantum model (or approximation) for typical classical states, the coherent states are classical-almost-quantum states, squeezed states are quantum-almost-classical, and the Fock states (of at least one quanta) are typical quantum states. While the terminology and classifications used here are non-standard, I find them helpful for our analysis.

A.1 VACUUM OR GROUND STATE

The vacuum state, also interchangeably referred to as the ground state, was introduced in our study of the quantum harmonic oscillator in Sec. 2.5. It is the eigenstate of the number operator $a^\dagger a$ with the lowest eigenvalue 0, and is denoted $|0\rangle$. This state is at the bottom of the excitation ladder so that $a|0\rangle = 0$, defining the state of absolute minimal energy of a harmonic mode – corresponding to the absence of harmonic excitation quanta. The minimal energy of a harmonic oscillator is not zero but half an excitation $E_0 = \hbar\omega/2$ a consequence of the fundamentally non-zero commutation relation between operators Eq. (2.20). It is an element of the Fock basis of the Hilbert space of states of harmonic oscillators hence it is a pure state.

The ground state is prepared by removing energy (i.e. cooling) until it is not possible any more. Practically, the remaining motion of an unexcited oscillator is due to thermal fluctuations and the vacuum state is a thermal state at temperature exactly 0, as we will see when discussing thermal states in Sec. A.6. The frequency of the oscillator determines how it is affected by its environment's temperature. High frequency oscillators can be prepared in their ground state by thermalisation with an environment cold enough: for example a photonic crystal at GHz frequency is close to its ground state in a dillusiton refrigerator at several tens of mK as in [Rie+16], or THz vibrational

modes of molecules at room temperature are also mostly in their ground state [Roe+16], and similarly for the "free" electromagnetic fields at optical frequencies (several hundreds of THz) in a room at 300K. Oscillators at lower frequencies must be cooled with some mechanism, for instance passively with a cavity [Teu+11] or by means of measurements and feedback [Mag+21].

Preparing the ground state of a harmonic oscillator is an important milestone in controlling the motion of massive objects. Because it is a pure state, preparing such a state is the typical starting point of many schemes involving genuinely quantum features [RI+11; RI11]. In this sense, the ground state of motion is a step towards the quantum regime of mechanical systems.

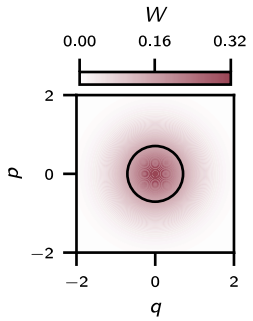

Fig. A.1 Wigner function of the ground state $|0\rangle$. Radii of ellipse indicate the normal distribution's std.

In Sec. 2.5, we saw that the modulus squared of the wavefunction of dimensionless quadratures of a harmonic mode (massive mechanical oscillator or light) is a normal probability distribution $\mathcal{N}(0, 1/2)$. The std $1/2$ is the uncertainty of the state in both quadratures and it saturates Heisenberg uncertainty relation. In phase space (cf. Ch. 3) the Wigner function representation Eq. (3.3) of the vacuum state is a bi-variate normal distribution

$$\begin{aligned} W(\mathbf{r}) &= (\pi\hbar)^{-1} \, \mathrm{e}^{-(x^2+p^2)/2} \\ &= \frac{\mathrm{e}^{-\mathbf{r}^\mathsf{T}\sigma^{-1}\mathbf{r}/2}}{2\pi\hbar\sqrt{\det|\sigma|}} \\ &\sim \mathcal{N}(0, \sigma) \end{aligned} \tag{A.1}$$

where $\mathbf{r}^\mathsf{T} = (x, p)$ is the 2-vector of (dimensionless) quadrature coordinates in phase space and

$$\sigma = \mathbb{I}_2/2 =: \sigma_{\mathrm{vac}} \tag{A.2}$$

is the 2-by-2 *covariance matrix*, with $\mathbb{I}_2$ the identity matrix. This means that $|0\rangle$ is a Gaussian state (cf. Sec. 3.2). In Fig. A.1 we plotted the Wigner function of a vacuum state in phase space.

A.2 FOCK STATES

Fock states, sometimes referred to as number states, are the eigenstates $|n\rangle$ of the number operator $a^\dagger a$ and are characterised by eigenvalues $n \in \mathbb{N}$. Notably, the vacuum state described in the previous section is a specific Fock state with eigenvalue zero. The Fock states with $n > 0$ are systematically constructed from the vacuum by successive application of the creation operator [CTDL05; Gri17]. These

states are pure and form an orthonormal basis of the Hilbert space called *Fock space*, $\forall n, m \in \mathbb{N}$

$$\langle n|m\rangle = \delta_{nm} \tag{A.3}$$

$$\sum_n |n\rangle\langle n| = \mathbb{I}. \tag{A.4}$$

The Fock states are the energy eigenstates of a quantum harmonic oscillator with spectrum $E_n = (n + 1/2)\hbar\omega$, cf. Sec. 2.5. Hence, the Hilbert space of the harmonic oscillator states is a Fock space. Their explicit wavefunctions is essentially Hermit polynomials, see for example [CTDL05, Ch. V.C] for a thorough presentation.

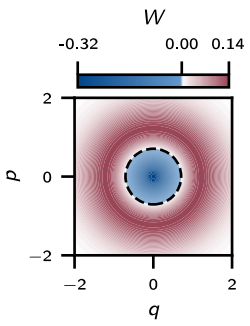

Fig. A.2 Wigner function of $|1\rangle$. The dashed circle is the transition to positive values and it is the same as the std of the ground state (black line circle in Fig. A.1)

In practice, Fock states are typically challenging to prepare. Single excitations $|1\rangle$ of an electromagnetic mode or a mechanical mode have already been prepared, as for example in [Mar+18] to violate a Bell-inequality with the state of two mechanical oscillators.

The Wigner function Eq. (3.3) of the Fock states can be expressed in terms of Laguerre polynomials [Sch01, Ch. 4] – i.e. it is not Gaussian. We plotted that of one quantum $|1\rangle$ in Fig. A.2. An interesting characteristic of Fock states $|n > 0\rangle$ is that their Wigner functions take on negative values, marking them as genuinely quantum and classifying them as non-classical. This property is pivotal to our discussions on Gaussian dynamics and maps in Sec. 3.3.

A.3 COHERENT STATES

The coherent states $|\alpha\rangle$ are the eigenstates of the annihilation operator a with eigenvalue α [GZ00]:

$$a\,|\alpha\rangle = \alpha\,|\alpha\rangle\,. \tag{A.5}$$

Because the annihilation operator is not Hermitian, α can be a complex scalar.

In practice they are, for instance, the state of the light produced by a laser. They also correspond to those states of a harmonic oscillator that remain unaffected by the (unitary) harmonic dynamics: i.e. an oscillator starting in a state $|\alpha(t = 0)\rangle$ remains a coherent state $|\alpha(t)\rangle$. Coherent states of mechanical motion are significantly more challenging to achieve because of their coupling to some thermal environment [Wol+22]. An operational way to produce a coherent state of motion is to first prepare the ground state by cooling and then displace the centre-of-mass in the harmonic, making sure not to disturb the mechanical state too much. For instance, this could be conveniently done in a levitated setup where one would displace the centre of the trapping tweezer forming the harmonic trap.

As just mentioned, a coherent state is a *displaced vacuum* state. Mathematically, one defines the unitary *displacement operator*

$$\mathcal{D}(\alpha) \coloneqq e^{\alpha a^\dagger - \alpha^* a} \tag{A.6}$$

with $\alpha \in \mathbb{C}$ and apply it to the ground state

$$|\alpha\rangle \coloneqq \mathcal{D}(\alpha)\,|0\rangle\,. \tag{A.7}$$

Here, the ground state is displaced by α. In particular, $\alpha = 0$ is a valid choice of displacement and the (undisplaced) vacuum is a coherent state as well. Coherent states are pure states. They are Gaussian too because the displacement unitary is a symplectic transformation (with linear Hermitian generator, see Sec. 3.3).

To make sense of the "displacement" terminology, it is useful to picture the state in phase space. One finds that the first and second moments in terms of (dimensionless) quadrature coordinates are [1]

$$\langle q\rangle = \sqrt{2}\mathrm{Re}[\alpha]\,; \quad \mathrm{var}[q] = 1/2 \tag{A.8a}$$

$$\langle p\rangle = \sqrt{2}\mathrm{Im}[\alpha]\,; \quad \mathrm{var}[p] = 1/2. \tag{A.8b}$$

Compare to the moments of the Wigner function of the vacuum $|0\rangle$ in Eq. (A.1), we see that the second moments are unchanged and only the first moments were shifted – a displaced indeed – by α: in a phase space, the real part of α is the abscissa and the imaginary part is the ordinate. The bi-variate normal Wigner function of a coherent state is depicted in Fig. A.3.

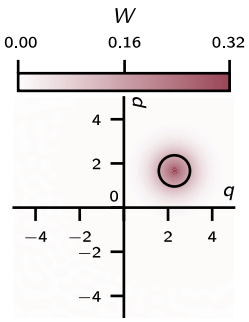

Fig. A.3 Wigner function of coherent $|\alpha\rangle$, where $\alpha = 2\,e^{i\,\pi/5}$ is the displacement; see also Fig. 3.1. Radii of ellipse indicate the normal distribution's std; they are the same as for the vacuum state in Fig. A.1, but the axes here are different.

Coherent states and vacuum state have the same covariances, therefore the same uncertainty properties, which are of fundamental quantum nature. They both saturate Heisenberg uncertainty in a symmetric fashion, hence coherent states are probes whoes accuracy is limited by quantum noise. I find it rather fascinating that this is the case of laser light at room temperature that is (to a very good approximation) in an almost pure coherent state. This particular property of optical light makes it a measurement probe of choice.

As discussed in Chapter 4, the "quantum features" (like entanglement) of Gaussian states are entirely encoded in the states' second moments. Therefore, displacements are deemed irrelevant, in particular in our study of entanglement. However, displacements play an important role in the background of our model because they allow to focus only on the states' covariances and not on the first moments; this is in essence the role of the *displaced frame* introduced in Sec. 5.3 where we assume tacit knowledge of the evolution of the first moments, allowing to displace the frame so that all the quadratures' means are zero at all times. All the derivations in this thesis are carried out within this frame. See [Hof15; AKM14; GB+19] for explicit details.

1. Using that $\langle q\rangle \coloneqq \langle\alpha|\,a + a^\dagger\,|\alpha\rangle\,/\sqrt{2} = (\alpha + \alpha^*)/\sqrt{2}$.

The decomposition of a coherent state in the Fock basis is

$$|\alpha\rangle = e^{-|\alpha|^2/2} \sum_{n=0}^{\infty} \frac{\alpha^n}{\sqrt{n!}} |n\rangle . \tag{A.9}$$

This means that coherent states are a superposition of different energies with an associated uncertainty (in energy) of genuine quantum nature. The vacuum, on the other hand, is an eigenstate of energy, but both have the same uncertainty in their measurable quadratures, as we noted above. The probability distribution of Fock state – of energies – is Poissonian

$$p(n) = |\langle n|\alpha\rangle|^2 = e^{-|\alpha|^2} \frac{|\alpha|^2 n}{n!} \tag{A.10}$$

with equal mean and variance $|\alpha|^2$. Physically, the mean Fock number relates to the mean energy of the state so that the intensity of a coherent state of light is proportional to $|\alpha|^2$ – in dimensionless units, this corresponds to the average number of photons in the state. Contrary to the Fock states, the ensembles of all coherent states $\{|\alpha\rangle \ : \ \alpha \in \mathbb{C}\}$ are not a basis of the Hilbert space [GZ00]: they do span it hence they resolve the identity

$$\int_{\mathbb{C}} d^2\alpha \, |\alpha\rangle\langle\alpha| = \pi \mathbb{1}. \tag{A.11}$$

but their ensemble is over-complete so that they cannot be orthonormal

$$\langle\alpha|\beta\rangle = \exp\left(-\frac{|\alpha|^2 + |\beta|^2 - 2\alpha^* \beta)}{2} \right). \tag{A.12}$$

A.4 SQUEEZED STATES

They are the generalised pure Gaussian states. Their distinguishing feature is that they saturate Heisenberg uncertainty bound *asymmetrically*, hence being less uncertain than the coherent states of Sec. A.3 along a particular observable, linear combination of quadratures. See Fig. A.4 for a representation of the Wigner function of such a squeezed state. It has an elliptical shape with its main axis rotated compared to the quadratures' axes; the direction of the smallest radius of the ellipse is the *squeezing axis*. Because it is a pure state, the indefiniteness of the state is of quantum nature – i.e. it corresponds to quantum fluctuations. An observable along the squeezed axis thus has improved (quantum) uncertainty. In this sense, squeezed states are considered genuine quantum states [Frö+18; WM06]. Along the *anti-squeezed* axis the uncertainty is larger as prescribed by Heisenberg uncertainty bound Eq. (2.9). We stress that the squeezing feature is the reduction

of uncertainty (or inherent noise upon measurements) below the reference set by the vacuum or the coherent states. This is different from *squashing* (this is jargon), where the (classical/technical) indefiniteness of the state in both quadratures is asymmetric, but not below the reference variance set by the vacuum state; we discuss squashed state along with thermal states below in Sec. A.6.

Squeezed states of light are more challenging to produce than coherent states. Commonly, they are generated via *down-conversion* of a pump laser that has the effect of converting single photons at the frequency of the pump, into two photons at half the frequency of the pump, in a coherent way [Sch17]. This phenomenon happens as second order (non-linear) effects in the transmission/susceptibility of certain crystals for instance. This is in principle the same mechanism as for producing pairs of single photons in spontaneous down-conversion (SPDC) sources; see [Kwi+95] for example. As mentioned in the introduction, squeezed light (with squeezing depending on frequency) is currently used in the LIGO/VIGRO gravitational-wave detectors to improve their sensitivity [Yu+20; Aba+11; BHS19; Tse+19; Ace+19]. To my knowledge, squeezing of massive mechanical oscillators is still an open challenge actively pursued in the optomechanical community.

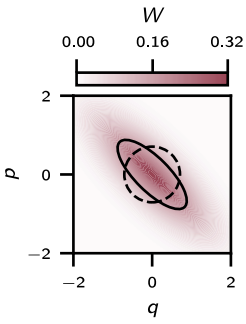

Fig. A.4 Wigner function of squeezed vacuum state $|\xi\rangle$, where $\xi = 0.5\,e^{i\,\pi/2}$ is the squeezing parameter; see also Fig. 3.1. The solid ellipse indicates the std of the squeezed state and the dashed one is that of the vacuum for comparison.

Define the *squeezing operator*

$$S(\xi) \coloneqq e^{\frac{\xi^*}{2}a^2 - \frac{\xi}{2}a^{\dagger 2}} \tag{A.13}$$

where $\xi = re^{i\,\theta}$, $r \geqslant 0$, is called the *squeezing parameter* [AI07; CS85; SC85]. In full generality, a squeezed state can be displaced [cf. Eq. (A.6)] and it is obtained from the vacuum as [GZ00; VW94]

$$|\alpha, \xi\rangle \coloneqq D(\alpha)S(\xi)\,|0\rangle\,. \tag{A.14}$$

Because both the squeezing and the displacement operators are at most second order in the operators, they preserve the Gaussian character of the ground state so that $|\alpha, \xi\rangle$ is a Gaussian state, see Sections 3.3. Let us first inspect the effect of the squeezing alone: it leaves the first moment unchanged [2] and the second moments become (for a squeezing angle $\theta = 0$)

$$\sigma_{sq}(\xi = r) = \frac{1}{2}\begin{pmatrix} e^{-2r} & 0 \\ 0 & e^{2r} \end{pmatrix}. \tag{A.15}$$

2. This is not trivial to show, afaict. One way is to apply the squeezing to the ladder operators and find that $S^\dagger(\xi)aS(\xi) = a\cosh(r) + a^\dagger \sinh(r)\,e^{i\,\theta}$ (typically applying Baker–Campbell–Hausdorff formula) and similarly, the squeezed creation operators is a linear combination of a and itself, see for example [BL05, Sec. II.E] or [Tru85; SC85]. This implies that any linear combination of the quadratures will be a linear combination of ladder operators whose expectation value for the ground state remains zero – this is not case for another state in general.

Combined with the displacements $\boldsymbol{\alpha} = (\mathrm{Re}[\alpha], \mathrm{Im}[\alpha])^{\mathsf{T}}$, one deduces that the Wigner function representation of a (single-mode) squeezed state is a bi-variate Gaussian

$$W \sim \mathcal{N}(\sqrt{2}\boldsymbol{\alpha}, \sigma_{\mathrm{sq}}(\xi)) \tag{A.16}$$

where for a complex ξ, $\sigma_{\mathrm{sq}}(\xi)$ is any covariance matrix that saturates Heisenberg bound on covariance matrices Eq. (3.9).

For completeness, we provide the (undisplaced) squeezed states expressed in the Fock basis [3] [Wee+12]

$$|r\rangle = S(r)\,|0\rangle = \cosh^{-1/2}(r) \sum_{n=0}^{\infty} \frac{\tanh^n(r)}{2^n} \frac{\sqrt{(2n)!}}{n!}\,|2n\rangle\,. \tag{A.17}$$

As the coherent state Eq. (A.9), this is a superposition of energy number states, but the quanta come in doublets – this is the essence of the quantum correlations between both quadratures that manifest as squeezing. Note that the squeezing operation manifestly "pumped" energy into the state because the vacuum state was unpopulated while the population of this squeezed state is $\langle r|\, a^\dagger a\,|r\rangle = \sinh^2(r)$.

A.5 TWO-MODE SQUEEZED STATES

When two (or more) harmonic modes are considered, the physics of squeezing becomes richer; in particular certain states are entangled. Consider a composite system with two modes, labelled 1 and 2, and with their joint states in the tensor product Hilbert space $\mathcal{H}_1 \otimes \mathcal{H}_2$. The ladder operators of each mode are a_j and $a_j^\dagger$, $j = 1, 2$. Then, the *two-mode squeezing* operator is [AI07]

$$S_{12}(\xi) \coloneqq e^{\xi^* a_1 a_2 - \xi a_1^\dagger a_2^\dagger} \tag{A.18}$$

with $\xi \in \mathbb{C}$. It is a generalisation of the single-mode squeezer Eq. (A.13) above. It squeezes both modes together simultaneously and should be distinguished from the *two squeezed-modes* operation

$$S_1(\xi_1) \otimes S_2(\xi_2) = \Pi_{j=1,2} \exp\left(\xi_j^* a_j^2 - \xi_j a_j^{\dagger 2}\right) \tag{A.19}$$

that squeezes both modes independently. A general *two-mode squeezed state* is given by the operation of S_{12} on the vacuum, followed by arbitrary displacements [cf. Eq. (A.6)] of both modes: we write

$$|\mathrm{TMS}\rangle \equiv |\alpha_1, \alpha_2, \xi\rangle \coloneqq D(\alpha_1) D(\alpha_2) S_{12}(\xi)\,|0\rangle \tag{A.20}$$

3. First, express the squeezing operator $S(\xi)$ from Eq. (A.13) in a normally ordered product of operators, or find it in the literature [SC85; Tru85]; then apply it to the vacuum state.

where $|0\rangle \equiv |0\rangle_1 \otimes |0\rangle_2$ is the joint ground state of the composite system, and we omitted the tensor product between the displacement operators.

Similarly to the considerations made for the (single-mode) squeezed state in Sec. A.4 above, $|\mathrm{TMS}\rangle$ is Gaussian and the operation S_{12} alone leaves the state's four first moments unchanged. The second moments of both systems become correlated. This is made explicit by the non-zero terms in the non-diagonal blocks of the covariance matrix (here for a real squeezing parameter $\xi = r \geqslant 0$) [AI07]

$$\sigma_{\mathrm{TMS}}(r) = \frac{1}{2}\begin{pmatrix} \cosh(2r) & 0 & -\sinh(2r) & 0 \\ 0 & \cosh(2r) & 0 & \sinh(2r) \\ -\sinh(2r) & 0 & \cosh(2r) & 0 \\ 0 & \sinh(2r) & 0 & \cosh(2r) \end{pmatrix} \tag{A.21}$$

where the quadrature coordinates are arranged like $\mathbf{r} = (q_1, p_1, q_2, p_2)^{\mathsf{T}}$. While the two-mode squeezed states are special because they are entangled (as we will see), there are other separable Gaussian states that share correlations among their modes and have non-zero non-diagonal blocks.

The associated Wigner function takes values in $\mathbb{R}^4$ and it is a four-variate normal distribution

$$W \sim \mathcal{N}(\sqrt{2}(\boldsymbol{\alpha}_1, \boldsymbol{\alpha}_2), \sigma_{\mathrm{TMS}}(\xi)). \tag{A.22}$$

In Fig. A.5 we plotted a cut of the Wigner function along the plane $(q_1 + q_2, p_1 - p_2)/\sqrt{2}$. Interestingly, the spread of the distribution – that relates to the uncertainty of the state – is below that of the vacuum state in all directions of that plane. This is a manifestation of a "strong" correlation between the modes. One can pictorially deduce that it is entanglement with the EPR-variance entanglement test Eq. (3.13) stating that the sum of the variances along the vertical and horizontal axes must be less than that for the vacuum state for entanglement.

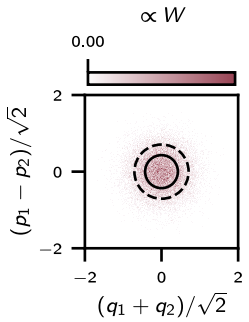

Fig. A.5 Two-dimensional histogram sampled from bi-variate normal distribution with covariances σ_{TMS} Eq. (A.21) with $r = 1$; shown here is a slice in the EPR-basis. In black continuous ellipse is the std of the distribution in that slice and the dashed ellipse is the std from a sampling of the corresponding 2-mode vacuum.

Two-mode squeezed states are entangled in general [AI07]. The necessary and sufficient logarithmic negativity (introduced in Sec. 3.4.4) applied to $\sigma_{\mathrm{TMS}}(r)$ gives r, so that the state is entangled for any $r > 0$ and it does not change under local symplectic transformations. [4] Therefore, as far as I can tell, squeezing along the linearly independent combinations of quadratures is the nature of Gaussian entanglement: *Gaussian entanglement is two-mode squeezing*. Gaussian entanglement is at the core of the work presented in this document because we attempt to demonstrate that it describes the state of a mechanical oscillator and the light measuring it in optomechanical devices.

4. Note that, in the bi-partite entanglement configuration, if both parties have more than one mode, then the logarithmic negativity is not necessary and sufficient any more [AI07].

To better grasp the kind of quantum correlation encoded in a two-mode squeezed state, we express it in the Fock basis [5] [Wee+12] (here undisplaced and with real squeezing parameter $\xi = r > 0$)

$$|\mathrm{TMS}\rangle \equiv |0,0,r\rangle = \cosh^{-1/2}(r) \sum_{n=0}^{\infty} (-\tanh(r))^n |n,n\rangle . \tag{A.23}$$

This state always has the same number of excitations in both modes: i.e. if one observes m excitations in one of the modes, then, with certainty, the other mode will be in a state of m excitations. The distribution of the excitations observed in the first place remains indefinite in the sense that it is a quantum superposition of number states; but once the energy of a mode has been measured no uncertainty remains regarding the energy state of the second mode – this is the typical symptom of the "action at a distance" enabled by entanglement. In fact, in the limit where r is small, the sum can be truncated after its first term and one obtains the (unnormalised) state of an SPDC source of entangled photon pairs [GAC10].

A.6 THERMAL STATES

It is useful to introduce the state of a harmonic oscillator mode that has some "temperature". In (classical) thermodynamics, temperature is (or relates to) a Bose-Einstein distribution of energies, where higher temperatures correspond to larger energies and broader distributions. In practice, an unprepared oscillator in contact with an unknown environment is in a thermal state. This is because one makes minimal assumptions about the environment and assumes it is itself in a thermal state at macroscopic/thermodynamical temperature T and the oscillator thermalised with it.

Quantum mechanically, we encode the Bose-Einstein distribution of energies in the (non-fundamental) indeterminacy of the state – reproducing the effects of uncontrollable and unknowable fluctuations of thermal origin. We write

$$\rho_{\mathrm{th}} \coloneqq \sum_{n}^{\infty} p_n |n\rangle\langle n| \tag{A.24}$$

where the (Bose-Einstein) probabilities are [6]

$$p_n \coloneqq \frac{e^{-E_n\beta}}{Z} = \frac{1-e^{-\beta\hbar\omega}}{e^{-\beta\hbar\omega/2}} e^{-(n+1/2)\hbar\omega\beta} \tag{A.25}$$

5. As in the single-mode squeezing case, use a normally ordered expression of $S_{12}(\xi)$ (given explicitly in [SC85] for instance) and apply it to the vacuum state.

6. We used the spectrum of a quantum harmonic oscillator $E_n = \hbar\omega(n+1/2)$ Eq. (2.21) and Z is the partition function of the harmonic Hamiltonian H_{HO} Eq. (2.20), $Z \coloneqq \mathrm{Tr}\left[e^{-\beta H_{\mathrm{HO}}}\right] = \frac{e^{-\beta\hbar\omega/2}}{1-e^{-\beta\hbar\omega}}$.

$\beta \coloneqq (k_B T)^{-1}$, with k_B Boltzmann's constant and T the state's temperature.

The mean energy of a thermal state is $E_{th} = \langle H_{HO} \rangle = \hbar\omega(n_{th} + 1/2)$, where n_{th} is the mean number of excitations in the state (or mean occupation number of the mode)[7]

$$\begin{aligned} n_{th} \coloneqq \langle n \rangle &= \mathrm{Tr}\left[a^\dagger a \rho_{th}\right] \\ &= \sum_n^\infty p_n n \\ &= \frac{1}{e^{\hbar\omega\beta} - 1}. \end{aligned} \tag{A.26}$$

It relates directly to the temperature β and one often speaks of n_{th} as the "temperature" of ρ_{th}. In the high temperature limit where $\beta^{-1} = k_B T \gg \hbar\omega$ then Eq. (A.26) is well approximated by

$$n_{th} \approx \frac{k_B T}{\hbar\omega} \gg 1. \tag{A.27}$$

In that limit, $E_{th} \approx k_B T + \hbar\omega/2 \approx k_B T$ which is the result of the equi-partition theorem from (classical) statistical physics. In the low temperature limit, $n_{th} \to 0$ and the mean energy tends to the ground state energy of the oscillatory mode $E_{th} \to E_0 = \hbar\omega/2$. Also, in the limit $T \to 0$, the thermal state becomes the (pure) vacuum state $|0\rangle\langle 0|$.

As discussed in Sec. A.1, the vacuum state is the state of lowest energy and it is prepared by cooling the mode initially in a thermal state at finite temperature into the ground state at ideally zero temperature $T \to 0$. In practice, one never reaches absolute zero and $n_{th} > 0$ and experimental realisations of a ground state of mechanical motion are characterised by $n_{th} < 1$ [Del+20b; Mag+21] – some have occupations much closer from 0 than 1 as in [Mee+15; Rie+16] for instance. Consider an oscillator at relatively high frequency, say ω is in the GHz regime. Then use Eq. (A.27) to get quickly an estimate of the temperatures at which it will be in its ground state: one finds $n_{th} < 1$ when $T < 0.1$K. These are temperatures accessible in dilution refrigerators, hence, a GHz oscillator can be prepared in its ground state by thermalising it with the cold finger of a dilution refrigerator, as in [Mee+15; Rie+16]. Similarly, for a mode of light at optical frequencies, i.e. some hundreds of THz, we find that it is populated by the black-body radiation of objects at room temperature (≈ 300K) to about $n_{th} \approx 0.1$ photons. Hence, the modes of the electromagnetic field in a laboratory – everywhere around an experiment – are almost the vacuum state. This is a point we will use in our model of the bath for the cavity mode in our model of an optomechanical device in Ch. 5.

7. Use that $\sum_{n=0}^\infty n r^n = r \sum_{n=0}^\infty \frac{d}{dr} r^n = r \frac{d}{dr}(1-r)^{-1} = r(1-r)^{-2}$ for $|r| < 1$.

Thermal states are Gaussian[8] [ARL14]. The first moment of its dimensionless quadrature q is

$$\langle q \rangle = \mathrm{Tr}\left[\sum_n (a + a^\dagger) p_n/\sqrt{2}\, |n\rangle\langle n|\right] = 0. \tag{A.28}$$

Similarly, one finds that the expectation values of p and of the ladder operators are zero as well. The second moment of q is

$$\langle q^2 \rangle = \frac{1}{2}\sum_n p_n \left(2\mathrm{Tr}\left[a^\dagger a\, |n\rangle\langle n|\right] + 1\right) = n_{\mathrm{th}} + \frac{1}{2} \tag{A.29}$$

where we used the definition of the average occupation number n_{th} Eq. (A.26) in the last step. The variance of p is the same. The Wigner function of a thermal state is thus a bi-variate normal distribution

$$W \sim \mathcal{N}(0, \sigma_{\mathrm{th}}) \tag{A.30}$$

with a covariance matrix $\sigma_{\mathrm{th}} \coloneqq (n_{\mathrm{th}} + 1/2)\mathbb{I} = (2n_{\mathrm{th}} + 1)\sigma_{\mathrm{vac}}$. Figure A.6 shows a thermal state in phase space. In terms of a fluctuating process, it means that a thermal oscillator moves randomly around its equilibrium position (the origin of phase space is also the minimum of the harmonic potential). The amplitude of the random motion is scaled by the (co)-variances that relate to the state's temperature via the mean excitation number n_{th} Eq. (A.26).

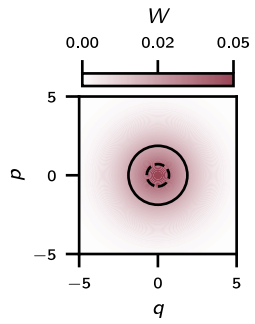

Fig. A.6 Wigner function of thermal state $|n_{\mathrm{th}}\rangle$. The solid ellipse is for the std of the thermal state and the dashed one is the std of the vacuum for comparison.

In full generality, a thermal state could be displaced and squeezed as $\rho_{\mathrm{Gauss}} = D(\alpha)S(\xi)\rho_{\mathrm{th}}S(\xi)^\dagger D(\alpha)^\dagger$, which defines the most general Gaussian state. Placed in a harmonic potential, the displacement would lead to the thermal state rotating around phase space like a harmonic oscillator and corresponds to a quantum model of a classical oscillator. Because thermal states do not saturate Heisenberg uncertainty bound, squeezing will not necessarily lead to uncertainty below that of a coherent state; to distinguish the cases where the squeezing leads to a quantum feature of the state (in the sense discussed in Sec. A.4) one speaks of *squashed* states when their uncertainty is not below that of a coherent state along any direction in phase space.

8. I know of no efficient way to prove it and would resort to compute its Wigner function Eq. (3.3) (or its characteristic function [ARL14]) and show that it is Gaussian.

B

BELL LOCAL-REALISM AND GAUSSIAN ENTANGLEMENT

Let us start with four statements:

1. All pure entangled states are non-local-realistic, i.e. they can be used to violate a Bell inequality [Gis91]. In particular, pure two-mode squeezed states discussed in this work are non-local.
2. Gaussian entangled states (e.g. two-mode squeezed states) and measurements of their quadratures (or linear combinations thereof) cannot violate a Bell inequality; see for example [PJR09].
3. Non-locality and entanglement are different resources [Bru+14].
4. There exist entangled mixed states that cannot violate a Bell inequality [Wer89].

They are all true but they leave a certain tension if left uncommented; specifically, the tension is due to point 2. We mentioned point 4. for completeness and to clarify that, in the remaining of this chapter, we focus on pure states (although the whole discussion holds for mixed states as well). Point 3. is certainly the most general resolution of the tension but it left me unsatisfied, which is why I wrote this appendix. In the end, we will see that 2. restricts the measurements, while 1. doesn't. The lesson I learned here is that, from the perspective of an operator, the description of a quantum system requires the specification of its state *and* the measurements by which it can be known.

First, I found it helpful to refresh Bell's theorem, e.g. from [Bru+14, Sec. 1]. Local-realism constraints joint probability distributions of measurement outcomes: let $p(a, b|x, y)$ be the joint probability of bounded outcomes a and b, given the measurement settings x and y. Then, a local-realist theory (or a hidden variable theory) states that there must exist past factors, summarised in a variable λ, such that

$$p(a, b|x, y, \lambda) = p(a|x, \lambda)p(b|y, \lambda). \tag{B.1}$$

In general, $p(a, b|x, y)$ is not equal to $p(a|x)p(b|y)$ because there can be correlations between the systems being measured. But in local-realistic models, it is always possible to find out the origin of these correlations and encode it in the variable λ. Then, given the knowledge of λ, the probability factorises as if the measurements were independent. Physically, the factorisability Eq. (B.1) is the expression that distant objects, possibly sharing a correlation, do not influence measurement results on each object separately. Lastly, λ might be imperfectly known

and described by a probability distribution $u(\lambda)$. Equation (B.1) is thus re-expressed as

$$p(a,b|x,y) = \int d\lambda\, p(a|x,\lambda)p(b|y,\lambda)u(\lambda) \tag{B.2}$$

and is a consequence of local-realistic assumptions [1] on joint probability distributions of measurements [Bel04; Bru+14]. It follows that correlators of an observables A_x and B_y are of the form

$$\begin{aligned}\langle A_x B_y\rangle &= \int da\, db\, ab\, p(a,b|x,y) \\ &= \int da\, db\, d\lambda\, a\, p(a|x,\lambda)\, b\, p(b|y,\lambda)u(\lambda).\end{aligned} \tag{B.3}$$

a and b denote particular measurement outcome of A_x and B_y, respectively. The indices x and y label the observables.

As explained in [BW98; PEW05], separated measurements of observables X and/or Y on both parts of the system [2] can be expressed as the Wigner representation (cf. Sec. 3.1) of the operators: the probability distribution measured on the first party is given by the Wigner representation Eq. (3.3) of the observable being measured, call it $W_x(q1,p1)$, with $x = X, Y$. For the second party, we have $W_y(q2,p2)$, with $y = X, Y$. In the Wigner representation of phase space, the expectation value of some operator K, given a state ρ, is Eq. (3.6)

$$\langle K\rangle = \int dq\, dp\, W_K(q,p)W_\rho(q,p) \tag{B.4}$$

where W_ρ is the state's Wigner function Eq. (3.3). For the correlators entering a Bell inequality

$$\begin{aligned}\langle Y\otimes X\rangle = \int dq_1\, dp_1\, dq_2\, dp_1\, W_Y(q_1,p_1)W_X(q_2,p_2) \\ \times W_\rho(q_1,p_1,q_2,p_2)\end{aligned} \tag{B.5}$$

which relates to Eq. (B.3) with the measurement settings being $x = Y$ and $y = X$. If W_ρ is a bona fide probability distribution, it can be identified with $u(\lambda)$ – so that the phase space coordinates q_j, p_j, $j = 1,2$ are the hidden variables. If $W_Y(q_1,p_1)$ can be identified with $\int da\, a\, p(a|x,\lambda)$ (similarly with $W_X(q_2,p_2)$) then Eq. (B.5) is an expectation value of a local hidden-variable model (the model being provided by the Wigner representation). In that case, Bell's theorem guaranties that it will satisfy Bell inequalities.

1. Reality is assumed to be (i) independent of observation, (ii) interactions and information is local and propagate from adjacent systems to the next (at most at the speed of light), and (iii) true randomness exists [Bru+14; Bel04].

2. Formally, $x, y = X, Y$ are labels, such that when $x = X = y$ then $A_x = A_X = B_y = B_X = X$ are the observables; and similarly for $x = Y = y$.

There are thus two ways in which Eq. (B.5) is not equivalent to Eq. (B.3) so that Bell's theorem does not apply (and a Bell inequality can be violated): first, if the state's Wigner function is negative (which is the case for any pure non-Gaussian states [Hud74]); second, if the Wigner function of the observables cannot be written as $\int d\alpha\, a\, p(a|x,\lambda)$, with the values of a bounded. I will not try to specify the latter further because I haven't understood it well enough yet; but see [BW98] and [PEW05] where they give (bounded) dichotomic observables, which Wigner representations are unbounded, and show that states with positive Wigner functions can violate a Bell inequality with these observables. [3]

Let us now get a little more concrete and consider continuous variables states of position and momentum of two objects, as we did in Chs. 2 and 3. The observables are the objects' quadratures position Q and momentum P, corresponding to the settings $x, y = Q, P$. Their Wigner representations are $W_Q(q,p) = q$ and $W_P(q,p) = p$, where the rhs are real number variable entering Eq. (B.5) or Eq. (3.6); cf. Sec. 3.1. Choose $p(a|x,\lambda = (q,p)) = q$ so that $\int_{-1}^{1} da\, a p(a|x,\lambda) = q = W_Q(q,p)$ (and similarly for W_P). Assume that the bi-partite (joint) state of the objects is a two-mode-squeezed state ρ_{TMS} with Gaussian Wigner function W_{TMS} (see Sec. A.5). Then any correlators of Q and P measured locally on both parties are of the form Eq. (B.5) and no Bell inequality can be violated.

An analogue argument is to acknowledge that Gaussian measurements (general-dyne) have Gaussian Wigner representation [GLS16], hence W_X and W_Y Eq. (B.5) are (bounded) normal distributions, they form a local hidden variable model, and non-local-realism cannot be demonstrated.

A final historical note, in [Bel04, Ch. 21] J. Bell demonstrated that the original (not normalisable infinitely squeezed) EPR-state, would not violate a Bell test if one measured the sign of the position operator [BW98] – which is a special case of our discussion of the two-mode squeezed state with Gaussian measurements. In [BW98] and [PEW05] they propose non-Gaussian continuous-variable measurements that would allow to violate a Bell inequality with Gaussian entangled states. I think it is quite fun!

3. Interestingly, the examples in both references obtain Dirac-delta-like Wigner representations of the observables, which are, in principle, bona fide probability distributions. The point that voids Bell theorem is the unbounded nature for the Dirac-delta.

C

SOLUTION OF CAVITY OPTOMECHANICAL DYNAMICS IN FOURIER SPACE

Start from the model and notations of Sec. 5.4. The QLE in matrix form are Eq. (5.19)

$$\dot{\mathbf{r}}(t) = M\mathbf{r}(t) + N\mathbf{n}(t) \tag{C.1}$$

with state vector

$$\begin{aligned}\mathbf{r} &\coloneqq (x, y, q_1, p_1, q_2, p_2)^T \\ &= (x, y, q_j, p_j)^T\end{aligned} \tag{C.2}$$

and input vector of noises

$$\mathbf{n} \coloneqq (x_{in}, y_{in}, 0, \xi_j)^T. \tag{C.3}$$

C.1 QUADRATURE AND LADDER REPRESENTATIONS CHANGE

The QLE above are given in terms of quadrature operators, but they could equally well be presented in terms of ladder operators – or any mixture of both. We introduce the 2-vector $\mathbf{r}^q = (q, p)^T$, where the superscript q indicates that it is a vector of quadratures – i.e. a state vector in the quadrature representation. Analogously, we define the 2-vector $\mathbf{r}^l = (a, a^\dagger)^T$ in the ladder representation. They are related via a linear transformation [cf. Eqs. (2.18)]

$$\mathbf{r}^l = R\mathbf{r}^q, \quad \text{where } R = \frac{1}{\sqrt{2}}\begin{pmatrix} 1 & i \\ 1 & -i \end{pmatrix}. \tag{C.4}$$

Note that R is unitary $R^{-1} = R^\dagger$. We generalise the transformation R to apply on n modes: $R_n \coloneqq R^{\oplus n}$. We obtain the QLE from Eq. (C.1), in terms of ladder operators as

$$\begin{aligned}\dot{\mathbf{r}}^l &= R_3\dot{\mathbf{r}}^q \\ &= R_3 M^q R_3^{-1} R_3 \mathbf{r}^q + R_3 N^q R_3^{-1} R_3 \mathbf{n}^q \\ &= M^l \mathbf{r}^l + N^l \mathbf{n}^l.\end{aligned} \tag{C.5}$$

The system matrix became $M = M^q \to R_3 M^q R_3^{-1} = M^l$ and for the input matrix $N = N^q \to R_3 N^q R_3^{-1} = N^l$; they are given explicitly, in ladder representation, in Eqs. (C.13) and (C.14), respectively. Similarly the input vector became

$$\mathbf{n}^l = (c_{in}, c_{in}^\dagger, i\,\xi_j/\sqrt{2}, -i\,\xi_j/\sqrt{2})^T. \tag{C.6}$$

(Notice how each entry is non-Hermitian and how the even entries are the adjoint of the odd entry before.)

Because the QLE have the same form in both representations, we will not indicate the superscripts l and q in the following and make sure the context makes clear which representation is used – or if the choice or representation is irrelevant because the presented relations are valid in either.

C.2 SOLVING THE QLE IN FOURIER SPACE

The QLE in time are ODE with formal solution [Gen+08]

$$\mathbf{r}(t) = e^{Mt}\mathbf{r}(t_0) + \int_{t_0}^{t} dt' e^{Ms}\mathbf{n}(t-t'). \tag{C.7}$$

It has a stable steady-state when the eigenvalues of the system matrix M all have negative real parts. The explicit mathematical expression of this criterion in terms of system parameters can be found in [Gen+08, eqs. (10), Sec. II.A] or [Hof15]. When the drive is resonant with the cavity $\Delta = 0$ (which is the relevant regime for our study), the dynamics are stable without conditions on the other parameters.

In the steady-state, we can Fourier transform the QLE and cast them into a linear system of equations that can be inverted. We set our convention for the Fourier transform, Eqs. (C.8) below, and how it behaves with respect to Hermitian conjugation. For a function or operator $g(t)$, we define its Fourier transform as

$$\mathcal{F}[g(t)]_\omega \coloneqq \int_{-\infty}^{\infty} \frac{dt}{\sqrt{2\pi}} e^{i\omega t} g(t) = g(\omega) \tag{C.8a}$$

$$\mathcal{F}^{-1}[g(\omega)]_t \coloneqq \int_{-\infty}^{\infty} \frac{dt}{\sqrt{2\pi}} e^{-i\omega t} g(\omega) = g(t). \tag{C.8b}$$

We mark Fourier transformed functions by their argument t or ω; when we omit the argument, the context will tell in which space the function is meant. The convention for the Hermitian conjugation $\square^\dagger$ of a Fourier transformed operator $g(\omega)$ is

$$g^\dagger(\omega) \coloneqq g(\omega)^\dagger = \mathcal{F}[g(t)]^\dagger_\omega = \mathcal{F}[g^\dagger(t)]_{-\omega}. \tag{C.8c}$$

This choice over the other one $g^\dagger(\omega) = \mathcal{F}[g^\dagger(t)]_\omega$ is arbitrary but it is important to stick to it strictly. Independently of the conventions, Hermitian operators in real space are not Hermitian in frequency space: for instance, position q is such that $q(\omega)^\dagger = \mathcal{F}[q^\dagger(t)]_{-\omega} = q(-\omega)$. This can lead to pitfalls when working with non-Hermitian operators in real space: indeed, the Fourier transformed state vector of quadrature is (rather intuitive)

$$\mathbf{r}^q(\omega) = \mathcal{F}[\mathbf{r}^q(t)]_\omega = \Big(x(\omega), y(\omega), q_j(\omega), p_j(\omega)\Big)^T \tag{C.8d}$$

but in the ladder operator representation we get

$$\mathbf{r}^{\mathrm{l}}(\omega) = \mathcal{F}[\mathbf{r}^{\mathrm{l}}(t)]_{\omega} = \left(c(\omega), c^{\dagger}(-\omega), b_j(\omega), b_j^{\dagger}(-\omega)\right)^{\mathsf{T}} \tag{C.8e}$$

with a rather non-intuitive sign change. Hence, our convention Eq. (C.8c) implies [1] a change of sign in the creation operators – and we see Eq. (C.8e) as part of the Fourier transformation convention Eqs. (C.8). Similarly, we obtain the input (noise) vector (in the ladder representation) in frequency space

$$\mathbf{n}(\omega) = \left(c_{\mathrm{in}}(\omega), c_{\mathrm{in}}^{\dagger}(-\omega), i\,\xi_j(\omega)/\sqrt{2}, -i\,\xi_j^{\dagger}(-\omega)/\sqrt{2}\right)^{\mathsf{T}}. \tag{C.8f}$$

(Observe how the thermal noise operator ξ is not Hermitian any more in frequency space.)

We find that the Fourier transformed QLE in matrix form

$$\mathcal{F}[\dot{\mathbf{r}}]_{\omega} = -i\,\omega\mathbb{I}\mathbf{r}(\omega) = M\mathbf{r}(\omega) + N\mathbf{n}(\omega) \tag{C.9}$$

assuming that the state vector vanishes at high frequencies. The explicit solution in Fourier space is then

$$\mathbf{r}(\omega) = -(M + i\,\omega\mathbb{I})^{-1}N\mathbf{n}(\omega). \tag{C.10}$$

This result holds in both representations with a suitable transformation of the matrices (cf. App. C.1) and using the sign convention for the transformed operators in ladder representation, cf. Eqs. (C.8).

C.3 OUTPUT OPERATORS

The input–output relations were presented in Sec. 4.3. They have the same form for both quadrature and ladder operators, and in time and frequency spaces. From Eqs. (4.12) we get

$$\mathbf{r}_{\mathrm{out}} = N_{\mathrm{out}}\mathbf{r} + N_{\mathrm{fdtr}}\mathbf{n}. \tag{C.11}$$

The output matrix N_{out} and thefeed-through matrix N_{fdtr} depend on the choice of representation, like the system- and input- matrices M and N above. The output 4-vector $\mathbf{r}_{\mathrm{out}}$ encodes the state of the output electromagnetic field propagating away from the cavity and the excitation of the mechanical substrate "propagating away" from the mechanical oscillator. Only the first two entries of $\mathbf{r}_{\mathrm{out}}$ are accessible (measurable) and we call them $\mathbf{r}_{\mathrm{c,out}}$. Output- and feedthrough- matrices are thus 2-by-6 rectangular matrices given Eqs. (C.16) and (C.17). The light field output operators solution of our model are

$$\mathbf{r}_{\mathrm{out}}(\omega) = \left[(-1)N_{\mathrm{out}}(M + i\,\omega\mathbb{I})^{-1}N_{\mathrm{in}} + N_{\mathrm{fdtr}}\right]\mathbf{n}(\omega). \tag{C.12}$$

1. Strictly speaking, it is not obligatory to do it this way and one could decide that all the operators in $\mathbf{r}(\omega)$ have the same argument. This would require dealing with each term individually when performing the Fourier transformation (according to our convention for the Hermitian conjugation) and changing between ladder and quadrature representations. The advantage here is that we can keep the compact matrix notation all the way.

C.4 STATE-SPACE MODEL IN LADDER OPERATOR REPRESENTATION

The system and input matrices of the state space model Eqs. (5.14) [Eq. (5.19) in matrix form] for two mechanical modes, in the ladder operator representation, are given by

$$\mathrm{M}^{\mathrm{l}} = \mathrm{i}\begin{pmatrix} \Delta\begin{pmatrix}1 & 0\\ 0 & -1\end{pmatrix} & g_1\begin{pmatrix}-1 & -1\\ 1 & 1\end{pmatrix} & g_2\begin{pmatrix}-1 & -1\\ 1 & 1\end{pmatrix} \\ g_1\begin{pmatrix}-1 & -1\\ 1 & 1\end{pmatrix} & \omega_1\begin{pmatrix}-1 & 0\\ 0 & 1\end{pmatrix} & \mathbb{O}_2 \\ g_2\begin{pmatrix}-1 & -1\\ 1 & 1\end{pmatrix} & \mathbb{O}_2 & \omega_2\begin{pmatrix}-1 & 0\\ 0 & 1\end{pmatrix} \quad \mathbb{O}_2 \end{pmatrix} - \frac{1}{2}\begin{pmatrix} \kappa\mathbb{I}_2 & \mathbb{O}_2 & \mathbb{O}_2 \\ \mathbb{O}_2 & \gamma_1\begin{pmatrix}1 & -1\\ -1 & 1\end{pmatrix} & \mathbb{O}_2 \\ \mathbb{O}_2 & \mathbb{O}_2 & \gamma_2\begin{pmatrix}1 & -1\\ -1 & 1\end{pmatrix} \end{pmatrix} \tag{C.13}$$

$$\mathrm{N}^{\mathrm{l}} = \begin{pmatrix} \sqrt{\kappa}\mathbb{I}_2 & \mathbb{O}_2 & \mathbb{O}_2 \\ \mathbb{O}_2 & \sqrt{\frac{\gamma_1}{2}}\begin{pmatrix}1 & -1\\ -1 & 1\end{pmatrix} & \mathbb{O}_2 \\ \mathbb{O}_2 & \mathbb{O}_2 & \sqrt{\frac{\gamma_2}{2}}\begin{pmatrix}1 & -1\\ -1 & 1\end{pmatrix} \end{pmatrix} \tag{C.14}$$

where $\mathbb{O}_2$ is the 2-by-2 null matrix and $\mathbb{I}_2$ is the 2-by-2 identity matrix. The corresponding input vector in the quadrature representation is [cf. Eq. (C.6)]

$$\begin{aligned}\mathbf{n}^{\mathrm{l}} &= (x_{\mathrm{in}}, y_{\mathrm{in}}, 0, \xi_1, 0, \xi_2)^{\mathsf{T}} R_3^{\mathsf{T}} \\ &= (c_{\mathrm{in}}, c_{\mathrm{in}}^{\dagger}, \mathrm{i}\,\xi_1, -\mathrm{i}\,\xi_1, \mathrm{i}\,\xi_2, -\mathrm{i}\,\xi_2)^{\mathsf{T}}.\end{aligned} \tag{C.15}$$

The expression of the cavity output field is given by the input–output relations Eq. (C.11) with the 2-by-6 output and feedthrough matrices

$$\mathrm{N}^{\mathrm{l}}_{\mathrm{out}} \coloneqq \begin{pmatrix}\sqrt{\kappa}\mathbb{I}_2 & \mathbb{O}_2 & \mathbb{O}_2\end{pmatrix} \tag{C.16}$$

$$\mathrm{N}^{\mathrm{l}}_{\mathrm{fdtr}} \coloneqq \begin{pmatrix}\mathbb{I}_2 & \mathbb{O}_2 & \mathbb{O}_2\end{pmatrix}. \tag{C.17}$$

The 6-by-6 noises correlation matrix, in time, in the ladder operator representation, is [cf. Eqs. (5.15) and (5.18)]

$$\begin{aligned}\left\langle \mathbf{n}^{\mathrm{l}}(t)\mathbf{n}^{\mathrm{l}}(t')^{\mathsf{T}}\right\rangle_{\mathrm{sym}} &= \left\langle \begin{pmatrix} c_{\mathrm{in}}(t)c_{\mathrm{in}}(t') & c_{\mathrm{in}}(t)c_{\mathrm{in}}^{\dagger}(t') \\ c_{\mathrm{in}}^{\dagger}(t)c_{\mathrm{in}} & c_{\mathrm{in}}^{\dagger}(t)c_{\mathrm{in}}^{\dagger}(t') \end{pmatrix} \right. \\ &\qquad \left. \bigoplus_{j=1}^{2} \frac{\xi_j(t)\xi_j(t')}{2} \begin{pmatrix} -1 & 1 \\ 1 & -1 \end{pmatrix} \right\rangle_{\mathrm{sym}} \\ &\approx \frac{1}{2}\left[\left(\begin{smallmatrix} 0 & 1 \\ 1 & 0 \end{smallmatrix}\right) \bigoplus_{j=1}^{2} n_j \left(\begin{smallmatrix} -1 & 1 \\ 1 & -1 \end{smallmatrix}\right) \right] \delta(t-t') \\ &=: D^{\mathrm{l}}\,\delta(t-t') \end{aligned} \tag{C.18}$$

where the approximation refers to the high temperature limit Eq. (5.17). The Fourier transform of this model gives

$$\begin{aligned} D^{\mathrm{l}}(\omega,\omega') &:= \left\langle \mathbf{n}^{\mathrm{l}}(\omega)\mathbf{n}^{\mathrm{l}}(\omega')^{\mathsf{T}}\right\rangle_{\mathrm{sym}} \\ &= \int \frac{dt\,dt'}{2\pi} e^{i\,\omega t + i\,\omega' t'} \left\langle \mathbf{n}^{\mathrm{l}}(t)\mathbf{n}^{\mathrm{l}}(t')^{\mathsf{T}}\right\rangle_{\mathrm{sym}} \\ &= D^{\mathrm{l}}\,\delta(\omega+\omega'). \end{aligned} \tag{C.19}$$

D

EXACT INTEGRATIONS

First, we show that the integrals we are concerned with in Sec. 9.1.1, Eq. (9.11), do converge. The denominator is a polynomial: the denominators of the mode functions is of order 1 [cf. Eqs. (8.10a)] and they always come as a product of two mode functions in the integrand; the functions C, R, and I from Eqs. (9.13) all have the same denominator product of $\left|\chi_{\text{opt}}\right|^2$ Eq. (5.23e) and $\left|\chi_j\right|^2$ Eq. (5.23d) which is of order $2+4=6$. The denominator of the function X is of order 12. From standard real analysis, we know that the usual Riemann-Stiljes integral over the real line of a (non-singular) polynomial function converges if the polynomial order of the function is < -1 [Mar19]. The numerators in C, R, I, and X are of order < 5, hence the integrals converge. Multiplying the numerators by a bounded function does not change the convergence, hence the oscillatory $e^{-i\,\omega\,T_{\text{sep}}}$ from the mode functions in the EL and LE sectors of σ^{tm} does not prevent convergence.

The term S, Eqs. (9.13a), in σ^{out} is a constant and its integration converges for our choice of mode functions, because the overall polynomial order is -2. This means that the mode functions must be of order $-1/2$ at most. In the absence of the mode functions the integral of this term would diverge. This is a remnant of the (unphysical) white-noise model for the vacuum noise of the electromagnetic bath of the cavity that has infinite energy if one assumes all frequencies on the real line are physical.

D.1 INTEGRATION FORMULA FOR $T_{\text{sep}} = 0$

When $T_{\text{sep}} = 0$, the integral of Eq. (9.11) is of a form that bears an explicit symbolic solution given by a formula [GZ15, entry 3.11.2 in 8th edition]. The derivation of this formula relies on residue integration [Jam47, sec. 7.9].

The usage of the formula is as follows. Consider the integral

$$I = \int_{-\infty}^{\infty} d\omega \, \frac{g(\omega)}{d(\omega)d(-\omega)} \tag{D.1}$$

where $g(\omega)$ and $d(\omega)$ are polynomials in ω so that the global order of the integrand is strictly less than -1, and the roots of $d(\omega)$ all have strictly positive complex parts. In that case, there is a known explicit formula providing the symbolic expression of the integral. We do not reproduce this formula here and refer the reader to standard tables of

integrals like [GZ15, entry 3.11.2 in 8th edition][1], or to [Hof15, app. B.5]. We implemented the formula in [Gut24, Theoretical predictions derivation .nb][2] based on a codes by Sebastian Hofer and Klemens Winkler.

We show that the integrand $F^{tm}(-\omega)\sigma^{out}(\omega)F^{tm\,T}(\omega)$ in Eq. (9.11) is of the right form to use the formula. First, we saw above that, for our choice of mode functions f_E and f_L, the integrand decays fast enough for the integral to converge, that is its polynomial order is < -1.

Second, we check that the denominators are of the form $d(\omega)d(-\omega)$, where the roots $d(\omega)$ all have strictly positive imaginary parts; consequently, the roots of $d(-\omega)$ have negative imaginary parts. The terms C, R, and I in σ^{out} all have the same denominators from $\left|\chi_{opt}\right|^2\left|\chi_j\right|^2$, cf. Eqs. (9.13). Because of the symmetry $\chi^*_{opt}(\omega) = \chi_{opt}(-\omega)$ and $\chi^*_j(\omega) = \chi_j(-\omega)$, their denominator is of the required form $d(\omega)d(-\omega)$. The roots of $\chi_{opt}(\omega)$ is $-i\frac{\kappa}{2}$ in the negative complex plane and $\chi_{opt}(\omega)$ must be associated to $d(-\omega)$ and $\chi_{opt}(-\omega)$ to $d(\omega)$ (because its root $i\frac{\kappa}{2}$ has positive a complex part). The roots of $\chi_j(\omega)$ are $\omega_\pm = (\pm\sqrt{4\omega_m^2 - \gamma_m^2} - i\gamma_m)/2$ which both have negative imaginary parts, so that $\chi_j(\omega)$ must be associated to $d(-\omega)$ and $\chi_j(-\omega)$ to $d(\omega)$.

The denominators of the mode functions $f_E(\omega)$ and $f_L(\omega)$ are first order polynomials with roots $\omega_E = \omega_m + i\Gamma$ in the upper complex plane and $\omega_L = -\omega_m - i\Gamma$ in the lower complex plane, cf. Eqs. (8.10a). In the integrand $F^{tm}(-\omega)\sigma^{out}(\omega)F^{tm\,T}(\omega)$ they come in different variations of $f_\alpha^{(*)}(\mp\omega)f_\beta^{(*)}(\pm\omega)$ where the (loose) notation here describes that sometimes there is a conjugation and/or a minus sign in the argument. There are three cases to treat: either both roots are in the positive or the negative complex plane, or one root has positive complex part and the other one has negative complex part:

- When both roots are in the positive complex plane, we call the product of their denominator $e(\omega)$. For example in the tensor notation of Eq. (9.14) $F_{L,1}(-\omega)F_{E,1}(\omega)$ gives $f_L(-\omega)f_E(\omega)$, whose denominator is $(-\omega - \omega_L)(\omega - \omega_E) = e(\omega)$ with both roots in the positive imaginary plane. Multiply the entry of the integrand by $1 = \frac{e(-\omega)}{e(-\omega)}$ – that is $F_{L,1}(-\omega)\sigma^{out}_{11}(\omega)F_{E,1}(\omega)\frac{f_L(\omega)f_E(-\omega)}{f_L(\omega)f_E(-\omega)}$ in the example. This changes the numerator and denominator but not the global polynomial order of the entry. The denominator becomes $e(\omega)e(-\omega)$, which is the form required to use the integration formula because the roots of $e(\omega)$ are in the upper complex plane. The denominators must be multiplied by the denominators of $\left|\chi_{opt}\right|^2$ and $\left|\chi_j\right|^2$ from σ^{out}. The modified numerator from the mode

1. Mind to use the 8th edition of 2015 (sometimes also referred to as published in 2014) onward, there were a typos before.

2. File path:
`Thesis_CGut_StationaryOptomechanicalEntanglement/chapter_structure/9ch_TheoreticalPredictions/TheoreticalPredictions_derivation.nb`

functions must be multiplied to the numerator of the corresponding entry of σ^{out} – in our example that would be σ^{out}_{11}.

- Proceed similarly if both roots have negative complex parts and assign them to $e(-\omega)$.
- If their complex parts have different signs – as for instance in $F_{E,2}(-\omega)F_{E,1}(\omega)$ which is $f^*_E(\omega)f_E(\omega)$ – then we call the one with the root in the positive complex plane $e(\omega)$ ($(\omega - \omega_E)$ in the example) and the one in the negative plane we call $e'(-\omega)$ ($(\omega - \omega^*_E)$ in the example). Then, multiply the whole entry by $1 = \frac{e(-\omega)e'(\omega)}{e(-\omega)e'(\omega)}$ so that the denominator is $e(\omega)e'(\omega)e(-\omega)e'(-\omega)$, which is of the right form with roots of $e(\omega)e'(\omega)$ in the upper half complex plane. And, again, the adapted numerator and denominator must be multiplied to the corresponding entry of σ^{out} – in our example that would be σ^{out}_{21} – in order to define $d(\omega)$ and $g(\omega)$ as in Eq. (D.1).

This shows that the integral entries of σ^{tm} Eq. (9.11) can be evaluated symbolically with the formula [Hof15, App. B.5] whenever $T_{\text{sep}} = 0$. In practice one must adapt the numerators and denominators carefully; see [Gut24, Theoretical predictions derivation .nb] [3], or Klemens Winkler's master thesis [Win18]. When $T_{\text{sep}} > 0$, the numerators of certain entries are non-polynomial and the formula does not apply.

D.2 METHOD OF RESIDUES

Consider integrals of the form

$$I = \int_{-\infty}^{\infty} dx\, I(x) \tag{D.2}$$

where x is real and the integrand $I(x)$ is complex with N (non-essential) poles $\{z_j\}_{j=1}^{N}$; for our use in this work, we also assume that all the z_j have non-zero complex parts. [4] Hence, the integrand can be rewritten as a rational function with a denominator proportional to

$$\Pi_{j=1}^{N}(x - z_j)^{n_j} \tag{D.3}$$

where $n_j \in \mathbb{N}^*$ are the (finite) order of the poles. For all the integrands in this work, it turns out that all the relevant poles are of order one.

To use the residue integration technique (see standard textbooks on complex analysis for reference, for example [Mar19, Ch. 9] and [RHB06, Ch. 24]) one first "promotes" the real argument x of the integrand to the complexes, and calls the new complex argument z. Experience showed that this step is a potential pitfall. It is important to write $I(x)$ as a function of real x explicitly and then perform the formal change of

3. File path: see footnote 2.

4. It is in principle possible to compute purely real poles of order one with Cauchy principal value of the integral [Mar19, Ch. 9].

variable $x \to z$. For instance, terms of the form $|x-c|^2 = (x-c)(x-c^*)$ which are different from $|z-c|^2 = (z-c)(z^*-c^*)$.

The technique then makes use of Cauchy theorem, that applies where the thus promoted integrand is holomorphic. In this document, all integrands $I(z)$ are holomorphic on the whole complex plane because they are all independent of z^* (zero Wirtinger derivative).

All the integrands we consider satisfy

$$\lim_{\substack{|z|\to\infty \\ \mathrm{Im}[z]\geqslant 0}} |I(z)| < \mathcal{O}\Big(|z|^{-1-d}\Big) \to 0, \quad d > 0 \tag{D.4}$$

that is, when the modulus of the argument is large, all the integrands decay strictly faster than $1/|z|$ in the upper complex plane. This is true, first, because we saw at the beginning of this Appendix D that the polynomial order of all the integrands in σ^{tm} Eq. (9.11) was strictly less than -1. Second, the non-polynomial contributions in σ^{tm} are complex oscillatory exponential $e^{i\,z\,T_{\mathrm{sep}}}$ that decays exponentially fast whenever the complex part of z is greater than zero. This suggests the following integration contour, identical for all the integrands: the interval $[-R, R]$ on the real axis and closed by a half circle C_R (of radius R) in the upper half-plane (the contour parameter R is strictly positive so that the path is positively oriented).

The poles enclosed by the contour are $\{z_j\}_{j\in J(R)}$, where $J(R)$ selects the appropriate indices. By Cauchy theorem we have

$$\int_{-R}^{R} dz\, I(z) + \int_{C_R} dz\, I(z) = 2\pi i \sum_{j\in J(R)} \mathrm{Res}\big[I, z_j\big] \tag{D.5}$$

where $\mathrm{Res}\big[I, z_j\big]$ is the *residue* of the pole z_j of I. The residue of poles of order one is

$$\mathrm{Res}\big[I, z_j\big] = \lim_{z\to z_j} (z-z_j) I(z) = \Big[(z-z_j) I(z)\Big|_{z=z_j}. \tag{D.6}$$

Using that the decay of the integrands is faster than $1/|z|$ Eq. (D.4), the contribution of the integral over the half circle will be $\mathcal{O}\big(R^{-d}\big)$, $d > 0$, that vanishes when $R \to \infty$. Therefore,

$$\begin{aligned} \lim_{R\to\infty} \int_{-R}^{R} dz\, I(z) + \int_{C_R} dz\, I(z) &= \int_{-\infty}^{\infty} dz\, I(z) \\ &= 2\pi i \sum_{\mathrm{Im}[z_j]>0} \mathrm{Res}\big[I, z_j\big] \\ &= I. \end{aligned} \tag{D.7}$$

In Eq. (9.16) we called the poles with positive imaginary part p_+.

E

DERIVATION OF EPR-VARIANCE FORMULA

We present here some details supporting the derivation of the approximate formula for Δ_{EPR} Eq. (9.27) and the analysis in the relevant limit cases from Sec. 9.4. The full (pedantic) derivations and systematic checks are performed and documented in [Gut24, Theoretical predictions derivation .nb][1].

E.1 SYMMETRY OF TEMPORAL MODES' COVARIANCES

With help of the tensorial form Eq. (9.14) we find that

$$\begin{aligned}\sigma^{\mathrm{tm}}_{12} = \sigma^{\mathrm{tm}}_{\mathrm{EE},12} &= \int \mathrm{d}\omega\, F_{E,1}(-\omega)\sigma^{\mathrm{out}}_{1,2}(\omega)F_{E,2}(\omega) \\ &= \int \mathrm{d}\omega\, f_E(-\omega)f^*_E(-\omega)\,[S + C(\omega) - I(\omega) + X(\omega)] \qquad \text{(E.1)}\end{aligned}$$

and

$$\begin{aligned}\sigma^{\mathrm{tm}}_{34} = \sigma^{\mathrm{tm}}_{\mathrm{LL},12} &= \int \mathrm{d}\omega\, F_{L,1}(-\omega)\sigma^{\mathrm{out}}_{1,2}(\omega)F_{L,2}(\omega) \\ &= \int \mathrm{d}\omega\, f_L(-\omega)\,[S + C(\omega) - I(\omega) + X(\omega)]\, f^*_L(-\omega) \\ &= \int \mathrm{d}\omega\, f_E(\omega)f^*_E(\omega)\,[S + C(\omega) - I(\omega) + X(\omega)] \\ &= \int \mathrm{d}\omega\, f_E(-\omega)f^*_E(-\omega)\,[S + C(\omega) + I(\omega) + X(\omega)] \qquad \text{(E.2)}\end{aligned}$$

where we used that $f_L(-\omega) = f_E(\omega)$ in the third line [cf. Eq. (8.10a)]; then we changed variable $\omega \to -\omega$ in the next step and used that $C(\omega)$ and $X(\omega)$ are even and $I(\omega)$ odd [cf. Eqs. (9.13)]. Hence, the integrands with I cancel upon summing them in Eq. (9.24) and the integral becomes

$$\begin{aligned}\sigma^{\mathrm{tm}}_{12} + \sigma^{\mathrm{tm}}_{34} &= \sigma^{\mathrm{tm}}_{\mathrm{EE},12} + \sigma^{\mathrm{tm}}_{\mathrm{LL},12} \\ &= 2\int \mathrm{d}\omega\, f_E(-\omega)f^*_E(-\omega)\,[S + C(\omega) + X(\omega)] \\ &= 1 + 2\int \mathrm{d}\omega\, f_E(-\omega)f^*_E(-\omega)\,[C(\omega) + X(\omega)]\,. \qquad \text{(E.3)}\end{aligned}$$

The unity factor comes from the integral involving $S = 1/2$ that can be pulled out so that we are left with the norm of f_E which is 1, cf. Eq. (8.12).

1. File path:
`Thesis_CGut_StationaryOptomechanicalEntanglement/chapter_structure/9ch_TheoreticalPredictions/TheoreticalPredictions_derivation.nb`

Similarly, we recognise that $\sigma_{24}^{\mathrm{tm}}$ is the complex conjugate of $\sigma_{13}^{\mathrm{tm}}$, as it is already explicit in the first line of Eq. (9.22):

$$\begin{aligned}
\sigma_{13}^{\mathrm{tm}} = \sigma_{\mathrm{EL},11}^{\mathrm{tm}} &= \int \mathrm{d}\omega\, f_{\mathrm{E}}(-\omega)\,[-C(\omega)+R(\omega)-X(\omega)]\, f_{\mathrm{L}}(\omega) \\
&= \int \mathrm{d}\omega\, f_{\mathrm{E}}^{2}(-\omega)\,[-C(\omega)+R(\omega)-X(\omega)] \qquad \text{(E.4)} \\
\sigma_{24}^{\mathrm{tm}} = \sigma_{\mathrm{EL},22}^{\mathrm{tm}} &= \int \mathrm{d}\omega\, f_{\mathrm{E}}^{*}(\omega)\,[-C(\omega)-R(\omega)-X(\omega)]\, f_{\mathrm{L}}^{*}(-\omega) \\
&= \int \mathrm{d}\omega\, (f_{\mathrm{E}}^{*}(-\omega))^{2}\,[-C(-\omega)-R(-\omega)-X(-\omega)] \\
&= \int \mathrm{d}\omega\, (f_{\mathrm{E}}^{2}(-\omega))^{*}\,[-C(\omega)-R(\omega)-X(\omega)] \\
&= \left(\int \mathrm{d}\omega\, f_{\mathrm{E}}^{2}(-\omega)\,[-C(\omega)+R(\omega)-X(\omega)]\right)^{*} \\
&= \left(\sigma_{1,3}^{\mathrm{tm}}\right)^{*} \qquad \text{(E.5)}
\end{aligned}$$

where we used that $f_{\mathrm{E}}(-\omega) = f_{\mathrm{L}}(\omega)$ and that C, R, and X are even functions of ω [cf. Eqs. (9.13)]. C and X are purely real and R is purely complex which allowed to write the next-to-last step. For Δ_{EPR} we need to compute

$$\begin{aligned}
\mathrm{e}^{\mathrm{i}\,\phi}\sigma_{13}^{\mathrm{tm}} + \mathrm{e}^{-\mathrm{i}\,\phi}\sigma_{24}^{\mathrm{tm}} = 2\,\mathrm{Re}\Big[\mathrm{e}^{\mathrm{i}\,\phi}\int \mathrm{d}\omega\, f_{\mathrm{E}}^{2}(-\omega)\,[-C(\omega) \\
+R(\omega)-X(\omega)]\Big]
\end{aligned} \qquad \text{(E.6)}$$

which is the result in Eq. (9.23).

E.2 DETAILS OF INTEGRATION AND APPROXIMATIONS

Here, we give only the detailed computation of $I_{\mathrm{EE},12}^{C}$ for a single mechanical mode[2]. It illustrates the logic fully and all the other terms (for one and two modes) are treated in detail in [Gut24, Theoretical predictions derivation .nb][3]. To lighten the notation in the single mode case here, no reference is made to the target mode because all quantities pertain to it, e.g. $\omega_j^{\pm}$ are $\omega_{\pm}$ here, Γ_1^{tot} is Γ^{tot}, etc.

2. For two mechanical modes the difference is that the sum over the poles $\omega_j^{\pm}$ and $\omega_j^{\pm *}$, plus the extra X-terms involving $|\chi_1|^2|\chi_2|^2$.

3. File path: see footnote 1.

We write the integrand explicitly as

$$\begin{aligned} I^{C}_{EE,12}(\omega) &= f_E(-\omega) f^*_E(-\omega) C(\omega) \\ &\approx \frac{N_E(\omega) N^*_E(\omega)}{(-\omega-\omega_E)(-\omega-\omega^*_E)} \Gamma^{ro}\Gamma^{tot} |\chi(\omega)|^2 \\ &= \frac{\Gamma\Gamma^{ro}\Gamma^{tot}}{\pi} (-\omega-\omega_E)^{-1}(-\omega-\omega^*_E)^{-1} \\ &\quad \times \left[(\omega-\omega_-)^{-1}(\omega-\omega^*_-)^{-1}\right. \\ &\quad\quad \left. +(\omega-\omega_+)^{-1}(\omega-\omega^*_+)^{-1}\right]. \end{aligned} \tag{E.7}$$

Promote ω to the complexes and find that the poles in the upper-half plane are $\{\omega^*_\pm, -\omega^*_E\}$, so that

$$\begin{aligned} I^{C}_{EE,12} &= 2i\,\Gamma\Gamma^{ro}\Gamma^{tot} \\ &\quad \times \left\{(\omega^*_- + \omega_E)^{-1}(\omega^*_- - \omega^*_E)^{-1}(\omega^*_- - \omega_-)^{-1}\right. \\ &\quad\quad +(\omega^*_+ + \omega_E)^{-1}(\omega^*_+ - \omega^*_E) - 1(\omega^*_+ - \omega_+)^{-1} \\ &\quad\quad +(-\omega^*_E + \omega_E)^{-1}\left[(-\omega^*_E - \omega_-)^{-1}(-\omega^*_E - \omega^*_-)^{-1}\right. \\ &\quad\quad\quad \left.\left. +(-\omega^*_E - \omega_+)^{-1}(-\omega^*_E - \omega^*_+)^{-1}\right]\right\}. \end{aligned} \tag{E.8}$$

If $\bar{\omega} = (1+d)\omega_m$ in $\omega_{E,L}$ with $1 \gg |d|$ we find

$$I^{C}_{EE,12} \approx \frac{8\Gamma^{ro}\Gamma^{tot}}{\gamma_m(2\Gamma+\gamma_m)} \frac{\nu^2+2}{\nu^2+4+4\frac{d^2}{\nu^2}}. \tag{E.9}$$

We introduced the notation $\nu \coloneqq \frac{\Gamma}{\omega_m}$. We used the high mechanical Q limit to neglect γ_m against ω_m. Also we neglected d against unity. Importantly, we do not neglect γ_m against the pulse bandwidth Γ or the demodulation mismatch $\omega_m d$. If $d = 0$ we find from Eq. (E.8)

$$\begin{aligned} I^{C}_{EE,12} &= \frac{8\Gamma^{ro}\Gamma^{tot}}{\gamma_m(2\Gamma+\gamma_m)} \frac{(2\Gamma+\gamma_m)^2+8\omega_m^2}{(2\Gamma+\gamma_m)^2+16\omega_m^2} \\ &\approx \frac{8\Gamma^{ro}\Gamma^{tot}}{\gamma_m(2\Gamma+\gamma_m)} \frac{\nu^2+2}{\nu^2+4} \end{aligned} \tag{E.10}$$

where we performed the same approximations as for Eq. (E.9) above. We see that these approximations lead to the same result as taking the limit $d \to 0$ in Eq. (E.9).

In [Gut+20], we truncated this integral and kept only the term from the residue at ω^*_- [the first term in the curly bracket of Eq. (E.8)]. There, we explained that this leads to an upper limit on the pulse bandwidth Γ [Gut+20, Eq. (25)]. In this more general derivation, the sufficient condition for entanglement Eqs. (9.46) is similar to that Equation (25).

We checked this explicit integration (by hand) with Mathematica's built-in integration function, for all terms and for both one and two mechanical modes cases. Also, we checked systematically the mathematical manipulations and simplifications not involving approximations.

And we compared the approximation steps numerically. These checks are performed and documented in [Gut24, Theoretical predictions derivation .nb][4].

E.3 LIMIT OF FINITE FILTER BANDWIDTH $\Gamma^2/\omega_1^2 > 0$

We give here the details to Sec. 9.4.2 treating the limit of finite but small ν, $1 \gg \nu^2 > 0$ [cf. Eq. (9.30)]. Expand $A(d=0) = 1 + \frac{\nu^2}{4} + \mathcal{O}(\nu^3)$ and neglect terms of order 3 in ν (for perfectly tuned filter functions $d = 0$, only A and N_1 depend explicitly on ν) in Eq. (9.27) to obtain

$$\begin{aligned}\Delta_{\mathrm{EPR}} &= 2 + G\left[E + \mathcal{N}_0 + \mathcal{N}_1\right] \\ &\approx 2 + G\left\{\left(1 - N_0\frac{\Gamma}{\Gamma_1^{\mathrm{tot}}}\right) + \frac{2\Gamma}{\gamma_1}(1 - N_0)\right. \\ &\qquad \left. + \frac{\Gamma}{2\gamma_1}\nu^2\left[\left(1 + \frac{\gamma_1}{2\Gamma}\right) + N_1\left(1 - \frac{\gamma_1}{2\Gamma_1^{\mathrm{tot}}}\right)\right]\right\}.\end{aligned} \tag{E.11}$$

The first term in the curly bracket originates from E and it becomes negative if $N_0 > 0$ and for Γ large enough. For that reason, we casually call E the *entanglement term*. The second term in the curly bracket is positive and at best zero when $N_0 = 1$. The square bracket term cannot become negative in the high temperature limit where $\Gamma_1^{\mathrm{tot}} \gg \gamma_1$. Hence, the second term and the square bracket term are detrimental to entanglement detection. Moreover, the second term is larger than the square bracket by a factor $\nu^{-2} \gg 1$.[5] Therefore, it is best to choose $N_0 = 1$ because it simultaneously cancels that relatively large second term and it is best to make the first term in the curly bracket negative. When $N_0 = 1$, the first (entangling) term becomes negative once the necessary condition Eq. (9.35) $\Gamma > \Gamma_1^{\mathrm{tot}}$ is satisfied.

N_0 is 1 when $\phi = 0$ and in the limit $T_{\mathrm{sep}} \to 0$. Then, $N_1 = \frac{4-\nu^2}{4+\nu^2} \approx 1$ which is sub-optimal for entanglement. We replace in Eq. (E.11) and find the following sufficient condition for detecting entanglement

$$\left(\frac{\Gamma}{\Gamma_1^{\mathrm{tot}}} - 1\right)\left(1 + \frac{\nu^2}{4}\right) > \frac{\Gamma}{\gamma_1}\nu^2. \tag{E.12}$$

It incorporates the necessary condition $\Gamma > \Gamma_1^{\mathrm{tot}}$ Eq. (9.35). Neglecting ν^2 against 1 we get

$$\frac{\Gamma}{\Gamma_1^{\mathrm{tot}}} - \frac{\Gamma^3}{\gamma_1\omega_1^2} > 1. \tag{E.13}$$

It encodes the asymptotic behaviour at large Γ where the cubic term dominates over the linear one, thus preventing entanglement detection in the limit. This is a 3rd order polynomial in Γ and Mathematica finds

4. File path: see footnote 1.
5. In N_1 only terms of order ν^0 will contribute.

that the inequality is satisfied when [Gut24, Theoretical predictions derivation .nb] [6]

$$(3\Gamma_1^{tot})^3 < 4\gamma_1\omega_1^2 \tag{E.14}$$

which leads to the expressions Eqs. (9.46) of the sufficient conditions for entanglement detection with the EPR-variance (in the single mechanical mode case).

E.4 LIMIT OF FINITE ϕ AND T_{sep}

We give here details on Sec. 9.4.3. The starting point is the formula for Δ_{EPR} in the limit $\nu^2 \ll 1$ Eq. (E.11). As we discussed there, it is best to have N_0 close to 1, therefore we expand with respect to ϕ close to zero (or close to $2\pi n$ with $n \in \mathbb{N}$) and small $T_{sep}\gamma_1 > 0$. The latter is guarantied to be small in the high-Q_1 Eq. (8.1) and sidebands unresolved Eq. (8.4) regime: $\kappa^{-1} \lesssim T_{sep} \ll \omega_1^{-1}$, so that $T_{sep}\gamma_1 \ll 1/Q_{11} \ll 1$. When $\nu^2 \ll 1$, the cosine term dominates in N_1. (This is the regime $N_1 \approx 1$ which is sub-optimal for entanglement; we postpone a possible optimisation with $N_1 < 0$ to the end of this section.) We replace the expansions of N_0 and N_1 up to order ν^3, ϕ^3, T_{sep}^2 in Eq. (E.11) and we use the necessary condition for entanglement in the high temperature limit $\Gamma > \Gamma_1^{tot} \gg \gamma_1$. After some manipulations detailed in [Gut24, Theoretical predictions derivation .nb] [7], one obtains the following expression

$$\begin{aligned}\Delta_{EPR} \approx 2 + G\Bigg[&\frac{\Gamma^3}{\gamma_1\omega_1^2} + 1 \\ &-\frac{\Gamma}{\Gamma_1^{tot}}\left(1 - T_{sep}\Gamma_1^{tot}(1 + \phi Q_{11}\nu^2) - \phi^2\frac{\Gamma_1^{tot}}{\gamma_1}\right)\Bigg].\end{aligned} \tag{E.15}$$

The last term in the square bracket is the one that can lead to entanglement detection. Its contribution is reduced by finite ϕ and T_{sep} in the rounded parenthesis. Entanglement detection is not affected when each term in the rounded parenthesis is much less than 1

$$T_{sep} \ll \frac{1}{\Gamma_1^{tot}} \quad \text{and} \quad \phi^2 \ll \frac{\gamma_1}{\Gamma_1^{tot}} \quad \text{and} \quad T_{sep}\phi\nu^2 \ll \frac{1}{Q_{11}\Gamma_1^{tot}}. \tag{E.16}$$

These conditions lead to Eqs. (9.47a) and (9.47b) in Sec. 9.4.3.

In Figure 9.8 one sees that the domain of detected entanglement is increased periodically for fintie T_{sep}. This is when N_1 becomes negative. In the limit $\nu^2 \ll 1$, the cosine dominates in N_1, so that N_1 is approximately minimised when $\phi + 2T_{sep}\omega_1 = \pi$ [or $2\pi(n + 1/2)$ with $n \in \mathbb{N}$]. We assume ϕ small, so that N_0 is remains close to its

6. File path: see footnote 1.
7. File path: see footnote 1.

maximum. To be close to N_1's minimum, we set $2T_{sep}\omega_1 = \pi + t$, where $|t| \ll 1$ is a small deviation. We repeat the analysis above for expansions in ϕ, ν, and t around zero in Eq. (E.11). We then neglect contributions $\mathcal{O}(\phi^3, t^2, \nu^3)$, and use $\Gamma > \Gamma_1^{tot} \gg \gamma_1$ and $Q_{11} \gg 1$. After some manipulations detailed in [Gut24, Theoretical predictions derivation .nb][8] we find

$$\Delta_{EPR} \approx 2 + G\,[1 - \frac{\Gamma}{\Gamma_1^{tot}}\left(1 - \frac{\Gamma_1^{tot} Q_{11}\phi\left(2\phi + t\nu^2\right) + \nu\gamma_1/4 + t\Gamma_1^{tot}}{2\omega_1}\right)]. \tag{E.17}$$

As in Eq. (E.15), the factor of Γ/Γ_1^{tot} can make the term in the square bracket negative (corresponding to entanglement detection) and the fraction term in the rounded parenthesis makes it less than 1 which is detrimental. Differently form Eq. (E.15) however, there is no term in Γ^3 opposing entanglement detection. The structure of the formula is then closer to that of Eq. (9.42) that led to unconditional entanglement for the optimal choice of Γ [cf. Δ_{EPR}^{opt} Eq. (9.45)]. This is also what we see here: if the term in the rounded parenthesis is positive, then entanglement is detected upon choosing Γ large enough (bearing in mind that $\nu^2 \gg 1$ must still hold).

As above, the contributions of finite ϕ, t and ν do not disturb entanglement detection if each of the terms of the fraction is much less than 1. We obtain four conditions

$$2\phi^2 \ll \frac{\gamma_1}{\Gamma_1^{tot}} \text{ and } t\phi\nu^2 \ll \frac{\gamma_1}{\Gamma_1^{tot}} \text{ and } \frac{\nu}{4Q_{11}} \ll 1 \text{ and } t \ll \frac{\omega_1}{\Gamma_1^{tot}}. \tag{E.18}$$

The last condition is trivial when $\Gamma_1^{tot2} < \Gamma^2 \ll \omega_1^2$ and for $|t| \ll 1$. The next-to-last condition is trivial as well in the high-Q limit. The first condition was encountered already in Eq. (E.16). Replacing the latter in the second condition we find

$$t < \frac{1}{\nu^2\sqrt{n_1(C_1+1)}}. \tag{E.19}$$

It is compatible with the assumption $\nu^2 \ll 1$ we used to derive it. The separation between the temporal modes is set by the choice of mode functions, hence there is, in principle, no uncertainty in the way it enters the analysis (alike ϕ for a fixed witness). Rather, it is ω_1 that might not be known perfectly. Given an estimate of the mechanical frequency $\bar{\omega}$ and its error $\delta\omega$ so that $\bar{\omega} = \omega_1 + \delta\omega$ [same notation as for the detuned filters, cf. Eq. (8.8)], then $2T_{sep}\bar{\omega} = \pi(2n+1) + t$ and $t = 2T_{sep}\delta\omega$. In the limit $\omega_1 \gg \delta\omega$, we can write

$$\frac{\delta\omega}{\omega_1} < \frac{1}{\pi\nu^2\sqrt{n_1(C_1+1)}}. \tag{E.20}$$

8. File path: see footnote 1.

In the high bath temperature limit, $\sqrt{n_1(C_1+1)}$ is large but $\frac{\omega_1^2}{\Gamma^2}$ can be large too (because $\nu^2 \ll 1$) and we cannot make a general statement based on this relation. An example gives some orientation with parameters of Tab. 9.1, and for Γ a few times Γ_1^{tot}, we find that $\delta\omega/\omega_1$ can be more than 1. This means that the constraint for setting T_{sep} is not strict in that case.

Theoretically, ϕ and t can be set to zero and the sufficient condition for detecting entanglement is

$$\Gamma_1^{\text{tot}} < 2\omega_1 Q_{11} \iff n_1\,(C_1+1) < 2Q_1^2. \tag{E.21}$$

This is much less stringent than the sufficient condition Eqs. (9.46) we had found for $T_{\text{sep}} = \phi = 0$ (lhs is the cubic root here). We see the effect in Fig. 9.8 where more states are found to be entangled (for a broader range of Γ) and in Fig. 9.9 where entanglement is detected for this optimised choice of separation during the modes, while it is not when $T_{\text{sep}} = 0$.

E.5 LIMIT OF IMPERFECTLY TUNED TEMPORAL FILTERS

We give here details on Sec. 9.4.4. Starting from Eq. (9.27) for a single mechanical mode, assume $1 > \nu \gg |d| > 0$, where the demodulation mismatch d was defined in Eq. (8.8). In the expression of N_0 Eq. (9.33) this means that the factor of the cosine is positive and it dominates the sine term. From E and $\mathcal{N}_0$ Eqs. (9.31) and (9.36), it is again advantageous to maximise N_0 with $\phi = T_{\text{sep}} = 0$ so that $N_1 \approx 1$; see discussion in Sec. E.3 above. After a number of approximations and manipulations, documented in [Gut24, Theoretical predictions derivation .nb][9], the thus approximated expression for the EPR-variance with imperfectly tuned filter functions is

$$\Delta_{\text{EPR}} \approx 2 + G\left[1 - \frac{\Gamma}{\Gamma_1^{\text{tot}}} + 4\frac{\delta\omega^2}{\gamma_1\Gamma} + \frac{\Gamma^3}{2\gamma_1\omega_1^2}\right]. \tag{E.22}$$

The EPR-variance detects entanglement when the square bracket is negative (it is a polynomial of order four in Γ). With Mathematica we find that Δ_{EPR} detects entanglement when the sufficient condition from Eqs. (9.46) (derived for perfectly tuned filters) holds and also when the following holds

$$d = \frac{\delta\omega}{\omega_1} < \frac{\Gamma}{\Gamma_1^{\text{tot}}}\frac{\sqrt{n_1(C_1+1)}}{2Q} \tag{E.23a}$$

$$\Leftrightarrow \frac{\delta\omega}{\Gamma} < \frac{1}{\sqrt{n_1(C_1+1)}}. \tag{E.23b}$$

9. File path: see footnote 1.

The explicit dependence in the filter bandwidth Γ is eliminated using the necessary condition Eq. (9.35) to lower-bound the rhs of the first line with $\Gamma = \Gamma_1^{\mathrm{tot}}$. It yields a strict condition on the knowledge of the mechanical frequency Eq. (9.48).

We do not study the optimisation of N_1 as we did in Sec. 9.4.3. Given that N_1 is as before – and becomes close to -1 for the same $T_{\mathrm{sep}} = \frac{\pi}{2\omega_1}$ – we expect that this optimisation yields similar improvements.

E.6 SPECTATOR MODE SCENARIO

We give here details on Sec. 9.4.5. Start from Eq. (9.27) with $g_2 > 0$ and the spectator mode frequency $\omega_2 = (1+D)\omega_1 = \omega_1 + \Delta\omega$, cf. Eq. (5.11). Assume as well that the spectator mode is unresolved by the temporal mode filters, i.e. $\Gamma^2 \ll \Delta\omega^2$ so that $\nu^2 \ll D^2$.

First, we justify neglecting the cross-term contributions (from the integrals I^X) in the derivation of Eq. (9.27). In Sec. 9.2 we argued that they are proportional to $1/Q_{jk}$ which is very small. In the high mechanical quality factors limit Eq. (5.16) one can safely assume $Q_{jj} \gg 1/D$, therefore it is consistent to assume $\Delta\omega > \Gamma \gg \gamma_j$. Therefore, it holds that

$$\left(\frac{1}{\Delta\omega} + \frac{\Gamma}{\Delta\omega^2 + \Gamma^2}\right) \ll \frac{1}{\gamma_1} \tag{E.24}$$

which justify ignoring certain cross-terms [Gut24, Theoretical predictions derivation .nb] [10]. To neglect the remaining cross-terms one must assume

$$\Delta\omega \gg \gamma_2 C_1 \tag{E.25}$$

which is fulfilled in most practical situations: for C_1 of order 100 and D ~1%, then $Q_{jj} \gtrsim 10^6 \gg \frac{C_1}{D} \sim 10^4$ and the assumption above is met. These approximations are detailed and checked in [Gut24, Theoretical predictions derivation .nb] [11].

For perfectly tuned mode functions $\bar{\omega} = \omega_1$ and $\phi = T_{\mathrm{sep}} = 0$ (so that $N_0 = 1$), Eq. (9.27) becomes

$$\begin{aligned}\Delta_{\mathrm{EPR}} \approx 2 + G \Bigg[& 1 - \frac{\Gamma}{\Gamma_1^{\mathrm{tot}}} \\ & + \frac{\Gamma^3}{2\gamma_1\omega_1^2}\left((1+N_1) + \frac{(2W\omega_1)^2}{\Gamma^2+\Delta\omega^2}(1+N_2)\right)\Bigg]\end{aligned} \tag{E.26}$$

where we neglected γ_j against Γ_j^{tot} and Γ in the large thermal occupation limit Eq. (5.17). One also has that $N_1 \approx 1$. When $\nu^2 \ll D^2$, then N_2 is also approximately 1 and one neglects Γ^2 against $\Delta\omega^2$ in the

10. File path: see footnote 1.
11. File path: see footnote 1.

last term. This leads to the condition Eq. (9.49) deciding whether this last term dominates over the factor 2 (from the term in N_1 originating from the single mode case); when it does, then the spectator mode is the main detrimental contribution preventing entanglement detection. In that case, the sufficient condition for entanglement is

$$\frac{\Gamma}{\Gamma_1^{\text{tot}}} - 1 > \frac{4W^2}{\gamma_1 \Delta\omega^2}\Gamma^3. \tag{E.27}$$

This is a cubic inequality in Γ that has solutions when Eqs. (9.50) hold, see [Gut24, Theoretical predictions derivation .nb] [12].

12. File path: see footnote 1.

F

ELEMENTS OF HOMODYNE DETECTION

In this appendix, we workout the principles of *homodyne* detection of light at optical frequencies. We begin by presenting a model for a homodyne detector [GZ00; SW84; Sha85; YC83; YS80; GLS16; Leo03; LP95], which we subsequently apply to describe *dual-rail homodyne detection* [WC86; Wal87; FOP05]. The latter enables simultaneous measurement of both quadratures of the light field, representing the typical detection scheme used to implement our entanglement protocol of Part II. Notably, this approach was used and detailed in the theses of Jason Hölscher-Obermaier and Ramon Moghadas Nia [HO17; MN17].

We extend the description with a basic model of inefficient detection and introduce *passive losses* [LP93], which is the particular technical (i.e. non-fundamental) sensing noise that is most relevant for the setups discussed in Part III. This model forms the basis for several steps in the postprocessing of experimental data presented in Ch. 11 and discussed more in detail in App. H. Based on the homodyne description, we briefly describe the principles of *heterodyne* detection [WM09; Hof15] and attempt to clarify why it is equivalent to a dual-rail homodyne.

F.1 IDEAL (BALANCED) HOMODYNE DETECTION

A *balanced homodyne detector* measures a single quadrature of a (directional) mode of light. The detector has three stages: amplification, measurement, and noise mitigation/cancellation. The amplification happens by mixing, on a beam splitter, the light carrying the signal with an intense local oscillator (LO) field. The beam splitter transitivity is η_h for the signal. It is a quadrature of the signal mode that is amplified, and the phase of the LO selects which quadrature (or linear combination thereof) is amplified and effectively measured. The physical measurement is a (linear) light intensity measurement (e.g. with a photodiode) after the beam splitter. There are several strategies to mitigate possible noise in the inputs before amplification, but the only one relevant for this work is *balanced* homodyne detection. In a balanced homodyne detector, the beam splitter is 50:50 (i.e. with $\eta_h = 0.5$, or almost) and both output ports are measured. The intensity

measurements are then subtracted, which cancels common (classical) noise from the amplification stage. [1]

Figure F.1 shows a beam splitter, whose Hamiltonian and dynamics are already introduced in Sec. 5.3.1. We use the following convention for the beam splitter transformation relating input and output channels (Heisenberg picture) [Lou00]

$$\begin{pmatrix} a_{out} \\ b_{out} \end{pmatrix} = \underbrace{\begin{pmatrix} \sqrt{\eta} & i\sqrt{1-\eta} \\ i\sqrt{1-\eta} & \sqrt{\eta} \end{pmatrix}}_{:=B(\eta)} \begin{pmatrix} a_{in} \\ b_{in} \end{pmatrix} \tag{F.1}$$

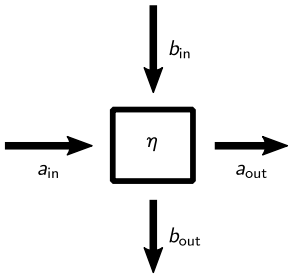

Fig. F.1 Icon of a beam splitter (BS) of transmitivity η for the horizontal a_{in} mode. In- and out- modes are mapped according to Eq. (F.1).

and similarly for the creation operators. B is called the *scattering-matrix* and $1 \geqslant \eta \geqslant 0$ is the transitivity of the port labelled 1. The two complex i guaranty unitarity of the transformation and lead to a relative phase between the output ports (there are several conventions for the matrix B). [2].

The schematic of a balanced homodyne detector is given in Fig. F.2. There are no losses or detection inefficiency (which will be treated in a later section) and if the transmitivity η_h is exactly $1/2$, then the detector is ideal. After this beam splitter mixes the input with the local oscillator, the annihilation operators are

$$b_1 = \sqrt{\eta_h} a_s + i\sqrt{1-\eta_h} A_{LO} \tag{F.2a}$$
$$b_2 = i\sqrt{1-\eta_h} a_s + \sqrt{\eta_h} A_{LO}. \tag{F.2b}$$

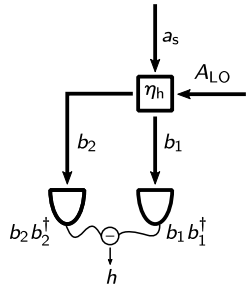

Fig. F.2 Ideal homodyne detector with amplification beam splitter η_h mixing signal mode to the bright local-oscillator (LO). The beam splitter outputs are detected by photodiodes measuring the light intensity in each mode. The homodyne measurement record h is the subtraction of the detector's photocurrent.

In the following we call this the *amplification* stage, and the beam splitter will be called *amplification beam splitter*. Subsequently, the photo-detectors measure the light intensity of both arms (i.e. they implement the number operators observable)

$$\begin{aligned} b_1^\dagger b_1 = {} & \eta_h a_s^\dagger a_s - i\sqrt{\eta_h(1-\eta_h)}\left(A_{LO}^\dagger a_s - A_{LO} a_s^\dagger\right) \\ & + (1-\eta_h) A_{LO}^\dagger A_{LO} \end{aligned} \tag{F.3a}$$

$$\begin{aligned} b_2^\dagger b_2 = {} & (1-\eta_h) a_s^\dagger a_s + i\sqrt{\eta_h(1-\eta_h)}\left(A_{LO}^\dagger a_s - A_{LO} a_s^\dagger\right) \\ & + \eta_h A_{LO}^\dagger A_{LO}. \end{aligned} \tag{F.3b}$$

We assume that the LO is of the form $A_{LO} = \alpha + a_{LO}$, where $\alpha = |\alpha| e^{-i\theta} \in \mathbb{C}$ is a displacement, a_{LO} is the annihilation operator of the undisplaced mode, and $|\alpha|^2 \gg 1$ corresponding to large LO intensity. The recorded signals are subtracted, providing perfect background

1. The interested reader can read on imbalanced homodyne and heterodyne measurements in [GZ00, Sec. 8.4].

2. B *is not* the unitary evolution matrix generated by the beam splitter interaction Hamiltonian H_{BS} from Eq. (3.11) [LP95]; see for example [Leo03, Sec. 3.3] for the explicit derivation of B from H_{BS}.

noise cancellation when $\eta_h = 0.5$; one finds the homodyne photocurrent

$$h = b_1^\dagger b_1 - b_2^\dagger b_2 \tag{F.4a}$$
$$\approx -i\,(\alpha^* a_s - \alpha a_s^\dagger) \tag{F.4b}$$
$$= \sqrt{2}|\alpha|\,(\cos(\theta)\,y_s - \sin(\theta)\,x_s) \tag{F.4c}$$

where the approximation neglected terms that are not at least of order $|\alpha| \gg 1$. The choice of the LO's phase θ determines which combination of quadrature of the signal mode is encoded in h – i.e. measured by the detection scheme. Measurement results are the expected values of operator h. In this ideal scenario, we see the principles of the detection at work: the difference of intensity measurements cancels exactly the spread (variance) of both inputs (i.e. the terms in $A_{LO}^\dagger A_{LO}$ and $a_s^\dagger a_s$). The LO amplifies the signal by $|\alpha|$. Mathematically, it led to neglecting the LO added noise (the fluctuations of a_{LO}) in Eq. (F.4b). Technologically, this leads to the use of linear photo-detection (as opposed to photon counting) that has high detection efficiency.

F.1.1 *Vacuum fluctuation detection*

The state of the signal mode is unspecified, in particular it can be the vacuum state. Let us be overly precise here: the vacuum state of that particular mode overlapping perfectly with the local oscillator upon mixing on the amplification beam splitter. At optical frequencies, the free fields are (almost) in the vacuum state (cf. Sec. A.6), hence a homodyne measurement of no signal is a measurement of the vacuum state quadratures – i.e. a *shotnoise measurement* [3] as in Sec. H.1. In that case, the quadratures in Eq. (F.4c) are those of the vacuum/shotnoise x_{sn} and y_{sn}, which statistics is that of the vacuum state Sec. A.1

$$\langle h_{sn}(\theta)\rangle = 0 \qquad \langle h_{sn}(\theta)(t) h_{sn}(\theta)(t')\rangle = \alpha^2 \delta(t-t'). \tag{F.5}$$

This is an instance of a quantum mechanical feature: measuring "quantum nothing" gives a non-zero signal. This is in contrast to a classical description of "measuring nothing" (no input signal): "clas-

3. Note the following jargon caveat here. Shotnoise is the intensity fluctuations of laser light with Poissonian statistics (related to its particle–like quantum nature) [Sch18]. In this sense, they are not the same physical thing as fluctuations of the electromagnetic ground/vacuum state. In Section A.3, we saw that the light state from an intense laser is a coherent state, with identical fluctuation statistics as the vacuum. This is why we use the terms "vacuum" and "shotnoise" interchangeably in the jargon of this thesis (although it is clearly misleading). Actually, for a long time, I thought that a shotnoise measurement yielded the fluctuations of the LO – the shotnoise indeed. The derivation of Eqs. (F.4) makes it clear that this is not the case, and a thermal LO, displaced much more than its fluctuations, leads to the same result.

sical nothing" is an electric field with zero amplitude. For a LO with (complex) amplitude $E \propto |\alpha|$, Eq. (F.1) gives

$$\begin{pmatrix} E_1^{out} \\ E_2^{out} \end{pmatrix} = B(\eta) \begin{pmatrix} E_1^{in} = 0 \\ E_2^{in} = E \end{pmatrix} = \begin{pmatrix} i\sqrt{1-\eta}E \\ \sqrt{\eta}E \end{pmatrix}. \tag{F.6}$$

When $\eta = 0.5$ we have a copy of the field with half the intensity in each output arm so that the homodyne current is identically zero: $h_{cl} = I_1 - I_2 = 0$. This remains true if the input is noisy and operator-valued: replace E by the LO operator $A_{LO} = \alpha + a_{LO}$ from above, then the homodyne current is still zero because half the e amplitude in both arms still cancels exactly. In the quantum case, it is the presence of a non-zero term a_{sn} in the first input that leads to a non-zero homodyne current h_{sn} in Eq. (F.4c) – this modelling is the acknowledgement that there are non-zero fluctuations corresponding to "quantum nothing". Lastly, a_{sn} and a_{LO} are independent and cannot cancel each other; this is a defining feature of quantum noise and goes hand-in-hand with the fact that it cannot be duplicated [4] and compensated for.

F.2 IMPERFECT HOMODYNE DETECTION

This section introduces two forms of imperfections in the detection scheme: light/photon losses, which are also called (quantum) inefficiencies; and detector darknoise.

F.2.1 *Inefficiencies*

Non-unit efficiency describes the fact that some of the photons in the mode a_s one intends to measure are not detected – e.g. they were lost on the way, there is a mismatch between the detected mode and the mode of the signal light, the photo-sensitive device does not to react to the presence of these photons, etc. A common quantum model of photon loss processes is to put a beam splitter of transmitivity η (for the mode to be detected) in front of the detectors [LP95]; $1 \geqslant \eta \geqslant 0$ is called the (quantum) *efficiency* of the photo-detection (unit efficiency corresponds to the ideal case of the previous section). In Figure F.3 beam splitters with transmitivities $\eta_{d,j}$ were placed in front of each detector in the homodyne set-up. A noise field $n_{d,j}$ enters at their second input ports. In principle, $n_{d,j}$ can be in any state, but at optical frequencies they are in the vacuum state. [5] This model of detection

4. This is the statement of the *non-cloning theorem* [WZ82].

5. For radiation at lower frequencies (like microwaves), the free fields have thermal excitations encoded in $n_{d,j}$, and the inefficiencies introduce more noise to the results.

inefficiency is called *passive losses*. The annihilation operators right before the photo-detectors are

$$e_j = \sqrt{\eta_{d,j}}\, d_j + i\sqrt{1-\eta_j}\, n_{d,j}. \tag{F.7}$$

This is the mathematical formulation of our beam splitter based model of photon loss channels. It is not a unitary map because we discard/ignore the second output port. This is a particular open-system model that couples the signal mode (system) to the free fields (environment) linearly with a beam splitter interaction, therefore it is a Gaussian map, cf. Secs. 3.3 and 4.1. The mechanism is to replace the portion of lost signal photons with a portion of vacuum noise.

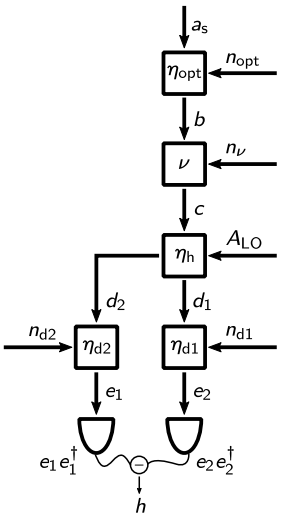

Fig. F.3 Imperfect homodyne detector with passive (photon) losses before and after the amplification. At optical frequencies, the loss mechanism mixes vacuum noise n_b, $b = s$, opt, ν, and dj, into the signal modes.

In Figure F.3 we also added two beam splitters in front of the homodyne amplification beam splitter. The first one, with transmitivity η_{opt}, models passive losses in the optical path to the detector (in optomechanical devices, this models all the losses between the mechanical oscillator's reflecting surface and the input of the homodyne detector, e.g. light scattered out of the cavity mode, losses at couplers, etc.). The second beam splitter with transmitivity ν models losses due to mode mismatch between the signal and the local oscillator at the amplification stage; these type of losses are also called *visibility* losses, see details in [HO17, App. C.5] for example. Importantly, shotnoise measurements (cf. F.1.1 above) are not susceptible to the passive losses upstream of the homodyne detector (i.e. before the amplification). [6].

For the configuration of Fig. F.3, we find the operators right in front of the photo-detectors

$$\begin{aligned} e_1 = {} & \sqrt{\eta_{d1}\eta_h\nu\eta_{opt}}\, a_s \\ & + i\sqrt{\eta_{d1}\eta_h\nu(1-\eta_{opt})}\, n_{opt} + i\sqrt{\eta_{d1}\eta_h(1-\nu)}\, n_\nu \\ & + i\sqrt{\eta_{d1}(1-\eta_h)}\, A_{LO} + i\sqrt{1-\eta_{d1}}\, n_{d1} \end{aligned} \tag{F.8a}$$

$$\begin{aligned} e_2 = {} & i\sqrt{\eta_{d2}(1-\eta_h)\nu\eta_{opt}}\, a_s \\ & - \sqrt{\eta_{d2}(1-\eta_h)\nu(1-\eta_{opt})}\, n_{opt} - \sqrt{\eta_{d2}(1-\eta_h)(1-\nu)}\, n_\nu \\ & + \sqrt{\eta_{d2}\eta_h}\, A_{LO} + i\sqrt{1-\eta_{d2}}\, n_{d2}. \end{aligned} \tag{F.8b}$$

Computing the photo-current with these bulky expressions is tedious and unpleasant (to say the least), therefore we evaluate already $\eta_h = 1/2$ (balanced detection) and assume that both detectors have the same

6. A picky remark is that, for imperfect visibility, the shotnoise thus characterised is not exactly in that of the mode of the signal – this is irrelevant for the purpose of this work.

efficiency $\eta_{d1} = \eta_{d2} = \eta_d$. In the limit of strong amplification $|\alpha| \gg 1$, we find

$$\begin{aligned} e_1^\dagger e_1 \approx & -i\sqrt{\frac{\eta_d}{2}}A_{LO}^\dagger(e_1 - i\sqrt{\frac{\eta_d}{2}}A_{LO}) \\ & + i\sqrt{\frac{\eta_d}{2}}(e_1 - i\sqrt{\frac{\eta_d}{2}}A_{LO})^\dagger A_{LO} + \frac{\eta_d}{2}|A_{LO}|^2 \\ = & \frac{\sqrt{\eta_d}}{2}\Big[\sqrt{\eta_d\nu\eta_{opt}}(-i)(\alpha^* a_s - \text{H.c.}) \\ & + \sqrt{\eta_d\nu(1-\eta_{opt})}(\alpha^* n_{opt} + \text{H.c.}) \\ & + \sqrt{\eta_d(1-\nu)}(\alpha^* n_\nu + \text{H.c.}) \\ & + \sqrt{2(1-\eta_d)}(\alpha^* n_{d1} + \text{H.c.})\Big] + \frac{\eta_d}{2}|A_{LO}|^2 \end{aligned} \tag{F.9a}$$

$$\begin{aligned} -e_2^\dagger e_2 = e_1^\dagger e_1 + \frac{\sqrt{\eta_d}}{2}\sqrt{2(1-\eta_d)}\,[&-(\alpha^* n_{d1} + \text{H.c.}) \\ &+(-i)(\alpha^* n_{d2} - \text{H.c.})]\,. \end{aligned} \tag{F.9b}$$

We introduce the shorthand notations

$$r_b(\theta) \coloneqq \cos(\theta)\,x_b + \sin(\theta)\,y_b \tag{F.10a}$$

$$r'_b(\theta) \coloneqq \cos(\theta)\,y_b - \sin(\theta)\,x_b \tag{F.10b}$$

where x and y are quadratures associated to the annihilation operators above and $b = s$, opt, ν, and dj is their label. Then we can write

$$(\alpha^* a_b + \text{H.c.}) = \sqrt{2}|\alpha| r_b(\theta) \tag{F.10c}$$

$$-i\,(\alpha^* a_b - \text{H.c.}) = \sqrt{2}|\alpha| r'_b(\theta). \tag{F.10d}$$

And we get the homodyne photo-current

$$\begin{aligned} h \approx \sqrt{2}|\alpha|\eta_d\Big[&\sqrt{\nu\eta_{opt}}r'_s + \sqrt{\nu(1-\eta_{opt})}r_{opt} + \sqrt{1-\nu}r_\nu \\ &+\sqrt{\frac{1-\eta_d}{2\eta_d}}\left(r_{d1} + r'_{d2}\right)\Big]. \end{aligned} \tag{F.11}$$

One finds that a measurement of the amplitude quadrature of the signal is encoded in the photo-current for a LO phase $-\pi/2$: i.e. $h_x = h(\theta = -\pi/2)$ encodes x_s plus some noise. The phase y_s is encoded in $h_y = h(\theta = 0)$. In the notation of Sec. H.2, the continuous outcomes of h_r correspond to the measured time traces R (where r is a label for x or y) If one knows the gain G_r of the detectors (in Volts) one can write $R = G_r h_r$.

The noise processes n_b are all independent vacuum fluctuations. Define the 2-vectors $\mathbf{r}_b = [r_b(\theta = -\pi/2), r_b(\theta = 0)]^T$ (and $\mathbf{r}'_b$ similarly) so that their covariances are

$$\left\langle \mathbf{r}_b {\mathbf{r}_b}^T \right\rangle = \sigma_{sn} = \mathbb{I}_2/2 = \left\langle \mathbf{r}'_b {\mathbf{r}'_b}^T \right\rangle. \tag{F.12}$$

(note that this is the case for arbitrary θ and a shift of $\pi/2$ between the measured quadratures.) Call $\mathbf{h} = (h_x, h_y)^T$, and write

$$\Sigma_h \coloneqq \left\langle \mathbf{h}\mathbf{h}^T \right\rangle_{sym} = 2|\alpha|^2 \eta_d \left[\eta_d \nu \eta_{opt} \sigma_s + \left(1 - \eta_d \nu \eta_{opt}\right) \sigma_{sn} \right] \quad \text{(F.13)}$$

where $\sigma_s =: \left\langle \mathbf{r}'_s \mathbf{r}'^T_s \right\rangle$ is the covariance matrix of the signal state.

When $\eta_d = \nu = \eta_{opt} = 1$ one retrieves the ideal detection case of Eqs. (F.4). A measurement of shotnoise, with $\sigma_s = \sigma_{sn}$, gives

$$\Sigma_{h_{sn}} = 2|\alpha|^2 \eta_d \sigma_{sn}. \quad \text{(F.14)}$$

That is shotnoise again (cf. Eq. (F.5)), amplified by $2|\alpha|^2$ and damped by the photodiodes efficiency η_d. It is independent of the losses before the homodyne amplification beam splitter, as mentioned above.

F.2.2 *Darknoise*

Opposite to photons lost or not counted, darknoise is the phenomenon where a detector outputs a signal in the absence of light at the input – and the detection threshold excludes that it comes from (unamplified) vacuum in front of the sensor. It is common to assume that darknoise arises from processes in the detector that are far from any quantum limit (e.g. electronics, thermal noise in the substrate where the electrons are located, etc.), so that darknoise as a whole is well described as a classical noise. Darknoise is characterised experimentally by a measurement with the light entering the photo-detectors completely blocked, and we call that a *darknoise measurement* in Ch. 11 and Sec. H.1.

In our homodyne model, we add an ad hoc fluctuation term $\mathcal{N}_{dn}$ to the homodyne photon-current h in Eq. (F.11) above. Moreover, we assume that $\mathcal{N}_{dn}$ is a white and normally distributed process

$$\mathcal{N}_{dn} \sim \mathcal{N}(0, \Sigma_{dn}) \quad \text{(F.15)}$$

where Σ_{dn} is a classical covariance matrix – in the sense that it needs only be positive definite – that can be reconstructed from darknoise measurements. Equation (F.13)

$$\Sigma_h = 2|\alpha|^2 \eta_d \left[\eta_d \nu \eta_{opt} \sigma_s + \left(1 - \eta_d \nu \eta_{opt}\right) \sigma_{sn} \right] + \Sigma_{dn}. \quad \text{(F.16)}$$

F.3 DUAL-RAIL HOMODYNE DETECTION

Heisenberg uncertainty relations set a bound on how precisely non-commuting observables can be known simultaneously. Now, it is not accurate to say that non-commuting observables cannot be known simultaneously: they can, given that their joint uncertainty fulfils the

Heisenberg bound [WM09]. A *dual-rail homodyne detector* is a set-up that measures non-commuting quadratures of a light simultaneously [WC86; Wal87; NFM91]. The principle is to combine two homodyne detectors, both of which measuring different quadratures, like h_x and h_y from Eq. (F.11) above. Figure F.4 depicts a schematic of a DRH subject to passive losses. The two homodyne detectors form the two arms of the dual-rail homodyne. The signal beam is split into the two arms by a beam splitter, which we call here the "entry beam splitter"; it has transmitivity η_{DR}, which is ideally 0.5.

As discussed above in the context of shotnoise measurements, quantum states cannot be duplicated [WZ82] and the outputs of the entry beam splitter are not identical quantum states. Indeed, vacuum fluctuations n_{DR} enter the second input port leading to uncorrelated noise between both arms.[7] Said differently, the outputs of beam splitters commute, because they correspond to modes with different Hilbert spaces, hence there are apparently no limitations from Heisenberg uncertainty on how precisely they can be known. Crucially, however, the information about the state of the signal before the entry beam splitter – that can be extracted from measurements of its output ports – is ultimately limited by Heisenberg uncertainty. In the present example, the unavoidable extra noise n_{DR} guarantees that it is the case.

We make the same assumptions as in Sec. F.2 with the imperfect homodyne detection model, namely: the photo-detectors within a homodyne detector have the same efficiency η_d (and $\bar{\eta}_d$ in the other arm), both homodyne are perfectly balanced with $\eta_h = \bar{\eta}_h = 0.5$, and, importantly, all loss channels are passive losses mixing independent vacuum fluctuations. Cascaded beam splitters before amplification (under the assumptions above) contribute multiplicatively so that the effect of the entry beam splitter is accounted for by replacing η_{opt} by $\eta_{opt}\eta_{DR} = \eta_{opt}/2$. The homodyne photo-current $\bar{h}$ is thus as in Eq. (F.11) with the replacement, and the signal in h has a factor i. Because we are ultimately interested in covariance matrices, the complexity of dealing with the latter is hidden in the notation Eqs. (F.10) that turns out to be irrelevant for passive losses, cf. Eq. (F.12).[8] We call the photo-current of the upper arm h_x, i.e. assuming the appropriate phase $\bar{\theta} = -\pi/2$ of the LO [cf. Eq. (F.11)]. Analogously, we label the photo-current of the lower arm h_y (with $\theta = 0$) and we define the 2-vector $\mathbf{h} = (h_x, h_y)^T$ as above. Additionally assuming identical visibility in both detectors $\nu = \bar{\nu}$ and identical LO strength $|\alpha| = |\bar{\alpha}|$, the covariance matrix Σ_{DRH} from this DRH detection scheme is the

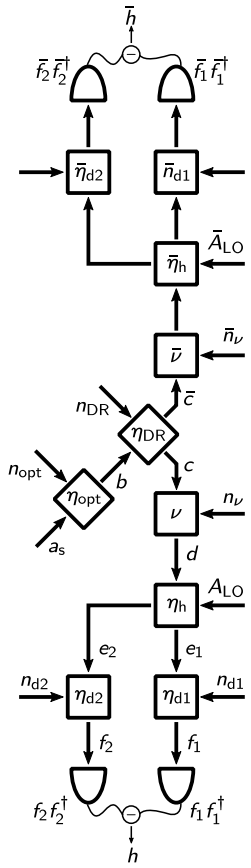

Fig. F.4 Imperfect dual-rail homodyne (DRH) detector measuring different quadratures simultaneously. It is a duplication of the imperfect homodyne detector of Fig. F.3 after the entry beam splitter and with the symmetric labels of the second arm with a bar $\bar{\square}$. (Redundant labels in the upper arm were ignored.)

7. The presence of this added noise is necessary to any such configuration. For example, in [Wal87] they propose a minimal configuration with a single LO and a single free port. It is the mere attempt of duplication that must lead to effectively different quantum states in the output arms.

8. Identical photo-detector efficiencies across the arms is necessary for the diagonal entries to have the same magnitudes.

same as Eq. (F.16), incorporating the entry beam splitter in the global optical losses

$$\Sigma_{\mathrm{DRH}} = 2|\alpha|^2\eta_{\mathrm{d}}\left[\eta_{\mathrm{d}}\nu\frac{\eta_{\mathrm{opt}}}{2}\sigma_{\mathrm{s}} + \left(1-\eta_{\mathrm{d}}\nu\frac{\eta_{\mathrm{opt}}}{2}\right)\sigma_{\mathrm{sn}}\right] + \Sigma_{\mathrm{dn}}. \qquad \text{(F.17)}$$

The configuration in Fig. F.4 examined here is an illustrative example of implementation (that was actually implemented in the setup described in [HO17; MN17]). Imperfect balancing of the entry beam splitter $\eta_{\mathrm{DR}} \neq 0.5$ and/or local oscillators with different power $|\alpha_x| \neq |\alpha_y|$ leads to different noise floor levels, as discussed in Sec. H.6. Configurations with a single local oscillator are possible; see for example [Wal87, Sec. 2.2 and Fig. 5a]; or using different polarisation and wave plates, as will be (perhaps) presented in the theses of my colleagues Kahan Dare and Manuel Reisenbauer.

F.4 HETERODYNE DETECTION

The heterodyne detection setup is the same as a single homodyne detector, like on Fig. F.2; the difference is that the LO frequency is different from the carrier frequency of the signal. We call the corresponding heterodyne detuning $\omega_{\mathrm{het}} = \omega_{\mathrm{LO}} - \omega_{\mathrm{s}}$ – it is the beating between both modes. The phase θ of the local oscillator with respect to the signal is changing (rotating) at a frequency ω_{het}; this means that the heterodyne output scans in time the signal light's quadrature $\cos(\theta)\,x_{\mathrm{s}} + \sin(\theta)\,y_{\mathrm{s}}$, with $\theta = 2\pi\omega_{\mathrm{het}}t$. If ω_{het} is much faster than the changes in the signal one wants to characterises, then one period of the scan is almost instantaneous relatively to the signal's dynamics, so that the heterodyne record encodes both quadratures (quasi) simultaneously – like the dual-rail homodyne detector of Sec. F.3. From a given heterodyne record, one retrieves x_{s} and y_{s} from the sine and cosine components at frequency ω_{het} [GZ00, Sec. 8], [WM09, Sec. 5.4.1], [Mag21, Sec. 5.2.1].

In the study of the DRH detector in App. F.3, we saw that there must be a beam splitter with an empty input port exposed to vacuum noise, which guaranties imperfect knowledge of both quadratures of the signal simultaneously. What about heterodyne detection where there is no free port? In the literature, see for instance [LP95, Sec. 4.3] or [FOP05, Sec. 5.6], it is explained that heterodyne detection is equivalent to dual-rail homodyne detection. In both these references, the necessary added noise comes from the frequency mode-mismatch between the signal and the LO: the signal at $\omega_{\mathrm{LO}} - \omega_{\mathrm{het}}$ and some free field (in the vacuum state) at $\omega_{\mathrm{LO}} + \omega_{\mathrm{het}}$ are amplified after the beam splitter that mixes them to the LO, thus both contribute to any information extracted from the heterodyne current demodulated at ω_{het}. Another approach to demonstrate the equivalence between heterodyne and DRH detection is by means of stochastic evolution for

the state of the detected light conditioned by a linear measurement as in [WM09, Sec. 4] and [Hof15, App. B]. In this approach, the mathematical mechanism inducing the effective loss of half the photons at the entry beam splitter is the constraint that the stochastic processes associated with each measurement are modelled by a Wiener process with unit variance.

G

ADDITIONAL CANDIDATE (CAVITY) SETUPS

This appendix presents the theoretical study of stationary optomechanical entanglement detection with the protocol and theoretical predictions of Part II, for three setups complementing the analysis in Ch. 10. We discuss a soft-clamped membrane (Sec. G.1)[Tsa+17] and a soft-clamped photonic crystal (Sec. G.2) [GNG19] that are elastically deforming solid-state objects clamped to some bulk substrate; then we discuss a levitated nano-particle trapped in an optical tweezer with a cavity perpendicular to the tweezer mode collecting (coherently) scattered light for detection (Sec. G.3) [Del+20b; Del19].

G.1 SOFT-CLAMPED MEMBRANE

In Sec. 10.1 we studied an implementation of a membrane *hard*-clamped to a (thick) rigid substrate patterned to produce a phononic bandgap. It is possible to pattern the (thin) membrane itself into a phononic shield, which allows to keep the bandgap isolation in addition to having locally smaller deformations because the deforming structure is larger. The mode of interest is localised to a relatively small defect cell at the centre of the membrane, and because the whole membrane deforms, the clamping and associated *bending losses* are strongly reduced. This technique is termed *soft*-clamping of the defect cell to the rigid substrate holding the patterned membrane. The relatively large size of the deformable membrane implies the presence of more modes closer to each other[1] compared to the hard-clamped membranes – and we saw that this is a possibly important disadvantage to perform our scheme. In Tab. G.1, we list achievable parameters for such systems; they were quoted to us by Albert Schliesser; examples of soft-clamped membranes in Albert Schliesser's group are [Ros+19] and [Che+20].

We start with the basic scenario where the drive is tuned to the cavity, there is only one mechanical mode, and the temporal modes are tuned perfectly to the mechanical sideband. The sufficient condition Eqs. (9.46) with the parameters of Tab. G.1 gives that entanglement would be detected – and the ratio between lhs and rhs is less than half. This is much better than the hard-clamped device. This is confirmed on Figs. G.1 (left) where we show the EPR-variance computed both exactly

1. Commonly, 1 to 5 mechanical modes in the bandgap and a high density of modes outside the bandgap.

Physical property	Symbol	Value	Units
mech. frequencies	ω_1	$1.2 \times 10^6 \times 2\pi$	[rad Hz]
	ω_2	$(1 + 0.1)\,\omega_1$	[rad Hz]
cavity linewidth (FWHM)	κ	$10\,\omega_1$	[rad Hz]
drive detuning	Δ	$-60 \times 10^3 \times 2\pi$	[rad Hz]
optomech. couplings	g_1	$21.5 \times 10^3 \times 2\pi$	[rad Hz]
	g_2	$g_1/3$	[rad Hz]
mech. linewidths (FWHM)	γ_1	$1.2 \times 10^{-3} \times 2\pi$	[rad Hz]
	γ_2	$132 \times 10^{-3} \times 2\pi$	[rad Hz]
mech. quality factors	Q_1	10^9	[]
	Q_2	10^7	[]
mech. baths temp.	T_1	7	[K]
	T_2	T_1	[K]
baths' occupation numbers	n_1	1.2×10^5	[]
	n_2	1.1×10^5	[]

Table G.1 Parameters of a soft-clamped membrane similar to [Ros+19; Che+20]. Details and comments were generously provided by Albert Schliesser in private communications. The coupling strength g_1 was chosen here so that $C_1 \approx 1$.

with the method of Sec. 9.1.2, and evaluating the approximate formula Eq. (9.27). Contrary to the hard-clamped membrane, the presence of detuning does not improve the "depth" of the separability violation (recall that it enabled entanglement detection with Δ_{EPR}, cf. Fig. 10.2); see the right panel of Figs. G.1. However, it detects entanglement in more states, i.e. of temporal modes with more different bandwidths Γ.

We saw that the presence of a spectator mode strongly deteriorates the detectable entanglement (cf. Sec. 9.4.5). To my knowledege, state-of-the-art nano-fabrication and mode-engineering nowadays can place the next closest mechanical mode a few percents away from the targeted mode: in Tab. G.1 we quote a slightly optimistic 10% (yet substantially less than the nearly 60% of the hard-clamped membrane). The sufficient condition for detecting entanglement with Δ_{EPR} in the presence of a spectator mode Eqs. (9.50) is not satisfied here; the ratio between lhs and rhs is about 1.3, again, better than for the hard-clamped membrane parameters. The logarithmic negativity does not reveal entanglement either.

As for the hard-clamped membrane, it is physically meaningful to fix the ratio between the couplings (1/3 in Tab. G.1) and between the bath occupation numbers $n_1/n_2 = \omega_2/\omega_1$ (corresponding to identical substrate temperature). We sweep over g_1 (and correspondingly g_2), which corresponds to varying the driving power, and over the bath's temperature n_1 (and correspondingly n_2). In Figures G.2 are contour

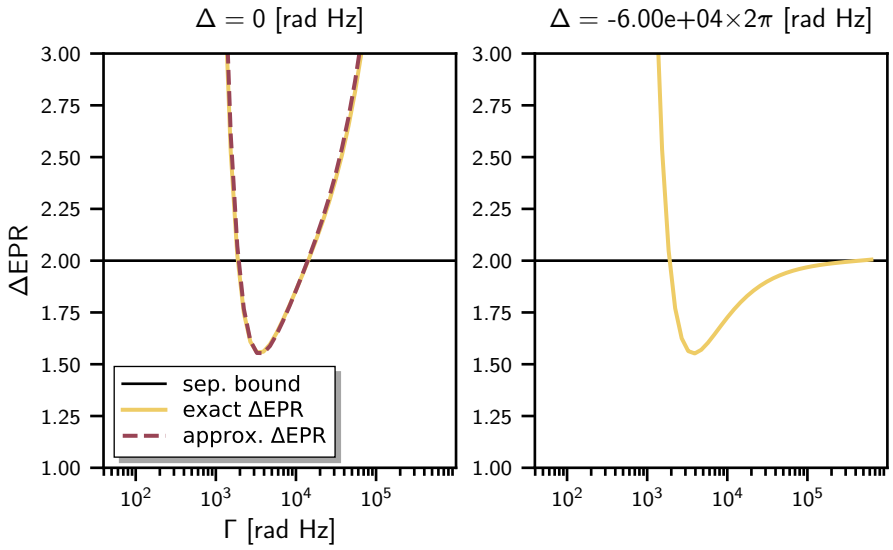

Figure G.1 EPR-variance for the parameters from Tab. G.1 but with $g_2 = 0$ (single mechanical mode). (left) Drive detuning is zero. The approximate formula Eq. (9.27) can be compared to the exact result and the overlap is good. (right) Exact EPR-variance with red detuning as in Tab. G.1.

plots of the EPR-variance minimised over Γ in the interval 10Hz to 1MHz (left) and logarithmic negativity (maximised over Γ; right panel). The nominal regime of Tab. G.1 is at 1 on both axes. The black lines guide the eye to show that entanglement is not detected by either of the tests – but the entanglement region is not far (!), as hinted by the sufficient condition Eqs. (9.50) not far from being met. Apparently, decreasing the driving power slightly would already suffice to detect entanglement, albeit in modest amount. Much more efficient is the reduction of the temperature. The parameter region where entanglement is detected by Δ_{EPR} is similar to that of the logarithmic negativity, hence the sufficient condition is also informative about the necessary and sufficient circumstances for entanglement in this regime.

Figure G.3 shows EPR-variance and logarithmic negativity minimised and maximised with respect to Γ respectively, for a parameter sweep of driving power (preserving the ratio between g_1 and g_2, as above) and relative spectral distance between the mechanical modes D Eq. (5.11). A spectator mode further away from the target leads to a fast increase of the separability violation. The decrease in power again leads to entanglement detection as in Figs. G.2. In the sweep over ω_2, we included the possibility that it is below the target mode (where $D < 0$). A slight asymmetry can be identified – it is much less pronounced than for the hard-clamped membrane (see Fig. 10.4) – and here as well, it is (slightly) harder to detect entanglement with a spectator mode below the target. We do not have a physical explanation or intuition for this behaviour. The approximate formula for Δ_{EPR} Eq. (9.27) leads to results very close to the exact ones (left panel); in

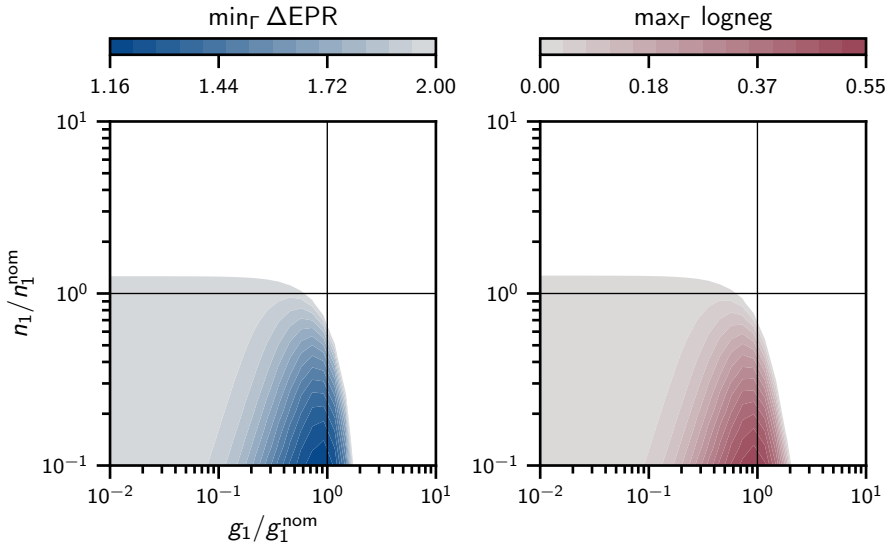

Figure G.2 (left) Exact Δ_{EPR} minimised over the early–late temporal modes' bandwidth $\Gamma \in [10, 10^6]$Hz. The results from the approximate formula Eq. (9.27) (not showed) are close to the exact computation. (right) Exact logarithmic negativity maximised over Γ analogously. The nominal parameter values are those from Tab. G.1; the black lines guide the eye to see that in this parameter regime, no entanglement is detected.

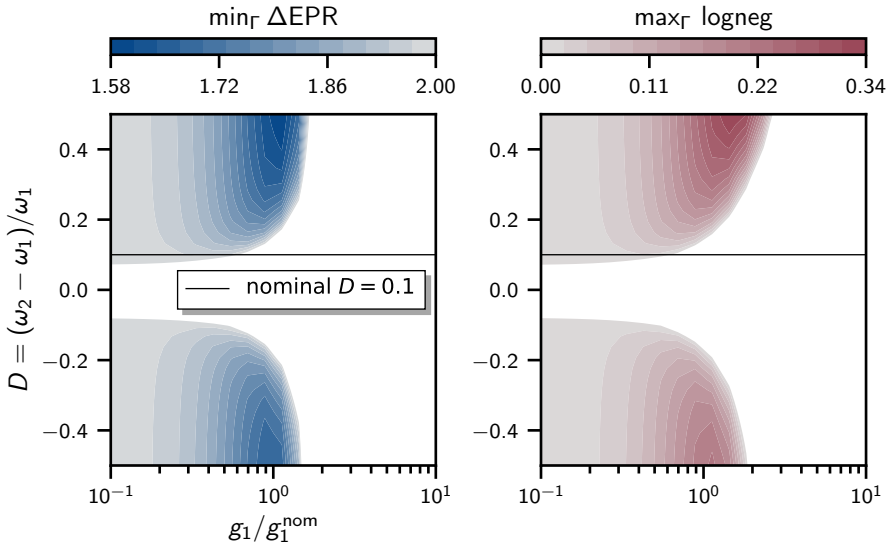

Figure G.3 (left) EPR-variance minimised over the early–late temporal modes' bandwidth Γ. The approximate results are very similar. (right) Logarithmic negativity maximised analogously.

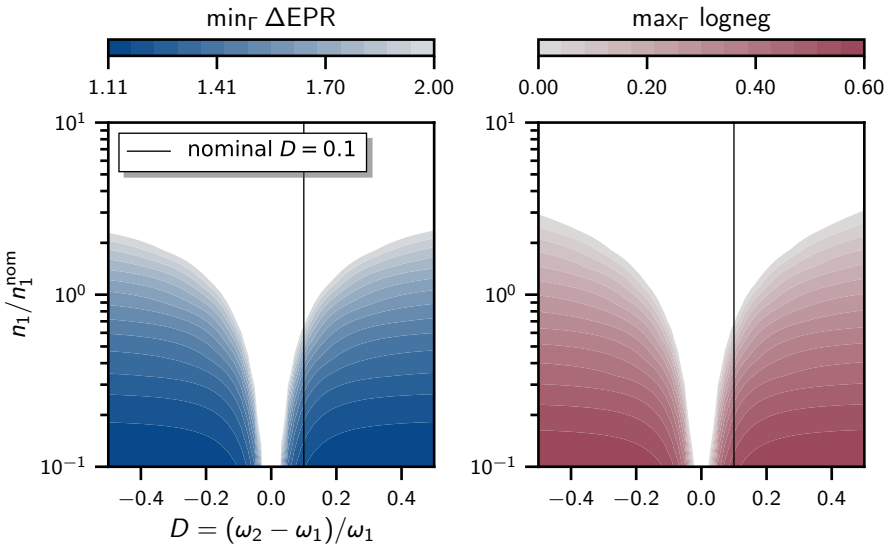

Figure G.4 (left) Exact EPR-variance minimised over the early–late temporal modes' bandwidth Γ. The approximate results are very similar. (right) Logarithmic negativity maximised analogously.

particular, it reproduces this asymmetry and could be used to study it. When the spectral resolution between target and spectator modes increases, then the sufficient condition allows for larger couplings as observed for the logarithmic negativity. On the other hand, the region of detectable entanglement with the EPR-variance seems to be bounded to finite coupling strength. This is because of the single mechanical mode sufficient condition Eqs. (9.46), which apparently does not apply to necessary and sufficient entanglement tests like the logarithmic negativity.

Finally, we sweep over the substrate temperature and the spectator mode's spectral distance to the target mode. For D at most 1, we approximate that changes of n_2 are only due to changes of substrate temperature and are independent of varying ω_2. Figures G.4 displays the maximised logarithmic negativity over Γ (right panel) and the minimised Δ_{EPR} (left panel). Lower temperatures quickly lead to appreciable entanglement, as observed in Figs. G.2 already.

G.2 PHOTONIC CRYSTAL

We move now to a different sort of optomechanical device: a photonic crystal with a phononic structure. The phononic structure implements, like the soft-clamped membrane, a bandgap for the mechanical vibration modes of interest. Additionally, (very) large aspect ratio of the deforming part minimises banding-losses (soft-clamping). Differently from the membranes, the deforming structure has a photonic crystal pattern forming an optical cavity and effect-

Physical property	Symbol	Value	Units
mech. frequencies	ω_1	$1.04 \times 10^6 \times 2\pi$	[rad Hz]
	ω_2	$1.15 \times 10^6 \times 2\pi$	[rad Hz]
cavity linewidth (FWHM)	κ	$5.25 \times 10^9 \times 2\pi$	[rad Hz]
drive detuning	Δ	$-10^8 \times 2\pi$	[rad Hz]
optomech. coupling	g_1	$2.55 \times 10^6 \times 2\pi$	[rad Hz]
	g_2	$0.8 \times 10^6 \times 2\pi$	[rad Hz]
mech. linewidth (FWHM)	γ_1	$0.02 \times 2\pi$	[rad Hz]
	γ_2	$0.1 \times 2\pi$	[rad Hz]
mech. quality factor	Q_1	5×10^7	[]
	Q_2	10^7	[]
mech. baths temp.	T_1	15	[K]
	T_2	T_1	[K]
baths' occupation numbers	n_1	3.27×10^5	[]
	n_2	3.26×10^5	[]

Table G.2 Photonic crystal with soft-clamped phononic shield structure as in [GNG19]. Parameters provided and generously commented by Jingkun Guo and Simon Gröblacher in private communications.

ively trapping the light within the material. The thus formed cavity light mode is *co-localised* with the mechanical deformation mode into a volume comparable to the mechanical deformation, therefore the cavity mode is very susceptible to the mechanical motion and vice versa – i.e. the single photon optomechanical coupling g_0 Eq. (5.8) is large (compared to other optomechanical devices like membranes). Another significant difference to the membrane setups is the linewidth of the photonic crystal cavity which is significantly larger.

The precise device we study is that of Ref. [GNG19] and its parameters are given in Tab. G.2 – and we benefited from the detailed comments and insights from Jingkun Guo. Presently, mechanical and optical environments are the same as for the membranes: the bulk of matter the phononic structure is (softly) clamped to and the free fields are at optical frequencies. Therefore the QLE model of Sec. 5.4 and the results of Ch. 9 apply as for the membranes.

The sufficient condition for the single mechanical mode scenario Eqs. (9.46) is not satisfied by a factor 6 so that the protocol would not detect entanglement with the EPR-variance. We find, however, that the logarithmic negativity does detect the entanglement, see Fig. G.6. With the detuning quoted in Tab. G.2, we found that Δ_{EPR} does not detect entanglement either, contrary to the hard-clamped membrane. In fact, we found no suitable detuning enabling entanglement detection with Δ_{EPR} in this operation regime.

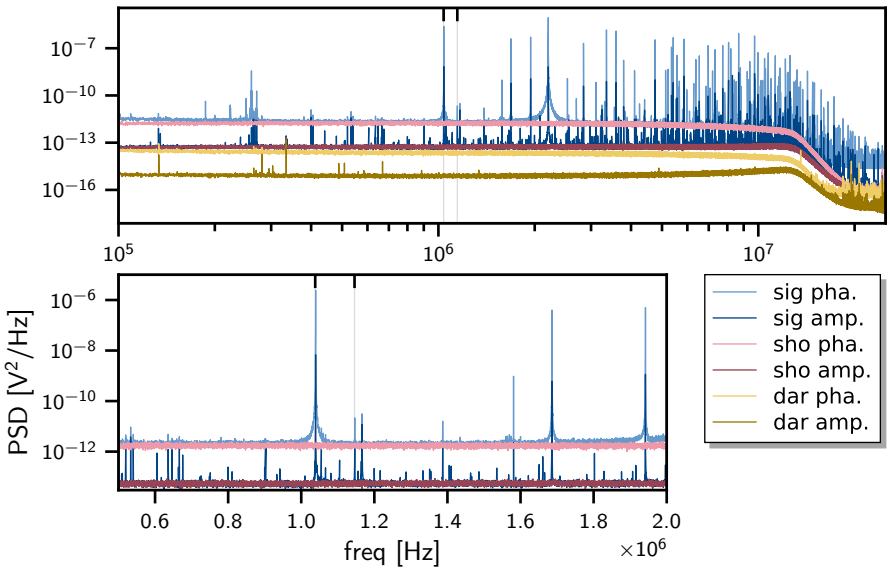

Figure G.5 Power spectral density of 10s of data. The target mode and the spectator mode are indicated with ticks on the top axis. The amplitude noise floor is lower than that of the phase which must be taken into account for calibrating to shotnoise units. Importantly, for a given quadrature, the shotnoise and signal noise floors overlap well; see App. H.6 for details.

Figure G.6 Exact logarithmic negativity for a single mechanical mode and the parameters of Tab. G.2, with or without detuing.

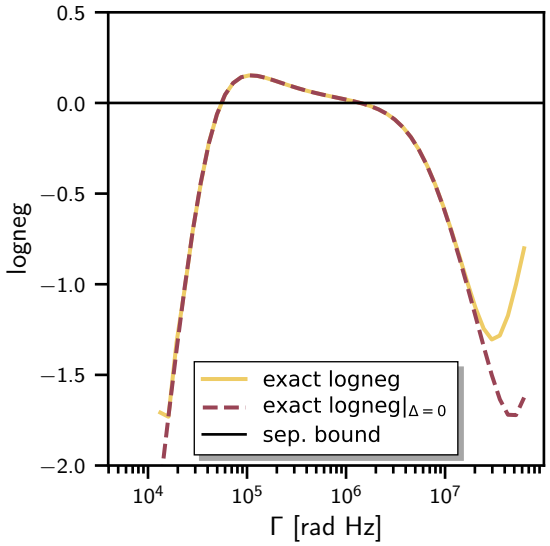

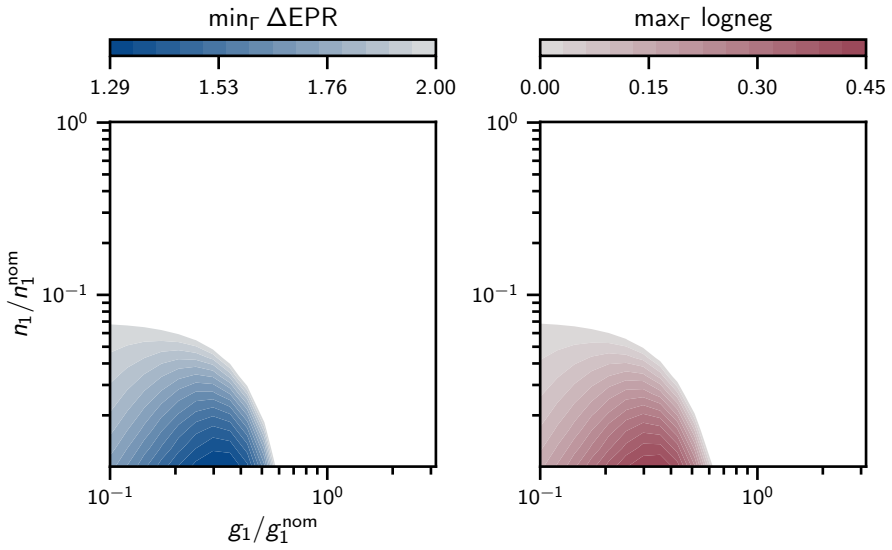

Figure G.7 (left) Exact EPR-variance minimised with respect to Γ between 1 Hz and 0.1 MHz. The results from the approximate formula Eq. (9.27) are very similar. (right) Logarithmic negativity maximised over Γ analogously. Sweep parameters given as ratios of nominal values from Tab. G.3. To the left of the plots, the number of photons in the cavity is just above 1, hence we cut the sweep there.

As one can see from the PSD of this device, Fig. G.5, there are many mechanical modes relatively close to the target: in Tab. G.2 we chose a spectator mode spaced by 100 kHz from the target mode, this is some 10% relative spectral distance. The coupling of the spectator mode g_2 is estimated to be about 1/3 of g_1 (like for the soft-clamped membrane). Therefore, one expects that the spectator mode will have a strong negative effect on the detection of entanglement. The sufficient criterion in the presence of a spectator mode Eqs. (9.50) is not satisfied by a factor 17.

Keeping the ratios g_1/g_2 and n_1/n_2 (same substrate temperature for the mechanical baths), we swept g_1 and n_1 over a few orders of magnitude. The results are in Figs. G.7. Logarithmic negativity and EPR-variance find entanglement at temperatures 6% of the nominal 15K, and lower coupling strengths with a sweet-spot at three times less power than in Tab. G.2. Decreasing the driving power decreases the couplings g_j, but with photonic crystals with large single photon coupling g_0 the cavity population is not so large. In the present case, the nominal driving power corresponds to about 118 cavity photons, therefore the sweet-spot of operation is $118/3^2 \approx 13$ photons or so. This becomes close to the weak drive regime where the linearisation of the interaction Hamiltonian is not accurate any more.

Guided by the sufficient condition Eqs. (9.50) and by the results of Figs. G.7, we set the temperature of the mechanical baths to 1.5 K, then sweep the spectral distance between the mechanical modes D Eq. (5.11) and g_1 (keeping the ratio of couplings fixed). The entanglement tests

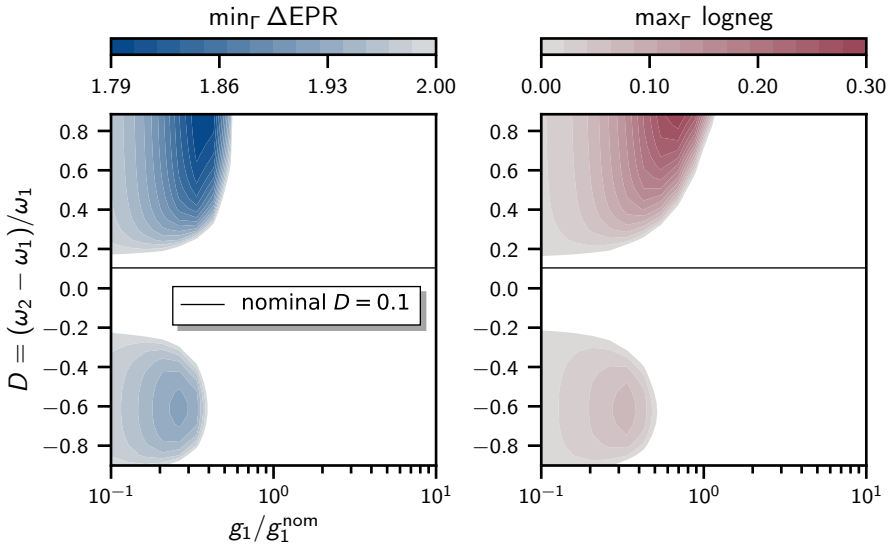

Figure G.8 The substrate temperature is 1.5K, i.e. 10 times less than in Tab. G.2. (left) Exact EPR-variance minimised with respect to Γ between 1 Hz and 0.1 MHz. The approximate results are very similar. (right) Logarithmic negativity maximised analogously.

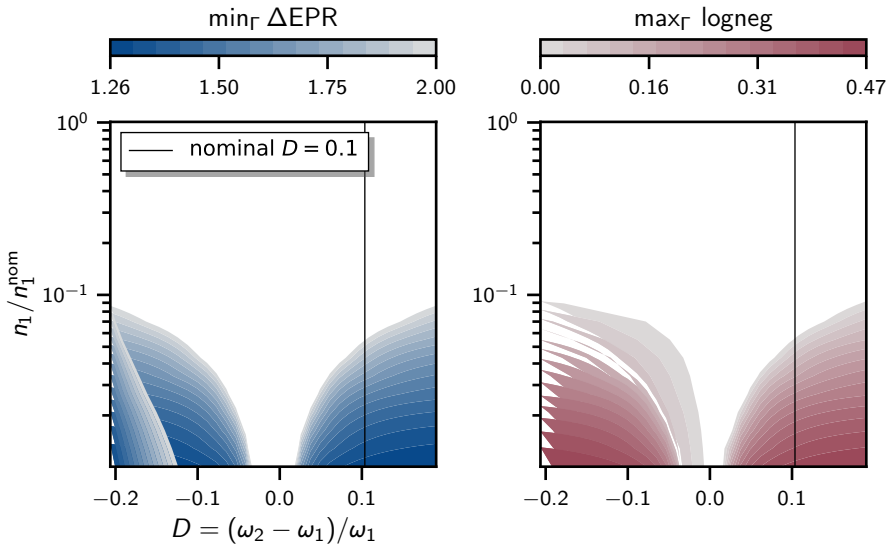

Figure G.9 The couplings g_1, g_2 are 30% of their nominal values in Tab. G.2. (left) Exact EPR-variance minimised with respect to Γ between 1 Hz and 0.1 MHz. The approximate result is very similar. (right) Logarithmic negativity maximised analogously. The weird (sharp) features for negative D are due to numerical instability, as far as we can tell.

optimised over Γ are showed in Figs. G.8. We recover the sweet-spot for g_1. In Figs. G.9, we fix g_1 to 30% its nominal value, then sweep over the spectator mode's frequency and the substrate temperature (with n_2 depending only on the substrate temperature and not on ω_2). In this parameter sweep, the results are affected by numerical instabilities.

G.3 COHERENT-SCATTERING LEVITATED NANO-PARTICLE

We study yet a different implementation of an optomechanical device: that of a levitated nano-particle. The reflecting object is a dielectric (e.g. glass) particle several tenths of nanometers in size. When placed in electromagnetic radiation of wavelength much larger than the particles' size (i.e. the *Rayleigh scattering regime*), the particle effectively looks like a (point-like) dipole emitter [Del+20b]. If the radiation is a tightly focused travelling wave, then the dipolar forces form a 3-dimensional trap for the particle, close to the intensity maximum of the light beam. A thus trapped particle can be moved or even levitated; at optical frequencies one calls these 3D traps *optical tweezers* [AD77; Pes+20].

In the small displacements limit, the potential experienced by the particle's centre-of-mass is quadratic, therefore we are again in presence of a harmonically moving mechanical oscillator. The scattered light and the particle's centre-of-mass exchange momentum leading to optomechanical interaction between them: the phase of the scattered light encodes information about the position of the particle, while the laser vacuum fluctuations disturb the particle's motion. In the limit of strong tweezer intensity, the (linear) optomechanical interaction Hamiltonian Eq. (5.7) describes this interaction well [Del19; GB+19]. Then the QLE Eqs. (4.10) are appropriate to describe this system, and the model of Sec. 5.4 is valid. In the setup we consider, the dominant dissipation rates are feedback cooling and gas damping, and the main noise processes are photon recoil and collisions with residual gas molecules [Del19].

In the setup studied here, the tweezer light is perpendicular to a cavity mode – the cavity defines the detected mode – and the particle is held in that cavity mode (i.e. the centre of the trap is in the standing wave of the cavity): this the so-called *coherent-scattering configuration*. It leads to rich tuning possibilities, as is discussed in detail in [Del+19; Del19; GB+19]. The experiment that provided the data we studied is the same that achieved the first passive cooling of a levitated nano-particle into its ground state of motion [Del+20b]. Table G.3 lists the parameters of this system for the purpose of detecting optomechanical entanglement.

Physical property	Symbol	Value	Units
mech. frequencies	ω_1	$190 \times 10^3 \times 2\pi$	[rad Hz]
	ω_2	$209 \times 10^3 \times 2\pi$	[rad Hz]
cavity linewidth (FWHM)	κ	$193 \times 10^3 \times 2\pi$	[rad Hz]
drive detuning	Δ	$-100 \times 10^3 \times 2\pi$	[rad Hz]
optomech. couplings	g_1	$55 \times 10^3 \times 2\pi$	[rad Hz]
	g_2	$10 \times 10^3 \times 2\pi$	[rad Hz]
mech. linewidths (FWHM)	γ_1	$10^{-3} \times 2\pi$	[rad Hz]
	γ_2	$1.8 \times 10^{-3} \times 2\pi$	[rad Hz]
mech. quality factors	Q_1	1.9×10^8	[]
	Q_2	1.16×10^8	[]
effective occupation numbers	n_1	30×10^6	[]
	n_2	n_1	[]

Table G.3 Parameters of a levitated nano-particle in coherent-scattering configuration. The set up is the same as that in [Del+20b] but some parameters were adapted: in particular, the mechanical frequencies of the mechanical modes was reduced compared to [Del+20b] so it is not in the sideband resolved regime. Here, $\kappa \approx \omega_1$ which is not the unresolved sidebands regime Eq. (8.4) and the approximate formula Eq. (9.27) might not be very accurate. The exact computation remains exact however. Parameters generously provided and commented for us by Uros Delic, Manuel Reisenbauer, Kahan Dare, and Aisling Johnson.

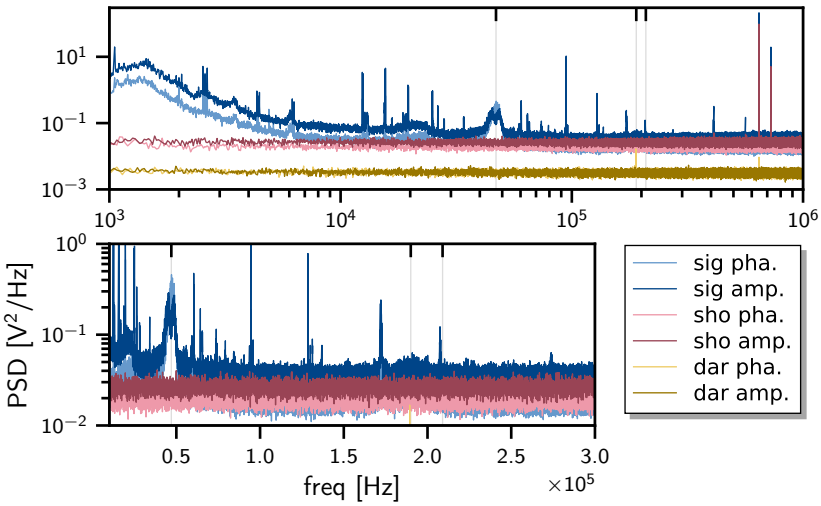

Figure G.10 Power spectral density of 8 seconds of measurement. The mechanical modes are indicated with ticks on the top axis: x-motion at 190 kHz is the targeted mode, y-motion at 209 kHz, and z-motion at 47 kHz are spectators. The target mode is not sharp because it is heavily cooled (passive cavity cooling when $\Delta < 0$ plus feedback). The z-mode is not Lorentzian because its motion explores the non-linear part of the Gaussian trapping potential.

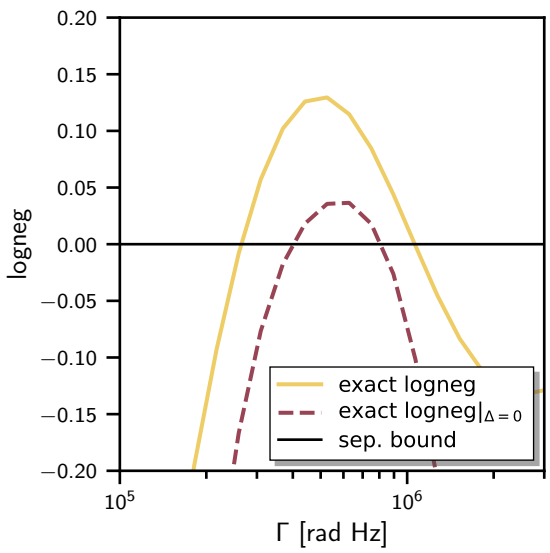

Figure G.11 Logarithmic negativity for the parameters of Tab. G.3, also without detuning $\Delta = 0$, and for a single mechanical mode. The non-smooth features are probably due to numerical imprecision.

With the parameters of Tab. G.3, the sufficient conditions Eqs. (9.46) and (9.50) for detecting entanglement with the protocol (for both the single and the spectator mode cases) are not satisfied by factors of several hundreds. In the single mechanical mode scenario, the logarithmic negativity does detect entanglement in the exactly computed covariance matrix, with and without detuning, see Fig. G.11. This reflects the universality on entanglement in that scenario [MDC10; Dir+24]. We did not find any detuning for which Δ_{EPR} detects entanglement. The detuning sweep tested with the logarithmic negativity on Fig. G.12 shows a sweet spot, close to the detuning in the Tab. G.3 – which is on purpose. On this figure, the bandwidth Γ of the temporal modes that are entangled is larger than the mechanical frequency $\Gamma > \omega_1$, which we did not expect would lead to entanglement in our theoretical explorations in Ch. 9.

We could not produce informing plots when the spectator mode is considered; entangled regimes typically showed suspicious behaviour that we associated to numerical instabilities or imprecision. It is worth noting that assuming perfect orthogonality between the cavity and the tweezer modes, then choosing the polarisation exactly perpendicular to the cavity axis and placing the particle at a minima of the cavity standing wave, then only the motion of the particle along the polarisation has finite overall coupling g_1, while the motion along the other two directions has vanishingly small coupling $g_2 \to 0$ [GB+19, Fig. 4], see also [Del19]. Therefore, the sufficient condition Eqs. (9.50) with a spectator mode can, in principle, always be fulfilled(!).

Then, in principle, the result of Fig. G.12 is that substantial entanglement can be detected. However the filter bandwidth are broad compared to the mechanical frequency in the present parameter and we saw that spectral features far from the mechanical peak relative

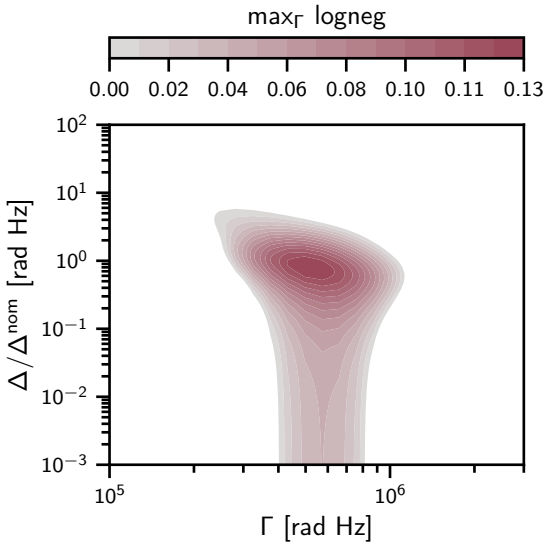

Figure G.12 Logarithmic negativity for the parameters of Tab. G.3. The detuning in the table was chosen so that it is in the region maximising the logarithmic negativity.

to Γ can have strong detrimental effect on entanglement detection. Therefore, it is advisable to work in a regime where the necessary Γ is smaller. The necessary condition Eq. (9.35) $\Gamma > \Gamma_1^{\mathrm{tot}}$ is helpful here. For the current parameter is ≈ 0.5 MHz, compatible with the entangled regions in Figs. G.11 and G.12. Presently, an optimisation approach would be using a cavity with a broader linewidth, along with less power which would reduce both g_1 and n_1 in the regime dominated by photon recoil heating. Less power also decreases the mechanical frequency, which does not enter the necessary condition. Our insights based on our study of the EPR-variance in Ch. 9, is that the relation between Γ and ω_1 is relevant and appears in the single mode sufficient condition; from that point of view it is not clear that one would actually gain from decreasing the power. On the other hand, necessary and sufficient entanglement tests like the logarithmic negativity can be used and working lower Γ_1^{tot} allows for temporal filters with narrower bandwidth.

H

DATA ANALYSIS PIPELINE

The main description of the protocol was thoroughly presented in Jason Hölscher-Obermaier's thesis [HO17, Ch. 5] and further discussed in Ramon Moghadas Nia's thesis [MN17, Part V], hence we do not reproduce them here. Rather we focus only on those points that we estimate meaningfully complement Jason's and Ramon's works.

We make a short note on the home-made data analysis software code runs on Matlab R2012a on a computer with (Linux) openSUSE operating system. It has a CPU Intel Xeon E5-2630 v3 2.40GHz with 32 cores, and 120GB of RAM. The code is not optimised to run on less memory and the full parallelisation capacity has not been attempted yet. The original and largest part of the implementation is due to Jason Hölscher-Obermaier; Sebastianimproved statistics, the and the present author contributed several parts. The full software has a wide range of functionalities implemented in a large number of functions; its usage is then accordingly involved. The code will be provided upon request.

H.1 MEASUREMENT RECORDS

According to the description of the protocol in Part II, the necessary data to perform the protocol are measurements of both quadratures of the light after it interacted with the mechanical oscillator. In the following, this measurement is called the *signal* data. The light is monitored continuously (i.e. in the limit where the sampling rate $1/dt$ is much faster than any relevant dynamics of the system) to form time traces of both quadratures. The protocol involves determining the matrix of covariances between temporal modes of the light: one applies the temporal mode profiles to successive chunks of the time traces (see Sec. H.3); the time traces of pulses form repeated measurements of the temporal modes that we use to estimate the covariance matrix; see explanations in [HO17, Sec. 5.3].

Tacit in its formulation, the protocol requires a reference for the fluctuation strength – or noise level – of the data. As we saw in Sec. 3.4, Gaussian entanglement is essentially squeezing along combinations of quadratures from both parties. Entanglement tests thus assess whether fluctuations are below those of the vacuum – which is the definition of squeezing, cf. Sec. 3.2. In the theoretical description, we worked with dimensionless units where the variances of the elec-

tromagnetic vacuum fluctuations are $1/2$, cf. Sec. 2.5. We call this reference of noise strength (or amplitude) a *unit of shotnoise* [1]. It sets the scale for the separability bounds; e.g. the EPR-variance Eq. (3.13) applied to early and late modes that are both in the vacuum state gives $\Delta_{\mathrm{EPR}} = 4 \times 1/2 + 4 \times 0 = 2$, which is precisely the separability bound. Practically, this noise reference is set by the calibration of the measurement records (typically in Volts) to the physical motion of the mechanical oscillator (in meters). Instead of converting Volts to (absolute) values in meters, we use *shotnoise limited* detectors (like homo- and hetero- dyne detection, cf. App. F) that resolve vacuum fluctuations – we call a measurement of electromagnetic field vacuum fluctuations a *shotnoise measurement*; see Sec. F.1.1. Such a measurement is then our reference for the vacuum noise amplitude and we rescale the signal data to that reference: this is the *calibration to shotnoise units* detailed in Sec. H.6 below.

Finally, all real detectors are subject to "dark signals" (also called "dark counts"): this is the non-zero output of a detector that receives no input; see Sec. F.2.2. A measurement of the detector's output when no light is sent to it (everything is turned off, including the local oscillator; or one blocks physically the entry of the photodiodes) is called a *darknoise measurement*. A darknoise measurement characterises the dark counts contribution that can be corrected from signal and shotnoise data, as explained in Sec. H.5 below.

In summary, the protocol needs six time traces: both quadratures of a signal measurement encoding the mechanical motion, of a shotnoise measurement as reference for the noise strength, and of a measurement of the darknoise of the detectors.

H.2 NOTATIONS

This section introduces the notation to describe the statistical problem of estimating the covariance matrix of temporal modes from discrete measurement records.

The results of amplitude and phase quadrature measurements are described by random variables $\mathcal{X}$ and $\mathcal{Y}$ respectively. Their individual statistics is that of measurements of the (quantum) observables amplitude $\hat{X}$ and phase $\hat{Y}$ observables of the quantum state of the light. (In this section, and in this section only, we use hats to distinguish operators.) We group the quadratures in a 2-vector of random variables $(\mathcal{X}, \mathcal{Y})^{\mathsf{T}}$, and we denote $\mathcal{R}$ either of its entries.

A measurement record of the observable $\hat{R}$, with the statistics of $\mathcal{R}$, is a list $R = \{R_j\}_{j=1}^{N}$, where the N samples R_j are the measurement

1. In this part, we use the terms vacuum and shotnoise interchangeably, although it is somewhat misleading; see Sec. F.1.1.

outcomes distributed according to the light's state (and $Ndt = T$ the duration of a time trace). The list R samples the statistics of $\mathcal{R}$. We define the 2-vector $\mathbf{R} \coloneqq (X, Y)^T$, and a single measurement sample is denoted X_j, Y_j or R_j.

We used capital letters so far because the quantities carry units: the records $\mathbf{R}$ are measured in volts. When rescaled to shotnoise units (see Sec. H.6), they are dimensionless and we denote the thus calibrated record $\mathbf{r}$. Relative to the model of Sec. 5.4, $\mathbf{r}$ here is a sampling of the statistics of $\hat{\mathbf{r}}_{c,out}$ Eqs. (5.23).

H.3 PULSED TIME TRACES

Ultimately, it is the state of the early–late temporal modes of the light that we need to estimate. To this end, we apply the mode functions f_E and f_L Eqs. (8.7) to the time traces repeatedly, so as to generate a sampling of the statistics of the quadratures of these temporal modes; as pedagogically and thoroughly explained in [HO17, Sec. 5.3].

First, we need to adapt the definition Eq. (8.6) of a temporal mode operator, with the temporal profile f_α ($\alpha = E, L$), to the discrete measurement records of quadratures $\mathbf{r}$. Define discretised mode functions $f_{\alpha,m} \coloneqq f_\alpha(t_m)$ evaluated at the m-th measurement time $t_m = m \times dt$. The mode functions are truncated after M samples and M is chosen such that the mode functions have decayed enough: if a set of G decay rates $\{\Gamma_g\}_g = 1^G$ is studied and Γ_{min} is the smallest, M is such that $e^{-\Gamma_{min} M dt} \sim 1\%$[2]. There are then $N_{pp} \coloneqq \lfloor N/(2M) \rfloor$ early–late pulse-pairs (pp) per time trace (where the bracket $\lfloor \square \rfloor$ takes the integer part of the number inside).

Second, we use the representation change described in App. C.1 to express the mode functions in the quadrature representation. In their matrix formulation Eq. (9.3), F^l_α is diagonal in the ladder operator representation and its counterpart in the quadrature representation is given by $F^q_\alpha(t) = R_2^{-1} F^l_\alpha(t) R_2$, where R_2 is the representation rotation matrix from Eq. (C.4) (not to confuse with the second entry of a measurement record!). Explicitly, in quadrature representation, we have[3]

$$F_\alpha(t_m) = F_{\alpha,m} = \begin{pmatrix} \mathrm{Re}[f_{\alpha,m}] & -\mathrm{Im}[f_{\alpha,m}] \\ \mathrm{Im}[f_{\alpha,m}] & \mathrm{Re}[f_{\alpha,m}] \end{pmatrix}. \tag{H.1}$$

The lists $R_\alpha = \{R_{\alpha,p}\}_{p=1}^{N_{pp}}$ of quadrature R, of temporal modes $\alpha = E, L$, have N_{pp} elements that sample the distribution of the observable

2. The threshold of one percent is not based on any particular consideration.

3. It is equivalent to use the relations Eqs. (2.18) between ladder and quadrature operators to convert the measurement record into an expression for the corresponding ladder operators, apply the mode functions as defined in Eqs. (8.7) and then turn the result back into quadratures, as explained in [HO17, Sec. 5.3].

$\hat{R}_\alpha$. They form (effective) measurements of the quadratures of the temporal modes. Given the lists of measurement records $\mathbf{R}$, the $R_{\alpha,p}$ are given by

$$R_{\alpha,p} = \begin{cases} \sum_{m=1}^{M} F_{E,m} R_{(p-1)\bar{M}+m}, & \text{if } \alpha = E \\ \sum_{m=1}^{M} F_{L,m} R_{(p-1)\bar{M}+M+M_{sep}+m}, & \text{if } \alpha = L \end{cases} \tag{H.2}$$

where $M_{sep} \coloneqq \lfloor T_{sep}/dt \rfloor$ is the number of samples in the duration T_{sep} between the pulses and $\bar{M} \coloneqq 2M + M_{sep}$ is the duration of a single early–late pulse-pair. See [HO17, Fig. 5.2] for a depiction without separation between early and late modes.

H.4 COVARIANCE MATRIX

The 4-vector of random variable $\mathcal{R}^{tm} \coloneqq (\mathcal{X}_E, \mathcal{Y}_E, \mathcal{X}_L, \mathcal{Y}_L)^T$ represents $\hat{\mathbf{r}}^{tm}$ form Eq. (9.6), up to a units calibration factor. The covariance matrix of the corresponding 4-variate (normal) distribution with zero mean is

$$\Sigma^{tm} \coloneqq \mathbb{E}\left[\mathcal{R}^{tm}\mathcal{R}^{tm\,T}\right] \tag{H.3}$$

where $\mathbb{E}$ is the mathematical expectation value. It accordingly represents the quantum state of the joint temporal modes σ^{tm} from Eq. (9.7), up to calibration (highlighted by the capitalisation). Given the 4-vector of lists of samples $\mathbf{R}^{tm} = (X_E, Y_E, X_L, Y_L)$, that we assume have zero mean, the best unbiased *estimate* of Σ^{tm} is

$$\Sigma^{tm} \approx \mathbb{\Sigma}^{tm} \coloneqq \frac{1}{N_{pp}-1} \sum_{p=1}^{N_{pp}} \mathbf{R}_p^{tm} \mathbf{R}_p^{tm\,T}. \tag{H.4}$$

The rhs is the reconstructed covariance matrix from a dataset. Just like σ^{tm}, it is 4-by-4 with the early sector (2-by-2 block) on the top left, the late sector on the bottom right, and the early–late correlations in the non-diagonal blocks. Bi-partite entanglement is assessed with respect to the early–late partition. In practice, we store $\mathbf{R}^{tm}$ as a 4-by-N_{pp} array, where the rows are the variables and the columns the observations, and use standard functions such as numpy's `numpy.cov()` or Matlab's `cov()` to compute $\mathbb{\Sigma}_S^{tm}$ [S = sig, sn, or dn for signal (sig), shotnoise (sn), and darknoise (dn) data]; and for the different mode function bandwidths Γ_g, $g = 1, \ldots, G$. Covariance matrices from signal and shotnoise data are faithful estimates of the quantum state of their temporal modes (state tomography). For darknoise data, it is the correlation matrix of the corresponding classical noise processes filtered by the temporal modes – we refrain from assigning any quantum interpretation to $\mathbb{\Sigma}_{dn}^{tm}$.

H.4.1 *Multi-mode evaluation*

In Sec. 5.6 of Ref. [HO17], Jason generalised the scheme to more temporal modes (see also Sec. 8.2.1): the early–late partition remains the same, but more demodulation frequencies are used – typically these frequencies are the resonance frequencies of other mechanical modes.[4] n demodulation frequencies ω_j lead to the definition of $2n$ mode functions

$$f_{Ej}(t) = N_{E,j}(t)e^{-i\omega_{Ej}t}, \quad \text{with } \omega_{Ej} = \omega_j + i\Gamma \tag{H.5a}$$

$$f_{Lj}(t) = N_{L,j}(t)e^{-i\omega_{Lj}t}, \quad \text{with } \omega_{Lj} = -\omega_{Ej} \tag{H.5b}$$

where $j = 1, \dots, n$. Define a multi-index labelling all the mode functions $\alpha \coloneqq E1, E2, \dots, L1, \dots, Ln$, then the $N_\alpha(t)$ insure orthonormality of all the mode functions and they depend on time.[5] In practice, one gives a list of mode functions – in the basic form $\{e^{-i\omega_\alpha t} \ : \ \alpha = E1, E2, \dots, Ln\}$ – to an othonormalisation algorithm like Gram-Schmidt or Householder.[6] We note that the exact shape of the orthonormal mode functions (i.e. the $N_\alpha(t)$) depends on the order in which the non-orthogonal temporal profiles are fed into the algorithm. Our rule of thumb is to order the list of frequencies with the "most important modes" first so that their temporal shape is least deformed by the orhtonormalisation: the target mode is the ad hoc most important mode; we have no rigorous, or systematic, or robust, or smart way to order the other modes. To our experience, we observe differences in the results for different ordering of the modes but they are typically not large or important, and we found no usable patterns.

The structure of the estimated multi-mode covariance matrices is set by the structure of the $4n$-vector

$$\mathbf{R}^{tm} \coloneqq (X_{E1}, Y_{E1}, X_{E2}, \dots, Y_{En}, X_{L1}, \dots, Y_{Ln})^T. \tag{H.6}$$

In this more complex reconstruction, we still test early–late bi-partite entanglement (where both parties have internal structures with n modes each) because it is the only relevant entanglement configuration to infer optomechanical entanglement with the theorem of Ch. 7. Now, for other purposes and sheer scientific curiosity, one could study all (possibly multi-partite) entanglement configurations of the thus estimated state of the light [HE06].

The whole procedure is repeated for a set of different decays $\{\Gamma_g\}_{g=1}^{G}$ thus generating G reconstructions of $4n$-by-$4n$ covariance matrices.

4. In principle the decay rates could be varied as well, and for each mode independently.

5. $N_\alpha(t)$ introduces oscillations of the exponential hull; see [HO17, App. C.2] for a depiction of this effect.

6. The difficulty here is that this input basis has long vectors that are quite colinear (with many entries that are close to zero). We prefer Matlab's `qr()` function, which is stable, accurate, and relatively fast.

We assumed symmetric (equal) decay rates in early and late parties, and for all demodulation frequencies, because it reduces the number of settings to explore but the procedure can be further generalised to arbitrary decay for each demodulation and asymmetric early–late modes.

Our experience with the analysis of various experiments' data is that including temporal modes demodulating the sidebands of neighbouring mechanical modes always helps, in the sense that the witness values (logarithmic negativities) are always smaller (larger) when including a few more of the mechanical modes. There is a limit where including too many stops being beneficial and unexpectedly high or wrong negative witness values are returned by the analysis – to our experience, including up to three modes yields reliable and stable results that can be interpreted physically.

H.4.2 *Two-sideband evaluation*

A particular form of multi-mode evaluation was suggested by Klemens Hammerer and was already documented in [HO17, Sec. 5.8]. We call it the *two-sided evaluation* and, to our experience, it always leads to smaller witness values (or larger logarithmic negativities). It consists in accounting for the other sideband in each temporal mode.

Recalling the discussion in Sec. 8.2, the early temporal mode demodulates the red sideband of light originating from the two-mode squeezing interaction. In a two-sided evaluation, one uses an additional early temporal mode that demodulates the blue sideband. Analogously, the late mode originally demodulates the up-converted photons in the blue sideband; in a two-sided evaluation one adds a late temporal mode demodulating the red sideband. It thus becomes a multi-mode evaluation where both the early and late parties are composed of two modes each (and the covariance matrices are 8-by-8), but it accounts only for the target mechanical mode. In practice, adding the opposite sideband amounts to demodulating at $-\omega_1$: explicitly, if $\omega_{E,1} = \omega_1 + i\,\Gamma$, then for the second sideband we have $\omega_{E,2} = -\omega_1 + i\,\Gamma$; the late demodulation frequencies are found by symmetry $\omega_{L,j} = -\omega_{E,j}$.

According to our argumentation in Ch. 6 about entanglement being generated first between the mechanical oscillator and the red sideband through the two-mode-squeezing interaction, and subsequently mapped coherently onto the blue sideband via the beam splitter interaction, then one should not expect any additional useful information about optomechanical entanglement from this two-sided evaluation. Jason has suggested that the effect is to purify the reconstructed state [HO17, Sec. 5.8] because the opposite sidebands provide more inform-

ation to reconstruct it faithfully. It sounds reasonable and it is our best explanation so far, but it has not been checked rigorously yet.

H.5 DARKNOISE CORRECTION

Because darknoise is independently characterised (by the darknoise measurement), and not related to entanglement, it can be corrected in the signal and shotnoise data. The central assumption is that it is not correlated with either of them, so that the correction can happen at the level of the covariances as follows:

$$\underline{\Sigma}_{s}^{tm} = \Sigma_{s}^{tm} - \Sigma_{dn}^{tm} \tag{H.7}$$

with $s = $ sig or sn.

H.6 CALIBRATION TO SHOTNOISE UNITS

As we already mentioned, the measurement records are in Volts while the entanglement tests, detailed in Secs. 3.4 and 8.3, are defined for operators in dimensionless units. We opt to rescale the data to the dimensionless units used throughout the theoretical developments of the first two parts. In these units, the commutator of the quadrature is complex i and the variance of the electromagnetic vacuum fluctuations is $1/2$ for both quadratures. We call these units *shotnoise units*.

A shotnoise measurement with shotnoise limited detection is an independent characterisation of the amplitude of the vacuum fluctuations. The random variable $\mathcal{R}_{sn}$ represents the statistics of an idealised measurement of the quadrature $\hat{R}$ of vacuum fluctuations; i.e. $\mathcal{R}_{sn}$ is a white-noise process with flat power spectral density (PSD), as discussed in Secs. H.1. A real measurement of shotnoise will not be perfectly white and one expects the PSD to display non-flat features: prominently a high frequency cut-off and possibly other frequency responses of the detector (see red curves in Fig. 10.1 for an example). The spectral region, which faithfully corresponds to vacuum noise, is where the frequency response is flat. One thus selects the largest possible frequency interval around the targeted mechanical frequency where the shotnoise PSD is flat. The median[7] of the PSD in this interval n_{sn} is what we call the *noise level* of the shotnoise data – it is in units of Volts squared per Hertz.

Take a data set of shotnoise R_{sn} sampled at a rate of $1/dt$ so that the highest resolvable frequency is $2/dt =: f_{Ny}$, also called Nyquist

7. The median is a more conservative estimate of the noise level than the mean because it is less susceptible to outliers orders of magnitude larger than the floor level (like noise peaks). Also, the computed PSD are averaged, thus forming a χ^2-distribution with as many degrees of freedom as averages (i.e. a sum of squared normal distributions), which might be asymmetric.

frequency. Denote its PSD $S_{R_{sn}R_{sn}}(\omega)$ (computed with the Welsch method averaged many times) and call n_{sn} its vacuum noise level – i.e. the median of $S_{R_{sn}R_{sn}}(\omega)$ for the selected frequency interval where it is flat. By the Wiener-Khinchin theorem [Cle+10, App. A.1.]

$$\left\langle R_{sn}^2 \right\rangle = \int_{-\infty}^{\infty} d\omega \, S_{R_{sn}R_{sn}}(\omega). \tag{H.8}$$

The rhs is approximately $n_{sn} f_{Ny}$. Because R_{sn} is a realisation of the statistics of the (dimensionless) observable $\hat{r}$ of the vacuum state, the lhs corresponds to the vacuum variance in Volts. Introduce the dimensionful calibration factor C_{sn} such that

$$1/2 = \mathrm{Tr}\left[\rho_{vac}\hat{r}^2\right] = \left\langle \hat{r}^2 \right\rangle = C_{sn}\left\langle R_{sn}^2 \right\rangle \approx C_{sn} n_{sn} f_{Ny}. \tag{H.9}$$

Given C_{sn}, one can perform the calibration to shotnoise units at the level of the time traces $\mathbf{R}_s$ (s = sig or sn): first subtracting by the darknoise level (diagonal entries of $\mathbb{\Sigma}^{tm}$) and multiplying by $\sqrt{C_{sn}}$. Or it can be done at the level of the covariance matrices, as in [HO17, Sec. 5.3.3], which is the preferred technique discussed in the next section.

Estimates of the variances of the quadratures $\left\langle R_{sn}^2 \right\rangle$ (in the frequency band where it is white) are on the diagonal of the covariance matrix of shotnoise data $\mathbb{\Sigma}_{sn}$. Moreover, $\mathbb{\Sigma}_{sn} = \mathbb{\Sigma}_{sn}^{tm}$ because applying the temporal profile to idealised shotnoise (white-noise) does not change the covariance matrix.[8] If the entries on the diagonal of $\mathbb{\Sigma}_{sn}^{tm}$ are the same up to the statistical uncertainty, then we use the minimal diagonal value of $\mathbb{\Sigma}_{sn}^{tm}$ as calibration factor

$$1/2 = C_{sn} \min\left[\mathrm{diag}\left[\underline{\underline{\Sigma}}_{sn}^{tm}\right]\right]. \tag{H.10a}$$

Taking the minimal value is a conservative choice because the result of the calibration underestimates the shotnoise level, thus overestimating the calibrated noise floors of signal and shotnoise; an overestimated shotnoise floor (after calibration) is like a thermal component that cannot be interpreted (falsely) as squeezing by the entanglement test, thus mitigating the daunting risk of false positive detection of entanglement.[9]

8. Indeed,

$$\mathbb{\Sigma}_{sn}^{tm} = \int dt\, dt'\, F_\alpha(t) \left\langle \mathbf{R}_{sn}(t)\mathbf{R}_{sn}(t')^T \right\rangle_{sym} F_\beta(t')^T = A\delta_{\alpha\beta}\sigma_{sn}$$

where we used that the processes that generated $\mathbf{R}_{sn}$ are white, uncorrelated, and with the same fluctuation amplitude $A = 1/C_{sn}$. $\delta_{\alpha\beta}$ comes from the orthonormalisation of the mode functions Eq. (8.12). For a single mode, the covariance matrix of shotnoise is $\sigma_{sn} \coloneqq \mathbb{I}_2/2$ in dimensionless (shotnoise) units, cf. Eq. (A.2).

9. This is different from the calibration proposed by Jason in [HO17, Sec. 5.3.3], where they use the mean of the diagonal entries of the reconstructed vacuum state. Moreover, here, the calibration factor C_{sn} accounts for the photo-detector's efficiency η_d (cf. Eq. (F.14)), while it explicitly doesn't in Jason's method. Lastly, they propose to perform the calibration after compensating for passive losses (discussed in the next section H.7).

We define the darknoise-corrected and shotnoise-calibrated estimated covariance matrices, s = sig or sn,

$$\varpi_s = C_{sn}\underline{\Sigma}_s. \tag{H.10b}$$

One is then in a position to perform any entanglement test on that estimate of the early–late state, as explained in Sec. 8.3. We explain the practical procedure in Sec. H.8 below.

Idealised vacuum noise is perfectly uncorrelated so that its covariance matrix is diagonal: $\Sigma_{sn}^{tm} \propto \sigma_{sn} = \sigma_{vac} \coloneqq \mathbb{I}_2/2$ Eq. (A.2). But imperfect – non-white – frequency response of the detection scheme might introduce finite non-diagonal elements in the reconstructed vacuum state. For broad Lorentzian filtering mode functions (i.e. with large Γ), we expect larger non-diagonal elements as more of the non-flat frequency features are picked up by the Lorentzians. Moreover, finite statistics leave an uncertainty scaling like $1/\sqrt{N_{pp}}$. If the latter is not the dominating reason for finite non-diagonal elements in Σ_{sn}^{tm}, then it is not a good characterisation of shotnoise – and one cannot use it for calibration (or detection inefficiencies compensation, cf. Sec. H.7). See also Sec. 11.1, [HO17, Sec. 5.11], and [MN17, Sec. 10.4] on witness values of shotnoise data "diving" below the separability bound due to the detection band-pass transfer function.

It can be that the measured variances of phase and amplitude quadratures are different [10], as it is for example the case in the signal data of the membrane datasets as can be seen in Fig. 10.1 where the noise floors of the signal (in blue) PSD are at different heights. In that case, one must calibrate the data of each quadrature independently. In Fig. 10.1 one also sees that the noise level of the phase of shotnoise (red) and signal (blue) are compatible because they are at the same height, while the level of the amplitude quadratures differs significantly between both measurements. This is much more problematic because it means that both measurements cannot be compared, in particular we cannot use the shotnoise to calibrate the signal data. In that case, one can still calibrate the signal to shotnoise units using the noise floor of the signal measurement as the reference. Any claim based on that strategy is necessarily weaker because vacuum fluctuations are not characterised independently; moreover, the heavy-tail of the Lorentzian mechanical peaks can lead to the overestimation of the noise floor, which is non-conservative for entanglement detection (i.e. it can lead to false positive detection).

10. This is for instance the case if the amplification (or local oscillator power) in both homodyne arms of a dual-rail homodyne detector is different (cf. Sec. F.3).

H.7 DETECTION INEFFICIENCY COMPENSATION

Detection inefficiencies are full-fledged decoherence mechanisms leading to irreversible loss of coherence and information. Therefore there is no hope of recovering what has been lost (quantum coherence) in the sense that the correction can "fix the state". However, given a model for the information loss and a characterisation of its parameters, it is possible to partially recover some *knowledge* of the state by inverting the lossy dynamics. This is, in essence, the method we present here to compensate for inefficiencies.

Measurement records of both quadratures were denoted $\mathbf{R}_s$ above – it is a 2-vector of N measurement realisations (i.e. a 2-by-N matrix) – where $s = \text{sig}$, sn, and dn, for measurements of signal, shotnoise, and darknoise, respectively. Then the covariance matrices estimated [cf. Eq. (H.4)] from this record was called $\mathbb{\Sigma}_s^{\text{tm}}$. It is an estimate of $\Sigma_{\text{DRH}}^{\text{tm}}$ when σ_s is $\sigma_{\text{sig}}^{\text{tm}}$ in Eq. (F.17) (where the superscript indicates that the state of the dual-rail homodyne output is in expressed in terms of the early–late modes). Similarly, $\mathbb{\Sigma}_{\text{sn}}^{\text{tm}}$ estimates the case where $\sigma_s = \sigma_{\text{sn}}^{\text{tm}} = \sigma_{\text{sn}}$ [cf. derivation of Eqs. (H.10)]; and $\mathbb{\Sigma}_{\text{dn}}^{\text{tm}}$ is an estimate for $\Sigma_{\text{dn}}^{\text{tm}}$ when no light enters the photodetectors ($\alpha = 0$).

Inverting Eq. (F.17) gives the postprocessing procedure to obtain an estimate of $\sigma_{\text{sig}}^{\text{tm}}$ from $\mathbb{\Sigma}_{\text{sig}}^{\text{tm}}$

$$\sigma_{\text{sig}}^{\text{tm}} \approx \underline{\sigma}_{\text{sig}}^{\text{tm}} \coloneqq \frac{2}{\eta_d \nu \eta_{\text{opt}}} \left[\frac{\left(\mathbb{\Sigma}_{\text{sig}} - \mathbb{\Sigma}_{\text{dn}}\right)}{2|\alpha|^2 \eta_d} - \left(1 - \eta_d \nu \frac{\eta_{\text{opt}}}{2}\right) \sigma_{\text{sn}} \right] \tag{H.11a}$$

$$= \frac{1}{\eta_{\text{det}}} \left[\sigma_{\text{sig}}^{\text{tm}} - (1 - \eta_{\text{det}})\, \sigma_{\text{sn}} \right]. \tag{H.11b}$$

In the first line, the subtraction in the rounded parenthesis is darknoise correction Eq. (H.7); the division by $C_{\text{sn}} = 2|\alpha|^2 \eta_d$ is the shotnoise unit calibration of Eqs. (H.10).[11] The remaining expression in the second line is what we refer to as the *inefficiency compensation*.

This is different from [HO17, Sec. 5.3.3 and App. C.5] where they use the darknoise-corrected and shotnoise-calibrated estimate of the vacuum state ϖ_{sn} instead of σ_{sn}.[12] The difference between both are the amplitude of the diagonal elements which are smaller in σ_{sn} due to our conservative shotnoise unit calibration Eqs. (H.10). In the compensation formula Eq. (11.2), our choice is therefore more conservative because it amounts to compensating less. Secondly, ϖ_{sn}

11. For the readers concerned that the operators and scalars forming $\mathfrak{h}$ in this section are dimensionless while $\mathbf{R}_s$ is in Volts and the estimated $\mathbb{\Sigma}_s$ in Volts squared, they can multiply $\mathfrak{h}$ by a detector gain G in Volts.

12. In [HO17, Sec. 5.3.3] the calibration factor is independent of the photo-detector's efficiency η_d and the calibration happens after compensating for passive posses. This leads to the difference in treatment of the detection efficiency and visibility in their treatment.

has finite non-diagonal elements, e.g. due to remaining correlations in the measurement records (relating to the necessarily non-white spectrum of real data) or finite statistics. The assumption is that these remaining imperfect non-diagonal elements are not significant so that the estimated shotnoise state can be used as reference in the units calibration (cf. Sec. H.6). Therefore, if compensating with σ_{sn} makes the compensated state entangled while it is separable with σ_{sn}, then this must be attributed to its non-diagonal elements. This means than that the remaining correlations in σ_{sn} *are* significant and it is not an accurate estimate of vacuum noise. This in turns implies that it cannot be used for the calibration as a reference of quantum noise amplitude.

H.7.1 *Gaussian channel formalism*

The results of Eqs. (F.17) (and consequently (H.11a)) can be derived with the formalism of Gaussian channels [Wee+12; EP03; EP02; Hol21]; see also [SC07, Sec. 2] for a smooth introduction. The completely positive maps [NC10] that leave Gaussian states Gaussian are the *Gaussian channels* (cf. Sec. 3.3). Given the covariance matrix of a Gaussian state at the input of such a channel σ_{in} and its vector of first moments $\mathbf{m}_{in}$, then the output state is given by

$$\sigma_{out} = X\sigma_{in}X^T + Y \tag{H.12a}$$

$$\mathbf{m}_{out} = X\mathbf{m}_{in} \tag{H.12b}$$

where X and Y are matrices, Y is symmetric, and they fulfil the condition

$$Y + i\,\frac{\Omega}{2} - i\,X\frac{\Omega}{2}X^T \geqslant 0. \tag{H.12c}$$

This is the complete mathematical description of the physical concepts introduced in Sec. 3.3.

The Gaussian channel model for passive losses has $X = \sqrt{\eta}\mathbb{I}$ and $Y = (1-\eta)\sigma_{sn} = (1-\eta)\mathbb{I}/2$. The dual-rail setup of Fig. F.4 is a series of four loss channels per arm – There are 5 beam splitter per arm, but, in our configuration, the amplifying beam splitter in front of the homodyne detectors is not a loss channel since both its output ports are detected and its added noise is cancelled in the balanced configuration $\eta_h = 0.5$. The cascade of two beam splitters gives with Eqs. (H.12)

$$\sigma_{out} = \eta_2\eta_1\sigma_{in} + (1-\eta_2\eta_1)\sigma_{sn}. \tag{H.13}$$

The pattern extends to the four beam splitters of the DRH detector and we find

$$\sigma_{DRH} = \eta_d\eta_{DR}\nu\eta_{opt}\sigma_s + (1-\eta_d\eta_{DR}\nu\eta_{opt})\sigma_{sn}. \tag{H.14}$$

It is the same as Eq. (F.17) found above – up to the additive classical darknoise contribution and the amplification by the LO. The method here is simpler and less error prone compared to the explicit computation of Apps. F.3 and F.2 but it hides the (very many) assumptions necessary to get there: identical photo-detector efficiencies, perfect homodyne balancing, identical visibility of both homodyne detectors, identical LO intensities, perfect $\pi/2$ phase shift between both homodyne detectors, and uncorrelated vacuum noise inputs.

H.8 ENTANGLEMENT TESTS IN PRACTICE

Consider the darknoise-corrected and shotnoise-calibrated covariance matrices σ^{tm}_{sig} (for different filtering bandwidths Γ_g). If they are 4-by-4, so that the early and late partition are single mode, then the PPT-criterion Eq. (3.17) is necessary and sufficient for entanglement – equivalently, the logarithmic negativity is a measure of entanglement (cf. Sec. 3.4 for details on Gaussian entanglement tests). In any case, they are superior to the EPR-variance test, which is only sufficient. If the early and late parties are composed of $n > 1$-modes (with $4n$-by-$4n$ covariance matrices), then the PPT-criterion is only sufficient for entanglement – and the logarithmic negativity is an equivalent sufficient criterion. On the other hand, the optimal witness is still necessary and sufficient in this scenario [HE06], therefore it is the test we use to analyse experimental data.

Given the estimated state, we need to optimise the witness matrix W_{opt} (only) for bi-partite entanglement across the fixed early–late partition. For this, we use the Matlab library available from [HE06]; the corresponding semi-definite optimisation problem is solver with the CVX package [GB14]. σ^{tm}_{sig} are given as input to the function and the output is the optimal $4n$-by-$4n$ witness matrix W_{opt} that minimises $\mathrm{Tr}\left[W_{opt}\sigma^{tm}_{sig}\right] =: w_{opt}$. For each bandwidth Γ_g, one records the optimal witness value $w_{opt,g}$: plots of w_{opt} against Γ are the typical output of the analysis; we call these plots *witness plots* (like Fig. 9.1 for example).

When $n > 1$-modes are accounted for in each temporal party, one may test different combinations of modes by tracing out the relevant rows and columns of σ^{tm}_{sig}. The relevant rows and columns depend on the ordering of the demodulated modes as explained in Secs. H.4.1. For example, if $n = 4$ and I want the witness plot for the first [13] mode only (the target), then I trace out rows and column 3 to 8 (early sector) and 11 to 16 (late sector) in σ^{tm}_{sig}; if I want the witness plot for mode 1 and 4, then I trace out rows and columns 3 to 6 and 11 to 14. [14]

13. Here, count starts at 1, like in regular maths, Matlab and Mathematica – unlike in Python or C.

14. $4n$-by-$4n$ matrices are for *single-sided evaluation*. For *two-sided evaluations* (cf. Sec. H.4.2) then σ^{tm}_{sig} is $8n$-by-$8n$ and the tracing also depends on the ordering of the

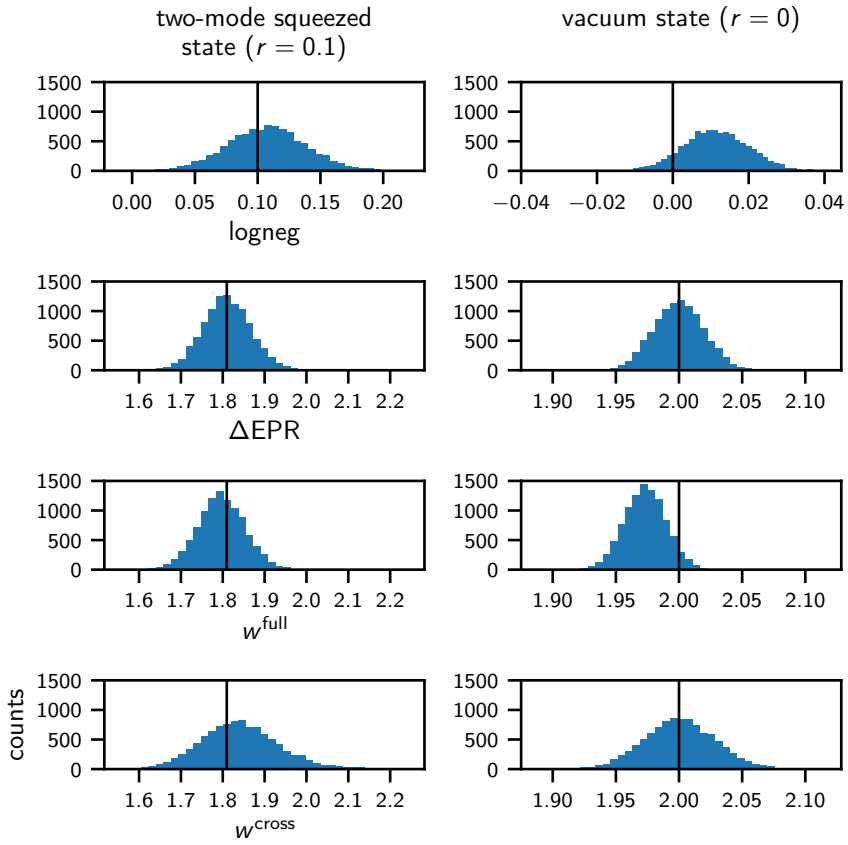

Figure H.1 In the left column, we sample 1000 data points from a bi-variate Gaussian distribution corresponding to a two-mode squeezed state Eq. (A.21) with real squeezing parameter $\xi = r = 0.1$, cf. Sec. A.4. This simulates a pulsed time trace of signal as in Sec. H.3. We estimate the 4-by-4 covariance matrix of the simulated data set and apply different entanglement tests indicated on the abscissa. We repeat the procedure 10^4 times and make histograms of the results of the different entanglement tests. The black solid lines are the result of the entanglement test on the (exact) two-mode squeezed state. In the right column, we sampled from the distribution of a two-mode ground state (i.e. $r = 0$) for comparison. Positive values of the logarithmic negativity measure the entanglement, and Δ_{EPR} and optimised witness values below 2 correspond to entanglement (cf. Sec. 3.4). The logarithmic negativity and the optimised witness over the entire data sets w^{full} are biased towards more entanglement, while the cross-validated optimised witness w^{cross} is biased towards separability. We checked systematically for more 100 to 10^4 samples drawn from the distributions and 100 to 10^5 repetitions: we found that these biases remain but their magnitude decreases as the number of samples increases.

There are several ways to find the optimal witness matrix W_{opt} from the data. Firstly, one can use the exact analytical code to find the expected state $\sigma_{\text{sig}}^{\text{tm}}$, feed it into the optimisation `BiWit()` to obtain $W_{\text{opt}}^{\text{thry}}$, and apply it to the estimated state to get $w_{\text{opt}}^{\text{thry}} = \text{Tr}\left[W_{\text{opt}}^{\text{thry}} \sigma_{\text{sig}}^{\text{tm}}\right]$. Because the model necessarily misses some of the real processes, we expect that $\sigma_{\text{sig}}^{\text{tm}}$ can be fairly different from $\sigma_{\text{sig}}^{\text{tm}}$ (or the "true" state of the temporal modes approximated by $\sigma_{\text{sig}}^{\text{tm}}$) so that the witness matrix is sensibly sub-optimal.

Secondly, one can use the entire information in the time trace and find the optimal witness matrix $W_{\text{opt}}^{\text{full}}$ from `BiWit()` applied to $\sigma_{\text{sig}}^{\text{tm}}$ estimated with the entire data set; we denote the corresponding witness values $w_{\text{opt}}^{\text{full}}$. This correlates the entanglement test to the imperfectly reconstructed covariance matrix and it can happen that the optimisation procedure identifies imperfections in $\sigma_{\text{sig}}^{\text{tm}}$ (e.g. due to finite sampling) as entanglement features and optimise over them. This leads to a bias towards entanglement, which is not conservative in terms of preventing false positive detection of entanglement; see Fig. H.1 for an example of this bias due to finite statistics.

To avoid this bias, the method adopted in the evaluations presented in this work uses a *cross-validated* optimised witness scheme described in Sec. 11.1. This method is (slightly) biased towards separability, as is shown in Fig. H.1; this is conservative and mitigates possible false positive detection of entanglement.

Figure H.1 also shows how logarithmic negativity and EPR-variance are biased due to finite sampling fluctuations. The former is biased towards entanglement, which is yet another reason not to use it; Δ_{EPR} seems unbiased on the other hand. The figure also shows the bias upon sampling from the ground state and we see similar biases. Importantly, in order to make the biases visible in the histograms, the number of samples drawn from the simulated distribution and the number of repetitions was kept relatively low compared to the analysis of real data sets. A systematic study with larger numbers showed that the biases decrease but remain.

H.9 CONFIDENCE INTERVALS WITH THE BOOTSTRAP METHOD

As highlighted in the numerical experiment that generated Fig. H.1, finite sample size leads to variable estimates of entanglement of the state; we see that the cross-validated optimised witness distribution is slightly broader than the other, accounting for the fact that it uses only half of the data to be reconstructed. Moreover, the measured

second sideband modes (recall, two-sided evaluation involves modes at frequencies ω_1 and $-\omega_1$). For convenience, one can systematically perform two-sided evaluations and trace out the second sideband in $\sigma_{\text{sig}}^{\text{tm}}$ to recover a *single-sided* evaluation.

record might be affected by some additional (hopefully small) uncharacterised technical noises or drifts over the course of a measurement campaign. To quantify the uncertainty on the cross-validated optimal witness values w^{cross} (cf. Sec. H.8), we re-sampled the estimated states with the *bootstrap* method [ET94] and see how the w^{cross} are distributed with respect to a single witness matrix $W_{\text{opt}}^{\text{cross}}$. The advantage of this method is that it is agnostic of the noisy processes and how the data are processed – it explores and realises the variability in the data set.

Before we describe the method, we note that, for our purpose (of witnessing entanglement only), it is not necessary to quantify the uncertainty on the optimised witness matrix $W_{\text{opt}}^{\text{cross}}$. This is because we make statements only when entanglement is detected, and one does not need to say how confident we are in the prescribed measurement corresponding to the witness – if it works, it works. For more specific statements on the nature of the entanglement, what is really the optimal witness, etc., then it can be interesting to bootstrap resample the optimised witness and see their variability. This is not in the scope of this work.

The optimisation algorithm processes the total uncertainty of $\varpi_{\text{sig}}^{\text{tm}}$ in a non-trivial way so that propagating it into an uncertainty on $W_{\text{opt}}^{\text{cross}}$ is possibly complicated. The method here involves computing $W_{\text{opt}}^{\text{cross}}$ only once with half of the data – i.e. no resmapling – and apply it to the bootstrapped covariance matrices. This bypasses the difficulty of quantifying the uncertainty on the witness matrix and remains a conservative approach (in terms of avoiding false positive detection of entanglement) because $W_{\text{opt}}^{\text{cross}}$ is, in principle, not optimal for any of the covariance matrices resampled by the bootstrap. One could imagine applying the bootstrap on the first half of the data to produce a distribution of witness matrices and thus sample its variability; then apply them to a bootstrapped set of covariance matrices reconstructed with the second half of the data.

The bootstrapping is thus performed on the second half of the data $\mathbf{R}^{\text{tm}}$ that we denote $\mathbf{R}^{\text{cross}}$. Bootstrapping consists in estimating the covariance matrix (which we had called ϖ^{cross}) from sets of randomly chosen samples from $\mathbf{R}^{\text{cross}}$ – the samples are drawn with replacement with uniform probability distribution [ET94]. Explicitly, the traces $\mathsf{R}_{\alpha}^{\text{cross}}$ from $\mathbf{R}^{\text{cross}}$ each have $\mathsf{K} \coloneqq \lfloor \mathsf{N}_{\text{pp}}/2 \rfloor$ samples $\mathsf{R}_{\alpha,\mathsf{k}}^{\text{cross}}$; draw from them K times with replacement and uniform $1/\mathsf{K}$ probability; this forms a bootstrap resampled traces $\mathsf{R}_{\alpha}^{\text{boot}}$ (most probably different from $\mathsf{R}_{\alpha}^{\text{cross}}$ because some samples appear multiple times); compute from $\mathbf{R}^{\text{boot}}$ the the thus resampled estimated state ϖ^{boot} (also probably different from ϖ^{cross}); apply the witness $W_{\text{opt}}^{\text{cross}}$ and obtain w^{boot} (different from w^{cross}); repeat the procedure N_{boot} times to generate a set $\{w^{\text{boot}}\}$ of N_{boot} bootstrapped resampled witness values.

The spread of the distribution of $\{w^{\text{boot}}\}$ is our estimate of the uncertainty of the witness values of the data set. In order to capture possible asymmetry in the distribution, we use the 5/95 percentile confidence interval of $\{w^{\text{boot}}\}$ as error bars for the result w^{cross}. Other choices of results are possible: e.g. the mean or the median of $\{w^{\text{boot}}\}$, but we opt for the unbootstrapped value w^{cross} because it is the one making use of most of the information in the available data. It is worth visualising the distribution of values to assess that it is "peaked" around w^{cross} so that the choice of error bars is meaningful – we performed regular checks and it has always been the case.

H.9.1 *Improved confidence interval*

Increasing the number of pulse-pairs N_{pp} does shrink error bars. Increasing the number of bootstrap resamplings as well and we see saturation for $N_{\text{boot}} > 500$.

The duration of experimental datasets is typically limited by the stability of the experiment or some technical reasons. There is no doubt that most of them have existing technological solutions that come with some experimental cost – potentially very high.

Rather than measuring longer, Lorenzo Magrini proposed to overlap the pulse-pairs in order to increase their number: that is, instead of defining pulse-pairs sequentially one after the other without overlap (as in Eq. (H.2)), we modify their starting point so that they overlap. For instance, if a single temporal mode needs 100 samples (i.e. the mode functions are truncated after 100 samples), then a pulse-pair has 200 samples (for no separation between the pulses, $T_{\text{sep}} = 0$). The first pulse-pair then terminates at sample 200 and the next would start at sample 201 (and end at sample 400). Instead, one could start the second pulse-pair at sample 51 so that it terminates at samples 250; the third pulse-pair would be between sample 101 to 300, etc. In so doing, one has increased the total number of pulse-pairs for the same time trace by a factor 4 (in that example).

From a pure statistical point of view, there is no fundamental added information in doing so because the data set is the same and no additional information is available. On the other hand, the temporal modes decay exponentially fast, effectively suppressing the information in their tails (especially at larger bandwidths when they are particularly short in time), by overlapping the pulse-pairs, one retrieves the information suppressed by the exponential decays.

H.10 PHYSICALITY TEST

The covariance matrices we reconstruct from experimental data are estimates of the measured physical state – they approximate it. Possibly the approximation is poor and the reconstructed matrix does not correspond to a quantum state. Indeed, we saw in Sec. 3.2 that the second moments of quantum states must be "a little more than positive definite" in order to fulfil Heisenberg uncertainty relations Eq. (3.9)

$$\sigma_{\text{sig}}^{\text{tm}} - \frac{\mathrm{i}}{2}\Omega \geqslant 0. \tag{H.15}$$

In fact, this condition characterises exactly the set of covariance matrices describing (entirely) all the Gaussian states (up to the independent first moments displacements) [AI07]: i.e. all matrices fulfilling this condition correspond to all undisplaced Gaussian states of the Hilbert space – by extension to non-zero first moments, they correspond to all the Gaussian states. The condition is necessary for non-Gaussian states. This Heisenberg bound can be formulated in terms of symplectic eigenvalues (i.e. the eigenvalues of $\left|\mathrm{i}\,\Omega\sigma_{\text{sig}}^{\text{tm}}\right|$, cf. Sec. 3.4.3) that must be $\geqslant 1/2$.

We systematically test Eq. (H.15) on the estimated covariance matrices: if $\sigma_{\text{sig}}^{\text{tm}}$ satisfies it, we say that it is *physical*; if it doesn't, we say that it is *unphysical*. This is analogous to checking that a density matrix estimated from data or computed numerically is Hermitian, of trace 1, and semi-positive definite. In principle, the entanglement tests presented in this work (in Sec. 3.4) are meaningful under the assumption that the tested covariance matrix is a (quantum) state, i.e. that it is physical. Therefore, one should discard unphysical estimates. As noted in [Gut+20, Sec. IV.C], for states of high purity, statistical fluctuations and other technical imperfection in the data may quickly make $\sigma_{\text{sig}}^{\text{tm}}$ unphysical.

Figure H.2 shows the effects of finite sampling on physicality for a squeezed state (with real squeezing parameter $\xi = r = 0.1$) and for the vacuum state ($r = 0$). With the same method as in Fig. H.1, we sample the distribution corresponding to the state to simulate a time trace (the y-axis of the figure is the number of samples in these simulated traces). We reconstruct the covariance matrix of the thus simulated time trace and determine whether it is physical or not. We repeat the procedure to determine how often the estimated state is physical (the number of repetitions is the x-axis of the figure). For large statistics (top right corner), between 5 and 10% of the reconstructed covariance matrices are physical. The lower part of the plots shows that if the time traces do not contain enough samples, then between 1 and 5% of the matrices are physical. And the larger portion of physical estimates on the top left of the plots is probably due to the lack of repetition.

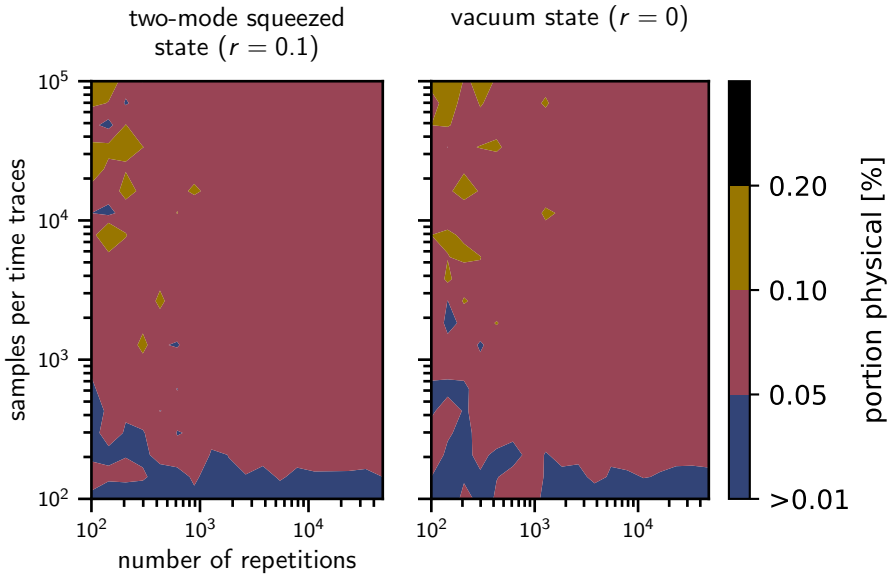

Figure H.2 Portion of physical covariance matrices in a sample size given by the number of repetitions on the x-axis, and for covariance matrices estimated out of traces of length given on the y-axis. The procedure is the same as in Fig. H.1 but we apply the physicality test instead of the entanglement tests.

Therefore, one must expect that most of the reconstructed states from experimental data may be unphysical if the state is close to being pure. We expect that mixedness will make the reconstructed state more likely to be physical.

H.11 ASYMMETRIC FILTERING BANDWIDTHS AND OVER-FITTING

We looked at asymmetric decay rates of the temporal functions demodulating the first and second modes; we denote them Γ_j, $j = 1, 2$. On Figure H.3 we show the analytical simulation of this scenario (3-mode simulation, 2-mode 1-sided evaluation). A systematic study of numerical simulations or experimental data would have been too time-consuming and we did not pursue it. We opted for a (naive) two-step gradient-decent optimisation on the experimental data (2-mode 2-sided evaluation). The logic is depicted on Figure H.3. First, we evaluate the data in the standard way, i.e. sweeping over symmetric bandwidths $\Gamma_1 = \Gamma_2$ (curved solid black line in the figure). Then, we fix Γ_2 to the value yielding minimal witness value and sweep the bandwidth Γ_1 of the target mode (keeping Γ_2 fixed, i.e. it is still a 2-mode evaluation); this is the upper solid line in the figure, which is not precisely correct for visibility. We fix Γ_1 achieving the minimum witness value and sweep Γ_2 (horizontal line). The bandwidth realising the minimal witness we call Γ_2^*: this is the white diamond in the figure. We found $\Gamma_2^* \approx 50$ kHz from the experimental data (dashed line). A

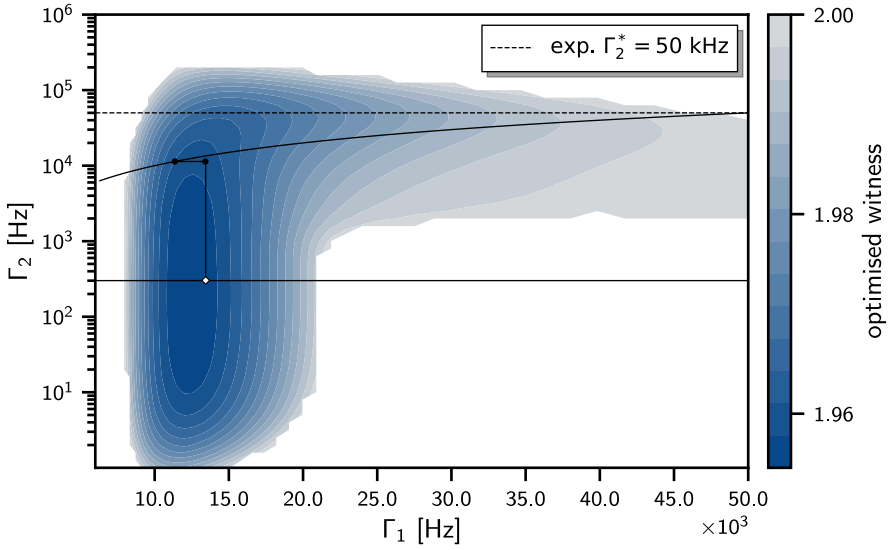

Figure H.3 Optimised witness of analytically computed temporal modes states: 3-mode simulation, 2-mode 1-sided evaluation. The bandwidths of the filters demodulated the two modes were chosen independently $\Gamma_1 \neq \Gamma_2$. The continuous black lines illustrate the two-step gradient decent optimisation strategy we used with experimental data (it is an exaggerated drawing); in this semi-log plot, the curves line is for the symmetric $\Gamma_1 = \Gamma_2$ sweep.

last sweep over Γ_1 (lower full width line) for fixed Γ_2^* yields the witness curves on Fig. H.4 (comparable to the lower right plot of Fig. 11.3). Note that, in the search for Γ_2^* with the experimental data, none of the preliminary sweeps showed entanglement, contrary to our depiction in Fig. H.3.

To obtain these results, we had to increase the statistics of the pulse-pairs by a factor five with the pulse-overlap method of H.9.1. To ensure that the overlapping does not introduce additional (auto-) correlations among the pulse-pairs, we included an additional – dummy – temporal mode demodulating at 310 kHz where the signal data are spectrally flat; cf. PSD in Fig. 11.2. The corresponding witness curves (1&2-mode evaluations) are significantly above the separability bound, indicating no entanglement-like correlation introduced by the pulse-pair overlap.

The two panels in Fig. H.4 show the effect of the compensation for inefficiencies. Using the original compensation formula [HO17, Sec. 5.3.3], involving the shotnoise covariance matrix estimated with the shotnoise data (cf. Sec. H.7), leads to even larger violation. In the first evaluation without improved statistics, the compensation using the ideal shotnoise state Eq. (11.2) lead to separable witness values on average. The round of discussions of these results concluded that, because the use of experimentally estimated shotnoise was decisive to witness entanglement, we could not exclude that the correlations highlighted by the witness are not due to the imperfection of the

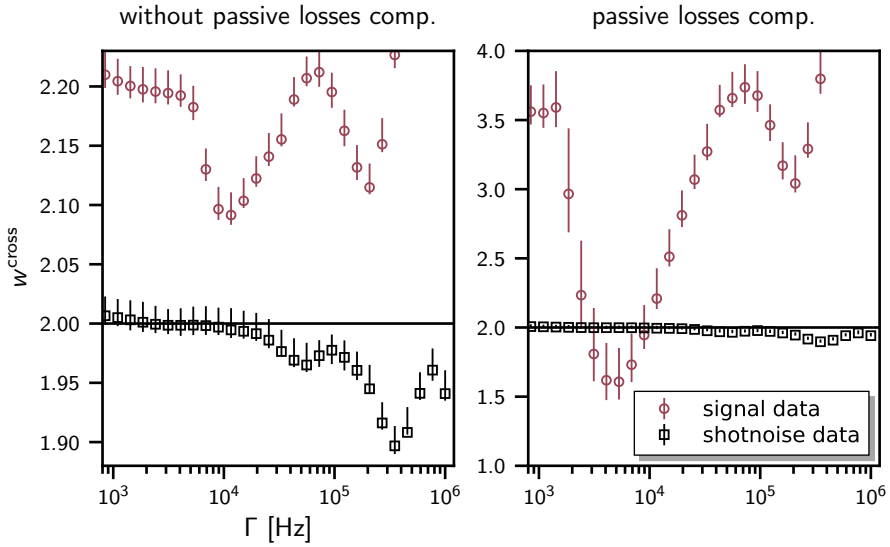

Figure H.4 2-modes 2-sided witness plots with fixed bandwidth of the second temporal mode (x-motion) $\Gamma_2^* = 50$ kHz. Left panel is without compensation for passive losses and right panel is using Eq. (H.11a) (for total detection losses $\eta_{\text{det}} = 0.11$ [Mag+22]).

reconstructed shotnoise state (e.g. due to finite statistics or effects similar to the "diving" witness values discussed around Fig. 11.1). It came to me as a surprise that, with the improved statistics, we would witness entanglement with the inefficiency compensation we propose Eq. (11.2). Although it would be more conservative not to compensate, I think that it is legitimate because there are Gaussian entangled states that become separable due to passive losses, as described in detail [Bar+11] for the $1+1$-mode scenario.

The witness curve on the right panel of Fig. H.4, on it own, meets all the criteria to be a successful detection of entanglement between the early and late temporal parties. It is not shown here, but all the reconstructed covariance matrices (also by the bootstrap resampling) that are entangled are also physical; cf. Sec. H.10.

Nevertheless, I do not have enough confidence in this results to call it a successful entanglement detection for the following reasons. None of the sweep in the two-step gradient-decent procedure showed entanglement and changing Γ_2^* by 10kHz is enough to loose entanglement: to my current knowledge, it is a special point and I could not find a behaviour in the experimental data that resemble the analytical simualtions of Fig. H.3. Additionally, I must acknowledge that we have been studying this precise dataset intensively: tweaking and optimising the analysis. Early on, when we started trying out various alternatives (relatively systematically) and optimising accordingly to the results, Sebastian Hofer pointed out that we might be *over-fitting* the data: i.e. introducing a global bias of the analysis towards the

wanted result, *given the data set*. I think this is relevant point and we cannot exclude it with that dataset.

This concern can be dissipated by applying the same procedure to another set of measurements from that experiment and applying the same logic, with the steps set before seeing the results. Datasets were available, but they revealed no entanglement. A closer look showed that the frequency of the target mode drifted by about a kHz in the course of the measurement runs. The requirement on the accuracy of the filter demodulation Eq. (9.48) indicates that this might be the reason for the failure with the additional datasets (although the relation was derived for devices with a cavity); see Sec. 9.4.4.

LIST OF FIGURES

LIST OF TABLES

BIBLIOGRAPHY

[Aas+15] J Aasi et al. (LIGO Scientific Collaboration), « Advanced LIGO », Class. Quantum Gravity **32**, 074001 (2015) (cit. on pp. 45, 55).

[Aba+11] J. Abadie et al. (LIGO Scientific Collaboration), « A gravitational wave observatory operating beyond the quantum shot-noise limit », Nat. Phys. **7**, 962–965 (2011) (cit. on pp. 5, 138, 147).

[Abb+16] B. P. Abbott et al. (LIGO–Virgo Collaboration), « Observation of gravitational waves from a binary black hole merger », Phys. Rev. Lett. **116**, 061102 (2016) (cit. on p. 5).

[Ace+19] F. Acernese et al. (Virgo Collaboration), « Increasing the astrophysical reach of the advanced Virgo detector via the application of squeezed vacuum states of light », Phys. Rev. Lett. **123**, 231108 (2019) (cit. on pp. 5, 138, 147).

[AI07] G. Adesso and F. Illuminati, « Entanglement in continuous-variable systems: recent advances and current perspectives », J. Phys. A **40**, 7821–7880 (2007) (cit. on pp. 23–26, 28–30, 32–33, 115, 147–149, 213).

[ARL14] G. Adesso, S. Ragy and A. R. Lee, « Continuous Variable Quantum Information: Gaussian States and Beyond », Open Syst. Inf. Dyn. **21**, 1440001 (2014) (cit. on pp. 21–22, 75, 152).

[AD77] A. Ashkin and J. M. Dziedzic, « Feedback stabilization of optically levitated particles », Appl. Phys. Lett. **30**, 202–204 (1977) (cit. on p. 193).

[ADR82] A. Aspect, J. Dalibard and G. Roger, « Experimental test of Bell's inequalities using time-varying analyzers », Phys. Rev. Lett. **49**, 1804–1807 (1982) (cit. on p. 3).

[AGR82] A. Aspect, P. Grangier and G. Roger, « Experimental realization of einstein-podolsky-rosen-bohm gedankenexperiment: a new violation of Bell's inequalities », Phys. Rev. Lett. **49**, 91–94 (1982) (cit. on p. 3).

[AGR81] A. Aspect, P. Grangier and G. Roger, « Experimental tests of realistic local theories via Bell's theorem », Phys. Rev. Lett. **47**, 460–463 (1981) (cit. on p. 3).

[AKM14] M. Aspelmeyer, T. J. Kippenberg and F. Marquardt, « Cavity optomechanics », Rev. Mod. Phys. **86**, 1391–1452 (2014) (cit. on pp. 4, 18, 28, 35, 38, 48–49, 56, 71, 145).

[BYZ94] L. E. Ballentine, Y. Yang and J. P. Zibin, « Inadequacy of Ehrenfest's theorem to characterize the classical regime », Phys. Rev. A **50**, 2854–2859 (1994) (cit. on p. 28).

[BW98] K. Banaszek and K. Wódkiewicz, « Nonlocality of the Einstein-Podolsky-Rosen state in the Wigner representation », Phys. Rev. A **58**, 4345–4347 (1998) (cit. on pp. 154–155).

[Bar+11] F. A. S. Barbosa, A. J. de Faria, A. S. Coelho, K. N. Cassemiro, A. S. Villar, P. Nussenzveig and M. Martinelli, « Disentanglement in bipartite continuous-variable systems », Phys. Rev. A **84**, 052330 (2011) (cit. on pp. 44, 49, 101, 137, 216).

[BHS19] L. Barsotti, J. Harms and R. Schnabel, « Squeezed vacuum states of light for gravitational wave detectors », Rep. Prog. Phys. **82**, 016905 (2019) (cit. on pp. 5, 138, 147).

[Bar+19] S. Barzanjeh, E. S. Redchenko, M. Peruzzo, M. Wulf, D. P. Lewis, G. Arnold and J. M. Fink, « Stationary entangled radiation from micromechanical motion », Nature **570**, 480–483 (2019) (cit. on pp. 1, 66, 71).

[BDU23] A. Bassi, M. Dorato and H. Ulbricht, « Collapse models: a theoretical, experimental and philosophical review », Entropy **25**, 645 (2023) (cit. on p. 6).

[Bel04] J. S. Bell, *Speakable and Unspeakable in Quantum Mechanics*, 2nd Edition (Cambridge University Press, 2004) (cit. on pp. 154–155).

[Ber22] M. Bereyhi, « Ultra low quantum decoherence nano-optomechanical systems », Ph.D. thesis (École Polytechnique Fédérale de Lausanne, 2022), p. 184 (cit. on pp. 35, 45–46).

[Ber+21] D. Bersanetti, B. Patricelli, O. J. Piccinni, F. Piergiovanni, F. Salemi and V. Sequino, « Advanced virgo: status of the detector, latest results and future prospects », Universe **7**, 322 (2021) (cit. on pp. 45, 55).

[BSS15] V. V. Bochkarev, A. V. Shevlyakova and V. D. Solovyev, « The average word length dynamics as an indicator of cultural changes in society », Soc. Evol. Hist. **14** (2015) (cit. on p. 95).

[BL05] S. L. Braunstein and P. van Loock, « Quantum information with continuous variables », Rev. Mod. Phys. **77**, 513–577 (2005) (cit. on pp. 23, 147).

[BP07] H.-P. Breuer and F. Petruccione, *The Theory of Open Quantum Systems* (Oxford University Press, 2007) (cit. on pp. 16, 36–37).

[Bru+14] N. Brunner, D. Cavalcanti, S. Pironio, V. Scarani and S. Wehner, « Bell nonlocality », Rev. Mod. Phys. **86**, 419–478 (2014) (cit. on pp. 153–154).

[BC03] A. Buonanno and Y. Chen, « Scaling law in signal recycled laser-interferometer gravitational-wave detectors », Phys. Rev. D **67**, 062002 (2003) (cit. on p. 138).

[CL83] A. Caldeira and A. Leggett, « Path integral approach to quantum Brownian motion », Physica A **121**, 587–616 (1983) (cit. on pp. 37, 39).

[CG52] H. B. Callen and R. F. Greene, « On a Theorem of Irreversible Thermodynamics », Phys. Rev. **86**, 702–710 (1952) (cit. on p. 38).

[CW51] H. B. Callen and T. A. Welton, « Irreversibility and Generalized Noise », Phys. Rev. **83**, 34–40 (1951) (cit. on p. 38).

[Cat+23] L. Catani, M. Leifer, D. Schmid and R. W. Spekkens, « Why interference phenomena do not capture the essence of quantum theory », Quantum **7**, 1119 (2023) (cit. on p. 27).

[CS85] C. M. Caves and B. L. Schumaker, « New formalism for two-photon quantum optics. I. Quadrature phases and squeezed states », Phys. Rev. A **31**, 3068–3092 (1985) (cit. on pp. 29, 147).

[Che+20] J. Chen, M. Rossi, D. Mason and A. Schliesser, « Entanglement of propagating optical modes via a mechanical interface », Nat. Commun. **11**, 943 (2020) (cit. on pp. 1, 66, 71, 93, 109, 184–185).

[Chi+17] L. Childress, M. P. Schmidt, A. D. Kashkanova, C. D. Brown, G. I. Harris, A. Aiello, F. Marquardt and J. G. E. Harris, « Cavity optomechanics in a levitated helium drop », Phys. Rev. A **96**, 063842 (2017) (cit. on pp. 40, 45).

[Chu+18] Y. Chu, P. Kharel, T. Yoon, L. Frunzio, P. T. Rakich and R. J. Schoelkopf, « Creation and control of multi-phonon fock states in a bulk acoustic-wave resonator », Nature **563**, 666–670 (2018) (cit. on p. 45).

[Cla74] J. F. Clauser, « Experimental distinction between the quantum and classical field-theoretic predictions for the photoelectric effect », Phys. Rev. D **9**, 853–860 (1974) (cit. on p. 3).

[Cle03] A. N. Cleland, *Foundations of nanomechanics*, Advanced Texts in Physics (Springer, 2003) (cit. on p. 35).

[Cle+10] A. A. Clerk, M. H. Devoret, S. M. Girvin, F. Marquardt and R. J. Schoelkopf, « Introduction to quantum noise, measurement, and amplification », Rev. Mod. Phys. **82**, 1155–1208 (2010) (cit. on p. 204).

[CTDL05] C. Cohen-Tannoudji, B. Diu and F. Laloë, *Quantum mechanics, volume 1: basic concepts, tools, and applications*, 2., rev. and enl. ed. (Wiley Hermann, New York, NY Paris, 2005) (cit. on pp. 12–13, 15, 17–19, 143–144).

[CTDRG97] C. Cohen-Tannoudji, J. Dupont-Roc and G. G., *Photons and atoms* (John Wiley & Sons, Ltd, 1997) (cit. on pp. 17, 35).

[Cri+19] J. Cripe, N. Aggarwal, R. Lanza, A. Libson, R. Singh, P. Heu, D. Follman, G. D. Cole, N. Mavalvala and T. Corbitt, « Measurement of quantum back action in the audio band at room temperature », Nature **568**, 364–367 (2019) (cit. on p. 55).

[Cub+03] T. S. Cubitt, F. Verstraete, W. Dür and J. I. Cirac, « Separable States Can Be Used To Distribute Entanglement », Phys. Rev. Lett. **91**, 037902 (2003) (cit. on pp. 63, 66).

[CFZ14] T. Curtright, D. B. Fairlie and C. K. Zachos, *A concise treatise on quantum mechanics in phase space* (World Scientific, Singapore Hackensack London, 2014) (cit. on pp. 23–24).

[DK12] S. L. Danilishin and F. Y. Khalili, « Quantum Measurement Theory in Gravitational-Wave Detectors », Living Rev. Relativ. **15**, 5 (2012) (cit. on p. 115).

[DG27] C. Davisson and L. Germer, « The scattering of electrons by a single crystal of nickel », Nature **119**, pages 558–560 (1927) (cit. on p. 3).

[Del19] U. Delic, « Cavity cooling by coherent scattering of a levitated nanosphere in vacuum », Ph.D. thesis (University of Vienna, 2019) (cit. on pp. 40, 42, 44–45, 109, 120, 137, 184, 193, 195).

[Del+20a] U. Delić, D. Grass, M. Reisenbauer, T. Damm, M. Weitz, N. Kiesel and M. Aspelmeyer, « Levitated cavity optomechanics in high vacuum », Quantum Sci. Technol. **5**, 025006 (2020) (cit. on p. 42).

[Del+20b] U. Delić, M. Reisenbauer, K. Dare, D. Grass, V. Vuletić, N. Kiesel and M. Aspelmeyer, « Cooling of a levitated nanoparticle to the motional quantum ground state », Science **367**, 892–895 (2020) (cit. on pp. 40, 42, 44, 109, 151, 184, 193–194).

[Del+19] U. Delić, M. Reisenbauer, D. Grass, N. Kiesel, V. Vuletić and M. Aspelmeyer, « Cavity cooling of a levitated nanosphere by coherent scattering », Phys. Rev. Lett. **122**, 123602 (2019) (cit. on pp. 109, 193).

[Dir+24] S. Direkci, K. Winkler, C. Gut, K. Hammerer, M. Aspelmeyer and Y. Chen, « Macroscopic quantum entanglement between an optomechanical cavity and a continuous field in presence of non-markovian noise », Phys. Rev. Res. **6**, 013175 (2024) (cit. on pp. 35, 55, 73, 101, 115, 138–140, 195).

[Dos+19] J. Doster, S. Hoenl, H. Lorenz, P. Paulitschke and E. M. Weig, « Collective dynamics of strain-coupled nanomechanical pillar resonators », Nat. Commun. **10**, 5246 (2019) (cit. on p. 45).

[Dua+00] L.-M. Duan, G Giedke, J. I. Cirac and P Zoller, « Inseparability Criterion for Continuous Variable Systems », Phys. Rev. Lett. **84**, 4 (2000) (cit. on pp. 31, 67).

[ET94] B. Efron and R. Tibshirani, *An introduction to the bootstrap*, Chapman & Hall/CRC Monographs on Statistics & Applied Probability (Taylor & Francis, 1994) (cit. on pp. 129, 211).

[EPR35] A. Einstein, B. Podolsky and N. Rosen, « Can Quantum-Mechanical Description of Physical Reality Be Considered Complete? », Phys. Rev. **47**, 777–780 (1935) (cit. on pp. 29–31).

[EP03] J. Eisert and M. B. Plenio, « Introduction to the basics of entanglement theory in continuous-variable systems », Int. J. Quantum Inf. **01**, 479–506 (2003) (cit. on pp. 28–30, 207).

[EG06] J. Eisert and D. Gross, « Multiparticle entanglement », in *Lectures on quantum information* (John Wiley & Sons, Ltd, 2006) Chap. 13, pp. 237–252 (cit. on p. 21).

[EP02] J. Eisert and M. B. Plenio, « Conditions for the local manipulation of gaussian states », Phys. Rev. Lett. **89**, 097901 (2002) (cit. on p. 207).

[EBK24] N. J. Engelsen, A. Beccari and T. J. Kippenberg, « Ultrahigh-quality-factor micro- and nanomechanical resonators using dissipation dilution », Nat. Nanotechnol., 1–13 (2024) (cit. on p. 35).

[Eve57] H. Everett, « "relative state" formulation of quantum mechanics », Rev. Mod. Phys. **29**, 454–462 (1957) (cit. on p. 6).

[Fed+18] S. Fedorov, V. Sudhir, R. Schilling, H. Schütz, D. Wilson and T. Kippenberg, « Evidence for structural damping in a high-stress silicon nitride nanobeam and its implications for quantum optomechanics », Phys. Lett. A **382**, 2251–2255 (2018) (cit. on p. 55).

[Fed+13] A. Fedrizzi, M. Zuppardo, G. G. Gillett, M. A. Broome, M. P. Almeida, M. Paternostro, A. G. White and T. Paterek, « Experimental distribution of entanglement with separable carriers », Phys. Rev. Lett. **111**, 230504 (2013) (cit. on pp. 63, 66).

[Fei+19] Y. Fein, P. Geyer, P. Zwick, F. Kiałka, S. Pedalino, M. Mayor, G. S. and M. Arndt, « Quantum superposition of molecules beyond 25 kda », Nat. Phys. **15**, 1242–1245 (2019) (cit. on p. 3).

[FOP05] A. Ferraro, S. Olivares and M. Paris, *Gaussian states in quantum information*, Napoli Series on physics and Astrophysics (Bibliopolis, 2005) (cit. on pp. 174, 182).

[FV63] R. Feynman and F. Vernon, « The theory of a general quantum system interacting with a linear dissipative system », Ann. Phys. **24**, 118–173 (1963) (cit. on pp. 37, 39).

[FC72] S. J. Freedman and J. F. Clauser, « Experimental test of local hidden-variable theories », Phys. Rev. Lett. **28**, 938–941 (1972) (cit. on p. 3).

[Frö+18] F. Fröwis, P. Sekatski, W. Dür, N. Gisin and N. Sangouard, « Macroscopic quantum states: Measures, fragility, and implementations », Rev. Mod. Phys. **90**, 025004 (2018) (cit. on p. 146).

[GC85] C. W. Gardiner and M. J. Collett, « Input and output in damped quantum systems: Quantum stochastic differential equations and the master equation », Phys. Rev. A **31**, 3761–3774 (1985) (cit. on pp. 37, 39, 43).

[GZ00] C. W. Gardiner and P. Zoller, *Quantum noise: a handbook of markovian and non-markovian quantum stochastic methods with applications to quantum optics*, 2nd enlarged ed, Springer series in synergetics (Springer, Berlin ; New York, 2000), 438 pp. (cit. on pp. 24, 36–37, 39, 144, 146–147, 174–175, 182).

[Gen+08] C. Genes, A. Mari, P. Tombesi and D. Vitali, « Robust entanglement of a micromechanical resonator with output optical fields », Phys. Rev. A **78**, 032316 (2008) (cit. on pp. 50, 52, 58, 69–70, 114, 157).

[GLS16] M. G. Genoni, L. L and A. Serafini, « Conditional and unconditional gaussian quantum dynamics », Contemp. Phys. **57**, 331–349 (2016) (cit. on pp. 155, 174).

[GLM11] V. Giovannetti, S. Lloyd and L. Maccone, « Advances in quantum metrology », Nat. Photonics **5**, 222–229 (2011) (cit. on pp. 5, 54).

[GLM06] V. Giovannetti, S. Lloyd and L. Maccone, « Quantum Metrology », Phys. Rev. Lett. **96**, 010401 (2006) (cit. on pp. 5, 54).

[GV01] V. Giovannetti and D. Vitali, « Phase-noise measurement in a cavity with a movable mirror undergoing quantum Brownian motion », Phys. Rev. A **63**, 023812 (2001) (cit. on pp. 40, 70).

[Gis91] N. Gisin, « Bell's inequality holds for all non-product states », Phys. Lett. A **154**, 201–202 (1991) (cit. on p. 153).

[Giu+15] M. Giustina et al., « Significant-loophole-free test of Bell's theorem with entangled photons », Phys. Rev. Lett. **115**, 250401 (2015) (cit. on p. 3).

[GB+19] C. Gonzalez-Ballestero, P. Maurer, D. Windey, L. Novotny, R. Reimann and O. Romero-Isart, « Theory for cavity cooling of levitated nanoparticles via coherent scattering: master equation approach », Phys. Rev. A **100**, 013805 (2019) (cit. on pp. 44, 120, 137, 145, 193, 195).

[GZ15] I. S. Gradshteĭn and D. Zwillinger, *Table of integrals, series, and products*, Eighth edition (Elsevier, Academic Press is an imprint of Elsevier, Amsterdam ; Boston, 2015), 1133 pp. (cit. on pp. 83, 161–162).

[GRA86] P. Grangier, G. Roger and A. Aspect, « Experimental evidence for a photon anticorrelation effect on a beam splitter: a new light on single-photon interferences », Europhys. Lett. **1**, 173 (1986) (cit. on p. 3).

[GB14] M. Grant and S. Boyd, *CVX: matlab software for disciplined convex programming, version 2.1*, `http://cvxr.com/cvx`, 2014 (cit. on pp. vii, 208).

[Gri17] D. Griffiths, *Introduction to quantum mechanics* (Cambridge University Press, 2017) (cit. on pp. 14, 19, 143).

[Grö+15] S. Gröblacher, A. Trubarov, N. Prigge, G. D. Cole, M. Aspelmeyer and J. Eisert, « Observation of non-markovian micromechanical brownian motion », Nat. Commun. **6**, 7606 (2015) (cit. on p. 55).

[GAC10] G. Grynberg, A Aspect and F. C., *Introduction to quantum optics : from the semi-classical approach to quantized light* (Cambridge University Press, Cambridge : 2010) (cit. on pp. 12, 18, 29, 150).

[GNG19] J. Guo, R. Norte and S. Gröblacher, « Feedback Cooling of a Room Temperature Mechanical Oscillator close to its Motional Ground State », Phys. Rev. Lett. **123**, 223602 (2019) (cit. on pp. 109, 184, 189).

[Gus+14] M. V. Gustafsson, T. Aref, A. F. Kockum, M. K. Ekström, G. Johansson and P. Delsing, « Propagating phonons coupled to an artificial atom », Science **346**, 207–211 (2014) (cit. on p. 45).

[Gut+20] C. Gut et al., « Stationary optomechanical entanglement between a mechanical oscillator and its measurement apparatus », Phys. Rev. Res. **2**, 033244 (2020) (cit. on pp. 8, 53, 58, 65–66, 72, 93, 96, 98–100, 114, 124, 135, 137, 167, 213).

[Gut24] C. Gut, « Thesis supplement: texts, images, data, codes, consent letters, etc. », Zenodo, `10.5281/zenodo.11176106` (2024) (cit. on pp. vi–vii, 50, 52–53, 60, 70, 78, 83, 86, 88, 95, 99, 104, 106, 109, 117, 120–121, 162–163, 165–166, 168–173).

[Gä20] C.-M. Gärtner, « Advanced membrane architectures for multimode optomechanics », Ph.D. thesis (University of Vienna, 2020) (cit. on pp. 35, 45–46, 109, 112, 116).

[GT09] O. Gühne and G. Tóth, « Entanglement detection », Phys. Rep. **474**, 1–75 (2009) (cit. on pp. 21–22, 32).

[Hal13] B. C. Hall, *Quantum theory for mathematicians*, 1st ed., Vol. 267, Graduate Texts in Mathematics (Springer Nature, New York, NY, 2013) (cit. on pp. 12, 14–15).

[Har+20] C. R. Harris et al., « Array programming with NumPy », Nature **585**, 357–362 (2020) (cit. on p. vii).

[Hen+15] B. Hensen et al., « Loophole-free Bell inequality violation using electron spins separated by 1.3 kilometres », Nature **526**, 682–686 (2015) (cit. on p. 3).

[HO17] J. Hoelscher-Obermaier, « Generation and detection of quantum entanglement in optomechanical systems », Ph.D. thesis (University of Vienna, 2017), 211 pp. (cit. on pp. 47, 62, 73, 75, 109–113, 115–116, 122–123, 127–129, 131–132, 136, 174, 178, 182, 197, 199–202, 204–206, 215).

[Hof+23] J. Hofer et al., « High-Q magnetic levitation and control of superconducting microspheres at millikelvin temperatures », Phys. Rev. Lett. **131**, 043603 (2023) (cit. on p. 40).

[Hof15] S. G. Hofer, « Quantum control of optomechanical systems », Ph.D. thesis (University of Vienna, 2015) (cit. on pp. 18, 39–40, 48–49, 51–52, 56, 69, 71, 83, 112, 114, 133, 145, 157, 162–163, 174, 183).

[HH15] S. G. Hofer and K. Hammerer, « Entanglement-enhanced time-continuous quantum control in optomechanics », Phys. Rev. A **91**, 033822 (2015) (cit. on pp. 56, 138).

[Hof+11a] S. G. Hofer, W. Wieczorek, M. Aspelmeyer and K. Hammerer, « Quantum entanglement and teleportation in pulsed cavity optomechanics », Phys. Rev. A **84**, 052327 (2011) (cit. on pp. 8, 66, 71).

[Hof+11b] S. G. Hofer, W. Wieczorek, M. Aspelmeyer and K. Hammerer, « Quantum entanglement and teleportation in pulsed cavity optomechanics », Phys. Rev. A **84**, 052327 (2011) (cit. on p. 61).

[Hol21] A. S. Holevo, « Structure of a General Quantum Gaussian Observable », Proc. Steklov Inst. Math. **313**, 70–77 (2021) (cit. on pp. 28, 207).

[HOM87] C. K. Hong, Z. Y. Ou and L. Mandel, « Measurement of subpicosecond time intervals between two photons by interference », Phys. Rev. Lett. **59**, 2044–2046 (1987) (cit. on p. 29).

[HHH96] M. Horodecki, P. Horodecki and R. Horodecki, « Separability of mixed states: necessary and sufficient conditions », Phys. Lett. A **223**, 1–8 (1996) (cit. on pp. 22, 32).

[Hor+09] R. Horodecki, P. Horodecki, M. Horodecki and K. Horodecki, « Quantum entanglement », Rev. Mod. Phys. **81**, 865–942 (2009) (cit. on pp. 21–22, 32).

[Hud74] R. L. Hudson, « When is the wigner quasi-probability density non-negative? », Rep. Math. Phys. **6**, 249–252 (1974) (cit. on pp. 25, 155).

[Hun07] J. D. Hunter, « Matplotlib: a 2d graphics environment », Comput. Sci. Eng. **9**, 90–95 (2007) (cit. on p. vi).

[HE06] P Hyllus and J Eisert, « Optimal entanglement witnesses for continuous-variable systems », New J. Phys. **8**, 51–51 (2006) (cit. on pp. xiii, 21–22, 30–31, 33, 76–77, 128–129, 140, 201, 208).

[Jac82] F. Jackson, « Epiphenomenal Qualia », Philos. Q. **32**, 127–136 (1982) (cit. on p. 3).

[Jac86] F. Jackson, « What mary didn't know », J. Philos. **83**, 291–295 (1986) (cit. on p. 3).

[Jai+16] V. Jain, J. Gieseler, C. Moritz, C. Dellago, R. Quidant and L. Novotny, « Direct measurement of photon recoil from a levitated nanoparticle », Phys. Rev. Lett. **116**, 243601 (2016) (cit. on pp. 41–42).

[Jam47] H. M. James, *Theory of servomechanisms* (Mcgraw Hill, 1947) (cit. on p. 161).

[JNN13] J. Johansson, P. Nation and F. Nori, « Qutip 2: a python framework for the dynamics of open quantum systems », Comput. Phys. Commun. **184**, 1234–1240 (2013) (cit. on pp. 27, 36).

[JNN12] J. Johansson, P. Nation and F. Nori, « Qutip: an open-source python framework for the dynamics of open quantum systems », Comput. Phys. Commun. **183**, 1760–1772 (2012) (cit. on pp. 27, 36).

[JZ85] E. Joos and H. Zeh, « The emergence of classical properties through interaction with the environment », Z. Phys. B: Condens. Matter **59**, 223–243 (1985) (cit. on p. 35).

[KFM08] K. Karrai, I. Favero and C. Metzger, « Doppler optomechanics of a photonic crystal », Phys. Rev. Lett. **100**, 240801 (2008) (cit. on p. 41).

[Kim+02] M. S. Kim, W. Son, V. Bužek and P. L. Knight, « Entanglement by a beam splitter: Nonclassicality as a prerequisite for entanglement », Phys. Rev. A **65**, 032323 (2002) (cit. on p. 29).

[Kot+21] S. Kotler et al., « Direct observation of deterministic macroscopic entanglement », Science **372**, 622–625 (2021) (cit. on p. 137).

[Krä+18] S. Krämer, D. Plankensteiner, L. Ostermann and H. Ritsch, « Quantumoptics. jl: a julia framework for simulating open quantum systems », Comput. Phys. Commun. **227**, 109–116 (2018) (cit. on p. 36).

[Kub66] R Kubo, « The fluctuation-dissipation theorem », Rep. Prog. Phys. **29**, 255 (1966) (cit. on p. 38).

[Kwi+95] P. G. Kwiat, K. Mattle, H. Weinfurter, A. Zeilinger, A. V. Sergienko and Y. Shih, « New high-intensity source of polarization-entangled photon pairs », Phys. Rev. Lett. **75**, 4337–4341 (1995) (cit. on p. 147).

[Kö21] P. M. Köhler, « Towards quantum experiments on gravitating objects », Ph.D. thesis (University of Vienna, 2021) (cit. on p. 6).

[LR23] L. Lami and B. Regula, « No second law of entanglement manipulation after all », Nat. Phys. **19**, 184–189 (2023) (cit. on p. 4).

[Lam18] J. Lammers, « Quantum state retrodiction in gaussian systems », Ph.D. thesis (Leibniz University Hannover, 2018) (cit. on pp. 35, 138).

[LH24] J. Lammers and K. Hammerer, « Quantum retrodiction in gaussian systems and applications in optomechanics », Front. Quantum Sci. Technol. **2**, 1294905 (2024) (cit. on p. 138).

[Lei+16] C. U. Lei, A. J. Weinstein, J. Suh, E. E. Wollman, A. Kronwald, F. Marquardt, A. A. Clerk and K. C. Schwab, « Quantum nondemolition measurement of a quantum squeezed state beyond the 3 db limit », Phys. Rev. Lett. **117**, 100801 (2016) (cit. on p. 54).

[LP95] U. Leonhardt and H. Paul, « Measuring the quantum state of light », Prog. Quantum Electron. **19**, 89–130 (1995) (cit. on pp. 133, 174–175, 177, 182).

[LP93] U. Leonhardt and H. Paul, « Realistic optical homodyne measurements and quasiprobability distributions », Phys. Rev. A **48**, 4598–4604 (1993) (cit. on p. 174).

[Leo03] U. Leonhardt, « Quantum Physics of Simple Optical Instruments », Rep. Prog. Phys. **66**, 1207–1249 (2003) (cit. on pp. 174–175).

[Lou00] R. Loudon, *The quantum theory of light*, 3. ed., Oxford science publications (Oxford Univ. Press, Oxford, 2000) (cit. on pp. 12, 17–18, 175).

[Mag21] L. Magrini, « Quantum measurement and control of mechanical motion at room temperature », Ph.D. thesis (University of Vienna, 2021) (cit. on pp. 40, 42–45, 55, 109, 120–121, 128, 182).

[Mag+22] L. Magrini, V. A. Camarena-Chávez, C. Bach, A. Johnson and M. Aspelmeyer, « Squeezed light from a levitated nanoparticle at room temperature », Phys. Rev. Lett. **129**, 053601 (2022) (cit. on pp. 42, 109, 121, 128, 132–133, 216).

[Mag+21] L. Magrini, P. Rosenzweig, C. Bach, A. Deutschmann-Olek, S. G. Hofer, S. Hong, N. Kiesel, A. Kugi and M. Aspelmeyer, « Real-time optimal quantum control of mechanical motion at room temperature », Nature **595**, 373–377 (2021) (cit. on pp. 40, 42, 44, 58, 109, 121, 138, 143, 151).

[MMS03] P. Marian, T. A. Marian and H. Scutaru, « Bures distance as a measure of entanglement for two-mode squeezed thermal states », Phys. Rev. A **68**, 062309 (2003) (cit. on pp. 49, 70).

[Mar+18] I. Marinković, A. Wallucks, R. Riedinger, S. Hong, M. Aspelmeyer and S. Gröblacher, « Optomechanical Bell test », Phys. Rev. Lett. **121**, 220404 (2018) (cit. on p. 144).

[Mar19] D. E. Marshall, *Complex analysis*, Cambridge mathematical textbooks (2019) (cit. on pp. 84, 161, 163).

[MH18] A. M. Mathai and H. J. Haubold, *Probability and statistics, A course for physicists and engineers* (De Gruyter, Berlin, Boston, 2018) (cit. on pp. 19, 25).

[Mee+15] S. M. Meenehan, J. D. Cohen, G. S. MacCabe, F. Marsili, M. D. Shaw and O. Painter, « Pulsed excitation dynamics of an optomechanical crystal resonator near its quantum ground state of motion », Phys. Rev. X **5**, 041002 (2015) (cit. on p. 151).

[MDC10] H. Miao, S. Danilishin and Y. Chen, « Universal quantum entanglement between an oscillator and continuous fields », Phys. Rev. A **81**, 052307 (2010) (cit. on pp. 58, 70, 73, 99, 101, 115, 138–140, 195).

[Mia+10a] H. Miao, S. Danilishin, H. Müller-Ebhardt and Y. Chen, « Achieving ground state and enhancing optomechanical entanglement by recovering information », New J. Phys. **12**, 083032 (2010) (cit. on pp. 58, 115, 138).

[Mia+10b] H. Miao, S. Danilishin, H. Müller-Ebhardt, H. Rehbein, K. Somiya and Y. Chen, « Probing macroscopic quantum states with a sub-Heisenberg accuracy », Phys. Rev. A **81**, 012114 (2010) (cit. on pp. 58, 115, 138).

[MK08] L. Mišta and N. Korolkova, « Distribution of continuous-variable entanglement by separable gaussian states », Phys. Rev. A **77**, 050302 (2008) (cit. on pp. 63, 66).

[Mod+20] G. Modica, R. Zhu, R. Horvath, G. Beaudoin, I. Sagnes and R. Braive, « Slow propagation of 2 GHz acoustical waves in a suspended GaAs phononic waveguide on insulator », Appl. Phys. Lett. **117**, 193501 (2020) (cit. on p. 45).

[MN17] R. Moghadas Nia, « Multimode optomechanics in the strong cooperativity regime », Ph.D. thesis (University of Vienna, 2017), p. 207 (cit. on pp. 93, 109–113, 116, 128–129, 131, 136, 174, 182, 197, 205).

[NC10] M. A. Nielsen and I. L. Chuang, *Quantum computation and quantum information*, 10th anniversary ed (Cambridge University Press, Cambridge ; New York, 2010), 676 pp. (cit. on pp. 4, 15, 64, 207).

[NFM91] J. W. Noh, A. Fougères and L. Mandel, « Measurement of the quantum phase by photon counting », Phys. Rev. Lett. **67**, 1426–1429 (1991) (cit. on p. 181).

[Nov17] L. Novotny, « Radiation damping of a polarizable particle », Phys. Rev. A **96**, 032108 (2017) (cit. on p. 41).

[O'C+10] A. D. O'Connell et al., « Quantum ground state and single-phonon control of a mechanical resonator », Nature **464**, 697–703 (2010) (cit. on p. 45).

[OK+18] C. F. Ockeloen-Korppi, E. Damskagg, J.-M. Pirkkalainen, A. A. Clerk, F. Massel, M. J. Woolley and M. A. Sillanpaa, « Stabilized entanglement of massive mechanical oscillators », Nature (2018) (cit. on p. 1).

[Pal+13] T. A. Palomaki, J. D. Teufel, R. W. Simmonds and K. W. Lehnert, « Entangling Mechanical Motion with Microwave Fields », Science **342**, 710–713 (2013) (cit. on pp. 1, 8, 58, 61, 66, 71).

[PJR09] M. Paternostro, H. Jeong and T. C. Ralph, « Violations of Bell's inequality for gaussian states with homodyne detection and nonlinear interactions », Phys. Rev. A **79**, 012101 (2009) (cit. on p. 153).

[Per96] A. Peres, « Separability criterion for density matrices », Phys. Rev. Lett. **77**, 1413–1415 (1996) (cit. on pp. 22, 32).

[Pes+20] G. Pesce, P. H. Jones, O. M. Maragò and G. Volpe, « Optical tweezers: theory and practice », Eur. Phys. J. **135**, 949 (2020) (cit. on p. 193).

[Peu+13] C. Peuntinger, V. Chille, L. Mišta, N. Korolkova, M. Förtsch, J. Korger, C. Marquardt and G. Leuchs, « Distributing entanglement with separable states », Phys. Rev. Lett. **111**, 230506 (2013) (cit. on pp. 63, 66).

[Ple05] M. B. Plenio, « Logarithmic negativity: a full entanglement monotone that is not convex », Phys. Rev. Lett. **95**, 090503 (2005) (cit. on pp. 22, 33).

[PEW05] L. Praxmeyer, B.-G. Englert and K. Wódkiewicz, « Violation of Bell?s inequality for continuous-variable EPR states », Eur. Phys. J. D **32**, 227–231 (2005) (cit. on pp. 154–155).

[Rie+16] R. Riedinger, S. Hong, R. A. Norte, J. A. Slater, J. Shang, A. G. Krause, V. Anant, M. Aspelmeyer and S. Gröblacher, « Non-classical correlations between single photons and phonons from a mechanical oscillator », Nature **530**, 313–316 (2016) (cit. on pp. 142, 151).

[Rie+18] R. Riedinger, A. Wallucks, I. Marinković, C. Löschnauer, M. Aspelmeyer, S. Hong and S. Gröblacher, « Remote quantum entanglement between two micromechanical oscillators », Nature **556**, 473–477 (2018) (cit. on p. 1).

[RHB06] K. F. Riley, M. P. Hobson and S. J. Bence, *Mathematical methods for physics and engineering*, 3rd ed (Cambridge University Press, Cambridge ; New York, 2006), 1333 pp. (cit. on p. 163).

[Rob29] H. P. Robertson, « The uncertainty principle », Phys. Rev. **34**, 163–164 (1929) (cit. on p. 14).

[Roe+16] P. Roelli, C. Galland, N. Piro and T. J. Kippenberg, « Molecular cavity optomechanics as a theory of plasmon-enhanced raman scattering », Nat. Nanotechnol. **11**, 164–169 (2016) (cit. on p. 143).

[RI+11] O. Romero-Isart, A. C. Pflanzer, M. L. Juan, R. Quidant, N. Kiesel, M. Aspelmeyer and J. I. Cirac, « Optically levitating dielectrics in the quantum regime: theory and protocols », Phys. Rev. A **83**, 013803 (2011) (cit. on p. 143).

[RI11] O. Romero-Isart, « Quantum superposition of massive objects and collapse models », Phys. Rev. A **84**, 052121 (2011) (cit. on p. 143).

[Ros+19] M. Rossi, D. Mason, J. Chen and A. Schliesser, « Observing and Verifying the Quantum Trajectory of a Mechanical Resonator », Phys. Rev. Lett. **123**, 163601 (2019) (cit. on pp. 58, 93, 109, 138, 184–185).

[Run+19] R. P. Rundle, T. Tilma, J. H. Samson, V. M. Dwyer, R. F. Bishop and M. J. Everitt, « General approach to quantum mechanics as a statistical theory », Phys. Rev. A **99**, 012115 (2019) (cit. on p. 23).

[RSV17] S. Ryl, J. Sperling and W. Vogel, « Quantifying nonclassicality by characteristic functions », Phys. Rev. A **95**, 053825 (2017) (cit. on p. 27).

[SN20] J. J. Sakurai and J. Napolitano, *Modern quantum mechanics*, Third edition. (Cambridge University Press, 2020) (cit. on p. 12).

[SC07] R. G.-P. Sanchez and N. J. Cerf, « Quantum information with optical continuous variables: from Bell tests to key distribution », Ph.D. thesis (Université libre de Bruxelles, 2007) (cit. on pp. 29–30, 207).

[Sch01] W. Schleich, *Quantum optics in phase space*, 1st ed. (Wiley-VCH, Berlin ; New York : 2001) (cit. on pp. 23–24, 144).

[SK10] A. Schliesser and T. J. Kippenberg, « Cavity optomechanics with whispering-gallery mode optical micro-resonators », Adv. At. Mol. Opt. Phys. **58**, 207–323 (2010) (cit. on p. 45).

[Sch07] M. Schlosshauer, *Decoherence and the quantum-to-classical transition*, The Frontiers Collection (Springer, 2007) (cit. on pp. 5, 35).

[Sch05] M. Schlosshauer, « Decoherence, the measurement problem, and interpretations of quantum mechanics », Rev. Mod. Phys. **76**, 1267–1305 (2005) (cit. on p. 35).

[Sch19] M. Schlosshauer, « Quantum decoherence », Phys. Rep. **831**, 1–57 (2019) (cit. on pp. 5, 35).

[Sch17] R. Schnabel, « Squeezed states of light and their applications in laser interferometers », Phys. Rep. **684**, 1–51 (2017) (cit. on p. 147).

[Sch18] W. Schottky, « Über spontane stromschwankungen in verschiedenen elektrizitätsleitern », Ann. Phys. **362**, 541–567 (1918) (cit. on p. 176).

[Sch30] E. Schroedinger, « Zum heisenbergschen unschärfeprinzip », Sitzungsber. K. Preuss. Akad. Wiss., Phys.-math. Kl. **14** (1930) (cit. on p. 14).

[SC85] B. L. Schumaker and C. M. Caves, « New formalism for two-photon quantum optics. II. Mathematical foundation and compact notation », Phys. Rev. A **31**, 3093–3111 (1985) (cit. on pp. 29, 147–148, 150).

[Sha+15] L. K. Shalm et al., « Strong loophole-free test of local realism », Phys. Rev. Lett. **115**, 250402 (2015) (cit. on p. 3).

[Sha85] J. Shapiro, « Quantum noise and excess noise in optical homodyne and heterodyne receivers », IEEE J. Quantum Electron. **21**, 237–250 (1985) (cit. on p. 174).

[SW84] J. Shapiro and S. Wagner, « Phase and amplitude uncertainties in heterodyne detection », IEEE J. Quantum Electron. **20**, 803–813 (1984) (cit. on p. 174).

[Sho+19] I. Shomroni, L. Qiu, D. Malz, A. Nunnenkamp and T. J. Kippenberg, « Optical backaction-evading measurement of a mechanical oscillator », Nat. Commun. **10**, 2086 (2019) (cit. on p. 54).

[Sim00] R. Simon, « Peres-Horodecki Separability Criterion for Continuous Variable Systems », Phys. Rev. Lett. **84**, 2726–2729 (2000) (cit. on pp. 22, 24, 26, 32, 67).

[Teb+21] F. Tebbenjohanns, M. L. Mattana, M. Rossi, M. Frimmer and L. Novotny, « Quantum control of a nanoparticle optically levitated in cryogenic free space », Nature **595**, 378–382 (2021) (cit. on p. 42).

[Teu+11] J. D. Teufel, T. Donner, D. Li, J. W. Harlow, M. S. Allman, K. Cicak, A. J. Sirois, J. D. Whittaker, K. W. Lehnert and R. W. Simmonds, « Sideband cooling of micromechanical motion to the quantum ground state », Nature **475**, 359–363 (2011) (cit. on pp. 137, 143).

[Til+16] T. Tilma, M. J. Everitt, J. H. Samson, W. J. Munro and K. Nemoto, « Wigner functions for arbitrary quantum systems », Phys. Rev. Lett. **117**, 180401 (2016) (cit. on p. 23).

[Tol] P. Tol, *Paul Tol's notes -> Qualitative color schemes -> Figure 5: Medium-contrast*, URL: `https://personal.sron.nl/~pault/` [online content created 2021-04-02; accessed 2024-05-29] (cit. on p. vii).

[Tru85] D. R. Truax, « Baker-Campbell-Hausdorff relations and unitarity of SU(2) and SU(1,1) squeeze operators », Phys. Rev. D **31**, 1988–1991 (1985) (cit. on pp. 147–148).

[Tsa+17] Y. Tsaturyan, A. Barg, E. Polzik and S. A., « Ultracoherent nanomechanical resonators via soft clamping and dissipation dilution », Nat. Nanotechnol. **12**, 776–783 (2017) (cit. on pp. 45–46, 93, 109, 184).

[Tse+19] M. Tse et al., « Quantum-enhanced Advanced LIGO detectors in the era of gravitational-wave astronomy », Phys. Rev. Lett. **123**, 231107 (2019) (cit. on pp. 5, 138, 147).

[VW02] G. Vidal and R. F. Werner, « Computable measure of entanglement », Phys. Rev. A **65**, 032314 (2002) (cit. on pp. 22, 33).

[VW94] W. Vogel and D.-G. Welsch, *Quantum optics* (Springer, Berlin [u.a.], 1994) (cit. on pp. 12, 29, 147).

[Vol+13] C. E. Vollmer, D. Schulze, T. Eberle, V. Händchen, J. Fiurášek and R. Schnabel, « Experimental entanglement distribution by separable states », Phys. Rev. Lett. **111**, 230505 (2013) (cit. on pp. 63, 66).

[VN96] J. Von Neumann, *Mathematical foundations of quantum mechanics*, Princeton landmarks in mathematics and physics (Princeton University Press, Princeton Chichester, 1996) (cit. on pp. 5, 7, 35).

[WC86] N. G. Walker and J. E. Carroll, « Multiport homodyne detection near the quantum noise limit », Opt. Quant. Electron. **18**, 355–363 (1986) (cit. on pp. 174, 181).

[Wal87] N. Walker, « Quantum Theory of Multiport Optical Homodyning », J. Mod. Opt. **34**, 15–60 (1987) (cit. on pp. 174, 181–182).

[WM06] D. F. Walls and G. J. Milburn, *Quantum optics* (John Wiley & Sons, Ltd, 2006) (cit. on pp. 12, 146).

[Wee+12] C. Weedbrook, S. Pirandola, R. García-Patrón, N. J. Cerf, T. C. Ralph, J. H. Shapiro and S. Lloyd, « Gaussian quantum information », Rev. Mod. Phys. **84**, 621–669 (2012) (cit. on pp. 23, 28–30, 148, 150, 207).

[WW01] R. F. Werner and M. M. Wolf, « Bound Entangled Gaussian States », Phys. Rev. Lett. **86**, 3658–3661 (2001) (cit. on pp. 22, 32).

[Wer89] R. F. Werner, « Quantum states with Einstein-Podolsky-Rosen correlations admitting a hidden-variable model », Phys. Rev. A **40**, 4277–4281 (1989) (cit. on pp. 21, 153).

[Wes+21] T. Westphal, H. Hepach, J. Pfaff and M. Aspelmeyer, « Measurement of gravitational coupling between millimetre-sized masses », Nature **591**, 225–228 (2021) (cit. on p. 46).

[Wie+15] W. Wieczorek, S. G. Hofer, J. Hoelscher-Obermaier, R. Riedinger, K. Hammerer and M. Aspelmeyer, « Optimal State Estimation for Cavity Optomechanical Systems », Phys. Rev. Lett. **114**, 223601 (2015) (cit. on pp. 58, 138).

[Wil+15] D. J. Wilson, V. Sudhir, N. Piro, R. Schilling, A. Ghadimi and T. J. Kippenberg, « Measurement-based control of a mechanical oscillator at its thermal decoherence rate », Nature **524**, 325–329 (2015) (cit. on p. 42).

[Win18] K. Winkler, « An analytical and computational approach to steady-state optomechanical systems by quantum langevin equations », Master thesis (University of Vienna, 2018) (cit. on p. 163).

[WM09] H. M. Wiseman and G. J. Milburn, *Quantum measurement and control*, 1st ed. (Cambridge University Press, 2009) (cit. on pp. 15, 35–36, 75, 133, 174, 181–183).

[WEP03] M. M. Wolf, J. Eisert and M. B. Plenio, « Entangling power of passive optical elements », Phys. Rev. Lett. **90**, 047904 (2003) (cit. on p. 29).

[Wol+22] E. A. Wollack, A. Y. Cleland, R. G. Gruenke, Z. Wang, P. Arrangoiz-Arriola and A. H. Safavi-Naeini, « Quantum state preparation and tomography of entangled mechanical resonators », Nature **604**, 10.1038/s41586-022-04500-y (2022) (cit. on p. 144).

[WZ82] W. K. Wootters and W. H. Zurek, « A single quantum cannot be cloned », Nature **299**, 802–803 (1982) (cit. on pp. 177, 181).

[Yu+20] H. Yu, L. McCuller, M. Tse, N. Kijbunchoo, L. Barsotti and N. Mavalvala, « Quantum correlations between light and the kilogram-mass mirrors of LIGO », Nature **583**, 43–47 (2020) (cit. on pp. 54, 138–139, 147).

[YS80] H. Yuen and J. Shapiro, « Optical communication with two-photon coherent states–Part III: Quantum measurements realizable with photoemissive detectors », IEEE Trans. Inf. Theory **26**, 78–92 (1980) (cit. on p. 174).

[YC83] H. P. Yuen and V. W. S. Chan, « Noise in homodyne and heterodyne detection », Opt. Lett. **8**, 177–179 (1983) (cit. on p. 174).

[Zeh70] H. Zeh, « On the interpretation of measurement in quantum theory », Found. Phys. **1**, 69–76 (1970) (cit. on pp. 5, 35).

[Zeh73] H. Zeh, « Toward a quantum theory of observation », Found. Phys. **3**, 109—116 (1973) (cit. on p. 35).

[Zur82] W. H. Zurek, « Environment-induced superselection rules », Phys. Rev. D **26**, 1862–1880 (1982) (cit. on pp. 5, 35, 40).

[Zur81] W. H. Zurek, « Pointer basis of quantum apparatus: Into what mixture does the wave packet collapse? », Phys. Rev. D **24**, 1516–1525 (1981) (cit. on pp. 35, 40).

[Zur03] W. H. Zurek, « Decoherence, einselection, and the quantum origins of the classical », Rev. Mod. Phys. **75**, 715–775 (2003) (cit. on pp. 5, 35).